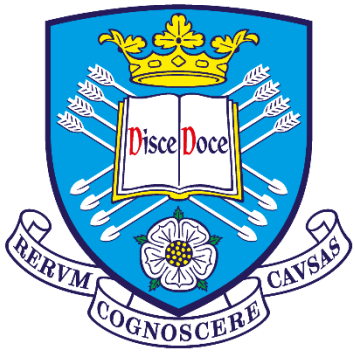

The University Of Sheffield.

High quality factor cold sintered composites for microwave applications

Thesis by

Sinan Faouri

Submitted in partial fulfilment for the degree of

Doctor of Philosophy

Thesis supervisors

Prof. Ian M Reaney[1]

Prof. Alan Tennant[2]

1 Department of Material Science and Engineering

2 Department of Electronic and Electrical Engineering

University of Sheffield

January 2019

To my lovely wife and adorable daughter that we had been blessed by this year, I dedicate this work…

Sinan

"Three rules of work: Out of clutter find simplicity; From discord find harmony; In the middle of difficulty lies opportunity. Don't waste your time worrying about uncertain future, just start doing your work and enjoy praising sense of urgency"

Inspired by: Albert Einstein, Ian M. Reaney and Anthony R. West

Published paper

- High quality factor cold sintered Li_2MoO_4-$BaFe_{12}O_{19}$ composites for microwave applications, Acta Materiala, published 2019

Conferences participation

1. 15^{th} conference and exhibition of European ceramics society, 2017, Budapest
2. Electronic Applications of Materials, American ceramics society, 2018, Orlando

Acknowledgments

I would like to express my gratitude to my supervisor, Prof Ian Reaney, who inspired and encouraged me from the beginning to enjoy research and whatever I am doing in general. We always discuss challenges and problems and I always leave his office relieved and assured that everything will surf in the right direction eventually. I never forget his reaction after texting him at 4:00 AM on 31st of May, 2018 to let him know about my wife's getting in labour way before her time back in Jordan. He insisted that this was an unmissable event in one's lifetime and urged me to book the first plane to witness the delivery of my first baby. Hats off to a significant personality indeed in my journey of life.

I would like to thank Prof Derek Sinclair as well for his help in impedance spectroscopy, and all the meetings and discussions that we had in his office even though I am not his student. A real kindness and dedication from a gentleman. Special thanks go also to Dr. Ali Mostaed for all his help in Transmission Electron Microscopy (TEM) and continuous support throughout my PhD. At the end of my PhD journey, he is now a friend more than a colleague. I express my gratitude also to Dr. Julian Dean for his contribution with Finite Element Modelling (FEM). All the meetings we had together were fruitful and helpful. Thanks go to Dr. Dawei Wang for his help in measuring microwave dielectric properties and for support in general. Prof Yiannis Vardaxoglou, Prof William Whittow and their team at University of Loughborough are acknowledged also for their efforts in measuring the magnetic properties of our samples.

Finally, I'd like to thank my parents and my brothers for their unconditional love and support all the way through. My lovely wife Leen and awesome angel daughter Fairouz, thanks for being in my life and supporting me in every step of this enjoyable journey as I would like to call it. I will never forget your effort and sacrifice for me. I'll finish my acknowledgements with big thanks to my fellow PhD students in Sheffield, and true friends in Jordan, United Kingdom and all over the world who care about me.

Disclaimer: 1. Magnetic permeability measurements have been performed courtesy of Prof. Yiannis Vardaxoglou's team at the University of Loughborough.

2. FEM has been performed courtesy of Dr. Julian Dean at the University of Sheffield.

3. TEM has been performed courtesy of Dr. Ali Mostaed at the University of Sheffield.

Abstract

Ceramic-ceramic composites intended for applications as substrates for microwave MW antennas have been fabricated and investigated. $BaTi_4O_9$ – $BaFe_{12}O_{19}$ (BT4-BF12) and BF12 – TiO_2 composites were initially prepared using conventional sintering but it became obvious early on in this study that interaction between the end-member phases resulted in a significant deterioration of properties. As a consequence, cold sintering was attempted in which ceramics densify at <200 ^{O}C and therefore interdiffusion between the end members is negligible. To facilitate cold sintering, Li_2MoO_4 (LMO) was used instead of BT4 as one end member since it has been shown to densify at 120 ^{O}C using a pressure mediated hydrothermal route. Dense cold sintered ceramics have competitive MW properties, with quality factor, Qf = 30,000 and relative permittivity, ε_r = 5.5.

(1-x)LMO-xBF12 (0.00≤x≤0.15) were cold sintered at 120^{o}C and their structure and properties characterized. X-ray diffraction (XRD), scanning electron microscopy (SEM) and transmission electron microscopy (TEM) confirmed that compositions were dual phase and had a dense microstructure. Composites in the xBF12-(1-x)LMO (0.0≤x≤0.15) series resonated at MW frequencies (~5-6GHz) with 5.6≤ε_r≤5.8 and 16,000≤Qf≤22,000 GHz, despite the black colour of compositions with x > 0. The permeability (μ) of the composites was measured in the X band (~8 GHz) and showed an increase from 0.94 (x=0.05) to 1.02 (x=0.15). Finite element modelling revealed that the volume fraction of BF12 dictates the conductivity of the material, with a percolation threshold at 10 vol.% BF12 but changes in ε_r as a function of x were readily explained using a series mixing model. In summary, these composites are considered suitable for the fabrication of dual mode or enhanced bandwidth microstrip patch antennas. Conventionally sintered LMO-BF12 composites failed to produce high quality ceramics and were brittle with unwanted second phases.

Cold sintering of several further composites was also performed, including LMO-TiO_2 and LMO-$BaTiO_3$. Of particular note however, were dense ($\simeq 95\%$) (1-x)K_2MoO_4-xBF12 composites which resonated at MW frequencies with a 5.6≤ε_r≤5.8, temperature coefficient factor of resonance, -66≤TCF≤-39 ppm/°C and Qf ≃14,000 GHz for 0.05≤x≤0.15. No interaction was noted between the two end members according to XRD, SEM and chemical mapping using energy dispersive X-ray spectroscopy. (1-x)LMO-$x$$Li_{1.5}Al_{0.5}Ge_{1.5}P_3O_{12}$ (LAGP) were also fabricated but as anticipated this composite became conducting for low values of x. TCF varied from -169 to -43 ppm/°C for x=0.05≤x≤0.15 but high relative density (94%) could be achieved.

Overall, cold sintering proved a successful route for the fabrication of ceramic-ceramic composites for MW applications with a number of systems showing great promise.

However, tuning TCF to zero proved problematic within the systems described due to the limited range of x (<0.2) for which dense ceramics could be achieved.

Contents

Chapter1: Introduction and aims

1.1 Microstrip patch antennas (MPAs)

Microwave (MW) dielectric ceramics have gained considerable attention because of their suitability for the fabrication of substrates, resonators and filters in wireless and satellite communication technology. MPAs have gained significant usage due to their light weight, ease of fabrication and low cost [1]. The main disadvantage of MPAs is their narrow bandwidth (BW) [2] since high relative permittivity (ε_r) substrates are used to shrink their dimensions to give ultra-small, high BW antennas, the goal of any MW engineer. This classic paradox of increasing ε_r at the expense of BW and quality factor (*Qf*) stimulates designers to derive different methods to enhance BW, such as the use of thicker substrates or parasitic patches [2]. However, thick substrates cause problems in impedance matching, while parasitic patches linearly increase the size of the antenna and complicate its design [2]. The 'holy grail' therefore is to design advanced materials, composites or metamaterials to act as dielectric substrates for MPAs which intrinsically give larger BWs.

Microstrip antennas are divided into four types: MPAs, microstrip dipoles, printed slot antennas, and microstrip travelling wave antennas [1]. An MPA consists mainly of a dielectric substrate sandwiched between a metallic patch on its top and a ground plane beneath which are connected via a feedline. Figure 1.1 shows the basic design of an MPA[3]:

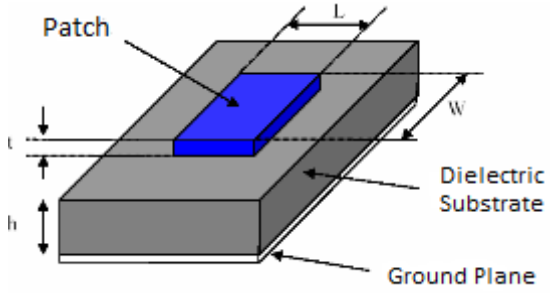

Figure 1.1. MPA schematic showing significant design parameters

1.2 Limitation of materials

The relationship between the size of an MPA, represented by the wavelength of the electromagnetic wave inside the patch, and ε_r of the waveguide is given in Equation 1.1 [4]:

$$\frac{\lambda g}{2} = \frac{\lambda}{2} * \frac{1}{\sqrt{\varepsilon_{eff}}} \qquad \text{Equ. 1.1}$$

where λg is the guide wavelength, λ is the wavelength of free space and ε_{eff} is the permittivity of the waveguide (usually equivalent to ε_r). From Equation 1.1, decreasing the size of the antenna requires increasing ε_r. However, it is undesirable for increasing ε_r to occur at the loss of the resonant quality of the dielectric (Q, often multiplied by the resonant frequency, f_o, to give the material constant, *Qf*). Q is approximately equal to $\frac{1}{tan\delta}$ where tanδ is the loss of the dielectric (for more detailed descriptions of key microwave material metrics see chapter 2). Reaney et al. [5] indicated an inverse relationship for commercial resonators between ε_r and $\log_{10}Qf$ as shown in Figure 1.2.

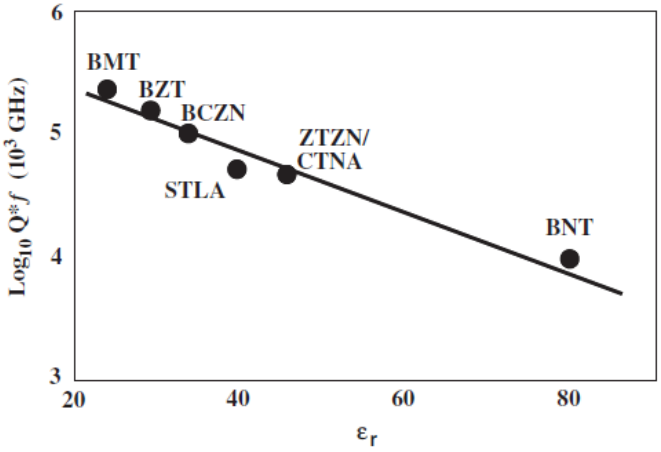

Figure 1.2. Relationship between ε_r and *Qf* for temperature-stable commercial resonators [5]

Generally speaking there is a wide range of temperature stable low loss dielectrics that can be used as antenna substrates but for some values of ε_r, e.g. between 45-75, no commercial materials are available. Moreover, most commercial systems have been optimised for ε_r > 20 but as frequencies of telecommunications increase to accommodate high transmission rates and we move from 4G to 5G technology, lower ε_r, temperature stable ceramics are required. Currently, all ceramic substrates for MPAs are fabricated using high temperature (>900 ^{o}C) conventional sintering. The dense ceramic bodies are then coated with the necessary metallic architecture before being placed as complete components onto PCBs.

1.3 Transition from 4G to 5G: the potential role of cold sintering

4G systems operate in the frequency range (2-8) GHz, while 5G systems will ultimately operate at much higher frequencies (up to 30 GHz) to increase network efficiency and data transmission rates. For low cost antennas, polymer printed circuit boards (PCBs) based on PTFE may be used for lower initial 5G frequencies [6], [7] but their dielectric losses

may prove too high for 5G application at ~30GHz. Thus, highly integratable (low processing temperature), lower loss substrates may be required as we move from 4G to 5G. Cold sintered ceramics process at <200 ^{o}C and thus may prove useful as replacements for polymers in 5G applications. In addition, cold sintering offers a huge reduction in temperature and sintering time which means less energy is wasted throughout the processing, reducing fabrication costs [8], [9] and simultaneously decreasing CO_2 emissions which may prove to be a critical motivator for its uptake by industry in the future[9]. Richard Clark, a senior technical specialist for Morgan Advanced Materials has stated that 'a scaled up cold sintering process could save up billions of dollars by substituting high temperature furnaces with low temperature (<300 ^{o}C) hot presses'[9].

In terms of antenna fabrication, metallic patches and ground planes are easily fabricated by screen printing. If similar slurry-based techniques could be adopted for cold sintered ceramics (tape casting for simple shapes and possibly 3D printing for complex shapes), the fabrication of components could be carried out cheaply and reliably at low temperatures [10]. However, presently the main challenges for cold sintering lie in our yet fledgling knowledge of densification [11]. For example, in this thesis, composites consisting of $BaFe_{12}O_{19}$ - Li_2MoO_4 (BF12-LMO) have been developed and show the most promise amongst related several systems but the big picture behind the densification is yet to fully emerge. It is worth noting however, that conventional sintering methods failed to produce useful composites, suggesting that cold sintering is not only environmentally advantageous but a viable route for new materials, that may one day circumvent the BW restrictions associated with high ε_r substrates.

1.4 Key aims of research

The key aims of the project are therefore to:

i) Fabricate composites utilising a range of cold sinterable compositions based on molybdates and to include end members that will enhance ε_r and magnetic permeability (μ) in a systematic manner.
ii) Utilise cold sintering to reduce energy, time and cost to produce the substrates for MPAs.
iii) Investigate the mechanism of cold sintering.
iv) Demonstrate the clear advantages that cold sintering has over conventionally sintering composites.

1.5 Objectives

i) Investigate $BaFe_{12}O_{19}$- $BaTi_4O_9$ composites using conventional solid state sintering and study its microstructure, phases and electrical properties.

ii) Fabricate $BaFe_{12}O_{19}$- TiO_2 using conventional solid state sintering and study its microstructure, phases and electrical properties.

iii) Cold sinter and study the microstructure and electrical properties of: $BaFe_{12}O_{19}$- Li_2MoO_4, TiO_2- Li_2MoO_4, $Y_3Fe_5O_{12}$- Li_2MoO_4, $BaFe_{12}O_{19}$- Na_2MoO_4, $BaFe_{12}O_{19}$- K_2MoO_4, $BaTiO_3$- Li_2MoO_4 "nano scale $BaTiO_3$", $BaTiO_3$- Li_2MoO_4 "micro scale $BaTiO_3$" and $Li_{1.5}Al_{0.5}Ge_{1.5}P_3O_{12}$ - Li_2MoO_4

1.6 References

[1] I. Singh and V. Tripathi, "Micro strip patch antenna and its applications: a Survey," *Int. j. comput. technol. appl.,* vol. 2, p. 1595-1599, 2011.

[2] C. Mak, K. Luk, K. Lee and Y. Chow, "Experimental study of a microstrip patch antenna with an L-shaped probe," *IEEE Trans. Antennas Propag.,* vol. 48, p. 777-783, 2000.

[3] I. Ahmed, M. S. Arefin, M. S. Hussain and M. Z. Shames, "Performance Study of Microstrip patch Antenna for GPS Communication System," *IJSER.,* vol. 4, p. 2030-2032, 2013.

[4] M. Mirsaneh, O. P. Leisten, B. Zalinska and I. M. Reaney, "Circularly Polarized Dielectric-Loaded Antennas," *Adv. Funct. Mater.,* vol. 18, p. 2293–2300, 2008.

[5] I. M. Reaney and D. Iddles, "Microwave dielectric ceramics for resonators and filters in mobile phone networks," *J. Am. Ceram. Soc.,* vol. 89, p. 2063-2072, 2006.

[6] [Online]. Available: https://www.rogerscorp.com/documents/1460/acm/articles/High-Frequency-Circuit-Materials-Attributes.pdf. [Accessed 9th April 2019].

[7] [Online]. Available: http://blog.rogerscorp.com/2017/08/14/5g-wireless-technology-paving-road-internet-things-iot/. [Accessed 9th April 2019].

[8] S. Funahashi, J. Guo, H. Guo, K. Wang, A. L. Baker, K. Shiratsuyu and C. A. Randall, "Demonstration of the cold sintering process study for the densification and grain growth of ZnO ceramics.," *J. Am. Ceram. Soc.,* vol. 100, p. 546–553, 2017.

[9] [Online]. Available: https://www.mri.psu.edu/mri/newspubs/focus-materials/advanced-manufacturing/new-process-sintering-ceramics-low-temperatures. [Accessed 2nd June 2018].

[10] A. M. Ramly, N. A. Malek, S. Y. Mohamad and M. A. Sukor, “Design of a Circular Patch Antenna for 3D Printing,” *ICCCE 2016.,* vol. 92, p. 406-410, 2016.

[11] J.-P. Maria, X. Kang, R. D. Floyd, E. C. Dickey, H. Guo, J. Guo, A. Baker, S. Funihashi and C. A. Randall, “Cold sintering: Current status and prospects,” *J. MATER. RES.,* vol. 32, p. 3205–3218, 2017.

Chapter 2: Literature survey

2.1 Microwave (MW) material properties

The concept of a MW resonators was first reported by Richtmyer in the 1930s [1]. It featured a cylindrical ceramic puck for single mode resonator applications where electric and magnetic fields are considered to form a standing wave according to Figure 2.1 [1].

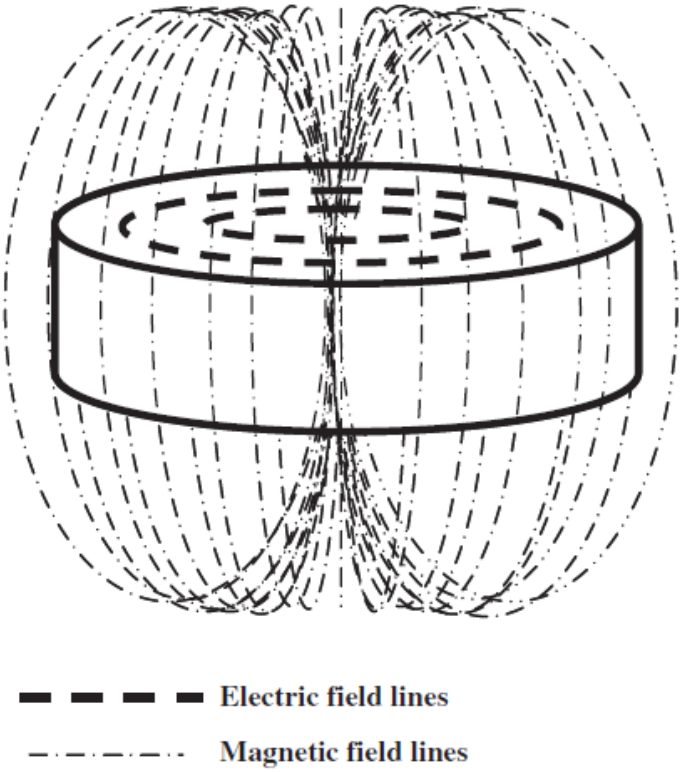

Figure 2.1. Richtmyer's concept of cylindrical ceramic pucks showing interaction of electric and magnetic fields, after Reaney and Iddles [1]

In modern electronics, three important parameters need to be enhanced in a dielectric ceramic; relative permittivity ε_r, quality factor (Q) and temperature coefficient of the resonant frequency (TCF) [1].

2.1.1 Relative Permittivity ε_r

According to Equation 2.1 increasing ε_r decreases resonator diameter for a given resonant frequency:

$$f_o \approx C/(\lambda_d \varepsilon_r^{1/2}) \approx C/(D \varepsilon_r^{1/2}) \qquad \text{Equ. 2.1}$$

where C is the speed of light in vacuum and λ_d is the wavelength of the standing wave along the diameter (D) of a resonator. The signal propagation delay or propagation time delay (T_{PD}) also varies with ε_r according to Equation 2.2 [2]:

$$T_{PD} = (\varepsilon_r)^{1/2} / C \qquad \text{Equ. 2.2}$$

Some high speed applications such as radar applications require decreased ε_r to allow a nonsignificant signal propagation time delay [2].

2.1.2 Quality factor, *Q*

The quality factor Q may be regarded as the inverse of dielectric loss (1/tan δ) and is given by Equation 2.3 [1]:

$$Q = f/\Delta f \qquad \text{Equ. 2.3}$$

where f is the resonance frequency and Δf is the bandwidth taken at 3 dB below the maximum transmitted power at resonance as appears in Figure 2.2 [1]:

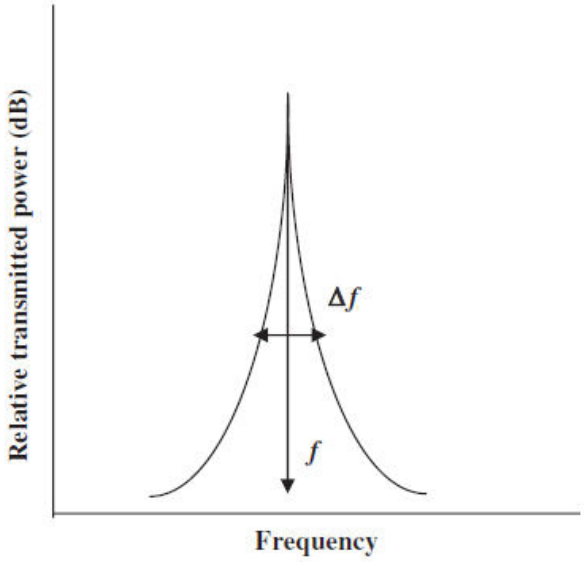

Figure 2.2. *Q* dependence on resonant frequency and bandwidth

Q is frequency dependent (decreases with increasing f) but when multiplied by f, *Qf* becomes an approximate material constant that can be used to compare ceramics.

2.1.3 Temperature coefficient factor of resonant frequency (TCF)

TCF represents the measurement of drift of resonant frequency with respect to temperature change as defined in Equation 2.4 [[1] , [3]] :

$$TCF = (f_2-f_1)/f_1(T_2-T_1) \qquad \text{Equ. 2.4}$$

where f_1 and f_2 are frequencies corresponding to temperatures T_1 and T_2, respectively. Ideally, materials to be used in MW circuits should have low values of TCF ($\pm 2\ MK^{-1}$) to compensate for the MW cavity's thermal expansion [1]. TCF is related to the temperature coefficient of permittivity (TCε) and temperature coefficient of capacitance (TCC) by Equations 2.5 and 2.6 [1] :

$$TCF = -(1/2\ TC\varepsilon + \alpha_L) \qquad \text{Equ. 2.5}$$

$$TCF = -1/2(TCC + \alpha_L) \qquad \text{Equ. 2.6}$$

where α_L is the linear expansion coefficient.

2.2 Factors which control MW properties

Table 2.1 shows the current and popular ceramics used as MW resonators [1].

Material	Abbreviation	ε_r	$Q \times f_0$ (GHz)	Structure
$BaMg_{1/3}Ta_{2/3}O_3$	(BMT)	24	250 000	Comp. Per.
$BaZn_{1/3}Ta_{2/3}O_3$	(BZT)	29	150 000	Comp. Per.
$Ba(Co,Zn)_{1/3}Nb_{2/3}O_3$	(BCZN)	34	90 000	Comp. Per.
$SrTiO_3$–$LaAlO_3$	(STLA)	39	60 000	Simp. Per
$CaTiO_3$–$NdAlO_3$	(CTNA)	45	48 000	Simp. Per
$ZrTiO_4$–$ZnNb_2O_6$	(ZTZN)	44	48 000	$\alpha\ pbO_2$

Comp., complex; Per, perovskite; Simp., simple; TTB, tetragonal tungsten bronze; MW, microwave.

Table 2.1. Current zero TCF commercial MW cavity resonators used as base stations

The current base station cavity resonator's market is dominated by CTNA and ZTZN with *Qf* ~48,000 GHz) which is sufficient for propagating and filtering signals [1]. The dependence between *Qf* and ε_r for commercial zero TCF ceramics is plotted in Figure 1.2 (see chapter 1). No commercial ceramics exist between ZTZN/CTNA and BNT for $45<\varepsilon_r<70$. A more general descriptive relation between ε_r and *Qf* for various applications is shown in Figure 2.3 [4].

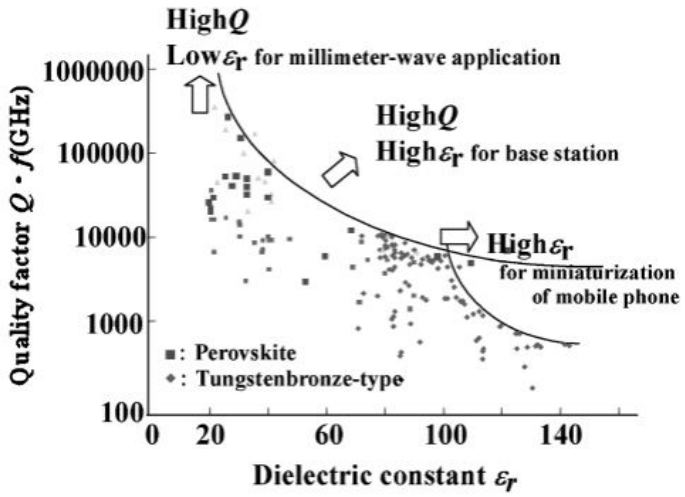

Figure 2.3. ε_r Vs. *Qf* of three different applications areas [4]

From Figure 2.3, base stations require materials with medium ε_r and high *Q* to act as cavity MW resonators, whereas the mobile handsets require higher ε_r which results in lower *Qf* (<10,000 GHz). Substrate and millimetre wave applications are in the third application area with low ε_r < 15 but with high *Qf*>70,000 GHz. ε_r increases in ceramics which contain ions with greater polarizability such as Nb^{+5} and Ti^{+4} or through the use crystal chemistries such as the perovskite structure that are known to enhance the polarizability of a given species through optimisation of its coordination [1] , [5].

2.2.1 Factors controlling TCF

2.2.1.1 The role of ε_r

Harrop [6] compared TCC and ε_r of some paraelectric materials for the first time in 1960s, as shown in Figure 2.4 [[1], [6]]. He observed that increasing ε_r invariably increased TCC.

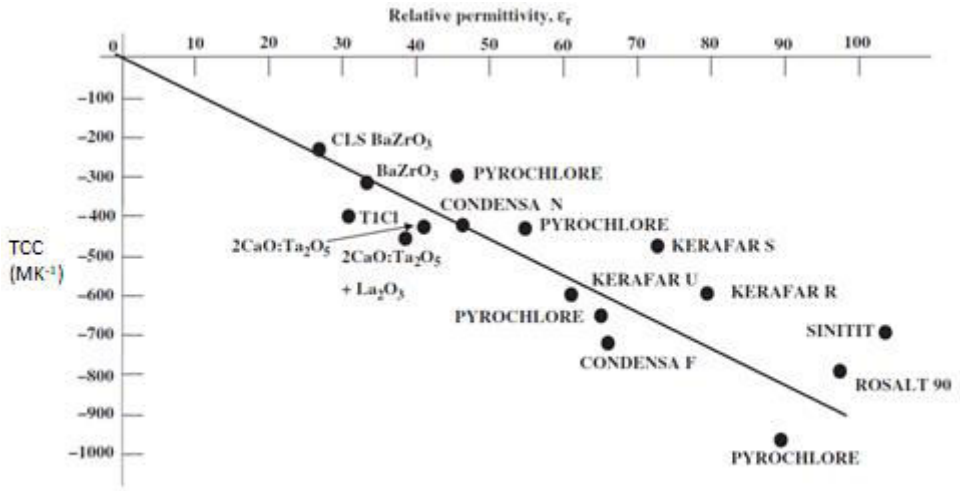

Figure 2.4. TCC as a function of ε_r of different paraelectric materials

Furthermore Harrop [6] worked on the Classius-Mosotti (CM) equation (Equation. 2.7) to justify the empirical relationships between αj, TCC, TCε, TCF and ε_r using and giving rise to the following equations (Equation 2.8-Equation 2.10) where Equation 2.10 is the Clausius-Mosotti equation in its differentiation form [1, 6]:

$$\frac{\varepsilon_r - 1}{\varepsilon_r + 2} = \frac{4\pi}{3} \sum N_j \alpha_j \qquad \text{Equ. 2.7}$$

$$TCC = -\alpha_L \varepsilon_r \qquad \text{Equ. 2.8}$$

$$TC\varepsilon = -\alpha \varepsilon_r \qquad \text{Equ. 2.9}$$

$$TCC = \frac{1}{C}\left(\frac{\partial C}{\partial T}\right)_p = \frac{(\varepsilon_r - 1)(\varepsilon_r + 2)}{\varepsilon_r}\left(\frac{1}{3\alpha}\left(\frac{\partial \alpha}{\partial T}\right)_p - \alpha_L\right) + \alpha_L \qquad \text{Equ. 2.10}$$

where N_j is the concentration of atoms, and α_j is the polarizability, C is capacitance, α_L is linear expansion coefficient, and α is the polarizability for a macroscopic volume V. Equations 2.8 and 2.9 can be justified where the value of $\frac{1}{3\alpha}\left(\frac{\partial \alpha}{\partial T}\right)_p$ is negligible and can be considered as zero. For small values of α_L, following Equ. 2.5, a linear relationship between ε_r and TCF has been demonstrated by Seabra et al [7] in their work on the $xCaTiO_3$- (1-x)$LaMg_{1/2}Ti_{1/2}O_3$ solid solution, Figure 2.5 [7]:

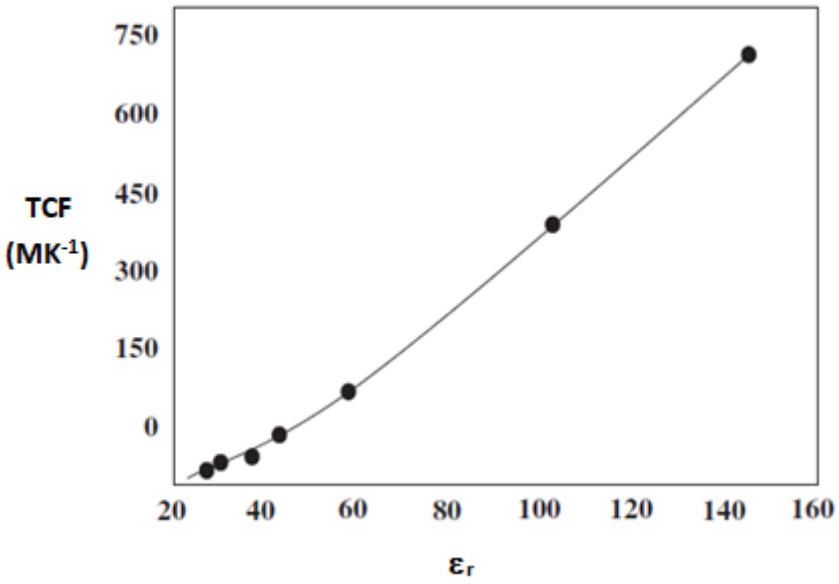

Figure 2.5. Linear relationship between ε_r and TCF of $CaTiO_3$- (1-x)$LaMg_{1/2}Ti_{1/2}O_3$

Harrop's method [6] was the first to indicate a relationship between TCC and ε_r, however, it did not take into account the role of phase transitions on TCC and therefore TCε and TCF.

2.2.1.2 Phase Transitions and TCF

The room temperature value of ε_r does not always control TCF as demonstrated by Colla et al. [8] who indicated that TCF was also controlled by the onset of octahedral tilt transitions for Ba- and Sr-based complex perovskites. For Sr- and Ba-based complex perovskites, TCF also depends on tolerance factor (*t*, Equation. 2.11) rather than uniquely ε_r [9]:

$$t = \frac{(R_A + R_O}{\sqrt{2}(R_B + R_O)} \qquad \text{Equ. 2.11}$$

where R_A, R_O and R_B are the radii of A, O and B site ions respectively. *t* controls the temperature of the onset of octahedral tilt transition and therefore TCF. The dependence of TCε on the *t* for a various Ba- and Sr- based complex perovskites is shown in Figure 2.6, after Reaney et al. [9]:

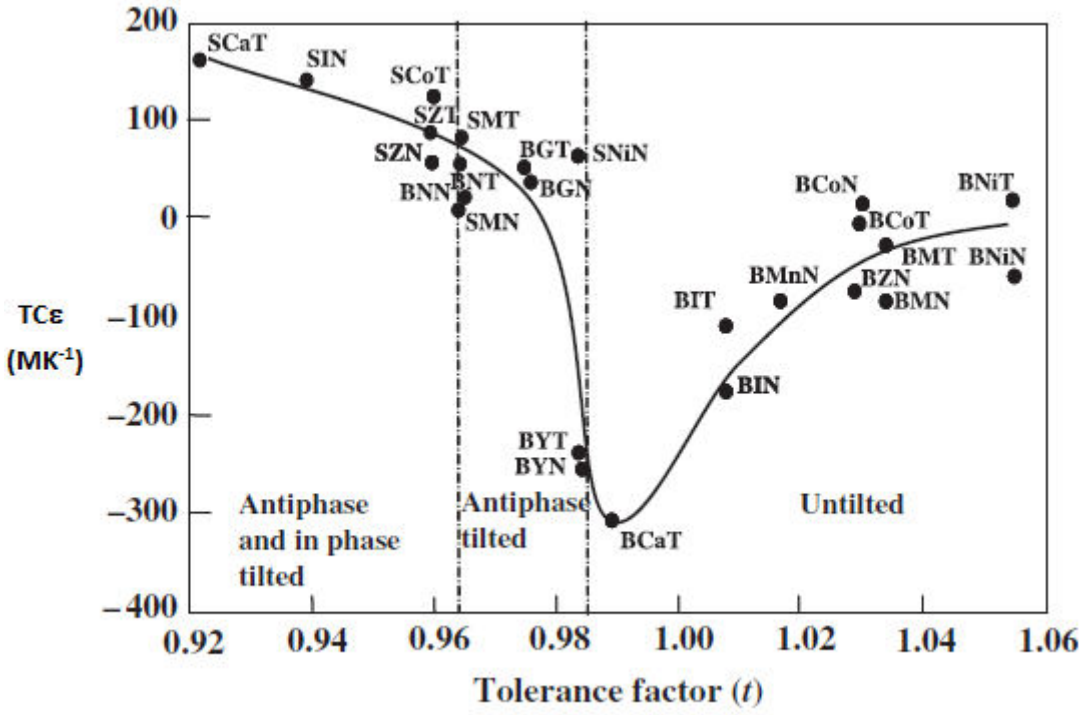

Figure 2.6. TCε as a function of tolerance factor *t* at room temperature for large number of Sr- and Ba- based complex perovskites [9]

Three obvious areas are denoted in Figure 2.6. The first on the right of the figure ($1.06 > t > 0.985$) in which TCε reduces from 0 to -300 MK^{-1} as the tilt transition approaches but does not rise above room temperature. The onset of a tilt transition above room temperature is observed around $t = 0.985$ at which value the O-octahedra rotate in antiphase ($0.985 > t > 0.965$) [1] . The third region where $0.964 > t > 0.92$ is where a second tilt transition occurs above ambient to an in-phase and antiphase tilted structure [1]. It can be concluded from Figure 2.6 that the *t* controls the amplitude of rotation of the octahedra as well as the onset temperature of a phase transition [1].

2.2.2 Factors controlling *Qf*

Qf is affected significantly by extrinsic losses and is dependent on composition, processing conditions and structure of material [1]. To deal better with extrinsic losses and to optimize *Qf*, the following points need to be considered:

2.2.2.1 Order/ disorder behaviour

Controlling sintering temperature and annealing are important in the optimisation of *Qf* [1]. Commercial ordered complex perovskites are often based on BZT [1]. Kawashima et al. [10] reported MW properties of pure BZT which resonated at 12 GHz with $\varepsilon_r = 30$, Q= 6500. Figure 2.7 shows peak splitting of BZT sintered at 1350 ℃ after 8 hours of sintering.

The increase in peak splitting (226,422) with sintering time is proportional to increase of *Qf* value of BZT [1].

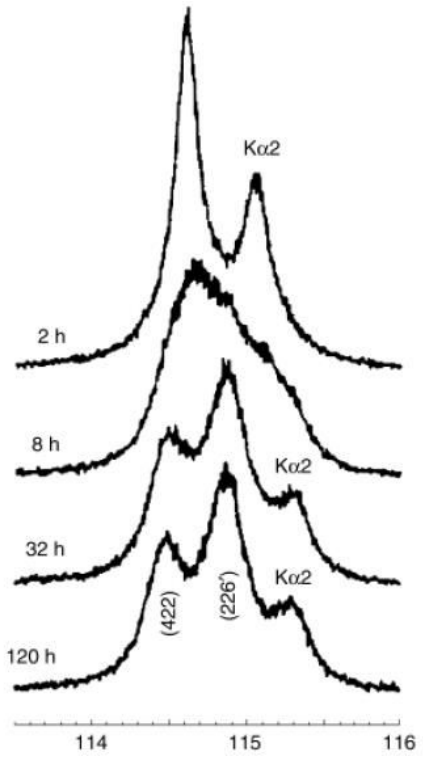

Figure 2.7. Peak splitting (226,422) of BZT sintered at 1350 ℃ showing time scale according to Kawashima [10]

Reaney et al. [11], [12] investigated the role of annealing temperature and time on the *Qf* of BZT. According to their studies, 0.95 BZT-0.05 $Sr(Ga_{1/2}Ta_{1/2})O_3$ (SGT) ceramics were sintered and annealed at different temperatures. Keeping in mind that ZnO loss is significant above 1300 ℃ as mentioned by Desu and O'Bryan [13], ceramics were annealed at 1275 ℃ for 24 hours by Reaney et al. [11] resulting in a significant increase of *Qf* by 40%

2.2.2.2 Processing and impurities effects

In a study carried by Negas et al. [14], reducing raw material impurities decreased *Qf* by a factor of 2, while minor contamination from milling media reduced Q by around 20%. Alford et al. [15] observed that increasing density of TiO_2 up to 95% increased *Qf* proportionally. However, increasing density further decreased *Qf* value, since re-oxidation of the reduced core ($1/2O_2 = V_O^{2+} + 2e^-$, $Ti^{4+} + e^- = Ti^{3+}$) caused by binder burnout became more difficult [1].

2.2.2.3 Solid solution effects

Many MW dielectrics are based on disordered perovskite solid solutions such as CTNA and STLA [1]. The *Qf* of CTNA and STLA (>40,000 GHz) are very high but many chemically and structurally equivalent solid solutions have low values (<10,000 GHz) [1], [9]. Reaney and Iddles [1] recognized that solid solutions with a wide spread of ion sizes on any given site exhibited anharmonic vibrations whereas more narrow spreads have more harmonic vibrations and higher *Qf* [1]. Reaney and Iddles [1] simplified this concept into a spread of tolerance factors (Δt) which they plotted against *Qf* for $SrTiO_3$ and $CaTiO_3$ based compounds whose ε_r values were equivalent.

2.3 MW ceramics used as end members in the present study

Many ceramics are used in MW applications due to their competitive temperature stability, medium to high ε_r and ultra-low tan δ. $BaTi_4O_9$ is synthesised by the traditional sintering methods at high temperature to exploit its high ε_r~ 36 and *Qf* ~25,000 GHz. Li_2MoO_4 is not only used in sensors for humidity detection because of water adsorption on its surface [16] but also for its MW dielectric properties in microstrip patch antennas (MPAs) [16]. Barium hexaferrite $BaFe_{12}O_{19}$ is an important magnetodielectric ceramic that is utilised throughout the electroceramic industry especially in magnetic storage systems, bank cards, and fridge magnets [17]. Adding barium hexaferrite to a dielectric material increases magnetic permeability (μ) and enhances its propagation characteristics [18]. Manipulation of ε_r and TCF can be carried out either as solid solutions as discussed previously in section 2.2 for ceramics such as CTNA and STLA [18] or through the formation of composites (the preferred approach in this contribution). *Qf* and TCF of TiO_2 and K_2MoO_4 have also been studied and compared to other similar materials. Here, the crystal chemistry and basic properties of the ceramic end members used in the thesis are presented.

2.3.1 Barium Tetratitanate, $BaTi_4O_9$ (BT4)

BT4 is one of several polytitanates sintered using a conventional solid-state method that are used as MW ceramics [19]. The BT4 structure data is summarized in the Table 2.2 [20]:

Compound	Structure	Crystal Data	Density
BT4	Orthorhombic, *Pnmn*	*a*=14.53 Å *b*=3.797 Å c=6.294 Å	4.522 g/cm^3

Table 2.2. BT4 structure properties

The crystal structure of the BT4 is orthorhombic [20] which can be viewed as a pentagonal prism tunnel structure which distorts the TiO_6 octahedra, as shown in Figure 2.8 [21]. *Qf* varies with sintering conditions and dopant additions but is typically ~30,000GHz with TCF ~ 15 and ε_r = 38 [20].

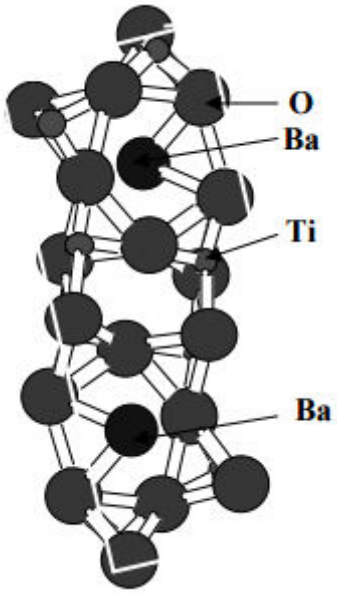

Figure 2.8. Orthorhombic structure of BT4 [21]

2.3.2 Titanium dioxide, TiO_2

Titanium dioxide is available in nature in three different mineral forms: anatase, brookite and rutile. The high dielectric constant of TiO_2 (≈100) allows it to be a nominal for LTCC (low temperature cofiring ceramics) and to be used in modern electronics as a nano-sized filler in organic-inorganic composites due to its low tan δ [22], [23]. The crystal structure of anatase TiO_2 is tetragonal with lattice parameters of a = 3.78 Å and c = 9.51 Å as shown in Figure 2.9 [24]. The MW properties and processing of TiO_2 have been discussed in section 2.2.2.2.

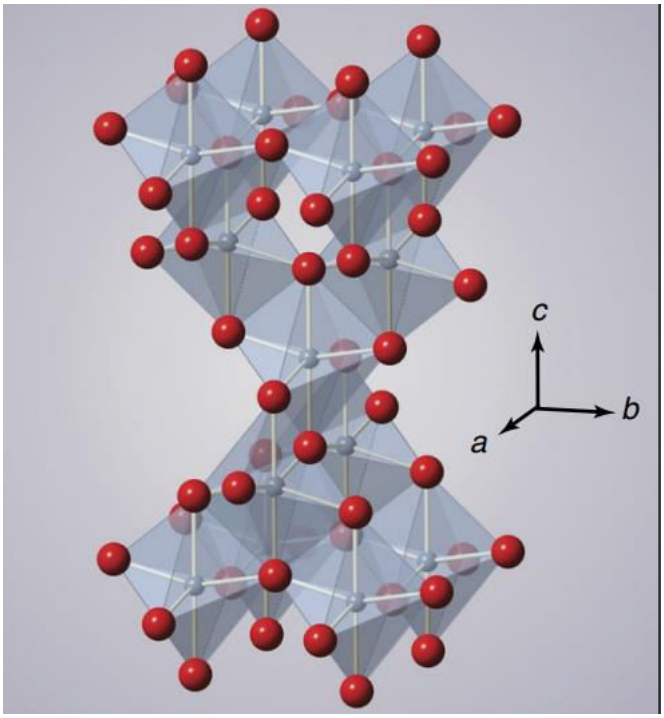

Figure 2.9. Crystal structure of anatase TiO_2, where blue and red atoms represent Ti and O respectively [24]

2.3.3 Lithium Molybdate Li_2MoO_4 (LMO)

LMO has been used as a humidity sensor [16], in cryogenic phonon-scintillating detectors [25], [26] and as a lithium ion battery anode [27], [28]. Figure 2.10 shows an image of a circular MPA fabricated using LMO as a dielectric substrate [16].

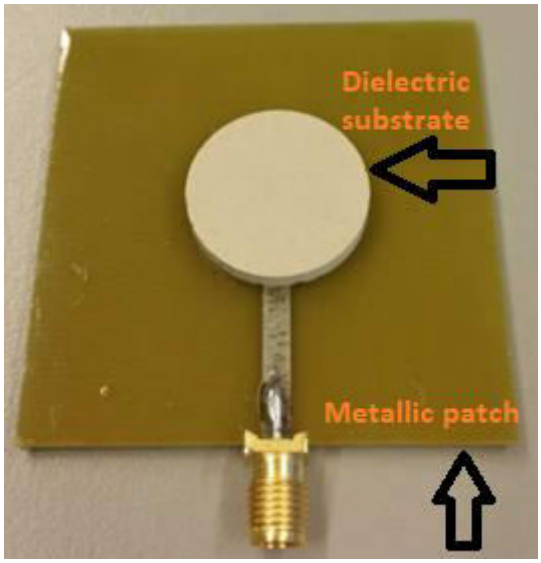

Figure 2.10. Typical fabricated circular patch antenna with LMO used as a dielectric substrate, reproduced from [16]

The MPA in (Figure 2.10) consists of a metallic patch with a dielectric LMO substrate separating it from ground. The design process for a cavity model can be done to find the radius *a* of the metallic patch as in Equation 2.12 [16]:

$$a = \frac{F}{\sqrt{\left(1+\frac{2h}{\pi F \varepsilon_r}\left[\ln\left(\frac{\pi F}{2h}\right)+1.7726\right]\right)}} \qquad \text{Equ. 2.12}$$

where

$$F = \frac{8.791 \times 10^9}{f_o \sqrt{\varepsilon_r}} \qquad \text{Equ. 2.13}$$

and $\varepsilon_r \sim 5$ [16] for LMO substrate of 3mm thickness (h).

Different sintering methods of LMO have been performed. Conventional sintering is carried out at 540 °C and gives tanδ = 0.00028 and ε_r of 5.5 (13.05 GHz) [29]. In contrast, the tanδ and ε_r of cold sintered LMO are 0.00035 and 5.1, respectively (9.6 GHz) [30], [31].

According to Barinova et al [32], LMO belongs to the trigonal system (space group $R\bar{3}$) and is isostructural with Be_2SiO_4 (Phenacite). The crystal structure of LMO is shown in Figure 2.11 where each Mo tetrahedron and two Li tetrahedra share an O atom [32].

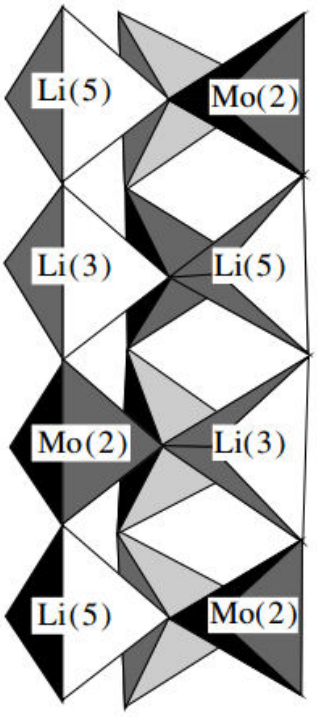

Figure 2.11. Tripled chains in the crystal structure of LMO **[32]**

2.3.4 Barium Hexaferrite, $BaFe_{12}O_{19}$ (BF12)

The ferrites of barium are important ceramics that are utilized throughout the electroceramic industry especially in magnetic storage systems, bank cards, and fridge magnets [17]. BF12 is a hard magnetic material which has been widely used as a MW absorber or hard magnetic material due to its high saturation magnetization (Ms=4.8), high coercivity, excellent chemical stability, relatively large magnetization with a magnetocrystalline constant, $K_1 = 3.2 X10^6$ erg cm^{-3}, and huge anisotropy field (H_a=16.8 kOe), high thermal stability, good magnetization per formula unit at 0K of 20μB, and corrosion resistance [33], [34], [35], [36].

Usually ferrites are electrically resistive with magnetic loss resulting from their ferrimagnetisim, the spin relaxation in the high frequency alternating electromagnetic fields, and the resonance reflection loss of moving magnetic domains [37]. Magnetic and electric energy storage capabilities of a material are represented by real parts of complex permeability (μ') and permittivity (ε'), the magnetic and dielectric loss represented by the imaginary parts (μ ' ', ε") [38]. Decreasing saturation magnetization or increasing anisotropy field or even changing other magnetic properties of BF12 such as improving coercivity may be achieved by doping or substituting Fe^{3+} with Ti-Cu, Co-Mo or Zn-Ti [37], [39]. Ferromagnetic resonance frequency is also affected by doping [37].

A number of studies have focused on finding a relationship between composition, structure and the MW absorption properties [37]. Structures with divalent ferrite ions and hexaferrites are thought to be the best MW absorbers and are used as a radar absorbing material (RAM) [37], [40]. Other studies have attempted to find a relationship between ε_r and μ with MW absorption of the hexaferrites [37].

The ferro- or ferrimagnetism of BF12 is better understood by investigating its crystal structure which has space group P63/mmc, as shown in Figure 2.12. The ferrimagnetism arises from inequivalent cancellation of spin states on the B site where 16 ions spin upwards in contrast to 8 ions spin downwards in Fe^{3+} per unit cell under 450 °C where they ferromagneticlly order which results in a net magnetization per formula unit 20 μB [41].

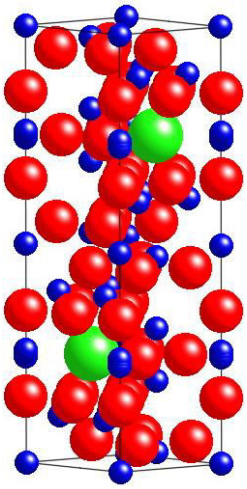

Figure 2.12. Crystal structure model of $BaFe_{12}O_{19}$ (Green: Ba, blue: Fe, red: O) [42]

Ferrimagnetism consists of opposing magnetic spin moments, such as anti-ferrimagnetism, however unlike other systems, they are unequal which is why there's a remnant of spontaneous magnetization due to different ions existence in same materials such as Fe^{2+} and Fe^{3+} [43]. Ferromagnetic ordering is shown in Figure 2.13.

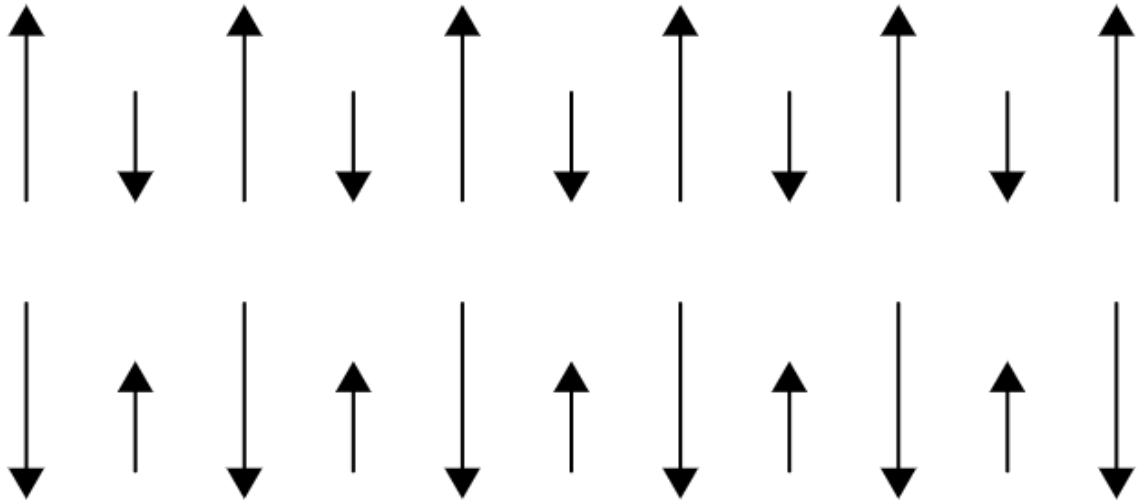

Figure 2.13. Ferrimagnetic ordering **[44]**

Magnetodielectrics such as YIG (Yittrium iron garnet) are also good candidates for MW resonators due to low tanδ, high resistivity and narrowest linewidth amongst all ferrites [45], [46]. In addition, YIG has been used in applications such as phase shifters, circulators and isolators [45], [46].

2.3.5 Potassium Molybdate, K_2MoO_4

Potassium molybdate K_2MoO_4 (KMO) in this work has a *Qf*= 5907 GHz with ε_r = 6.59 (this study). It is monoclinic with space group C2/m and lattice parameters, *a*= 12.348, *b*= 6.081, *c*= 7.538 Å [47]. Figure 2.14 shows a part of the structure of K_2MoO_4 as cited from Gatehouse et. Al [47] with a view normal to 001 showing two types of O and K polyhedra.

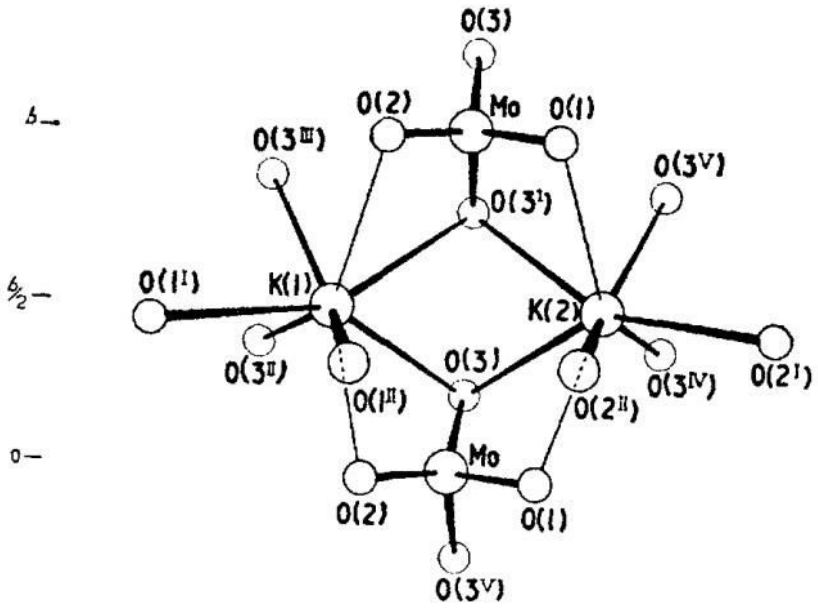

Figure 2.14. 001 view of part of K_2MoO_4 crystal structure showing two types of O-K bonds [47]

2.4 Conventional sintering of ceramics (Solid state)

Sintering is a thermal treatment process of forming a dense bulk solid material by heat or pressure before reaching its melting point [48], [49]. The conventional sintering process is a high temperature method where powders are heated between 50-75% of melting temperature to obtain > 95% theoretical density of the required product [50]. The densification occurring in conventional sintering is essentially pressureless [51]. According to Kingery [52] changes that occur in solid state sintering are shape and size of grains and pores. Solid state sintering is divided to three stages; initial, intermediate and final stage[52, 53]. Figure 2.15 shows those stages [52]:

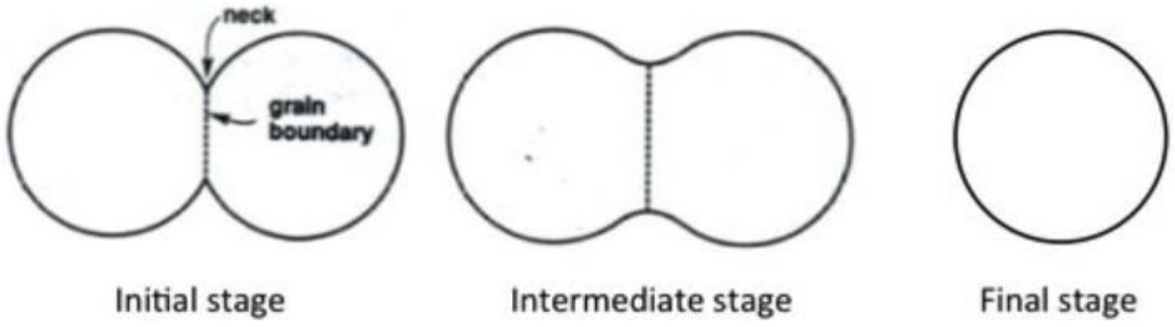

Figure 2.15. Stages of conventional solid state sintering [52]

The initial stage of conventional sintering features neck growth and first interfaces forming between grains [52]. Neck growth will continue in this stage before it stops due to equilibrium fulfilment in next stages, however no grain growth happens at this stage [52]. The intermediate stage is where grain growth starts and grain boundaries are formed but not connected [52]. Pores are still connected in intermediate stage, however, most of the densification and microstructural change occurs in this stage [52]. The final stage is where the pores are isolated and grain boundaries are connected instead [52]. Density increases to some degree in final stage, however, grain growth rate is very high at the final phase of sintering [52]. According to Kingery [52] changes in pore shape does not necessarily include shrinkage, as shown in Figure 2.16:

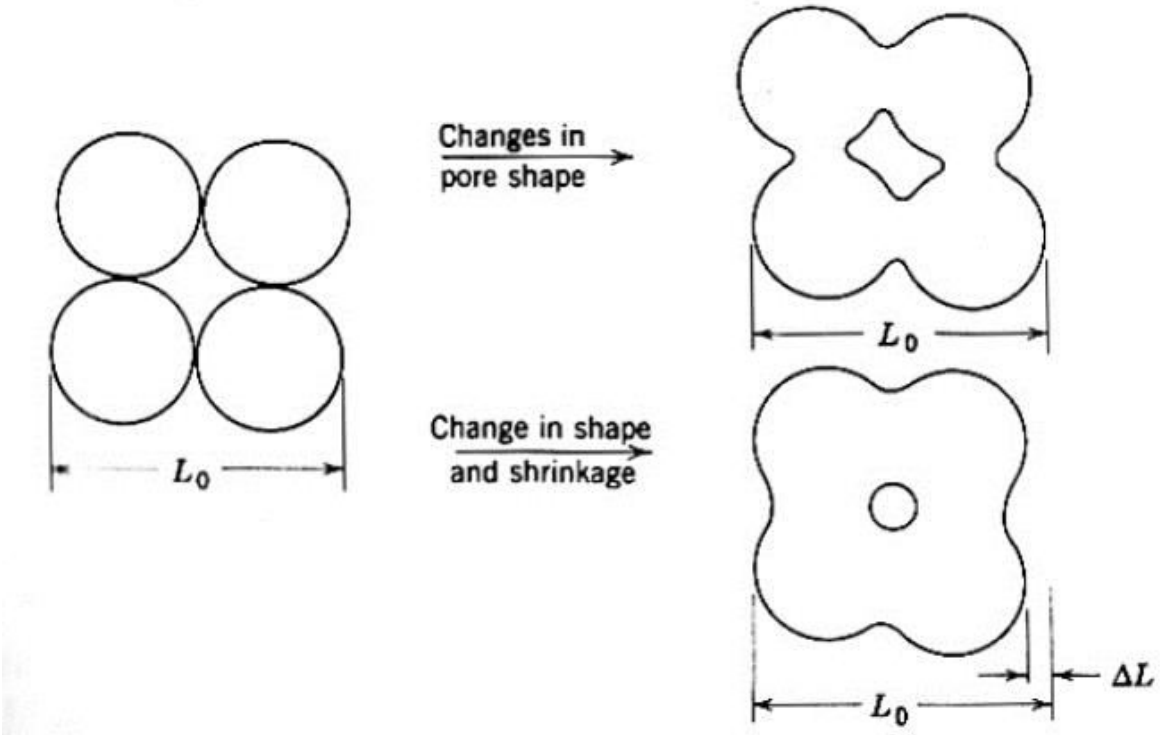

Figure 2.16. Change in pore shape doesn't mean shrinkage necessarily **[52]**

Grain growth mechanisms

After calcination, limited factors play a critical role in sintering efficiency and they are: Grain growth, pores size and pore shape [52]. Grain growth or increasing grain size occurs normally through three main mechanisms [52]:

1. **Primary recrystallization**

- It is the stage when new strain-free grains nucleate in a plastic deformed matrix.

2. **Grain growth**

- This stage is when the grains size increase throughout the heating process without damaging grain size distribution.

3. **Secondary recrystallization**

- The last stage of grain growth is when larger grains nucleate at the expense of finer or strain-free grains. This is considered abnormal or discontinuous grain growth.

Sintering is all about increasing density by producing less pores in addition to the grain growth factors mentioned above.

Driving force for densification

The free energy source of densification occurs when surface area decreases combined with disappearance of solid-vapour interfaces due to lowering of surface free energy [52]. This means new, lower energetic solid-solid interfaces (grain boundaries). The small particle size of most ceramics (few microns) results in an increase of mass transfer and hence, better densification [52].

Since the driving force of densification in this case is free surface energy, the degree of change of materials behaviour depends on various mechanisms of mass transfer such as evaporation and condensation, viscous flow, surface diffusion, grain boundary and plastic deformation [52]. From all of these, evaporation-condensation is considered one of the most important and easily visualised densification mechanisms [52].

Evaporation- condensation

There is a tendency for mass transfer during sintering heat treatment due to differences in surface curvature, hence vapour pressure difference [52]. Concentrating on two adjacent particles during sintering, it can be observed in Figure2.17 that there's a positive radius of curvature and higher vapour pressure than on a flat surface [52]. However, on the neck between the two particles there is a negative radius of curvature and consequently lower vapour pressure which facilitates mass transfer from particles area to neck and therefore reducing surface free energy [52].

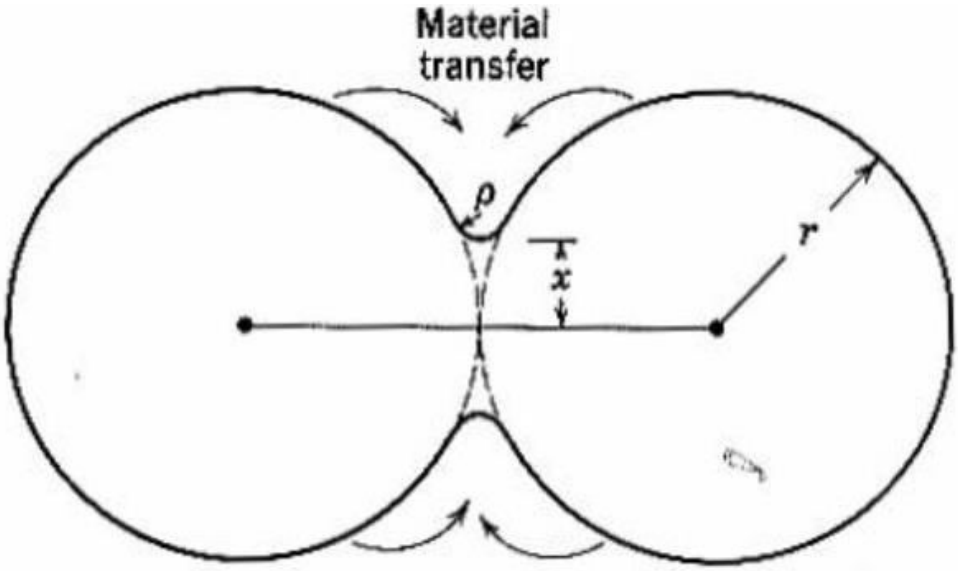

Figure 2.17. Initial stages of sintering by evaporation-condensation technique [52]

Other solid state processes

The difference in free energy or chemical potential between the surface of the particle and the neck region is the main driver of densification where material transfer occurs quickly between the two adjacent areas [52]. As shown in Figure 2.18 and Table 2.3, other ways of transport than vapour are from the surface of particles, bulk particles or grain boundaries by alternative paths such as surface, lattice or grain boundary diffusion [52].

Mechanism number	Transport path	Source of matter	Sink of matter
1	Surface diffusion	Surface	Neck
2	Lattice diffusion	Surface	Neck
3	Vapour transport	Surface	Neck
4	Boundary diffusion	Grain boundary	Neck
5	Lattice diffusion	Grain boundary	Neck
6	Lattice diffusion	Dislocations	Neck

Table 2.3. Alternative paths of transport during initial stages of sintering [52]

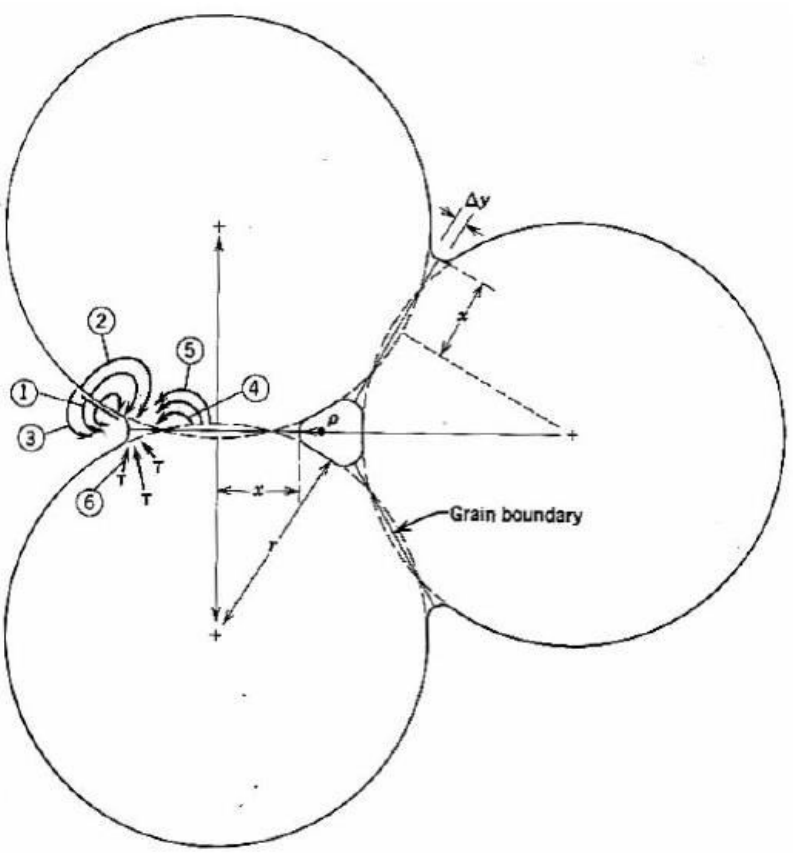

Figure 2.18. Illustration of alternative paths of transport during initial phases of sintering [52]

The numbered circles in Figure 2.18 represent alternative mechanisms numbers as listed in Table 2.3.

It is noted by Kingery [52] that particle size and its control are the most significant factors in sintering rather than the relationship between sintering rate and sintering time which becomes unrealistic after a threshold value when the sintering rate decreases [52]. Additionally, during initial phases of sintering, surface diffusion transfer is the most critical factor of sintering followed by grain boundary and volume diffusion at later stages [52].

2.5 Cold sintering process

The cold sintering processing (CSP) is a novel technique developed recently to achieve dense ceramic solids at extremely low temperatures (<180 °C) [49]. The process includes using aqueous-based solutions (eg: water) as a transient solvents to aid densification by a non-equilibrium mediated dissolution–precipitation process [54]. To provide a good environment and conditions for precipitation and recrystallization in hydrothermal reactions, the aqueous solution should be chosen carefully [55].

Conventional sintering requires a high temperature to facilitate mass transport of molecules or ions based on kinetic energy principles of bulk diffusion, while the CSP

provides a more efficient mass transport for molecules/atom clusters or ions since the aqueous solution facilitates the movement of the atomic/molecular species [55]. It is based on hydrothermal principles which previous studies and research have proved advantageous for minimizing the demand for Gibbs free energy changes [55].

Figure 2.19 represents Gibbs free energy diagram regarding temperature dependency for different material states. The conventional sintering method requires more Gibbs free energy change than cold sintering to form solid crystals from aqueous solution [55].

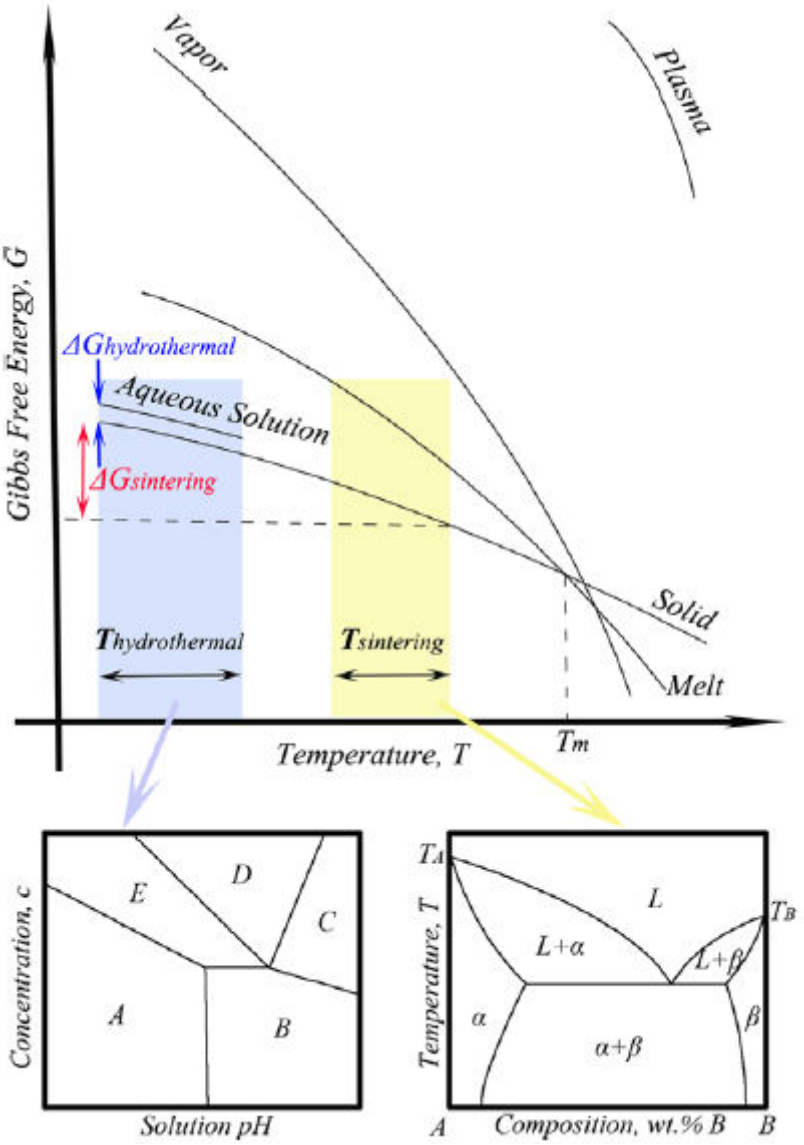

Figure 2.19. Schematic Gibbs free energy diagram showing temperature dependency **[55]**

Crystal structure, eutectic point, melting temperature are some of the pertinent characteristics of a phase diagram in conventional sintering [55]. However, for cold sintering the predominant diagrams include ionic species as a function of solution concentration, pH environment and intermediate chemistries [55].

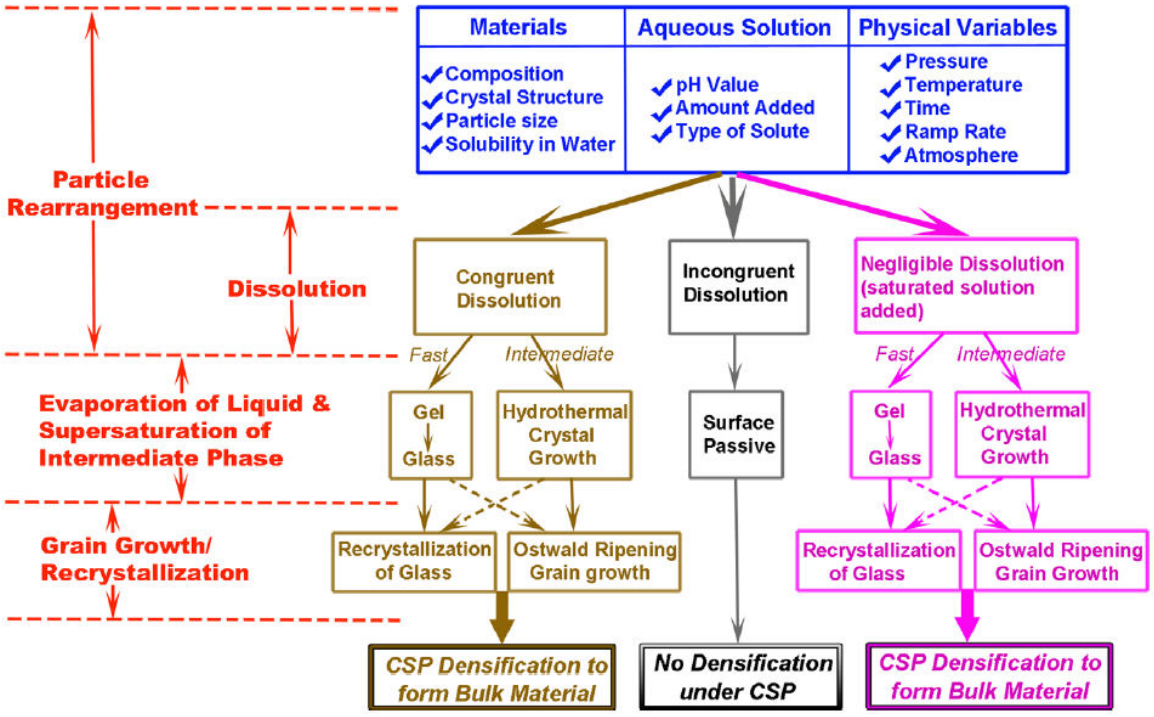

Figure 2.20. Flowchart summary of CSP stages [55].

Figure 2.20 is a flowchart for the possible routs of CSP from particle rearrangement to densification. The internal characteristics that affect CSP are represented by a material's composition, crystal structure, particle size and solubility in water [55]. Some of the physical variables determining kinetic process for mass transport are hot press pressure, temperature, time of sintering, ramp rate and atmosphere [55]. Preparing a convenient aqueous solution is part of important external influences as well as some other significant factors such as solute type, concentration and pH. [55].

The dissolution characteristics play a significant role in determining whether a densification will eventually occur or not. Congruent dissolution facilitates a direct and simple cold sintering process since the surface of a material can be easily dissolved in water with a homogenous chemical stoichiometry [55]. However, no densification will occur in the case of incongruent dissolution because the crystalline and aqueous phases are separated by a passive surface [55]. Negligible dissolution can work well in cold sintering if a saturated solution is added targeting the chemical compounds of the material to be densified [55]. After dissolution, evaporation of liquid is the next step in cold sintering which leads to hydrothermal crystal growth (in case of water as a dissolution) or formation of glass/intermediate phase, and eventually grain growth and densification or recrystallization as shown in in Figure 2.20 [55]. By introducing more solid-liquid interfaces, i.e the use of or introducing nanoparticles, cold sintering is likely to work more efficiently by improving

dissolution and crystal growth [55]. Cold sintering has been recently used in fabricating MW and packaging dielectric substrates, including ceramics and ceramic–polymer composites. In addition, an LMO – Ag multilayer co-fired ceramic structures were successfully fabricated without warping, interdiffusion, or delamination [54].

Guo et al. [54], compare the MW properties of LMO with other ceramics and composites sintered via conventional thermal sintering process (TSP) and CSP as shown in Table 2.4 [54]:

Sample	Process	Sintering temperature (°C)	Density (g/cm^3)	Relative density (%)	ε_r	$Q \times f$ (GHz)	τ_f (ppm/°C)
Li_2MoO_4	TSP[5]	540	2.895	95.5	5.5	46 000	−160
Li_2MoO_4	CSP-120	120	2.9	95.7	5.6	30 500	−174
$Na_2Mo_2O_7$	TSP[24]	575	3.59	97	12.9	62 400	−72
$Na_2Mo_2O_7$	CSP-120	120	3.45	93.7	13.4	14 900	−90
$K_2Mo_2O_7$	TSP[25]	460			7.5	22 000	−63
$K_2Mo_2O_7$	CSP-120	120	3.39	94.1	9.8	16 000	−66
$(LiBi)_{0.5}MoO_4$	TSP[20]	560	5.476	96.7	41.7	3200	+240
$(LiBi)_{0.5}MoO_4$	CSP-120	120	5.1	88.5	33.7	2300	+184
$(LiBi)_{0.5}MoO_4$	CSP-RT to 120	120	5.06	87.8	37.1	1700	+179

Table 2.4. MW properties and densities of LMO and other ceramics and composites sintered under different methods [54]

LMO shows a slight improvement in relative density and ε_r by cold sintering compared to TSP. However, the *Qf* values of cold are smaller than conventionally sintered samples possibly due to the presence of amorphous phase [54].

Guo et al. [50] also studied the role of temperature and pressure in cold sintering in a compound related to LMO, $K_2Mo_2O_7$. Figure 2.21 illustrates graphs in which two sintering process parameters are kept constant and the third varied during densification. The variable processing parameters are temperature, applied pressure and holding time. Guo el al concluded that finding the right sintering parameters is vital to the success of cold sintering process and obtaining dense pellets.

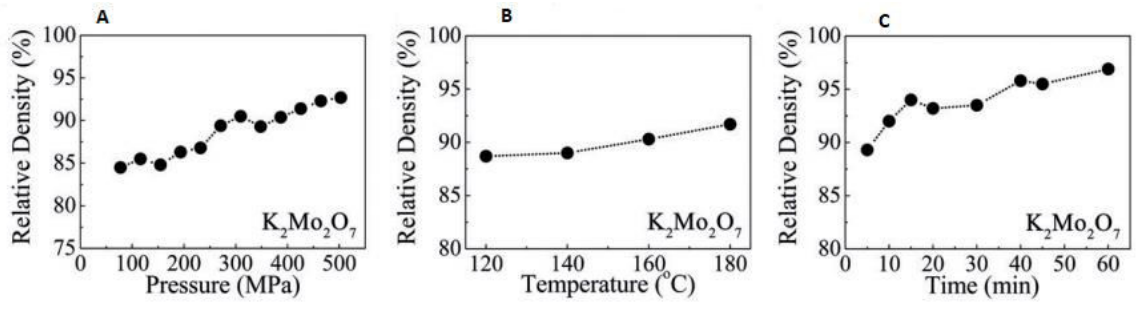

Figure 2.21. Varying cold sintering processing conditions (pressure, temperature, time) and their relation to relative density [50].

In summary, several recent studies have demonstrated that cold sintering is an efficient densifying method, energy saver, simple and thermally stable. It overcomes many

issues associated with conventional sintering with an overall reduction in the Gibbs free energy [55].

2.6 Introduction to antennas

2.6.1 History

An antenna is a device that transforms electrical power into electromagnetic waves in free space and vice versa. The history of antennas began when Faraday showed a definitive relationship in the 1830s between electric and magnetic field. He placed a magnet around the coils of a wire attached to a galvanometer. As Maxwell explained in his equations, a time- varying magnetic field was created as a result of moving the magnet. The coil received the electromagnetic radiation and acted as a loop antenna. Despite this empirical observation, the general principles of electromagnetism were not yet established. A wireless crude communication system was first developed by Hertz in which he forced an electrical spark to occur in the gap of a dipole antenna [56]. Subsequent research and experiments have resulted in the fabrication of many different types of antennas from large Yagi-Uda's designs to tiny microstrip as described in the following sections.

2.6.2 Antenna fundamentals

2.6.2.1 Directivity

Directivity is defined in the 1983 version of *IEEE Standard Definitions of Terms for Antennas* as: "the ratio of the radiation intensity in a given direction from the antenna to the radiation intensity averaged over all directions". In other words, it means concentrating beam waves while transmitting or receiving into a wanted and focused direction which makes the antenna efficient [58].

2.6.2.2 Gain

Antenna gain term is used sometimes to mean directivity, while the real definition of gain includes both perspectives of directivity and efficiency of transferring radio waves to input current and vice versa, depending on whether transmitting or receiving [57],[59]. It can be defined according to Balanis [57] as: "the ratio of the intensity in a given direction to the radiation intensity that would be obtained if the power accepted by the antenna were radiated isotopically". Equation. 2.14 shows the relationship:

$$\boldsymbol{Gain} = \frac{\mathbf{4\pi\ radiation\ intensity}}{\mathbf{total\ input(accepted)power}} \qquad \text{Equ. 2.14}$$

2.6.2.3 Input impedance

Input impedance of an antenna represents standing up to the current in the electrical circuit and gives an indication to the relationship between voltage and current at the input of the electrical circuit. According to Balanis [57], the input impedance of an antenna can be defined as “the impedance presented by an antenna at its terminals or the ratio of the voltage to current at a pair of terminals or the ratio of the appropriate components of the electric to magnetic fields at a point”. This can be represented by Equation. 2.15:

$$Z = R + jX \qquad \text{Equ. 2.15}$$

where Z represents the input impedance at the antenna’s terminals, R and X represent resistance and reactance of input terminals respectively [57].

Another important term related to antenna’s input impedance is impedance matching. The latter aims to fulfil the maximum power from antenna’s terminals with lower losses associated with faults such as reflected waves, attenuation, standing waves and other factors. Figure 2.22 shows an electrical circuit with a source and load that enter in the definition of impedance matching [60], [61].

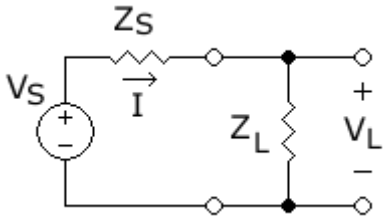

Figure 2.22. Source and load circuit impedance [60]

Looking at Figure 2.22, the maximum power transfer; thus impedance matching is fulfilled when source impedance (ZS)=load impedance (ZL). Reflectionless matching can be equivalent to maximum power transfer matching if source impedance, load impedance and transmission characteristic impedance are purely resistive[60]. In high frequency applications such as MPAs the impedance matching term is important in enhancing antenna performance by using matching network between source and load to ensure that maximum power is being transferred with least reflected waves as possible throughout the system.

2.6.2.4 Bandwidth

Bandwidth is considered a detrimental and essential parameter while designing an antenna. It can be defined as the range of frequencies where the antenna performs as designed and expected to radiate depending on a number of parameters such as VSWR (voltage standing wave ratio), radiation pattern, impedance matching and many other factors [57]. It can be differentiated in the resonance frequency wave from left to right from there depending on the specified range [57].

2.6.3 Antenna types

Typical antenna designs in the real world can be a combination or derivative of the following types: a) Wire antennas (e.g. Half-wave dipole, monopole, loops), b) Travelling wave antennas (Yagi-Uda, helical, spiral), c) Log-periodic antennas (bow tie), d) Reflector antennas (corner reflector, parabolic reflector), e) aperture antennas (e.g. inverted-F, horn, slot, Vivaldi, telescopes), f) microstrip antennas (e.g. rectangular microstrip "Patch", Planar Inverted-F "PIFA"), g) other antennas such as NFC and wearable. This project's work will be focused on MPAs and how to fabricate the appropriate composites for effective antenna substrates.

2.7 Microstrip Patch Antennas (MPAs)

The idea of the MPA was first proposed in 1953 by G.A. Deschamps, but did not become popular until the 1970s when its usage was primarily for spaceborne applications [56], [57]. These antennas consist of a metallic patch on a grounded substrate which can be printed directly onto a circuit board. Figure 2.23 shows a rectangular patch which is the most popular in its category because of ease of analysis and fabrication and its attractive radiation characteristics [57].

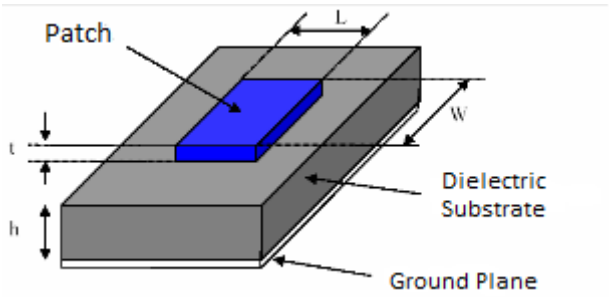

Figure 2.23. Microstrip rectangular patch [62]

MPAs are simple, low profile, compatible with planar and nonplanar surfaces, mechanically robust when mounted on rigid surfaces, inexpensive to fabricate using modern printed- circuit technology, compatible with MMIC designs (Monolithic MW Integrated Circuit) and very versatile in terms of polarization, resonant frequency, impedance and pattern [57]. Their application can fit into mobile phones, surfaces of high-performance aircraft, spacecraft, missiles, satellites and cars [57].

A rectangular MPA as in Figure 2.23 consists of a very thin ($t << \lambda_0$, where λ_0 is the free space wavelength) metallic patch (strip) placed on a small fraction dielectric substrate of a wavelength ($h << \lambda_0$) above a ground plane [57]. Figure 2.24 shows a microstrip antenna fed by a source connected via a microstrip transmission line.

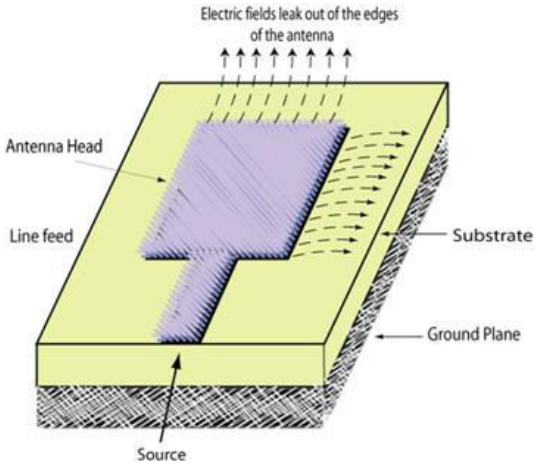

Figure 2.24. Radiation of MPA [63]

The fields at the edges of the patch undergo fringing because the dimensions of the patch are finite along the length and the width [56], [57]. Figure 2.25 shows the fringing fields that cause the MPA to radiate.

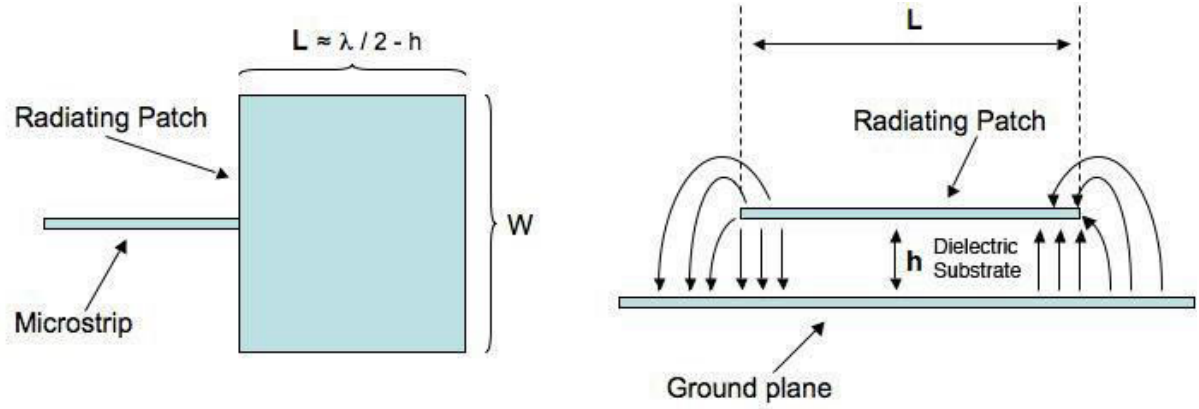

Figure 2.25. Fringing fields in rectangular MPAs [64]

The fringing fields in system are controlled by the ratio of the patch's length (L) to the substrate's thickness (h), where the fringing fields can be lowered by manipulating the

value of L/h to be >>1 . However, the one is advised to be cautious and careful because the resonance frequency can be altered easily by changing the latter ratio [56].

The bandwidth of the MPA is very small, which makes it a narrow band antenna. If designed to operate at 100 MHz, it will resonate at ~96 MHz due to fringing fields around the antenna. Hence, when designing a patch antenna, it is typically trimmed by 2-4% to achieve resonance at the desired frequency [56]. The aim is that the materials used in the dielectric substrate in the MPA in this project will engender high bandwidth and overcome restrictions based on miniaturization.

2.8 References

[1] I. M. Reaney and D. Iddles, "Microwave dielectric ceramics for resonators and filters in mobile phone networks," *J. Am. Ceram. Soc.,* vol. 89, p. 2063-2072, 2006.

[2] H. Ohsato, "Functional advances of microwave dielectrics for next generation," *Ceram. Int.,* vol. 38, p. S141-S146, 2012.

[3] A. Manan and I. Qazi, "Dielectric properties of ceramics for microwave and millimeterwave applications," *ICASE 2013.,* At.6785564, p. 1-7, 2013.

[4] H. Ohsato, L. Pan and G. Zhu, "Microwave Dielectrics with Perovskite-Type Structure," in *Perovskite Materials*, 2016, At. 61718. Available from: https://www.intechopen.com/books/perovskite-materials-synthesis-characterisation-properties-and-applications/microwave-dielectrics-with-perovskite-type-structure.

[5] R. C. Pullar, S. J. Penn, X. Wang, I. M. Reaney and N. M. Alford, "Dielectric loss caused by oxygen vacancies in titania ceramics," *J. Eur. Ceram. Soc.,* vol. 29, p. 419-424, 2009.

[6] P. J. Harrop, "Temperature coefficients of capacitance of solids," *J. Mater. Sci.,* vol. 4, p. 370-374, 1969.

[7] M. P. Seabra, V. M. Ferreira, H. Zheng and I. M. Reaney, "Structure Property Relations in $La(Mg_{1/2}Ti_{1/2})O_3$-Based Solid Solutions," *J. Appl. Phys.,* vol. 87, p. 584-590, 2005.

[8] E. L. Colla, I. M. Reaney and N. Setter, "Effect of structural changes in complex perovskites on the temperature coefficient of the relative permittivity," *J. Appl. Phys.,* vol. 74, p. 3414-3425, 1993.

[9] I. M. Reaney, E. L. Colla and N. Setter, "Dielectric and Structural Characteristics of Ba- and Sr-based Complex Perovskites as a Function of Tolerance Factor," *Jpn. J. Appl. Phys. ,* vol. 33, At. 3984, 1994.

[10] S. KAWASHIMA, M. NISHIDA, I. UEDA and H. OUCHI, "$Ba(Zn_{1/3}Ta_{2/3})O_3$ Ceramics with Low

Dielectric Loss at Microwave Frequencies," *J. Am. Ceram. Soc.,* vol. 66, p. 421-423, 1983.

[11] I. Reaney, P. Wise, C. M. I. Qazi, T. Price, D. Cannell, D. Iddles, M. Rosseinsky, S. Moussa, M. Bieringer, L. Noailles and R. Ibberson, "Ordering and quality factor in $0.95BaZn_{1/3}Ta_{2/3}O_3$–$0.05SrGa_{1/2}Ta_{1/2}O_3$ production resonators," *J. Eur. Ceram. Soc.,* vol. 23, p. 3021-3034, 2003.

[12] I. M. Reaney, I. Qazi and W. E. Lee, "Order–disorder behavior in $Ba(Zn_{1/3}Ta_{2/3})O_3$," *J. Appl. Phys.,* vol. 88, At. 1290737, 2000.

[13] S. Desu and H. M. O'BRYAN, "Microwave Loss Quality of $BaZn_{13}Ta_{2/3}O_3$ Ceramics," *J. Am. Ceram. Soc.,* vol. 68, p. 546 - 551, 1985.

[14] T. Negas, G. Yeager, S. Bell, N. Coats and I. Minis, "$BaTi_4O_9$/$Ba2Ti_9O_{20}$-based ceramics resurrected for modern microwave applications," *J. Am. Ceram. Soc. Bull.,* vol. 72, p. 80-89, 1993.

[15] A. Templeton, X. Wang, S. J. Penn, S. J. Webb, L. Cohen and N. Alford, "Microwave Dielectric Loss of Titanium Dioxide," *J. Am. Ceram. Soc.,* vol. 83, p. 95 - 100, 2008.

[16] H. Kähäri, P. Ramachandran, J. Juuti and H. Jantunen, "Room-Temperature Densified Li_2MoO_4 Ceramic Patch Antenna and the Effect of Humidity," *INT. J. APPL. CERAM. TEC.,* vol. 14, p. 50-55, 2017.

[17] D. Vinnik, A. Tarasova, D. Zherebtsov, S. Gudkova, D. Galimov, V. Zhivulin, E. Trofimov, S. Nemrava, N. Perov, L. Isaenko and R. Niewa, "Magnetic and Structural Properties of Barium Hexaferrite $BaFe_{12}O_{19}$ from Various Growth Techniques,," *Materials,* vol. 10, At. 10060578, 2017.

[18] D. D. Khalyavin, A. N. Salak, A. M. R. Senos, P. Q. Mantas and V. M. Ferreira, "Structure Sequence in the $CaTiO_3$–$LaAlO_3$ Microwave Ceramics—Revised," *J. Am. Ceram. Soc.,* vol. 89, p. 1721-1723, 2006.

[19] S. Kumar, V. Raju and T. Kutty, "Preparation of $BaTi_4O_9$ and $Ba_2Ti_9O_{20}$ ceramics by the wet chemical gel-carbonate method and their dielectric properties," *Mater. Sci. Eng., B,* vol. 142, p. 78-85, 2007.

[20] M. T. SEBASTIAN, "CHAPTER THREE - MICROWAVE DIELECTRIC MATERIALS IN THE BaO–TiO_2 SYSTEM," in *Dielectric Materials for Wireless Communication*, Elsevier, 2008, p. 49-82.

[21] M. C. Negrila Catalin, "Characterization of $BaTi_4O_9$ ceramics by Raman spectroscopy and XPS after ion etching," *J. OPTOELECTRON. ADV. M.,* vol. 8, p. 1879 – 1883, 2006.

[22] A. Wypych, I. Bobowska, M. Tracz, A. Opasińska, S. Kadlubowski, A. Krzywania-Kaliszewska, J. Grobelny and P. Wojciechowski, "Dielectric Properties and Characterisation of Titanium Dioxide Obtained by Different Chemistry Methods," *Nanomaterials,* vol. 5, At. 124814, 2014.

[23] L. J. Berberich and M. E. Bell, “The dielectric properties of the rutile form of TiO_2,” *J. Appl. Phys.,* vol. 11, p. 681–692, 1940.

[24] E. Baldini, L. Chiodo, A. Dominguez Garcia, M. Palummo, S. Moser, M. Yazdi-Rizi, G. Aub¨ock, B. Mallett, H. Berger, A. Magrez, C. Bernhard, M. Grioni, A. Rubio and M. Chergui, “Strongly bound excitons in anatase TiO_2 single crystals and nanoparticles,” *Nat. Commun.,* vol. 8, At. 13, 2016.

[25] S. F. Solodovnikov, Z. A. Solodovnikova, E. S. Zolotova, L. I.Yudanova, T. Y. Kardash, A. A. Pavlyuk and V. A. Nadolinny, “Revised phase diagram of Li_2MoO_4–$ZnMoO_4$ system, crystal structure and crystal growth of lithium zinc molybdate,” *J. Solid State Chem.,* vol. 182, p. 1935–1943, 2009.

[26] O. Barinovan, S. Kirsanova, A. Sadovskiy and I. Avetissov, “Properties of Li_2MoO_4 single crystals grown by Czochralski technique.,” *J. Cryst. Growth.,* vol. 401, p. 853–856, 2014.

[27] M. Inagaki, Y. Nishikawa and M. Sakai, “Room-temperature preparation of Li_2MoO_4 and its sintering,” *J. Eur. Ceram. Soc.,* vol. 10, p. 123-128, 1992.

[28] X. Liu, Y. Zhao, Y. Lyu, Z. Zhang, H. Li, Y.-S. Hu, Z. Wang, Q. Kuang, Y. Dong, Z. Liang, Q. Fan and L. Chen, “Nanotube Li_2MoO_4: A Novel and High-Capacity Material as Lithium-Ion Batteries Anode,” *Nanoscale,* vol. 6, At. C4NR04226C, 2014.

[29] D. Zhou, C. A. Randall, H. Wang, L.-X. Pang and X. Yao, “Microwave Dielectric Ceramics in Li_2O–Bi_2O_3–MoO_3 System with Ultra-Low Sintering Temperatures,” *J.Am. Ceram. Soc,* vol. 93, p. 1096–1100, 2010.

[30] H. Kähäri, M. Teirikangas, J. Juuti and H. Jantunen, “Dielectric Properties of Lithium Molybdate Ceramic Fabricated at Room Temperature,” *J. Am. Ceram. Soc.,* vol. 97, p. 3378–3379, 2014.

[31] H. Kähäri, M. Teirikangas, J. Juuti and H. Jantunen, “Improvements and Modifications to Room-Temperature Fabrication Method for Dielectric Li_2MoO_4 Ceramics,” *J. Am. Ceram. Soc.,* vol. 98, p. 687–689, 2015.

[32] A. V. Barinova, R. Rastsvetaeva, Y. V. Nekrasov and D. Yu. Pushcharovskii, “Crystal structure of Li_2MoO_4,” *DOKL. CHEM.,* vol. 376, p. 16-19, 2001.

[33] M. Molaei and M. Rahimipour, “Microwave Reflection loss of magnetic/ dielectric nanocomposites of $BaFe_{12}O_{19}$/TiO_2,” *Mater. Chem. Phys.,* vol. 167, p. 145-151, 2015.

[34] L. B. Kong, Z. W. Li, L. Liu, R. Huang, M. Abshinova, Z. H. Yang, C. B. Tang, P. K. Tan, C. R. Deng and S. Matitsine, “Recent progress in some composite materials and structures for specific electromagnetic applications,” *Int. Mater. Rev.,* vol. 58, p. 203-259, 2013.

[35] P. Xu, X. Han, J. Jiang, X. Wang, X. Li and A. Wen, “Synthesis and Characterization of Novel Coralloid Polyaniline/$BaFe_{12}O_{19}$ Nanocomposites,” *J. Phys. Chem. C .,* vol. 111, p. 12603-12608, 2007.

[36] X. Chen and G. Tan, “Multiferroic Properties of $BaFe_{12}O_{19}$ Ceramics,” 2012.

[37] A. H. Ali Ghasemi, A. Morisako, X. Liu and A. Ashrafizadeh, “Investigation of the microwave absorptive behaviour of doped barium ferrites,” *Mater. Des.,* vol. 29, p. 112-117, 2008.

[38] A. Kumar, V. Agarwala and D. Singh, “Effect of particle size of $BaFe_{12}O_{19}$ on the microwave absorption characteristics in X-band,” *PIER M.,* vol. 29, p. 223-236, 2013.

[39] J. Y. Shin and J. H. Oh, “The microwave absorbing phenomena of ferrite microwave absorbers,” *IEEE Trans. Magn.,* vol. 29, p. 3437-3439, 1993.

[40] M. Meshram, N. K. Agrawal, B. Sinha and P. Misra, “Characterization of M-type barium hexagonal ferrite-based wide band microwave absorber,” *J. Magn. Magn. Mater.,* vol. 271, p. 207-214, 2004.

[41] P. Wang and H. Xiang, “Room-Temperature Ferrimagnet with Frustrated Antiferroelectricity: Promising Candidate Toward Multiple State Memory,” *Phys. Rev. X.,* vol. 4, At. 011035, 2014.

[42] R. C. Pullar, “Hexagonal ferrites: A review of the synthesis, properties and applications of hexaferrite ceramics,” *Prog. Mater. Sci.,* vol. 57, p. 1191–1334, 2012.

[43] [Online]. Available: https://en.wikipedia.org/wiki/Ferrimagnetism. [Accessed November 2018].

[44] [Online]. Available: https://commons.wikimedia.org/wiki/File:Ferrimagnetic_ordering_illustration.svg. [Accessed November 2018].

[45] S. Chen and M. N. Afsar, “Fabry-Perot Open Resonator Technique for Dielectric Permittivity and Loss Tangent Measurements of Yttrium Iron Garnet,” *IEEE Trans. Magn.,* vol. 43, p. 2734-2736, 2007.

[46] M. A. Musaa, R. S. Azisa, N. H. Osmana, J. Hassana and T. Zangina, “Structural and magnetic properties of yttrium iron garnet (YIG) and yttrium aluminum iron garnet (YAlG) nanoferrite via sol-gel synthesis,” *Results in Physics,* vol. 7, p. 1135-1142, 2017.

[47] B. M. Gatehouse and P. Leverett, “The crystal structure of potassium heptamolybdate tetrahydrate, $K_6Mo_7O_{24}$, $4H_2O$,” *ChemComm.,* no. 15, p. 901-902, 1968.

[47] B. M. Gatehouse and P. Leverett, “The crystal structure of potassium molybdate, K_2MoO_4,” *J. Chem. SOC. A.,* vol. 0, p. 849-854, 1969.

[48] [Online]. Available: https://en.wikipedia.org/wiki/Sintering. [Accessed January 2017].

[49] H. Guo, J. Guo, A. Baker and C. A. Randall, “Hydrothermal-Assisted Cold Sintering Process: A New Guidance for Low-Temperature Ceramic Sintering,” *ACS Appl. Mater. Interfaces.,* vol. 8, p.

20909−20915, 2016.

[50] D. J. Guo, D. H. Guo, A. L. Baker, P. M. T. Lanagan, D. E. R. Kupp, P. G. L. Messing and P. C. A. Randall., “Cold Sintering: A Paradigm Shift for Processing and Integration of Ceramics,” *Angew. Chem. Int. Ed.,* vol. 55, p. 11457–11461, 2016.

[51] J. L. Shi, “Solid state sintering of ceramics: pore microstructure models, densification equations and applications,” *J. Mater. Sci.,* vol. 34, p. 3801-3812, 1999.

[52] W. D. Kingery, H. K. Bowen and D. R. Uhlmann, Introduction to ceramics, 2nd edition, New York: Wiley, 1976.

[53] H. Zheng, “Processing and properties of die-attachment on copper surface by low-temperature sintering of nanosilver paste processing,” Thesis accessed via: DOI: 10.13140/RG.2.2.20828.39040, 2012.

[54] J. Guo, A. L.Baker, H. Guo, M. Lanagan and C. A. Randall, “Cold sintering process: A new era for ceramic packaging and microwave device development,” *J. Am. Ceram. Soc.,* vol. 100, p. 669–677, 2017.

[55] H. Guo, A. Baker, J. Guo and C. A. Randall, “ Cold Sintering Process: A Novel Technique for Low-Temperature Ceramic Processing of Ferroelectrics,” *J. Am. Ceram. Soc.,* vol. 99, p. 3489-3507, 2016.

[56] [Online]. Available: http://antenna-theory.com. [Accessed June 2016].

[57] C. A. Balanis, Antenna theory analysis and design, fourth edition, John Wiley & Sons, Inc., 2016 .

[58] [Online]. Available: http://wireless.ictp.it/handbook/C4.pdf. [Accessed January 2017].

[59] [Online]. Available: https://en.wikipedia.org/wiki/Antenna_gain. [Accessed September 2017].

[60] [Online]. Available: https://en.wikipedia.org/wiki/Impedance_matching. [Accessed September 2017].

[61] S. Khmailia, H. Taghouti, S. Jmal and A. Mami, “Impedance matching of a microstrip antenna,” *IJACSA 2017.,* vol. 8, p. 19-23, 2017.

[62] I. Ahmed, M. S. Arefin, M. S. Hussain and M. Z. Shames, “Performance Study of Microstrip patch Antenna for GPS Communication System,” *IJSER.,* vol. 4, p. 2030-2032, 2013.

[63] G. Misra, A. Agarwal and K. Agarwal, “Design and Performance Evaluation of Microstrip Antenna for Ultra-Wideband Applications Using Microstrip Feed,” *AJEEE.,* vol. 3, p. 93-99, 2015.

[64] [Online]. Available: http://fab.cba.mit.edu/classes/862.06/students/alki/GA.html. [Accessed February 2017].

Chapter 3: Experimental procedure

3.1 Ceramic fabrication

The appropriate weighed raw materials for $BaTi_4O_9$ (BT4), $BaFe_{12}O_{19}$ (BF12) and Ti-doped BF12 (BFT100x) ceramics were ball-milled in isopropanol using yttria stabilised zirconia (YSZ) media for 24 hours and dried overnight at 120 ^{o}C. Powders were sieved to remove the media and any large agglomerates and calcined 2h at 1150 °C and 6h at 1200 ^{o}C for BT4 and BF12, respectively. Powders were re-milled and sieved after calcination before pressing into 10 mm pellets using a uniaxial press at ~27.5 MPa. BT4 and BF12 were sintered for 4hr and 6hr, respectively, from 1300 to 1400 ^{o}C.

The appropriate proportions of BF12 and Li_2MoO_4 (LMO) were weighed and either ball or attrition milled in isopropanol using YSZ media. Powders were sieved after milling and 10-20% of water added using a pestle and mortar. Powders were placed in 30X30 mm square and 20mm cylindrical dies and cold sintered for 20-40 minutes at 120 ^{o}C at 55 to 70 MPa. The temperature ramp was 1.85 ^{o}C /second. After reaching the target temperature, the pressure was applied by closing the valve, and pumping through the manual attached arm in an even controlled way till reaching the aimed equivalent force/inch^2 to the wanted MPa pressure (see Figure 3.1).

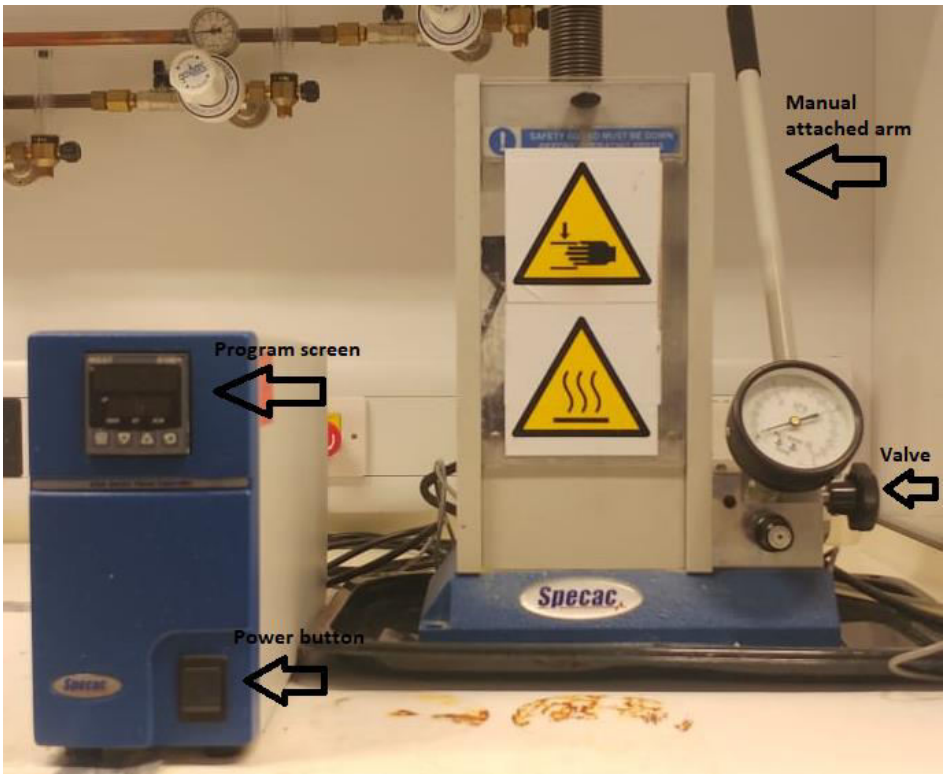

Figure 3.1. Hot press used for cold sintering in the present study

Similar procedures were followed for TiO_2-LMO, $Y_3Fe_5O_{12}$-LMO, BF12-Na_2MoO_4, BF12-K_2MoO_4, $Li_{1.5}Al_{0.5}Ge_{1.5}P_3O_{12}$ - LMO, $BaTiO_3$ - LMO with a list of fabricated compositions given in Table 3.1.

Fabricated compositions	Sintering method
BF12-BT4	Conventional
BF12-TiO2	Conventional
LMO	Cold
BF12-LMO	Cold
TiO_2-LMO	Cold
$Y_3Fe_5O_{12}$-LMO	Cold
BF12-Na_2MoO_4	Cold
BF12-K_2MoO_4	Cold
$BaTiO_3$-LMO “nano scale $BaTiO_3$”	Cold
$BaTiO_3$-LMO “micro scale $BaTiO_3$”	Cold
$Li_{1.5}Al_{0.5}Ge_{1.5}P_3O_{12}$ -LMO	Cold

Table 3.1. Fabricated composites and their used sintering method

Table 3.2 shows raw materials and compounds suppliers’ source and their purity percentage. It is noted that the LMO bought from Alfa Aesar had better microwave properties after the cold sintering process than the LMO bought from Sigma Aldrich in an earlier stage. Table 3.3 shows raw materials drying temperature before being weighed and used in composites.

Compounds	Supplier	Purity %
$BaCO_3$	Sigma Adlrich	99
TiO_2	Sigma Adlrich	99.99
Fe_2O_3	Sigma Adlrich	99
LMO	Alfa Aesar	99
$Y_3Fe_5O_{12}$	Sigma Adlrich	99.9
Na_2MoO_4	Alfa Aesar	Mo, 46.2
K_2MoO_4	Alfa Aesar	95
$BaTiO_3$ “nano scale”	Sigma Adlrich	99
$BaTiO_3$ “nano scale”	Sigma Adlrich	99
$Li_{1.5}Al_{0.5}Ge_{1.5}P_3O_{12}$	MSE supplies	99.99

Table 3.2. Compounds used in fabrication showing supplier and purity percentage

Raw materials	Drying temperature (^{o}C)
$BaCO_3$	180
TiO_2	900
Fe_2O_3	600

Table 3.3. Drying temperature of raw materials prior to ball milling

3.2 Particle size

The particle size of raw materials ($BaCO_3$, Fe_2O_3, TiO_2), pre-calcined and calcined powders of BT4 and BF12 were measured using Malvern Mastersizer 3000 with laser obscuration's range between 3-5% and background measurement duration and sample measurement duration of 30 and 10 seconds respectively. The background stability timeout was 300s and the stirrer speed 2000 rpm throughout the measurement process. The wet dispersion method was used which depends on surface tension, so the concentration of surfactant to powder is significant in deciding how well the powder will be dispersed. In this case, one to two droplets of surfactants were typically enough to disperse the particles. Increasing surfactant concentration cause further agglomeration, foaming and bubble formation. Small amount of powder (<1g) were stirred into distilled water using a Hydro dispersion unit. As the laser beam scatters through the suspension at different intensities, the variation of angle measures the particle distribution and size.

3.3 Density measurements

The densities of samples insoluble in water were measured using the Archimedes' principle, Equation. 3.1:

$$\boldsymbol{\rho = \frac{A}{A-B}\ (\rho_L - d) + d} \qquad \text{Equ. 3.1}$$

where ρ is density of the ceramic, A and B represent the weight of the sample in air and water, respectively, ρ_L is the density of water and d the density of air (1.225 x10^{-3} g/cm^3) respectively. A Mettler Toledo MS104S Newclassic MS Analytical Balance, (120g x 0.1mg) has been used to record all weights.

The densities of samples soluble in water were measured according to Equation. 3.2:

$$\boldsymbol{Density = \frac{Mass(g)}{Volume\ (cm^3)}} \qquad \text{Equ. 3.2}$$

Volume was calculated from the thickness and diameter or square side measured using a Vernier Calliper with an accuracy of ± 0.05 mm. Mass was measured by using a digital balance. The relative density was calculated by comparing measured densities to theoretical

values obtained from literature. The following equation shows how a relative density of a composite consisting of compounds A and B is measured:

$$\boldsymbol{Relative\ density = Ex.Dens \div \frac{1}{\frac{wt\%A}{C}+\frac{wt\%B}{D}}} \qquad \text{Equ. 3.3}$$

Where Ex.Dens is the experimental density (calculated in Equ. 3.2), C and D represent theoretical densities of compounds A and B respectively as obtained from literature.

3.4 X-ray diffraction (XRD)

X-ray diffraction (XRD) is a technique used to the determine the structure and phase assemblage of a crystalline solid and is based on the interaction of X-ray radiation with the crystal lattice in accordance with Bragg's law

$$2d\sin\theta = n\lambda \qquad \text{Equ. 3.4}$$

where d is the separation distance between two lattice points, and θ is the incidence angle of X-radiation in accordance with Figure 3.2[1]:

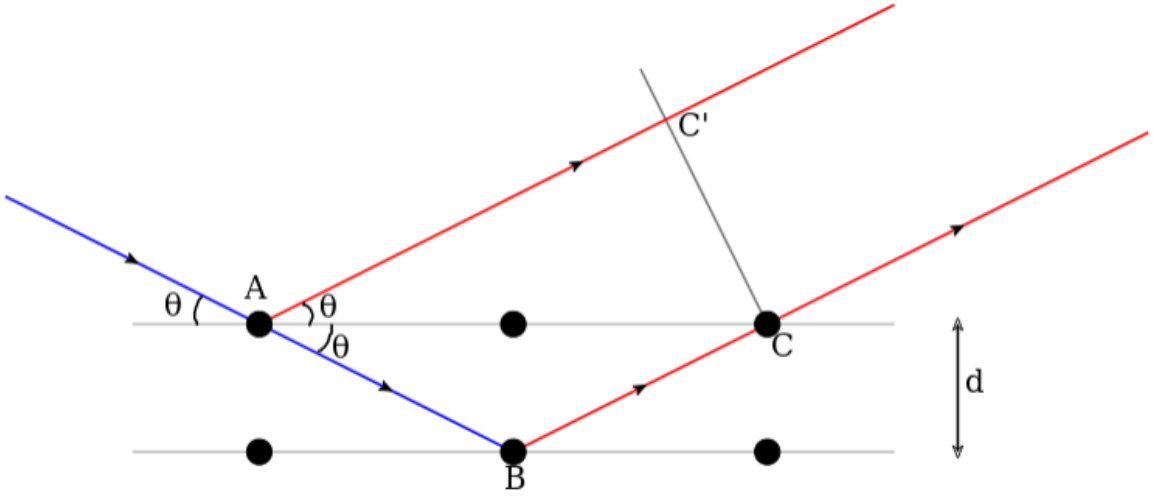

Figure 3.2. Representation of Bragg's law through lattice points **[1]**

When Bragg's law is satisfied, reflections are detected with periodic intensities proportional to the lattice spacings with the crystal. *Hkl* indices are assigned to the Bragg peaks using either WinXpow or by visual inspection. For this work, XRD was used to assign crystal structure and to distinguish phases within the composites. Crushed pellets were analysed using a Bruker D2 Phaser with Cu*K*α (λ = 1.5418 Å). The scanning drive axis was taken as 2θ, with the scan recording in the range of 10-80°, a scanning interval of $\Delta 2\theta$= 0.02, and a time step of t=0.45 seconds operated at 40kV and 30mA. The specimens were crushed using a pellet crusher followed by Quartz pestle and mortar mixing without solution. Then the powder was put into plastic holders exploiting glass slides to ensure flatness of surface

before turning radiation on. Processing of the raw data was conducted using WinXpow software (version 2.10, Germany) and the analysis of the diffraction patterns was conducted using Jade 6.0 software.

3.5 Scanning electron microscopy (SEM)

In SEM electrons interact with atoms at or just below the surface of the specimen. In this study, mainly secondary electrons were used to image topographic features along with backscattered electrons to determine different phases and characteristic X-rays to determine the local composition of the sample. Fracture surfaces might have given some further data but would not easily reveal the phase assemblage as the samples would fracture along regions dominated by the non-cold sintering end member and therefore would risk being unrepresentative of the bulk composition, hence surface SEM images have been used in this study. Figure 3.3 [2] shows how signals generating from different depths require different detectors to be detected when reacting with the specimen depending on some factors such as sample density and accelerating voltage [3]:

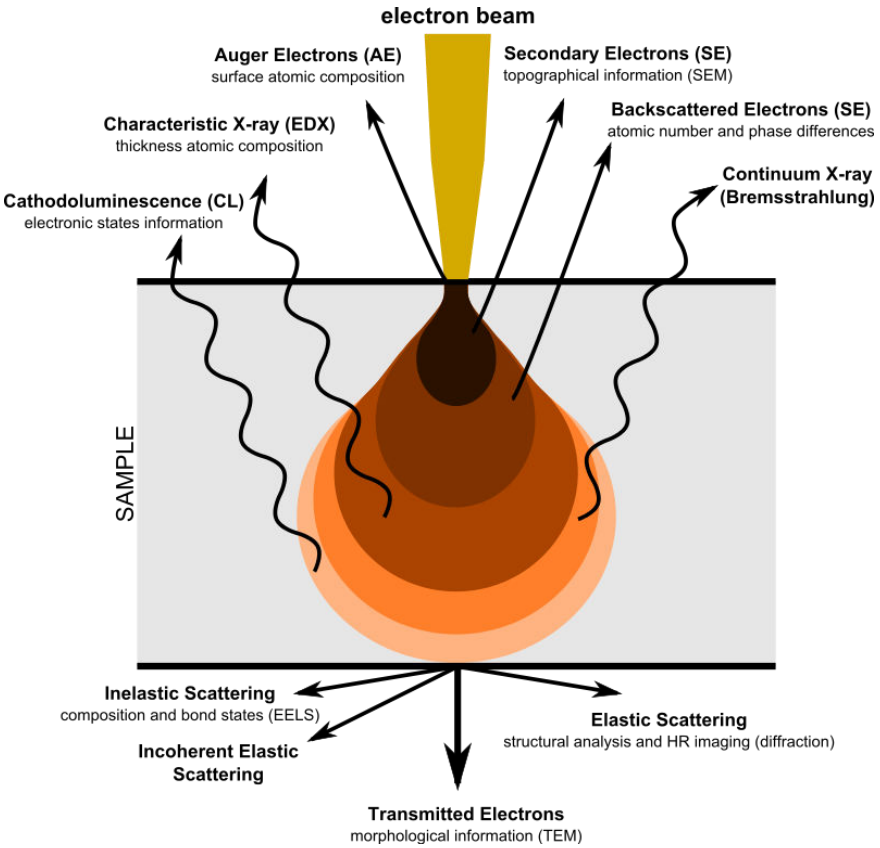

Figure 3.3. Variant detectors detecting electron beam penetrating through specimen [2]

Secondary electron (SE) detector is used to produce topographic images, while backscattered electron detector allows lower vacuum levels than SE detector which reduces

beam damage and detects elastically scattered electrons in layers below sample's surface [3]. Backscattered electrons depend on atomic number of elements, so it is a good method to study chemical variation throughout composites. Characteristic X-rays generated from Energy dispersive spectroscopy (EDS) depend on the difference in energy between outer and inner shells of electron [3]. Since characteristic X-rays have specific wavelengths and energies relating to the atom type, EDS is considered an important method to collect qualitative and quantitative chemical information about the sample. However, the detectors available to the project were unable to detect low atomic number (<11) [4], [5].

SEM and EDS were carried out using Inspect F and Inspect F50 SEM operating at 10-15kV equipped with an EDAX energy dispersive X-ray detector. The pellets were mounted on an aluminium stub and positioned inside the microscope within a working distance of 10mm. The chamber pressure operated at <5.00 x 10^{-5} mbar, with accelerating voltage of 10-15 KV and spot size of 3. GENESIS spectrum software from EDAX was used for EDS elemental mapping.

3.6 Transmission electron microscopy (TEM)

TEM differs from transmission light microscopes in that it yields a much better resolution because the wavelength of electrons is shorter than light according to de Broglie. Equation 3.5 shows the relationship of image resolution and wavelength of light microscope [6]:

$$\boldsymbol{d = \frac{\lambda}{2n\,sin\alpha} = \frac{\lambda}{2\,NA}} \qquad \text{Equ. 3.5}$$

where d is the maximum resolution, λ is the wavelength, n is the lens's index of refraction, α is the maximum half angle of cone of light entering the lens, and NA is the numerical aperture of the system. The exceptional resolution afforded by using electrons permits atomic resolution imaging. Advanced TEMs, not only have a high image resolution but can achieve probe sizes for a focussed electron beam <5 nm. This unprecedented spatial resolution has led to a new generation of highly performant analytical instruments which are able to obtain atomic resolution chemical mapping of a crystal lattice by electron energy loss spectroscopy.

In this study, conventional TEM was performed on an EM420 operating at 120 kV to obtain bright field diffraction contrast images and electron diffraction patterns of pertinent phases. Figure 3.4 shows the two basic operation modes of TEM; imaging and diffraction [6]:

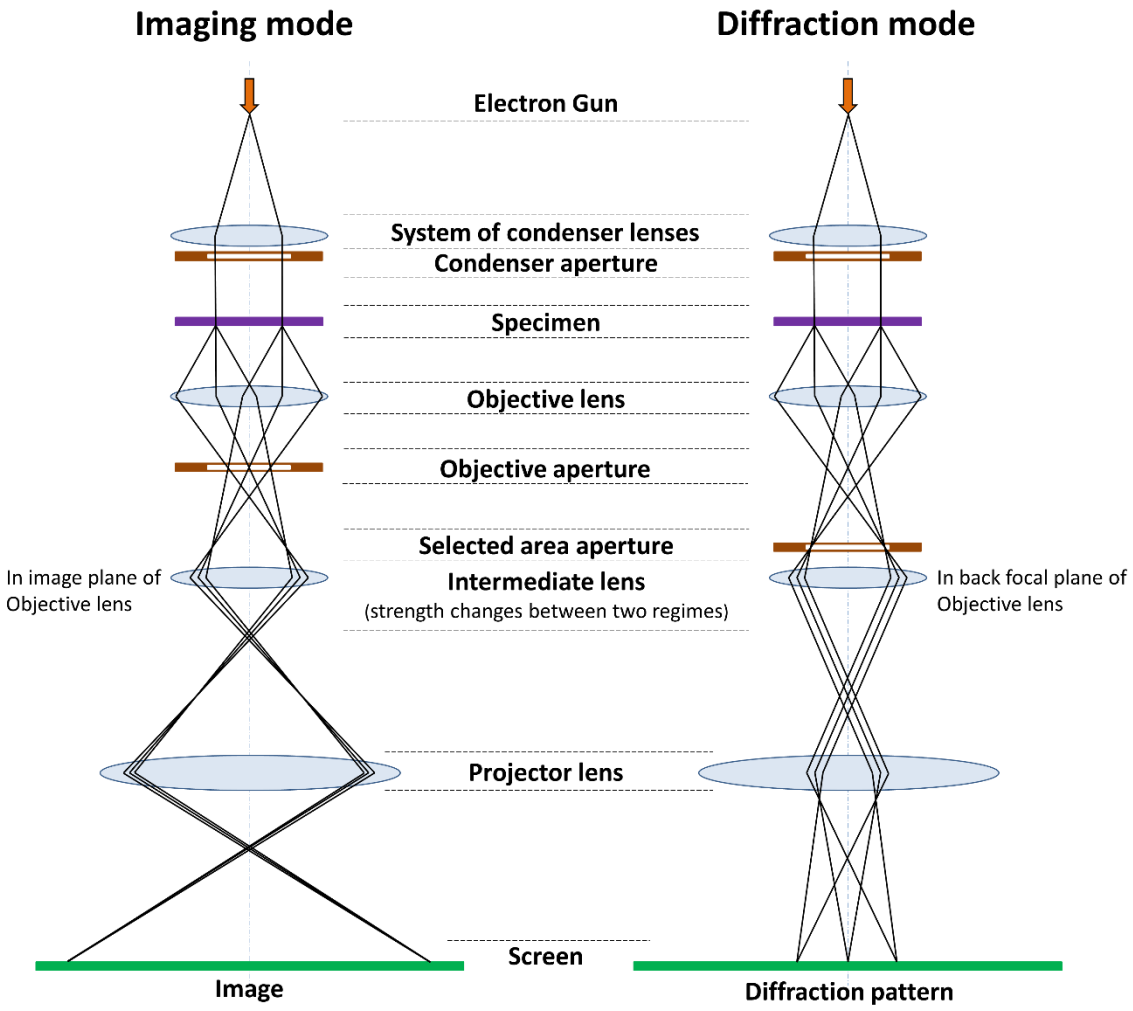

Figure 3.4. Schematic showing imaging and diffraction mode of TEM **[6]:**

The focal plane is used in imaging mode while back focal plane is used to project diffraction patterns, as shown in Figure 3.4 [6]. The parallel beam of electrons is fired from gun and shaped in condenser lenses to reach the specimen [6]. After passing through the specimen, two types of electrons are formed; scattered electrons which change their trajectories due to interaction with material, and unscattered electrons which are represented by the bright central beam [6].

Atomic resolution transmission electron microscopy was performed using JEOLR005 aberration corrected TEM operating at 300 kV. In each case, TEM specimens were pre-thinned to a thickness of 20 - 50 μm by mechanical grinding in acetone and then ion milled to electron transparency using a GATAN precision ion polishing system (PIPS II). TEM was performed courtesy of Dr. Ali Mostaed.

3.7 Microwave measurements

3.7.1 Dielectric

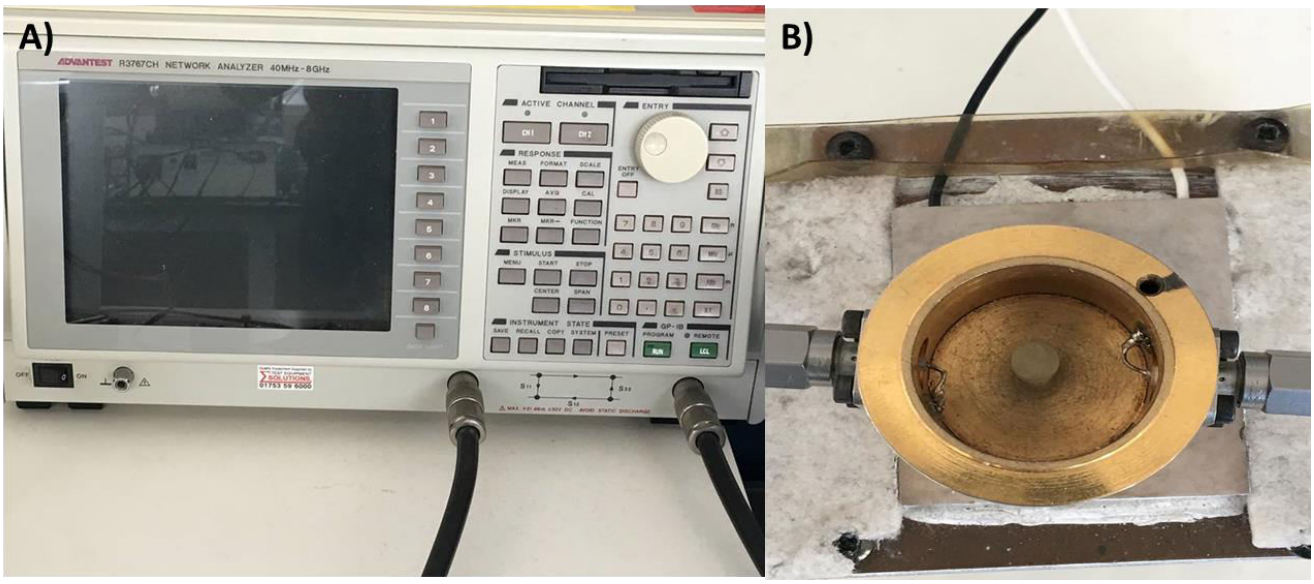

Figure 3.5. A) Advantest R3767CH VNA B) Brass cavity attached to VNA

An Advantest R3767CH vector network analyser (Figure 3.5 A) was used to measure dielectric microwave properties for samples that resonated below 8 GHz with a Rohde & Schwarz ZVB20 network analyser used at high frequencies. In both cases, a brass cavity with the height of 25mm and a diameter of 30mm including a spacer of 4.77mm (Figure 3.5 B) was connected to the VNA. ε_r was calculated using the TE01 delta technique invented by Krupka et al.[7] in a DOS software called ***Permittivity.exe*** after inputting Q, dimensions of the pellet into the software. *Q* is calculated from Equation. 3.6:

$$\boldsymbol{Q = \frac{f_o}{BW}} \qquad \text{Equ. 3.6}$$

where f_o is the resonance frequency, and BW is the bandwidth of the signal. Those two parameters are provided by the VNA spectrum within the scattering parameter S_{21}. Value of Q is converted to a material constant by multiplying by f_o according to Equation 3.7 and is measured in GHz:

$$\boldsymbol{Qf_o = Q \text{ x } f_o} \qquad \text{Equ. 3.7}$$

A Peltier heating unit was used to vary temperature and the resulting deviation in f_o is recorded. This permitted calculation of temperature coefficient of resonant frequency (TCF) according to Equation 3.8.

$$\text{TCF} = \left(\frac{\mathbf{f_T - f_{T_o}}}{\mathbf{f_{T_o}(T - T_o)}}\right) * \mathbf{10^6} \qquad \text{Equ. 3.8}$$

Where f_T and f_{To} represent the final and initial frequency corresponding to the temperatures T and $T_{o,}$ respectively.

3.7.2 Magnetic

*x*BF12-(1-*x*) LMO samples were polished to the dimensions of 22.86mm × 10.16mm with a thickness ~ 2mm, which ensures the samples can be fitted in an X-band (8-12 GHz) rectangular waveguide. Vector Network Analyser Anritsu Lighting 37397D was used for measuring the reflection coefficient (S11) and transmission coefficient (S21) parameters at the two ends of the waveguide. The complex permeability could then be extracted from the measured complex S-parameters by using the Nicolson-Ross-Weir technique (NRW) method [8], [9].

3.8 Impedance Spectroscopy

Electroceramics' electrical properties are significantly affected by crystal structure of their particles. One effective way to analyse and characterize the electrical properties is using Impedance spectroscopy, which can show impedance, permittivity, modulus and conductivity dependencies on frequency and their change with temperature.

Impedance Z is related to three other complex variables; admittance Y, permittivity ε, and electric modulus M. Mathematical formulas link between these variables from Equs. (3.9- 3.12) as follows:

$$Z = \mathrm{Z}' - \mathrm{jZ}'' \qquad \text{Equ. 3.9}$$

$$M = j\omega C_o Z = j\omega C_o(Z' - jZ'') = \omega C_o Z'' + j\omega C_o Z'$$

$$M' = \omega C_o Z''$$

$$M'' = \omega C_o Z'$$

$$C_o = \varepsilon_o \frac{A}{d} \qquad \text{Equs. 3. 10}$$

$$Y = \frac{1}{Z} = \frac{1}{Z' - jZ''} = \frac{Z' + jZ''}{(Z')^2 + (Z'')^2}$$

$$Y' = \frac{Z'}{(Z')^2+(Z'')^2} \qquad \text{Equs. 3. 11}$$

$$Y'' = \frac{Z''}{(Z')^2+(Z'')^2}$$

$$\varepsilon = \frac{1}{M} = \frac{1}{M'+jM''} = \frac{1}{\omega C_o} \cdot \frac{Z''-jZ'}{(Z')^2+(Z'')^2}$$

$$\varepsilon' = \frac{1}{\omega C_o} \cdot \frac{Z''}{(Z')^2+(Z'')^2} \qquad \text{Equs. 3. 12}$$

$$\varepsilon'' = \frac{1}{\omega C_o} \cdot \frac{Z\prime}{(Z')^2+(Z'')^2}$$

Where Z' and Z'' are real and imaginary components of complex impedance Z respectively, j=√-1, $\omega = 2\pi f_o$ and is angular frequency, C_o is capacitance of free space and d is the distance between two plate areas in capacitor.

Capacitance can be calculated directly from Equs. 3.10 and 3.12 and resistance therefore is known by the relation $\omega RC = 1$. Another method to calculate resistance R, capacitance C and conductivity σ which is used in this thesis is shown in Equs. 3.13:

$$C = \frac{1}{2M''max}$$

$$R = \frac{1}{2\pi\, f_m C} \qquad \text{Equs. 3. 13}$$

$$\sigma = \frac{1}{R}$$

Where f_m is the maximum frequency. Equs. 3.13 are extracted from spectra of imaginary part of electric modulus M''.

Geometry and thickness of sample are significant parameters in predicting possible capacitance values as shown in Table 3.4[10]. Grain boundaries for example have higher capacitance than bulk grains because of their lower thickness.

Capacitance (F)	Phenomenon Responsible
10^{-12}	bulk
10^{-11}	secondary phase(s)
10^{-11} - 10^{-8}	grain boundary
10^{-10}- 10^{-9}	bulk ferroelectric
10^{-9} - 10^{-7}	surface layers
10^{-7}- 10^{-5}	sample-electrode interface
10^{-4}	electrochemical reaction

Table 3.4. Capacitance values and their possible interpretation [10]

The samples were coated using silver paste as a conducting electrode, and then loaded into a jig in a tube furnace which is connected to Agilent Precision LCR Meter E4980A, (20 Hz to 2 MHz) applying 0.1V and collecting data of temperature range (23-300°C). Data was corrected for geometry using ZViewTM software (Scribner Associates Inc, USA).

3.9 References

[1] [Online]. Available: https://en.wikipedia.org/wiki/Bragg%27s_law. [Accessed June 2018].

[2] [Online]. Available: http://www.wikiwand.com/en/Scanning_electron_microscope. [Accessed November 2018].

[3] [Online]. Available: https://www.nanoscience.com/techniques/scanning-electron-microscopy/components/. [Accessed November 2018].

[4] A. R. West, Solid state chemistry and its applications, second edition, John Wiley & Sons, Ltd., 2014.

[5] J. I. Goldstein, D. E. Newbury, P. Echlin, D. C. Joy, C. E. Lyman, E. Lifshin, L. Sawyer and J. R. Michael, Scanning Electron Microscopy and X-ray Microanalysis, Boston, MA: Springer US, 2003.

[6] [Online]. Available: https://en.wikipedia.org/wiki/Transmission_electron_microscopy.

[Accessed June 2018].

[7] J. Krupka, K. Derzakowski, B. Riddle and J. Baker-Jarvis, “A dielectric resonator for measurements of complex permittivity of low loss dielectric materials as a function of temperature,” *Meas. Sci. Technol.,* vol. 9, p. 1751–1756, 1998

[8] A. M. Nicolson and G. F. Ross, “Measurement of the Intrinsic Properties of Materials by Time-Domain Techniques,” *IEEE Trans. Instrum. Meas.,* vol. 19, p. 377–382, 1970.

[9] W. B. Weir, “Automatic measurement of complex dielectric constant and permeability at microwave frequencies,” *Proc. IEEE .,* vol. 62, p. 33–36, 1974.

[10] J.T.S. Irvine, D.C. Sinclair and A.R. West, “Electroceramics: Characterization by Impedance Spectroscopy,” *Adv. Mater.,* vol. 2, p. 132-138, 1990.

Chapter 4: Fabrication and characterisation of conventionally sintered composites, (1-x)$BaFe_{12}O_{19}$ – xTiO_2) and $BaTi_4O_9$ – $BaFe_{12}O_{19}$ (BT4-BF12).

In this chapter, BT4, BF12, BT4-BF12 composites and (1-*x*) BF12-*x*TiO_2 are fabricated using conventional solid state sintering with a view to developing ceramics which interact with the electric and magnetic components EM radiation at resonance. Magnetodielectric ceramics of this type have the potential for a broadband response, particular if $\varepsilon_r/\mu = 1$. In addition, this chapter will characterise the raw materials and processing steps involved in solid state synthesis.

4.1 Raw Materials

4.1.1 $BaCO_3$

The $BaCO_3$ particle refractive and absorption index are 1.529 and 0.01, respectively with the laser obscuration's range is between 3-5%. This gave an average particle size of $BaCO_3$ measured after stabilisation of ~9 µm (Figure 4.1) with a small number of significantly larger, and probably still agglomerated particles, and some fines.

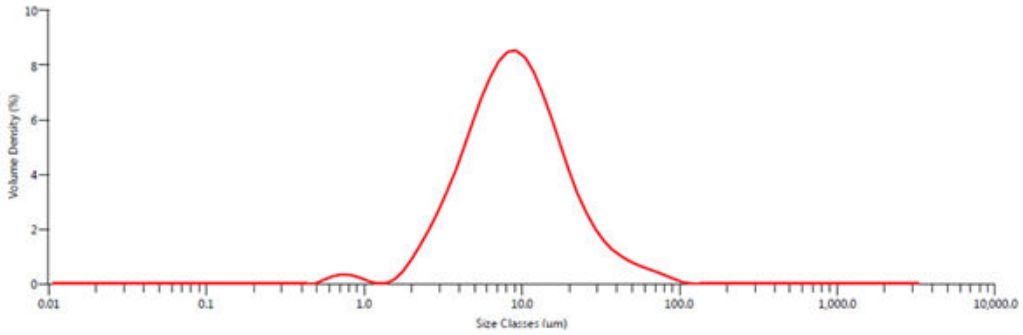

Figure 4.1. Particle size distribution of $BaCO_3$ after stabilisation using water as a dispersant.

The XRD trace of the $BaCO_3$ raw material is shown in (Figure 4.2). The peaks were indexed to an orthorhombic phase (witherite) as shown in Figure 4.2 in agreement with Islam and Hill [1] and the ICDD data base (PDF#41-0373).

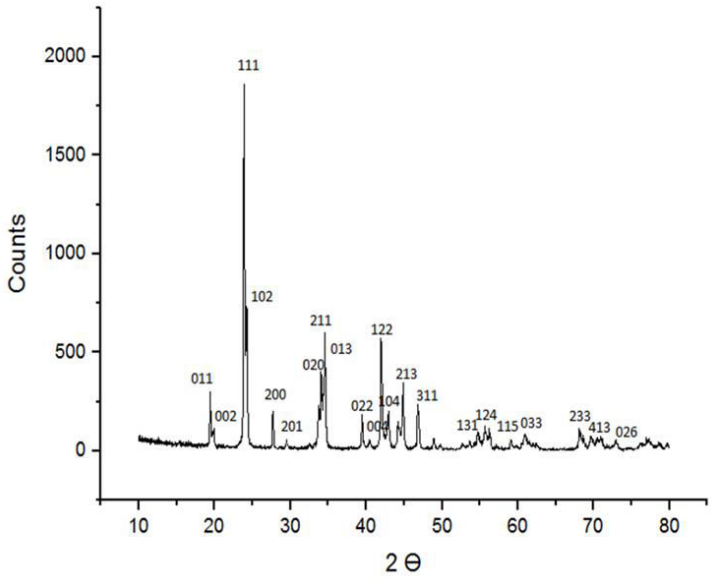

Figure 4.2. X- ray diffraction trace for $BaCO_3$

4.1.2 TiO_2

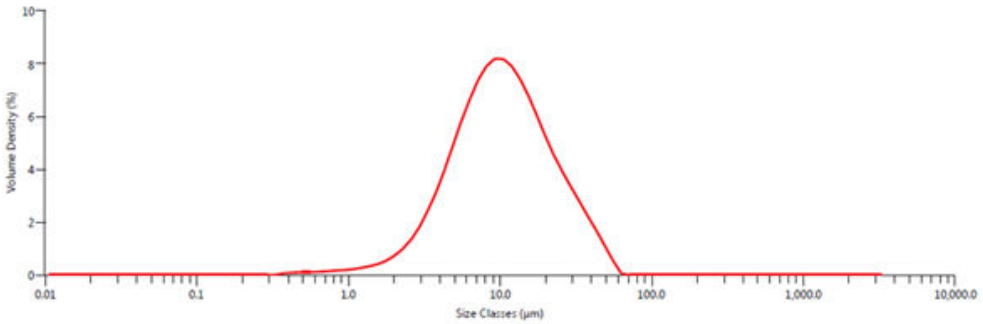

Figure 4.3. Particle size distribution of TiO_2 after stabilisation using water as a dispersant.

The TiO_2 particle refractive and absorption index are 2.614 and 0.1, respectively with a laser obscuration range between 3-5%. This gave an average particle size of TiO_2 measured after stabilisation of ~10 µm (Figure 4.3). Strong diffraction peaks attributed to rutile occur at 27, 36 and 54 2θ as shown in Figure 4.4 with a tetragonal unit cell in agreement with Kheamrutai et al [2].

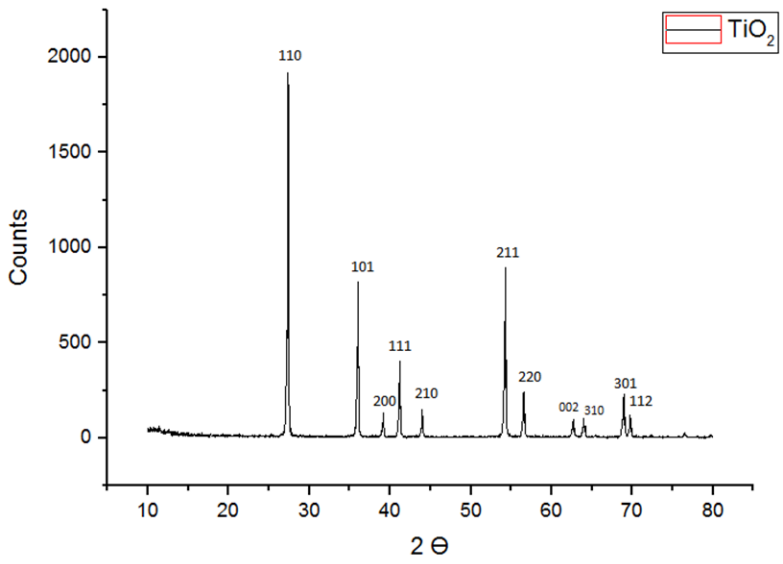

Figure 4.4. X- ray diffraction result of TiO_2

4.1.3 Fe_2O_3

The particle refractive index of Fe_2O_3 is 2.918 and the particle absorption index 0.01 with a laser obscuration range between 3-5%.The average particle size of Fe_2O_3 measured after stabilisation is ~21 µm (Figure 4.5) but with a small number of significantly larger agglomerated particles and some fines.

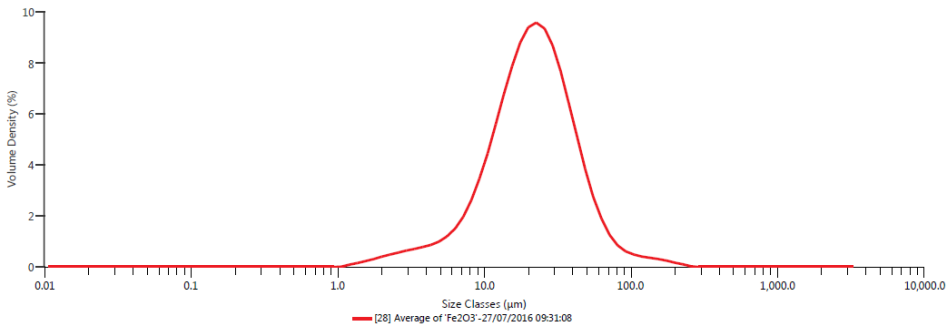

Figure 4.5. Particle size distribution of Fe_2O_3 after stabilisation using water as a dispersant.

Waseem et al. [3] reported that an electrolytic dispersion method for measuring particle size of Fe_2O_3 can avoid agglomerations if sonicated for 30 minutes. In this study, Fe_2O_3 was sonicated for only 30 seconds, therefore there is a significant level of residual agglomeration and a large average particle size. Figure 4.6 illustrates the repeated attempts to reduce particle size through iteration. Unusually, repeated sonication had the effect of

narrowing the particle size distribution but increasing the average particle size, supporting the conclusion that agglomeration was occurring.

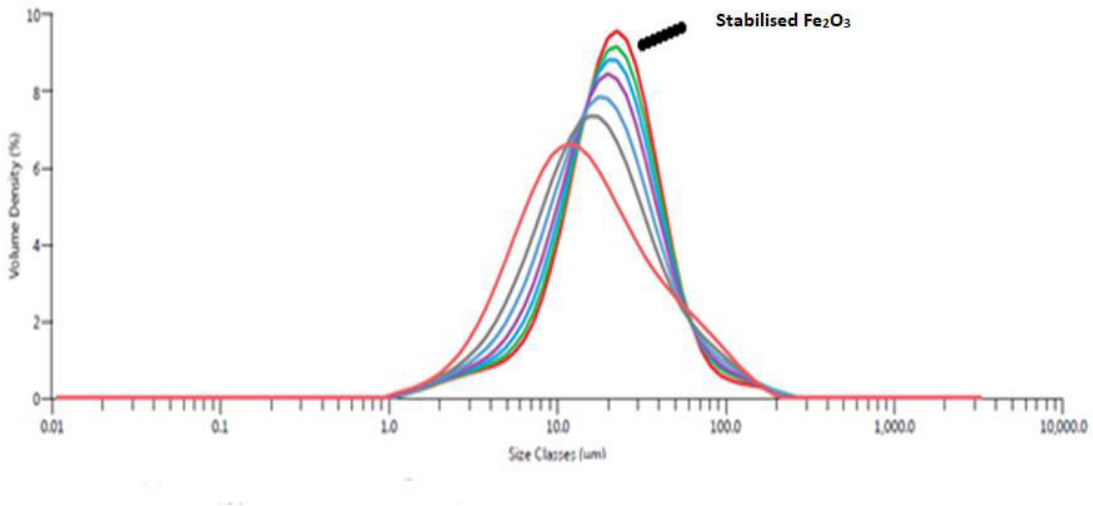

Figure 4.6. Particle size distribution attempts of Fe_2O_3 till stabilisation using water as a dispersant

Figure 4.7 shows the XRD trace of Fe_2O_3 with nine distinguishable peaks indexed according to a rhombohedral structure, in agreement with hematite Fe_2O_3 (JCPDS No. 24-0072) and with Joya et al [4].

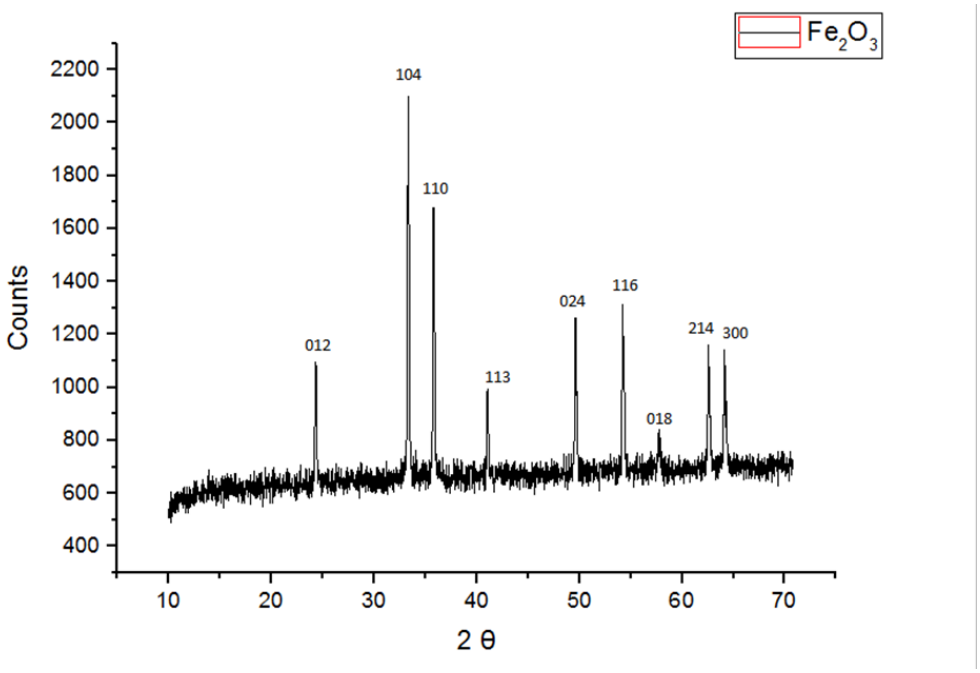

Figure 4.7. X- ray diffraction result of Fe_2O_3

4.2 Fabrication and Characterisation of $BaTi_4O_9$ and $BaFe_{12}O_{19}$

4.2.1 $BaTi_4O_9$

The particle size of powders was measured before and after calcination with reacted $BaTi_4O_9$ (BT4, 23.8 µm) (Figure 4.9) showing a significant increase with respect to unreacted raw powder (6.6 µm) (Figure 4.8). Large particle size generally causes problems during pressing and densification, hence the calcined powder was re-milled. According to Wang et al [5], the greater the eventual grain size for BT4, the larger the relative permittivity ε_r, and high the quality factor *Qf*. Sebastian [6] commented on the importance of sintering in BT4 and described a linear relationship between temperature, grain size and theoretical density till a saturation temperature around 1300 °C [7].

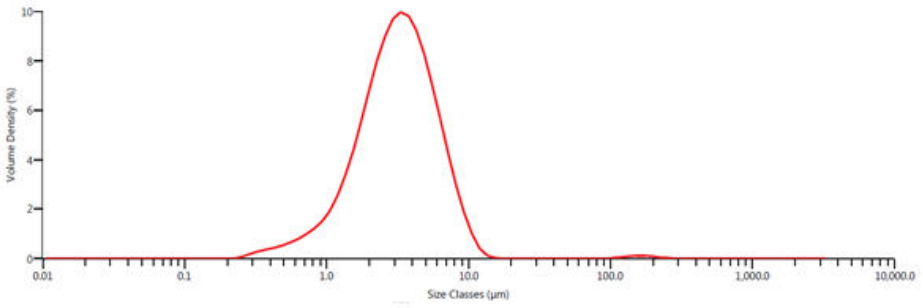

Figure 4.8. Particle size distribution of pre calcined BT4 after stabilisation using water as a dispersant.

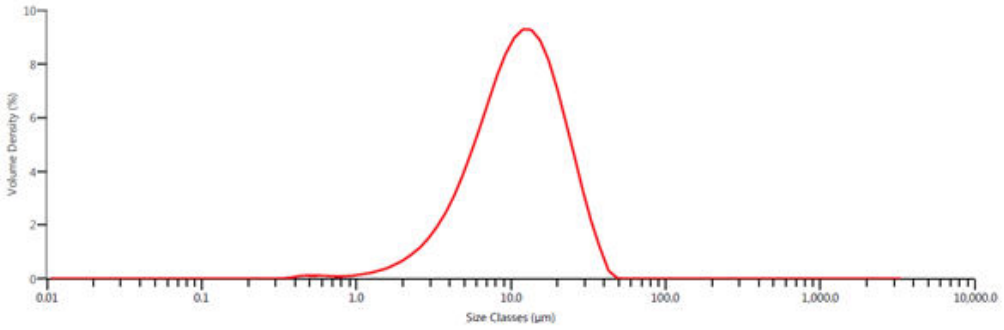

Figure 4.9. Particle size distribution of calcined BT4 for 2h at 1150 ^{o}C using water as a dispersant.

Figure 4.10 shows the XRD trace of the BT4 powder calcined 2hr at 1150 ^{o}C with all peaks indexed to one phase of BT4 according to an orthorhombic structure in agreement with Juang and Huang [8]. It is noted in Figure 4.10 that only significant peaks of BT4 are indexed.

Figure 4.11 is a scanning electron micrograph of the final sintered microstructure of BT4. Elongated grains are observed with an aspect ratio of 1 x 10 µm. The shape of the

particles is influenced by the anisotropy of the BT4 crystal structure. These results are in agreement with the microstructure reported by Anjana and Sebastian's [6] with little apparent porosity and good densification. Table 4.1 shows dimensions and measured densities for BT4 samples using the Archimedes principle.

Sample No.	Diameter (mm)	Thickness (mm)	Density (g/cm^3)
1	8.37	3.8	4.403
2	8.23	5.42	4.366
3	8.23	4.8	4.351
4	8.26	4.46	4.291
5	8.24	4.53	4.314

Table 4.1. BT4 samples dimensions and densities

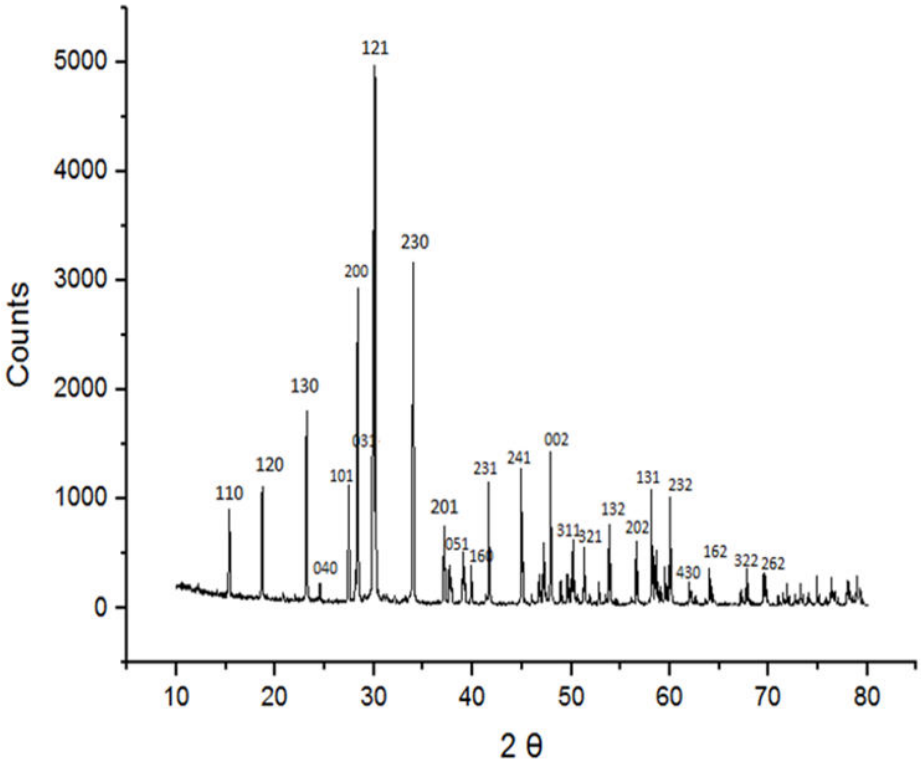

Figure 4.10. X- ray diffraction trace of BT4 calcined 2h at 1150 ^{o}C

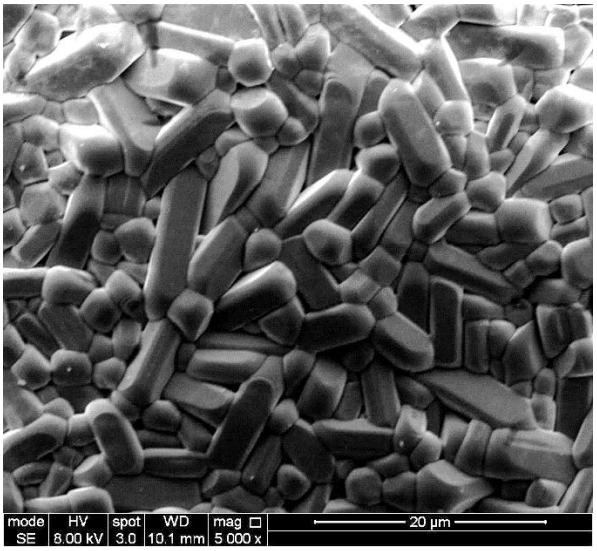

Figure 4.11. Scanning electron micrograph of BT4 sintered for 4 hr at 1350°C.

The microwave properties of BT4 samples at different sintering temperatures, dimensions and densities are shown in Table 4.2. The average measured ε_r was around 36 with TCF~ 17 MK^{-1} and Qf ~ 25,000 GHz, in close agreement with Mhaisalkar et al [7].

4.2.2 $BaFe_{12}O_{19}$

The average powder particle size for $BaFe_{12}O_{19}$ (BF12) increased from 23.3 µm to 44.3 µm before and after calcination, respectively (Figure 4.12 and 4.13). The increase in particle size is thought to be due agglomeration by partial sintering at high temperatures. Sadhana et al. [9] also recognized that by solid state synthesis, hard-agglomerated particles with large diameters and irregular morphologies were produced in BF12 [9].

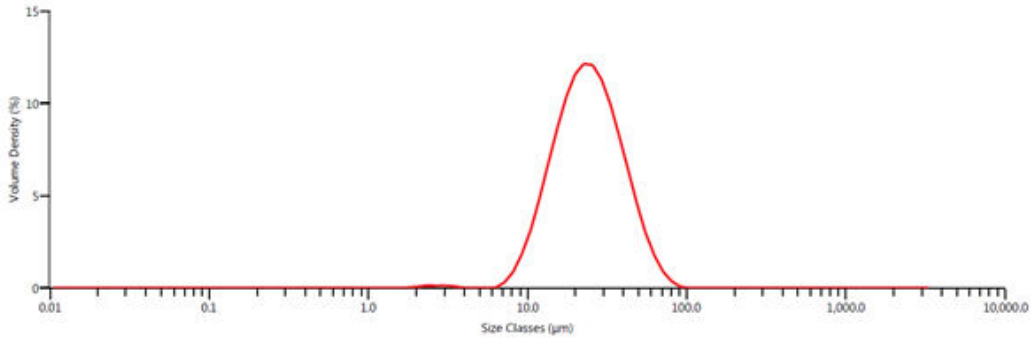

Figure 4.12. Particle size distribution of pre-calcined BF12 after stabilisation using wet dispersant.

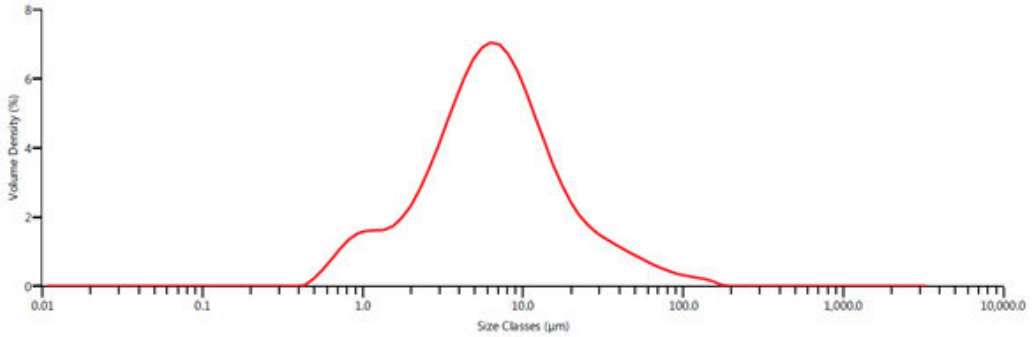

Figure 4.13. Particle size distribution of calcined BF12 for 6hr at 1200 ^{o}C using wet dispersant.

Figure 4.14 shows the XRD trace of the BF12 powder calcined 6hr at 1200 ^{o}C with all peaks indexed to one phase of BF12 according to an hexagonal structure and matching PDF# 43-0002, in agreement with Chen and Tan [10].It is noted that only significant peaks of BF12 are indexed. The relative intensities of the (107) and (114) peaks, which correspond to the inclined c-axis orientation, are higher than those of (112) and (200) peaks, suggesting that particles are randomly oriented [10].

Sample No.	f_o (GHz)	S_{21} (db)	BW (MHz)	Q	tanδ	*Qf* (GHz)	ε_r	TCF (ppm/°C)	Sintering Details
1	6.315416667	-9.8	2.94	3186	0.00031	20121	37.1	16	1350°C, 4 hr
1	6.313804	-10.4	2.853333	3181	0.00031	20084	37.2	17	(Sample 1 after drying)
2	5.958657666	-7.0	2.7466666	3933	0.00025	23435	36.2	17	1400°C, 4 hr
3	6.291986667	-9.6	2.7	3495	0.00028	21990	34.2	10	1400°C, 4 hr
4	6.2348955	-7.924	2.3325	4486	0.00022	27970	35.9	13	1300°C, 4 hr
5	6.169951667	-7.85	2.35	4431	0.00022	27339	36.5	19	1300°C, 4 hr

Table 4.2. Microwave property measurements for BT4 samples sintered 4hr at 1300-1400 °C

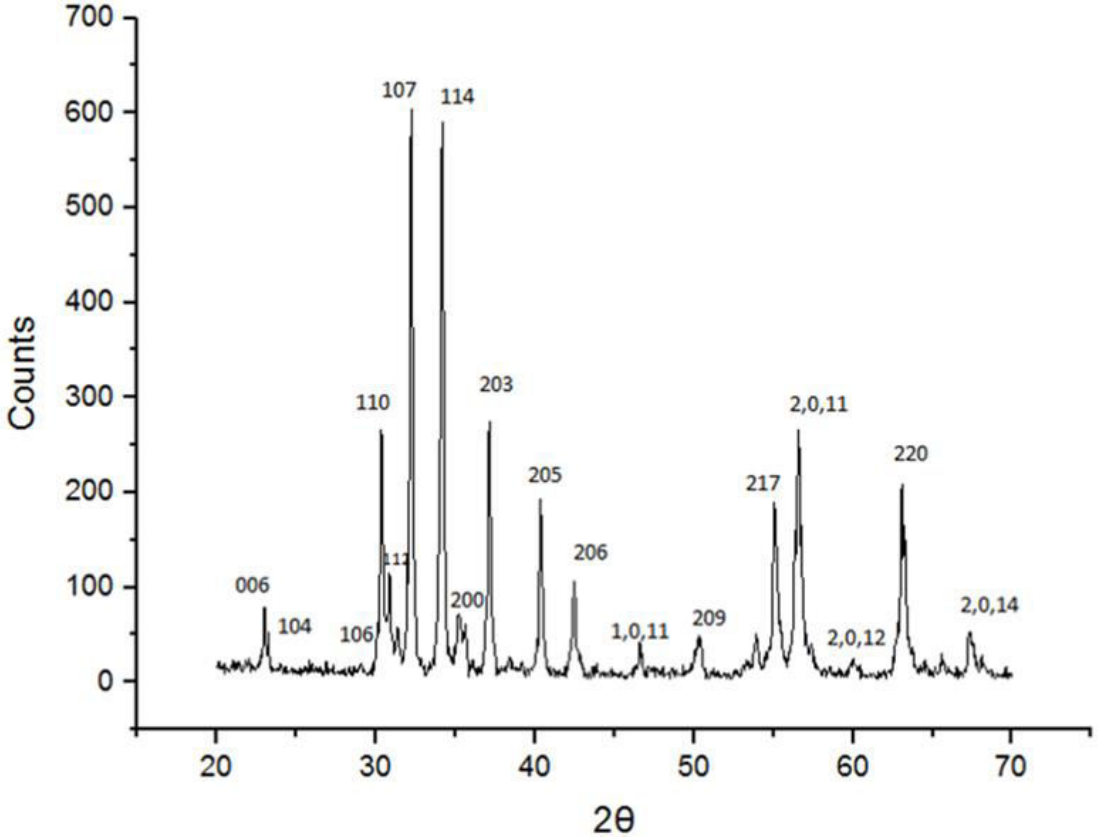

Figure 4.14. X- ray diffraction trace of BF12 calcined 6h at 1200 °C

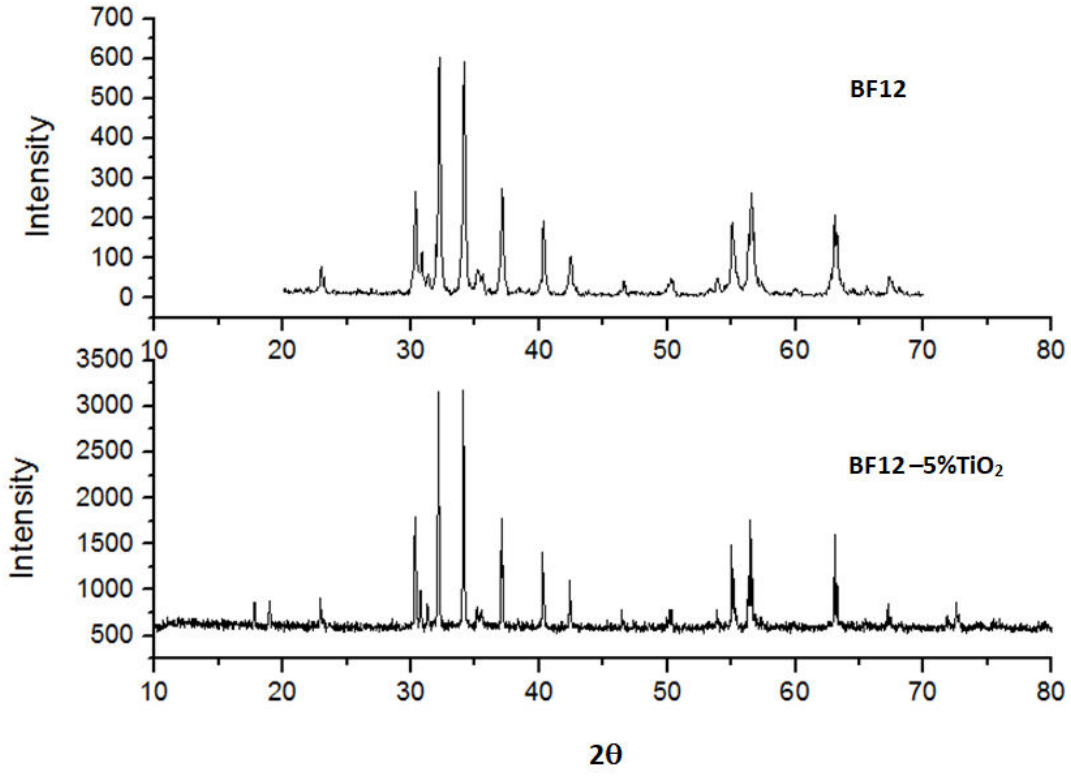

Figure 4.15. X- Ray Diffraction trace for undoped BF12 and doped BF12 –5%TiO_2, calcined 6h at 1200 °C

Figure 4.15 compares the X-Ray diffraction patterns in the doped BF12-5%TiO_2 with undoped BF12. Assuming Ti^{4+} enters the lattice substituting of Fe^{3+} either some must be converted to Fe^{2+} or cation vacancies must be produced to maintain electroneutrality [11].

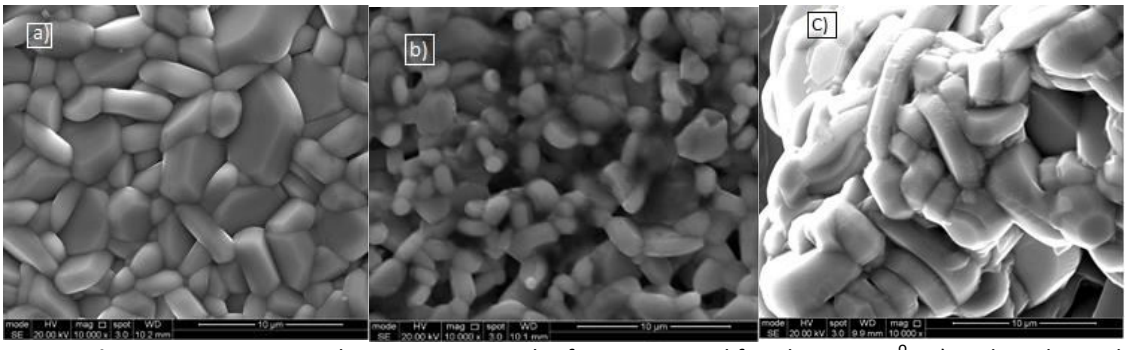

Figure 4.16. Scanning electron micrograph of BF12 sintered for 6hr at 1300°C a) undoped BF12 b) doped BF12-1%TiO_2 and c) doped BF12-5%TiO_2

Figure 4.16 is a scanning electron micrograph of the final sintered microstructure of BF12 and BF12-1%TiO_2 and BF12-5%TiO_2. Homogeneous rounded edge shapes and some hexagonal-shaped (1 x 2 µm, aspect ratio) particles are observed, especially in BF12 (Figure 4.16 a). The shape of the particles is presumably influenced by the anisotropy of the BF12 crystal structure. These result for BF12 are in agreement with the microstructure reported by Chen and Tan [10] with little apparent porosity and good densification.

Table 4.3 shows the microwave properties for the BF12 sample. BF12 resonated at MW frequencies with ε_r = 25.4, *Qf* = 1673 GHz and TCF = -46 ppm/°C. For TiO_2 doped compositions, the dielectric loss was high and no resonance peak could be observed.

Sample details	f_o (GHz)	S21 (dB)	Bandwidth BW (MHz)	Q	tanδ	*Qf* (GHz)	ε_r	TCF ppm/°C
BF12 (1300°C)	7.20	-28.1	32.31	232	0.00431	1673	25.42	-46

Table 4.3. Microwave property measurements for BF12 sample sintered 6hr at 1300 °C

Preliminary data on TiO_2 doped BF12 suggested that the compositions increase in loss and do not resonate at high frequencies. This dramatic result after doping only with 5%TiO_2 suggests that the MW properties of BF12 cannot be readily tuned following a conventional solid-solution approach, as adopted by researchers over several decades. Consequently, BF12-BT4 composites were fabricated with a view to developing ceramics with a magnetic as well as a dielectric component capable of interacting with the magnetic and electrical field in MW EM radiation at resonance. In this manner, new materials for antenna applications could be fabricated with a broader frequency response.

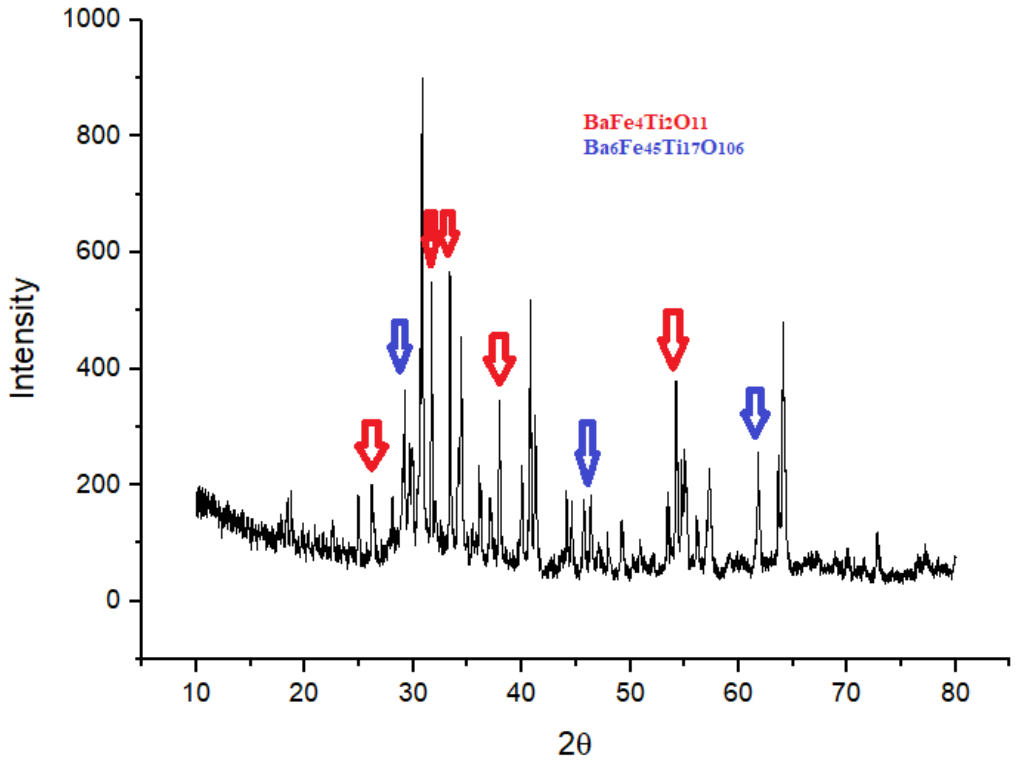

Figure 4.17. XRD trace of conventionally sintered 0.5BF12-0.5BT4

4.2.3 Composites, BF12-BT4 (Conventional sintering)

Figure 4.17 shows the XRD trace of a 0.5BF12-0.5BT4 composite. In addition to peaks of BT4 and BF12, secondary phases ($BaFe_4Ti_2O_{11}$, $Ba_6Fe_{45}Ti_{17}O_{106}$) are arrowed which are formed by interaction of the two end members at high temperature. Figure 4.18 is a scanning electron micrograph of a pellet of the 0.5BF12-0.5BT4 composite. At least two distinct grain morphologies are present: i) the matrix which consists generally of equiaxed grains (1-4 μm) and ii) smaller grains of a bright contrast phase (100 nm).

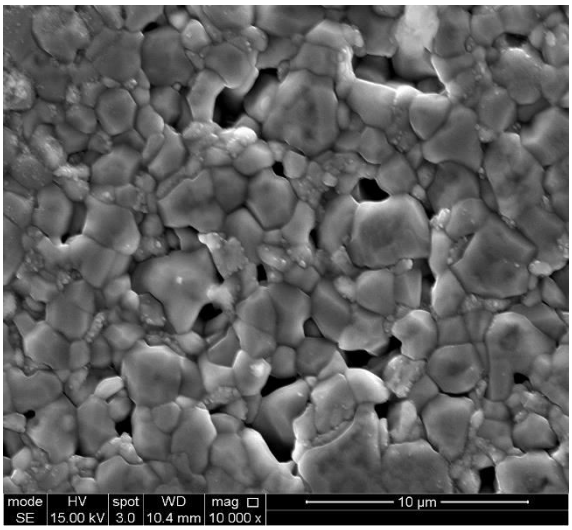

Figure 4.18. SEM of conventionally sintered 0.5BF12-0.5BT4 at 1200 ^{o}C for 6h

Attempts to measure the dielectric properties of BF12-BT4 composites were fruitless as no resonance peaks were observed. The reaction of BF12 with BT4 at the sintering temperature has led to interdiffusion of the constituent ions and the creation of a defect structure that inhibits MW resonance. These compositions were thus considered non-viable as dielectric resonators.

4.3 Conclusion

BF12 and BT4 were synthesised separately from raw materials using conventional sintering and their microwave properties measured. Both ceramics showed good densification with low porosity in agreement with previous studies. ε_r (36) of BT4 at MW frequencies compared well with literature values as did the MW *Qf* (25,000 GHz) and TCF (17 MK^{-1}). BF12 resonated at MW frequencies with ε_r = 25.4, *Qf* = 1673 GHz and TCF= -46. However, BF12-TiO_2 and BF12-BT4 composites did not resonate and were considered unsuitable for RF applications. It was concluded therefore that conventional sintering was unsuccessful in developing MW composite ceramics with a magnetic and dielectric response. Future chapters will therefore focus on the use of cold sintering (120 ^{o}C) which limits interdiffusion and this in principle could prevent interaction of end member compositions, thereby giving viable magnetodielectric composites that resonate at MW frequencies and with usable values of *Qf*.

4.4 References

[1] S. Islam and J. M. Hill, "Barium oxide promoted Ni/YSZ solid-oxide fuel cells for direct utilization of methane," *J. Mater. Chem. A.,* vol. 2, p. 1922-1929, 2014.

[2] K. Thamaphat, P. Limsuwan and B. Ngotawornchai, "Phase Characterization of TiO_2 Powder by XRD and TEM," *Kasetsart J. (Nat. Sci.).,* vol. 42, p. 357-361, 2008.

[3] M. Waseem, S. Munsif, U. Rashid and Imad-ud-Din., "Physical properties of α-Fe_2O_3 nanoparticles fabricated by modified hydrolysis technique," *Appl Nanosci.,* vol. 4, p. 643–648, 2014.

[4] M.R. Joya, J.B Jaimez, and J. B. Ortega, "Preparation and characterization of Fe_2O_3 nanoparticles," *JPCS.,* vol. 466, At. 012004, 2013.

[5] S.F. Wang, Y.F. Hsu, T.H. Ueng, C.C. Chiang, J.P. Chu and C.Y. Huang, "Effects of additives on the microstructure and dielectric properties of $Ba_2Ti_9O_{20}$ microwave ceramic.," *J. MATER. RES.,* vol. 18, p. 1179-1187, 2003.

[6] P. S. Anjana and M. T. Sebastian, "Microwave Dielectric Properties and Low-Temperature Sintering of (1-x)CeO_2--- x$BaTi_4O_9$ Ceramics.," *Int. J. Appl. Ceram. Technol.,* vol. 5, p. 84–93, 2008.

[7] S. G. Mhaisalkar, W. E. Lee and D. W. Readey, "Processing and Characterization of $BaTi_4O_9$," *J. Am. Ceram. Soc.,* vol. 72, p. 2154-2158, 1989.

[8] J. Juang and Y.-C. Huang, Intelligent Technologies and Engineering Systems, Springer-Verlag New York, 2013.

[9] K. Sadhana, K. Praveena, S. Matteppanavar and B. Angadi, "Structural and magnetic properties of nanocrystalline $BaFe_{12}O_{19}$ synthesized by microwave-hydrothermal method," *Appl. Nanosci.,* vol. 2, p. 247–252, 2012.

[10] X. Chen and G. Tan, "Multiferroic Properties of $BaFe_{12}O_{19}$ Ceramics," arXiv:1201.3963v1, 2012.

[11] D. A. Vinnik, D. A. Zherebtsov, L. S. Mashkovtseva, S. Nemrava, N. S. Perov, A. S. Semisalova, I. V. Krivtsov, L. I. Isaenko, G. G. Mikhailov and R. Niewa, "Ti-Substituted $BaFe_{12}O_{19}$ Single Crystal Growth and Characterization.," *Cryst. Growth. Des.,* vol. 14, p. 5834−5839, 2014.

Chapter 5: Cold sintered composites for MW substrates

Cold sintering was first proposed by Kähäri et al [1] in a paper which described the densification of Li_2MO_4 (LMO) at unusually low temperatures (<200 ^oC) when pellets were wet and placed within a furnace. This initial work was subsequently expanded upon by Guo et al who recognised that the principles applied to LMO could also be used on a wide range of other compounds for applications such as varistors and MW packaging [2], [3], [4]. The result was a paradigm shift in the processing of ceramics that had the potential to develop new composites and as well decarbonise an industry which is notoriously heavy on energy usage and associated CO_2 emissions. This chapter expands on the initial work by Kähäri et al [1] and Guo et al [2], [3], [4] and aims to develop a range of composites that densify at low temperature but which potentially have new functionalities.

5.1 Li_2MO_4 (LMO)

LMO has the Phenacite structure and densifies during cold sintering at 120 ^oC at around 200 – 500 MPa. Figure 5.1a shows an SEM image of the surface of cold sintered LMO and compares the microstructure to a conventionally sintered sample, Figure 5.1b). Each exhibits a dense microstructure with greater grain growth evident in the conventionally sintered sample (≈10 μm).

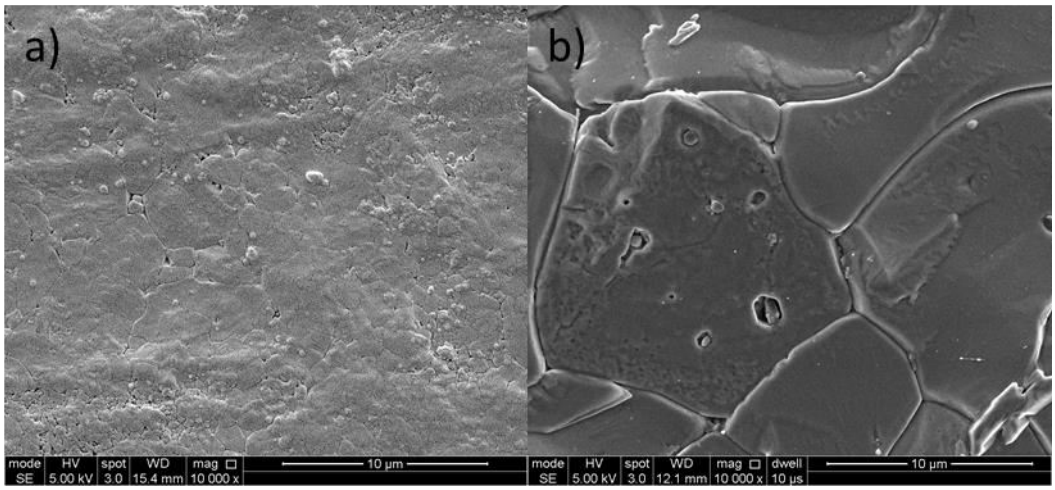

Figure 5.1. SEM of a) cold sintered LMO at 120 ^oC, b) conventionally sintered LMO at 620 ^oC

XRD of cold sintered samples are shown in Figure 5.2. There is no evidence of secondary phases.

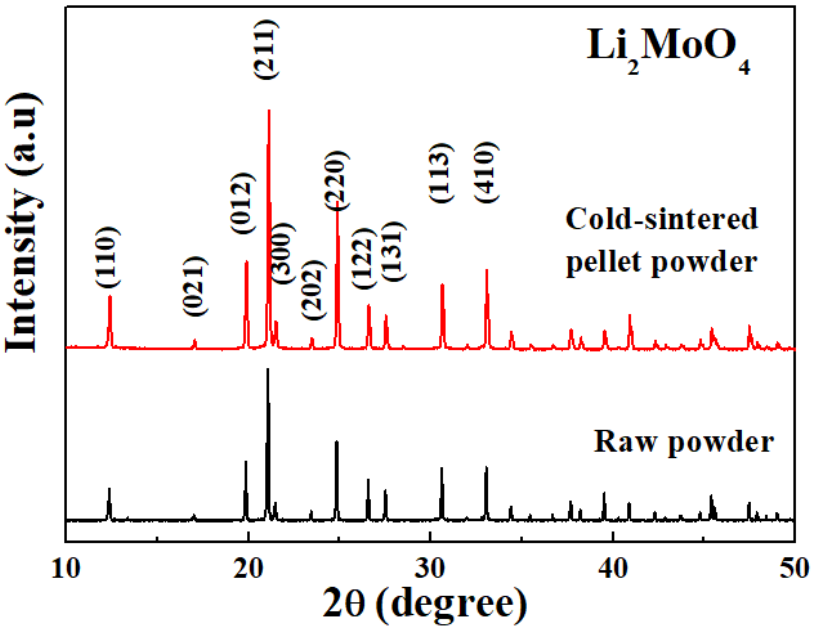

Figure 5.2. XRD of cold sintered sample and raw powder of LMO

The MW properties of conventional and cold sintered LMO were measured, Table 5.1. There are some small differences in properties (*Qf* is greater for conventional vs. cold), but it is evident from Table 5.1 that cold sintered LMO has competitive MW properties and is thus an ideal potential end member with which to explore the fabrication of ceramic-ceramic composites for RF applications.

Sintering method	Sintering temperature (°C)	Relative density(%)	Dielectric permittivity (ε_r)	Quality factor (*Qf*) *GHz*	Temperature coefficient factor of resonance frequency (TCF) MK^{-1}
Cold	120	97	5.3	24,320	-160
Conventional	620	96	5.4	42,000	-158

Table 5.1. Microwave properties comparison of cold and conventionally sintered LMO

The following sections report and discuss results relating to a wide range of cold sintered composites**,** the majority of which are based on LMO. The aim of this chapter is to explore the extent of composite formation by cold sintering and in instances where promising data is obtained, study in greater detail, structure property relations and their potential for applications.

$BaFe_{12}O_{19}$(BF12) has competitive magnetic properties and the composite of BF12-LMO is anticipated to fulfil the balance of matched ε/μ while having a tuned TCF closer to zero than LMO. TiO_2 is a high ε_r (~100) ceramic with *Qf* ~ 14,000 GHz depending on temperature and frequency [5]. It can be readily obtained as nano-powder and is potentially an ideal end member with LMO to form a dielectric composite which cold sinters at <200 ^oC. Its TCF is highly positive +400 MK^{-1} and hence in principle could be used to tune composites to zero since LMO has a large –ve value (~160 MK^{-1}). As discussed in the literature survey, $Y_3Fe_5O_{12}$ is a garnet which is known to have a ferrimagnetic response. In the context of the thesis, it is used as a comparison with BF12. The success in fabricating BF12-LMO composites suggested that further studies should be carried out to ascertain whether TCF could be further tuned to zero by starting with Na_2MoO4 (- 70 MK^{-1}) instead of LMO as an end member (-160 MK^{-1}) [6]. The higher ε_r of Na_2MoO_4 (13) could also potentially lead to a high ε_r composite. K_2MoO_4 was also explored as a possible alternative end member to LMO to form K_2MoO_4-BF12 composites. To the best of the authors knowledge, no previous work has been carried out of cold sintered K_2MoO_4 , however, Guo et al. have reported that $K_2Mo_2O_7$ cold sinters at 120 ^oC with ε_r =9.8 and *Qf* =16,000 GHz [2].

$BaTiO_3$ is a high ε_r compound which could potentially modify the composite properties. Nano $BaTiO_3$ powders were initially chosen for this study as it was anticipated that they could be better incorporated into the composite. There was no anticipation that $BaTiO_3$ would cold sinter at 120 ^oC, since Guo et al have reported that additions of TiO_2 nano-powder and $Ba(OH)_2$ must be used before densification occurs [3], [7]. To further expand the knowledge base of LMO cold sintered composites, LAGP-LMO pellets were prepared. LAGP is unlikley to result in materials with a high *Qf*, since it is known to have a high Li ion mobility. However, Li^+ and PO_4^{3-} are likley to dissolve partially in water in a similar manner to the constituent ions of LMO. Hence, this composite has very different characteristics to many of the ones attempted throughout this study since all others are composed of a cold sintering with a non-cold sintering end-member. Consequently, the values of x at which high densities/mechanical integrity can be achieved should exceed 0.15. A nanopowder source of LAGP was chosen with a particle size of 50 nm. The high surface area of the nano LAGP is anticipated to make this phase readily soluble in water. Moreover, the mixture of MoO_4^{2-} and PO_4^{3-} ions may influence the crystallisation of an amorphous phase.

5.2 $BaFe_{12}O_{19}$-Li_2MoO_4 (BF12-LMO)

0.05BF12-0.95LMO

Figure 5.3 shows the XRD trace of 0.05BF12-0.95LMO synthesised by cold sintering at 120 ^{o}C for 20-40 minutes at a pressure of 69 MPa. The trace reveals two phases, BF12 and LMO with no reaction. If this data is qualitatively compared with the conventionally sintered composites in Chapter 4, the great promise of cold sintering for the fabrication of novel RF materials is succinctly demonstrated. Moreover, if cold sintering is compared with other 'energy efficient' densification technologies such as FAST, flash and microwave sintering, the temperatures are lower and the equipment cost significantly less. Guo et al. [2]have proposed that solid state sintering requires high temperatures because of slow diffusion between grains and grain boundaries. Cold sintering allows more efficient diffusion between particles while applying pressure due to transport through an aqueous medium which results in a reduction in Gibbs energy in mass transfer [2].

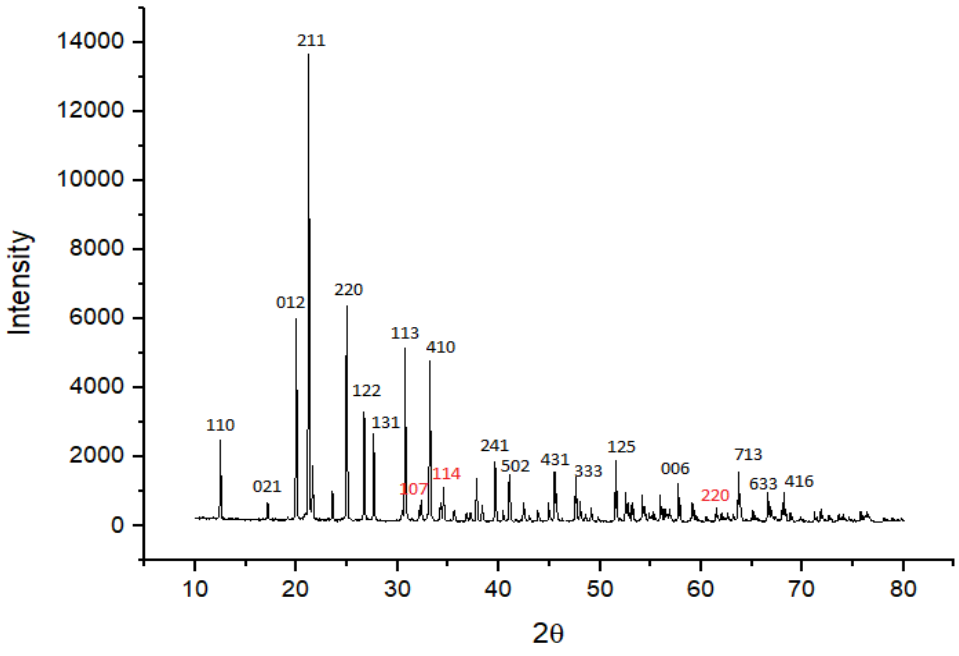

Figure 5.3. XRD of 0.05BF12-0.95LMO, where peak indices in red is BF12 phase

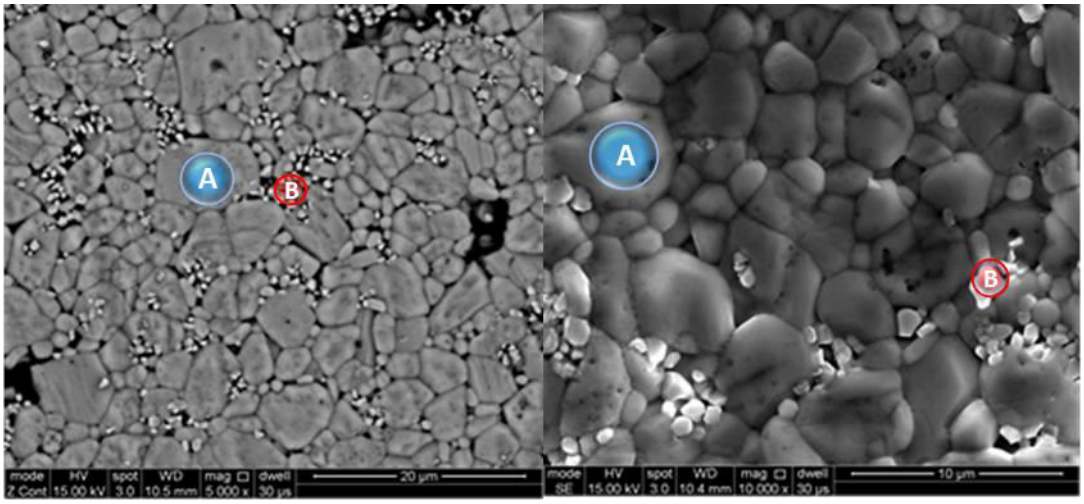

Figure 5.4. SEM of 0.05BF12-0.95LMO, where areas marked by A and B represent LMO and BF12 phases respectively

Figure 5.4 shows scanning electron microscopy (SEM) images with a dense composite of BF12-LMO, featuring few pores. Consistent with the XRD data, no interaction is apparent between the BF12 and LMO. Figure 5.5 shows an SEM image and an energy dispersive x-ray spectrum of 0.05BF12-0.95LMO for two different areas. The smaller grains of BF12 surround the larger grains of LMO with no intermediate phases identified, in direct contrast with attempts to form composites through conventional sintering in Chapter 4.

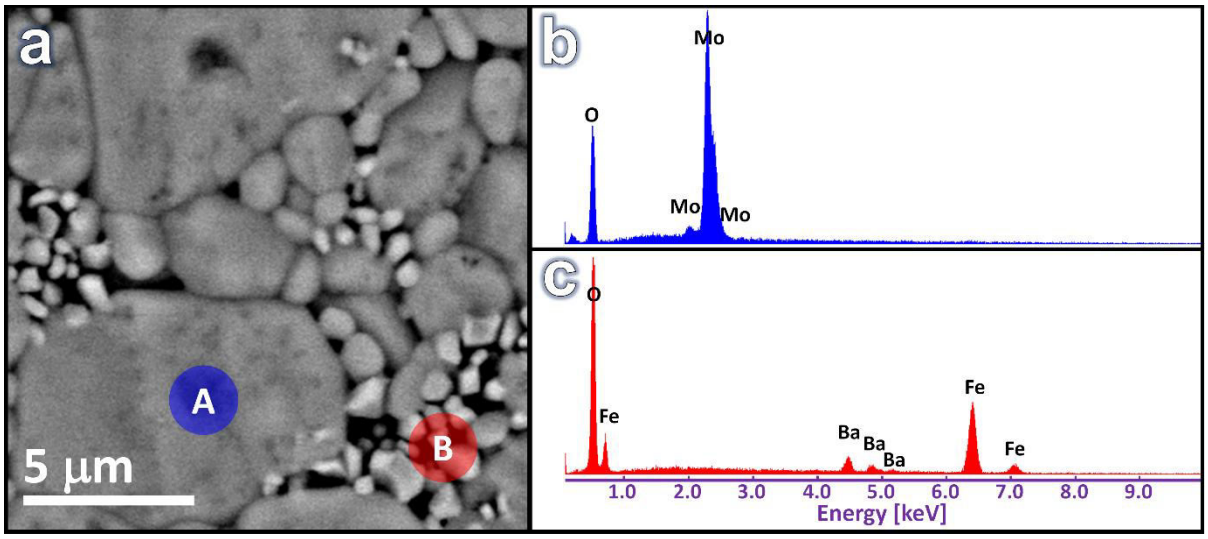

Figure 5.5. (a) SEM image of obtained from the adjacent two phases in cold sintered 0.05BF12-0.95LMO sample (scale bar is 5 µm). (b) and (c) show representative energy dispersive X-ray spectra acquired from the large grains (area marked by "A" in (a)) and the small grains (area marked by "B" in (a)), respectively.

0.05BF12-0.95LMO resonated at microwave frequencies with ε_r of 5.5 and a *Qf* of 22,448 GHz and TCF of -154 ppm/ ^{o}C. The relative density of sample is 95%.

0.1BF12-0.9LMO

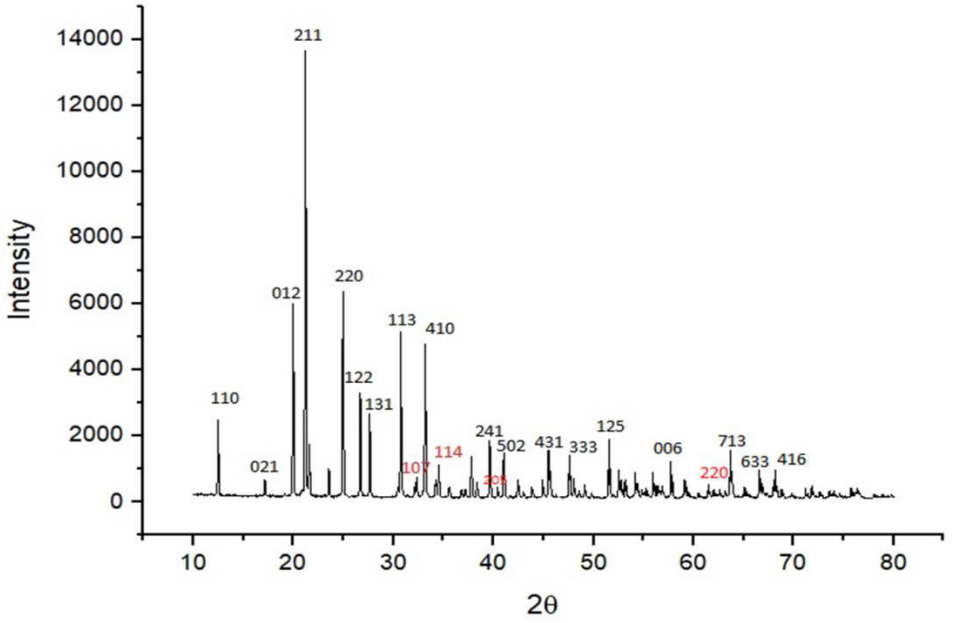

Figure 5.6. XRD of 0.1BF12-0.9LMO, where peak indices in red is BF12 phase

Figure 5.6 shows the XRD trace of 0.1BF12-0.9LMO synthesised by cold sintering at 120 ^{o}C for 20-40 minutes 69 MPa. The XRD trace shows distinct two phases of BF12 and LMO with no evidence of an intermediate phase.

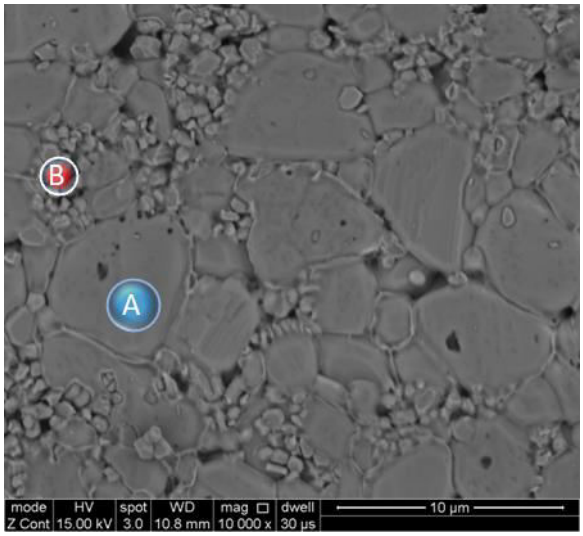

Figure 5.7. SEM of 0.1BF12-0.9LMO, where areas marked by A(large grains) and B(small grains) represent LMO and BF12 phases respectively

Figure 5.7 shows SEM image of dense 0.1BF12-0.9LMO composite. Consistent with XRD traces and 0.05BF12-0.95LMO, there is no evidence of an intermediate phase and the samples exhibit little porosity.

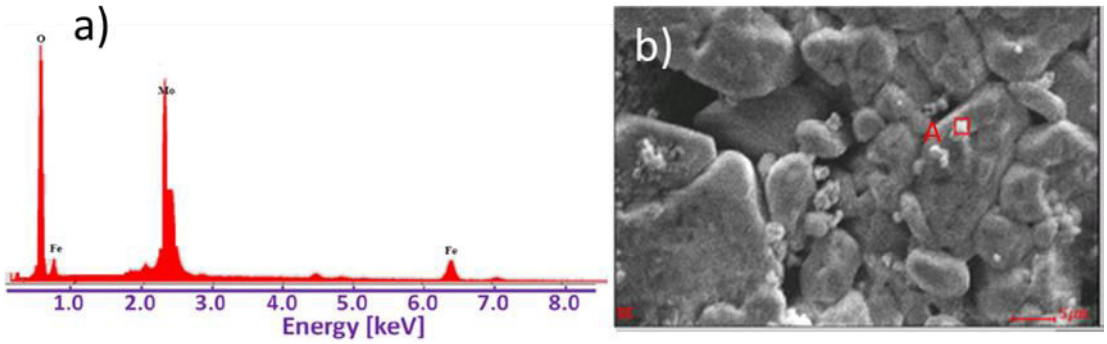

Figure 5.8. Energy dispersive X-ray spectrum of 0.1BF12-0.9LMO a) from the area A selected in b)

Figure 5.8 shows energy dispersive X-ray spectroscopy of 0.1BF12-0.9LMO for a selected area (A). The selected area (A) features high amount of LMO with some BF12 as expected. No interaction occurred between the two different phases.

0.1BF12-0.9LMO has resonated at microwave frequencies with ε_r of 5.6, Qf of 17,452 GHz and TCF of -128 ppm/ ^{o}C with relative density of 98%.

0.15BF12-0.85LMO

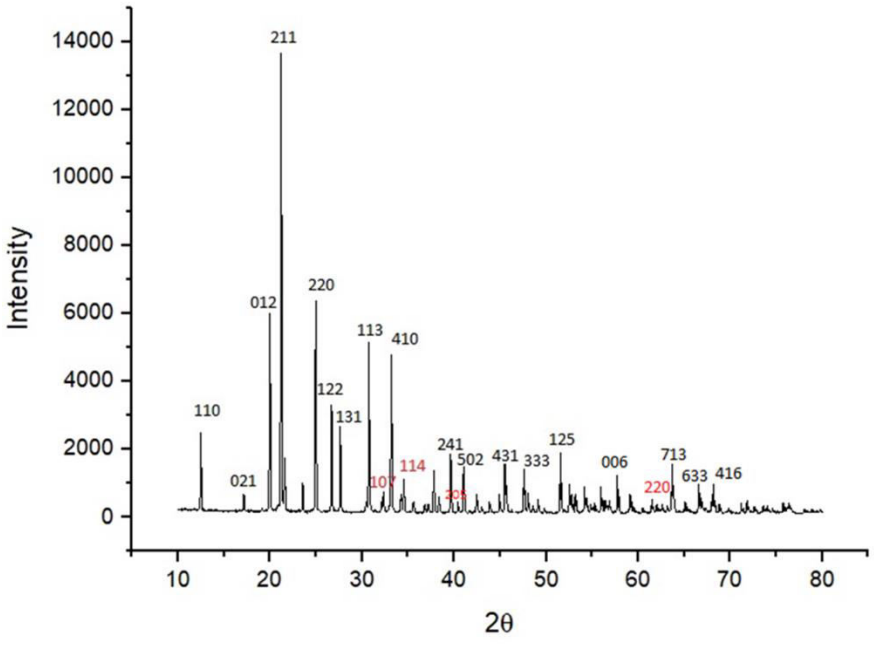

Figure 5.9. XRD of 0.15BF12-0.85LMO, where peak indices in red is BF12 phase

Figure 5.9 shows XRD trace of 0.15BF12-0.85LMO synthesised by cold sintering at 120 ^{o}C for 20-40 minutes at 69 MPa. The trace reveals two distinct phases of BF12 and LMO with no impurities.

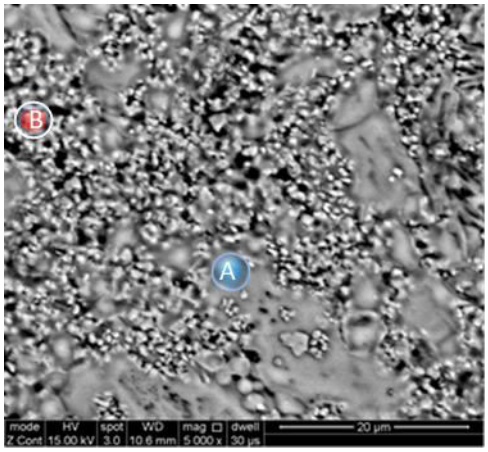

Figure 5.10. SEM of 0.15BF12-0.85LMO, where areas marked by A and B represent LMO and BF12 phases, respectively

Figure 5.10 shows an SEM of 0.15BF12-0.85LMO which reveals a dense two phase composite with few pores. Consistent with the XRD data, no interaction is apparent between the BF12 and LMO.

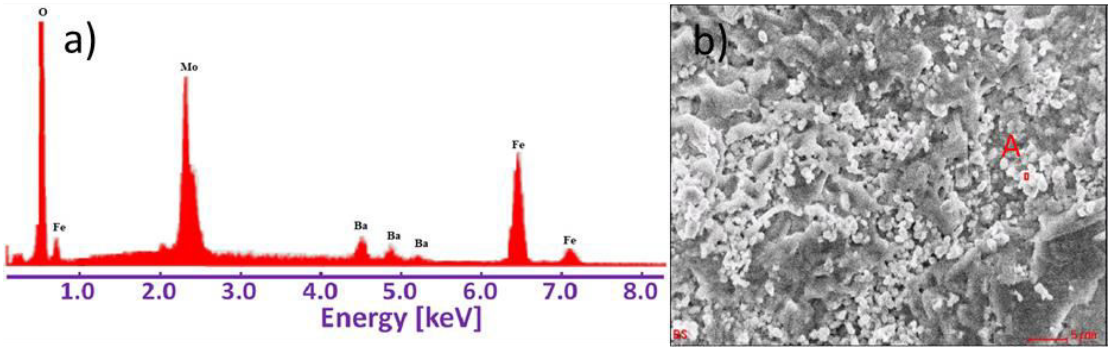

Figure 5.11. Energy dispersive X-ray spectrum of 0.15BF12-0.85LMO a) from the area (A, BF12) selected in b).

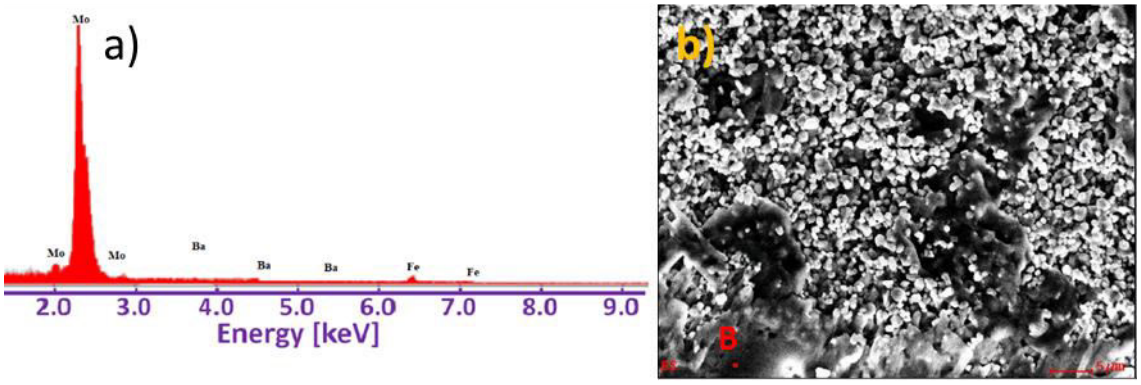

Figure 5.12 Energy dispersive X-ray spectrum of 0.15BF12-0.85LMO a) from the area (B, LMO) selected in b).

Figure 5.11 and Figure 5.12 show energy dispersive X-ray spectra from of 0.15BF12-0.85LMO for two different areas. The selected area (A) in Figure 5.11 is from the BF12 phase. Some Mo appears in the spectrum because of the high voltage (15KV) used which penetrated below the sample's surface into the underlying LMO phase. In contrast, the selected area (B) in Figure 5.12 features LMO only.

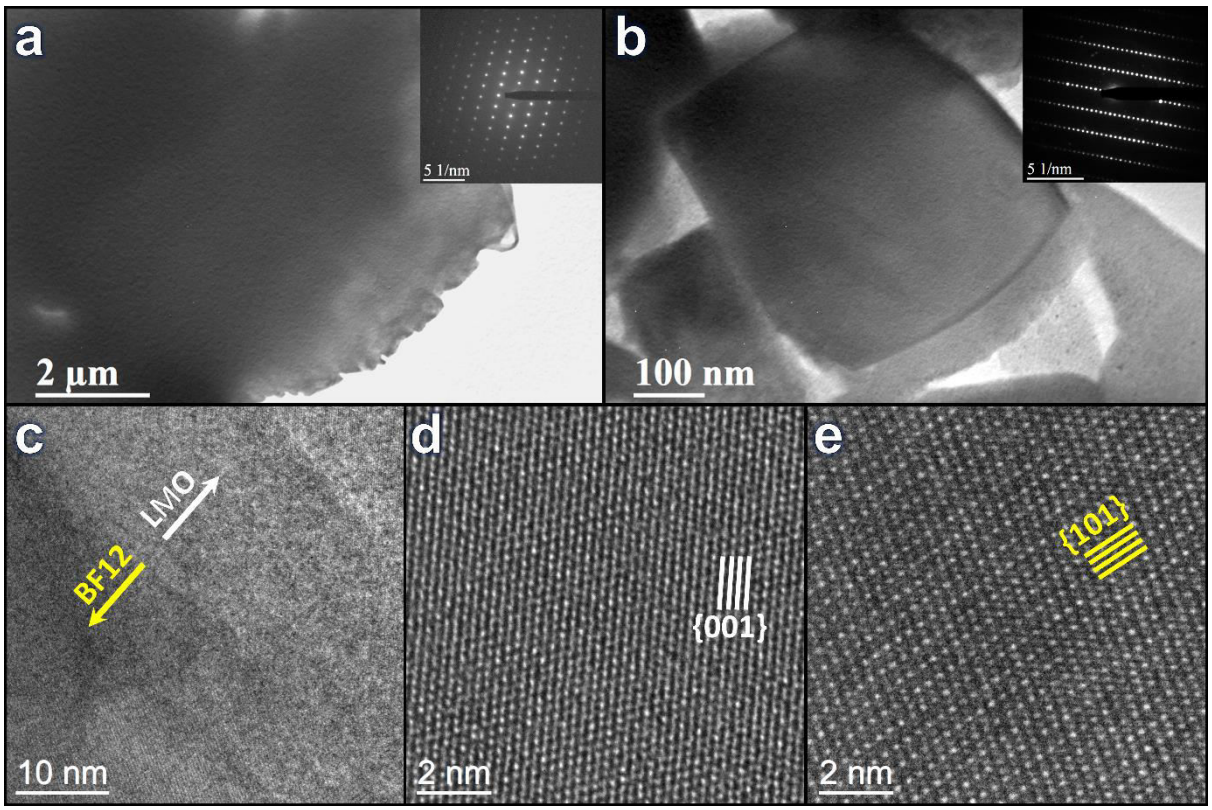

Figure 5.13. TEM image from cold sintered 0.15BF12-0.85LMO showing (a) An LMO grain; inset is the 010 zone axis diffraction pattern of the LMO grain. (b) A BF12 grain; inset is the 100 zone axis diffraction pattern of the BF12 grain. (c) An HRTEM image obtained from the interface of a BF12 and LMO grains. (d) and (e) show HRTEM images at a higher magnification from the LMO and BF12 sides of the interface shown in (c), respectively. Note that LMO surrounds the BF12 grains.

Figure 5.13 (a) and (b) are TEM images of grains of LMO and BF12 in cold sintered 0.15BF12-0.85LMO, respectively. Inset in Figure 5.13 (a) and (b) are [010] and [100] zone axis diffraction patterns from LMO and BF12, respectively which conclusivley identify each phase. The TEM images confirm the two phase mix identified by XRD and SEM. In addition, HRTEM images from the surface of BF12 particles (e.g. Figure 5.13 (c-e)) reveal that LMO surrounds each grain of BF12. The mechanism of densification therefore, relies on the dissolution of LMO grains into the added water which under a combination of pressure and capillary action surrounds BF12 grains. The BF12 grains themselves do not undergo significant dissolution. Simultaneously, particle rearrangement and enhanced packing occur under pressure in the die. As water evaporates, Li^{+} and $(MoO_4)^{-2}$ ions crystallise on the surface of the LMO and BF12 grains, thus densifying not only clusters of LMO particles but also regions of BF12. The net result is a dense composite with limited interaction between the end member phases. A schematic of this mechanism is shown in Figure 5.14.

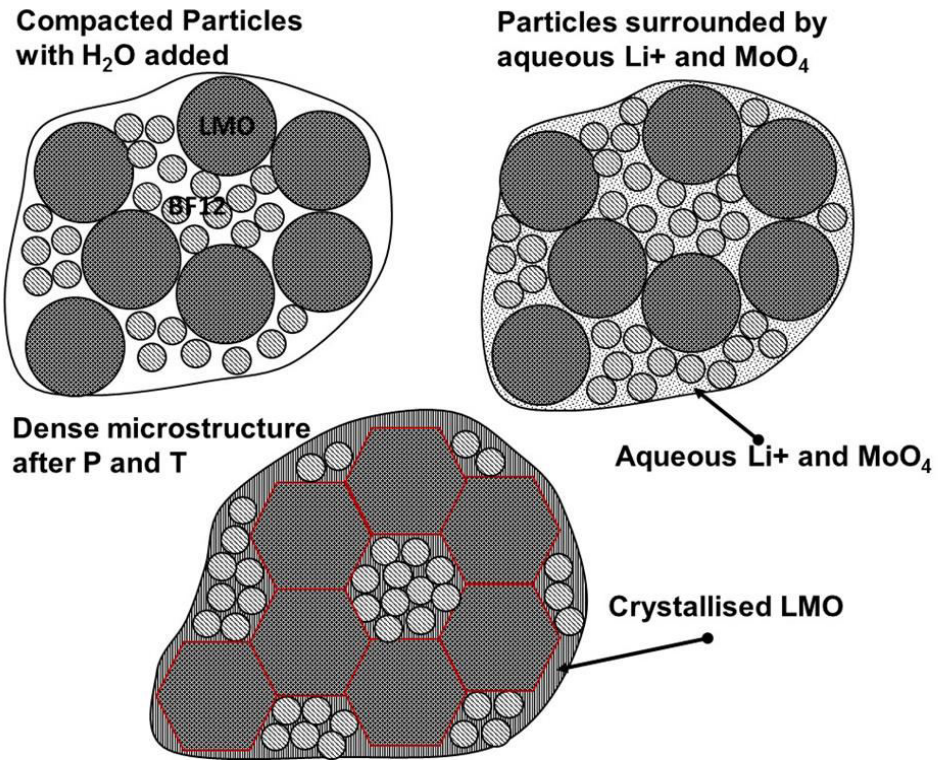

Figure 5.14. Schematic representation of the densification of LMO-BF12 composites at 120 ^{o}C.

0.15BF12-0.85LMO resonated at microwave frequencies with a ε_r of 5.8, Qf of 17,430 GHz and TCF of -134 ppm/ ^{o}C. The relative density of sample is 94%.

Impedance Spectroscopy of BF12 – LMO composites

Figure 5.15 shows Arrhenius plots of bulk conductivity (σ) data obtained from spectroscopic plots of the imaginary components of the electric modulus (M'') which compare cold sintered 0.1BF12-0.9LMO composites with, conventionally sintered BF12 and conventionally sintered LMO. As expected, the BF12 ceramic has much higher bulk σ compared to LMO. The σ of the composite ceramics is intermediate in magnitude compared to the end members. The values of activation energy associated with the bulk response extracted from the data reveal that cold sintered 0.1BF12-0.9LMO has an activation energy of 0.25 eV which is comparable to 0.29 eV of the more conductive end member (BF12) and is much lower than 1.28 eV associated with conventionally sintered LMO. These data suggest that a percolation pathway exists in the composite with the current choosing the path of least resistance via the higher conducting BF12 phase.

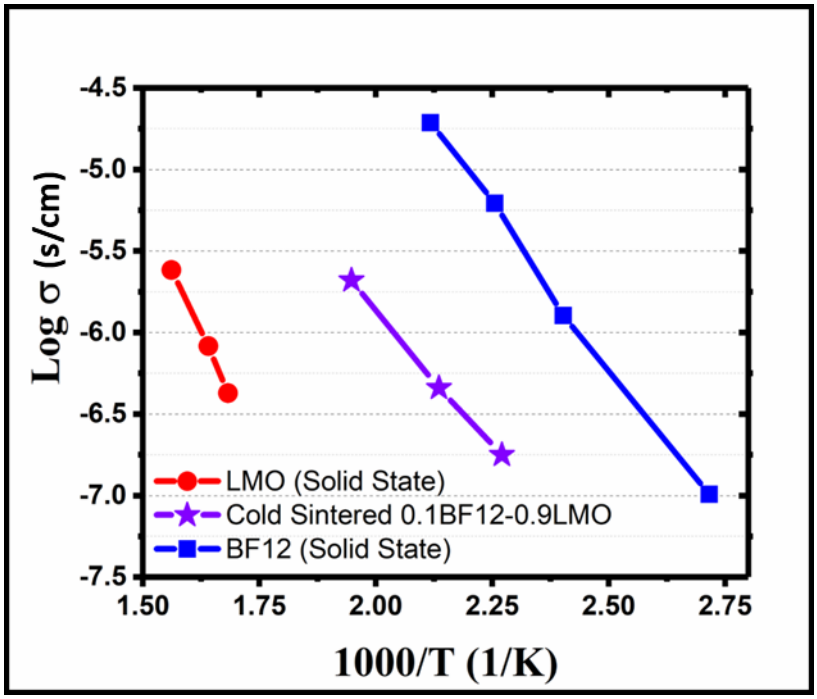

Figure 5.15. Arrhenius plot of bulk σ of conventionally sintered ceramics of the end members with a cold sintered 0.1BF12-0.9LMO. NB: details for the fabrication of conevntionally sintered BF12 and LMO can be found in [8], [1], respectively.

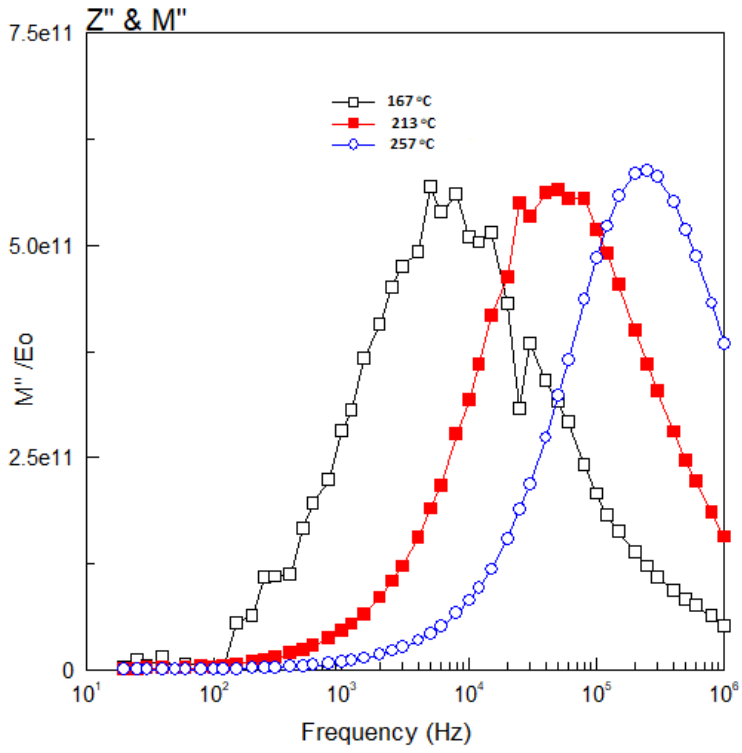

Figure 5.16. Spectroscopic plot of the relationship between the imaginary component of the electric modulus (M'') and frequency of cold sintered 0.1BF12-0.9LMO

Figure 5.16 shows a spectroscopic plot of the relationship between the imaginary component of the electric modulus (M'') and frequency of cold sintered 0.1BF12-0.9LMO taken at different temperatures, which is used to extract bulk conductivity (σ) to input into

the Arrhenius plot in Figure 5.15. Table 5.2 shows capcitance values of 0.1BF12-0.9LMO at the selected temperatures:

Temperature (^{o}C)	Capacitance (F/cm)
167	$1.75*10^{-12}$
213	$1.76*10^{-12}$
257	$1.70*10^{-12}$

Table 5.2. Capacitance values of cold sintered 0.1BF12-0.9LMO measured at selected temperatures

Figure 5.17 shows Arrhenius plots of bulk frequency data depndence on temperature obtained from spectroscopic plots of the imaginary component of the electric modulus (M'') which compare cold sintered BF12-LMO composite with, conventionally sintered BF12 and conventionally sintered LMO.

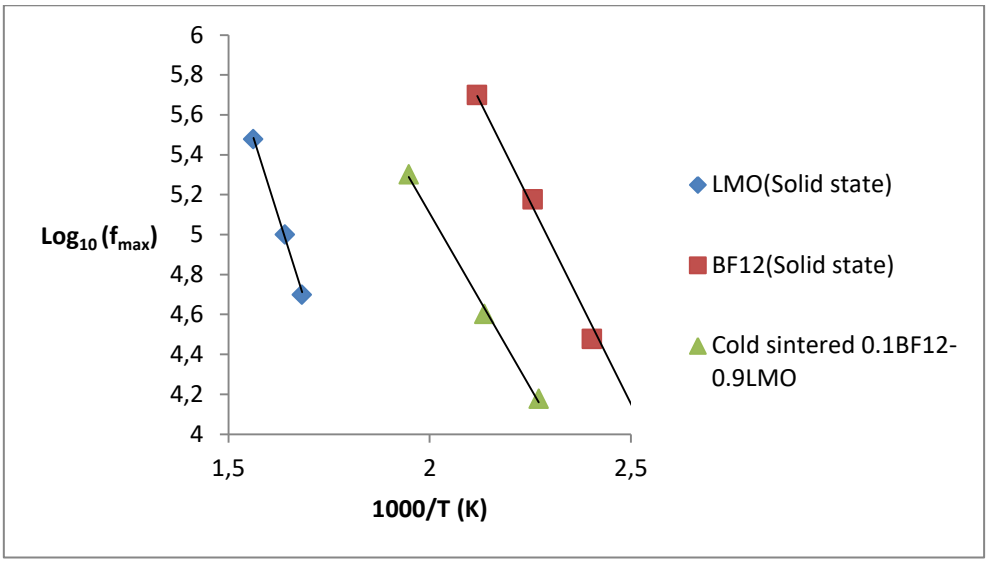

Figure 5.17. Arrhenius plot of frequency dependence for comparison of conventionally sintered ceramics of the end members with a cold sintered composite.

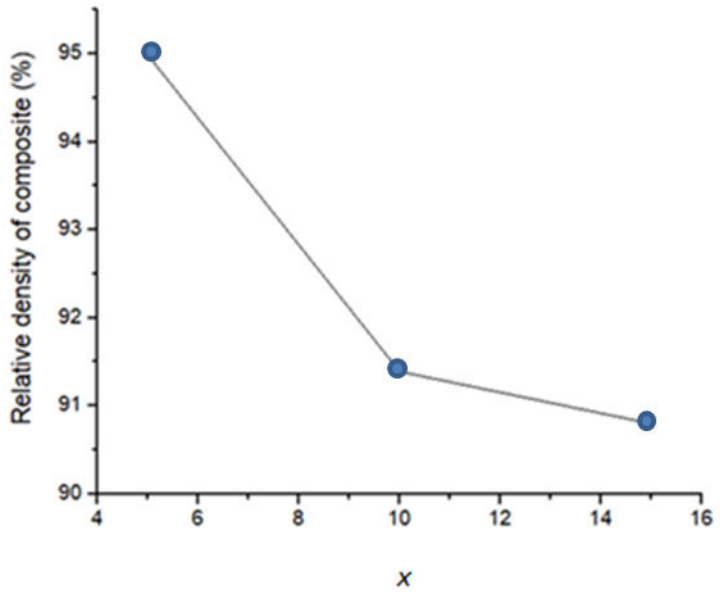

Figure 5.18. Relative density as a function of x in *x*BF12-(1-*x*)LMO composites

Figure 5.18 shows the relationship between BF12 proportion in BF12-LMO composite and the relative density of the pellets. It is clearly shown that relative density decreases gradually with increase in BF12. BF12 does not cold sinter unlike LMO in addition to having a lower Qf. Densification after x=0.15 is thus difficult to achieve because of the predicted discontinuity of the soluble LMO grains within the insoluble BF12 grains leading to porous and brittle ceramics.

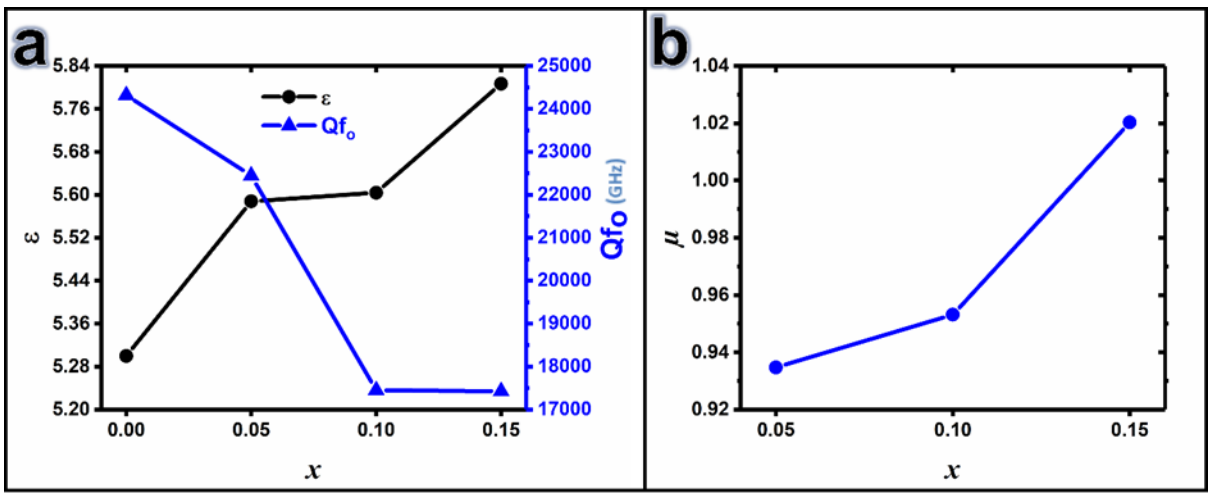

Figure 5.19. (a) (ε, *Qf*) and (b) μ at X band frequencies *x*BF12-(1-*x*)LMO composites

Figure 5.19 (a) shows ε_r (black line) and *Qf* (blue line) as a function of *x*. ε_r increased with inceasing BF12 concentration but *Qf* decreased from around 24,000 GHz to 17,000 GHz. These results are consistent with BF12 having a higher ε_r (25) and lower *Qf* (<2000GHz) than LMO. However, the values of *Qf* are competitively high for a composite material and show great promise for MW applications, provided there is also an enhancement in μ from the addition of the BF12 end member.

Figure 5.19(b) shows μ measured in the X-band (~8 GHz) for *x*BF12-(1-*x*)LMO composites. μ increases with the volume fraction of BF12 from ~0.93 at *x* = 0.05 to 1.02 at *x* = 0.15. Although these are comparatively low values, we note that Bahadoor et al. [9] show μ = 1 for BF12 at frequencies from 8-26.5 GHz which rises as frequency decreases. The likely frequency range for applications of these composites is ~0.5-3GHz and thus the value of μ at these frequencies is potentially more relevant. Nonetheless, the values of μ attained in the X band suggest a systematic increase as a function of *x* coupled with a high *Qf.*

Finite Element Modelling of the composite microstructure

Finite element modelling of *x*BF12-(1-*x*)LMO composite was carried out in collaboration with the group of Dr JulianDean. One challenge in replicating the composite is the simulation of a microstructure that consists of two distinct grain sizes. Adopting a Voronoi tessellation [10] is insufficient to replicate this microstructure, as the algorithm divides up the space between the initial seed points. The small grains thus grow as they near the larger grains, generating a normal distribution. Here, we use a feature in Voro++ [11] known as radical Voronoi tessellation. Each discretized seed point is weighted with lower and higher values to give smaller and larger BF12 and LMO grains, respectively. A binomial grain size of polydisperse particles is generated which is matched to the experimental distribution. Each of the two materials is assigned experimental values from which we extract the room temperature σ (Figure 5.15) and ε_r. The values extracted for LMO gave σ = 2.26×10^{-15} Scm^{-1} and ε_r = 5.33, compared to σ = $4.07\text{x}10^{-8}$ Scm^{-1} and ε_r = 25 for BF12. Various volume fractions of LMO were then simulated, generating approximately 2000 small grains for a pure BF12 model, and over 500 large grains for LMO (Figure 5.20 a). The structures were then meshed with between 1-2M tetrahedral elements and run using the *in-house* finite element package ElCer [10] to simulate the effective ε_r and σ [10], [12].

In generating these microstructures, the volume fraction of the smaller BF12 is crucial since they surround the larger LMO grains and relatively few are needed to create a conductive network. The BF12 grains effectively by-pass the resistive LMO grains, as shown in Figure 5.20(b) and (c) for 20 vol.% BF12. At lower values of *x*, these paths become discontinuous with gaps forming, Figure 5.20 (d) and (e) for 5 vol.%. This percolation threshold is observed directly in the measured σ. Figure 5.21 highlights the extracted σ and ε_r arising from the FEM simulations. For 5 vol.% BF12, σ rises but at 10 vol.% there is a discontinuous change, attributed to the formation and conducting pathways. For > 10 vol.% BF12, there is gradual convergence towards σ of the BF12 end member. However, for ε_r no percolation effect is observed and the value tends towards LMO, consistent with a parallel summation, predicted by series mixing rules:

$$\frac{1}{\varepsilon} = \frac{V_{BF}}{\varepsilon_{BF}} + \frac{V_{LMO}}{\varepsilon_{LMO}}$$

where V_{BF}, V_{LMO}, ε_{BF} , ε_{LMO} are the volume fractions and ε_r of the BF and LMO phases, respectively. It is worth it to note that σ has been measured through impedance spectroscopy at MHz frequencies while ε has been extracted at microwave GHz frequencies. However, to our knowledge, this is the first time that a polydisperse Voronoi tessellation algorithm has been used to control and generate two distinct grain sizes which adds further novelty to this study.

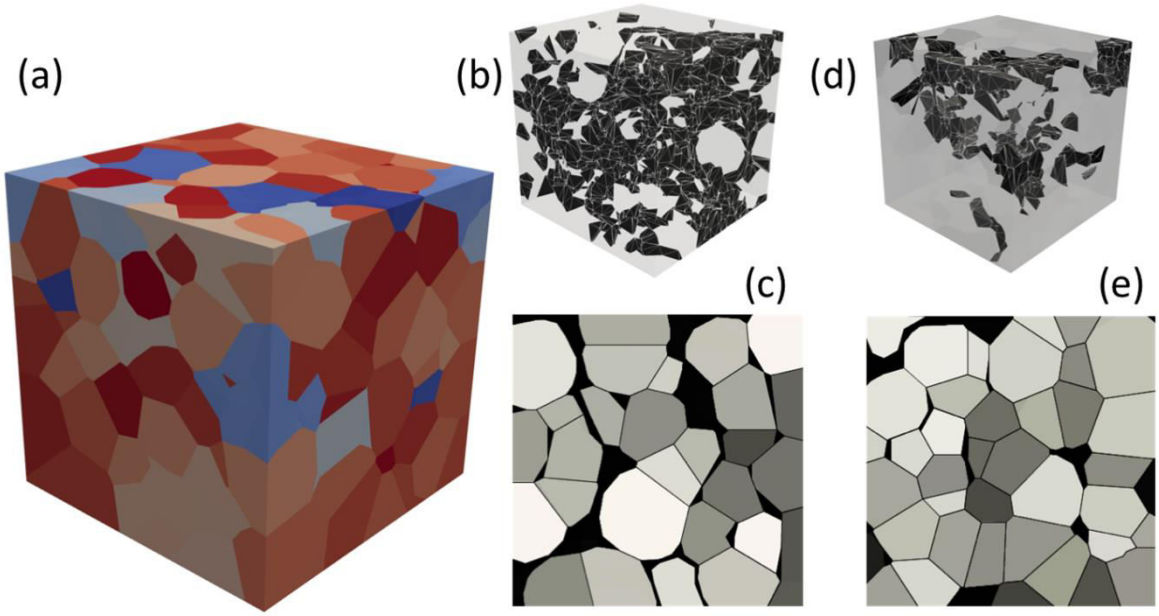

Figure 5.20. (a) an example of the full 3D finite element microstructure containing between 500 - 1500 individual grains of an a LMO microstructure. (b) and (d) show the microstructure, by displaying the smaller more conducting BF12 grains in black. (c) and (e) are slice plots of the models where for simplicity, the black regions are designated as collections of small BF12 grains. For a volume fraction with 20%BF12 (b and c), a continuous network of BF12 grains describes a conductive path from the top to the bottom but which is absent for 5 vol% BF12 (d and e).

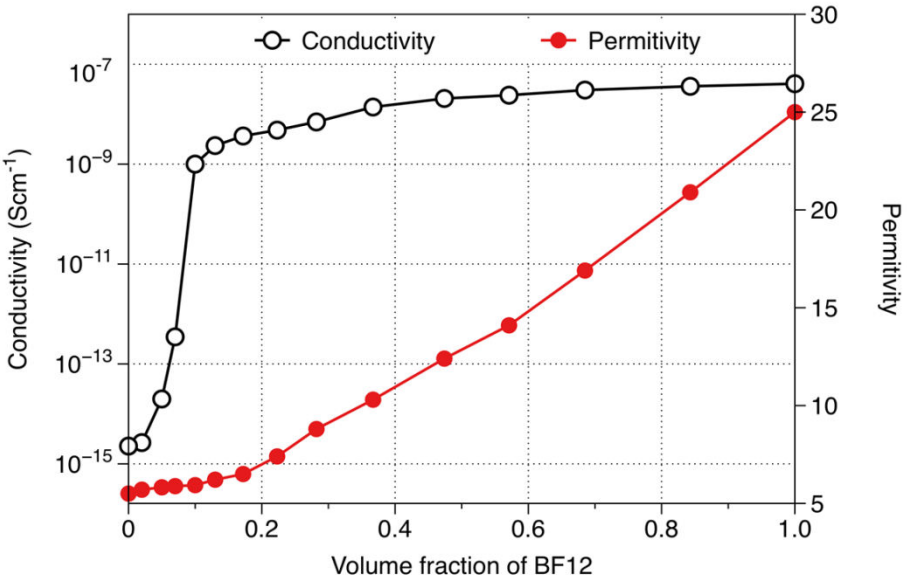

Figure 5.21. The extracted conductivity (σ) and permittivity (ε_r) from the finite element simulations highlighting a percolation threshold for conductivity below for $x < 0.1$ volume fraction.

5.3 TiO_2-LMO

TiO_2 is a high ε_r (~100) ceramic with Qf ~ 14,000 GHz depending on temperature and frequency [5]. It can be readily obtained as nano-powder and is potentially an ideal end member with LMO to form a dielectric composite which cold sinters at <200 ^{o}C. Its TCF is highly positive +400 MK^{-1} and hence in principle could be used to tune composites to zero since LMO has a large –ve value (~160 MK^{-1}).

0.05TiO_2-0.95LMO

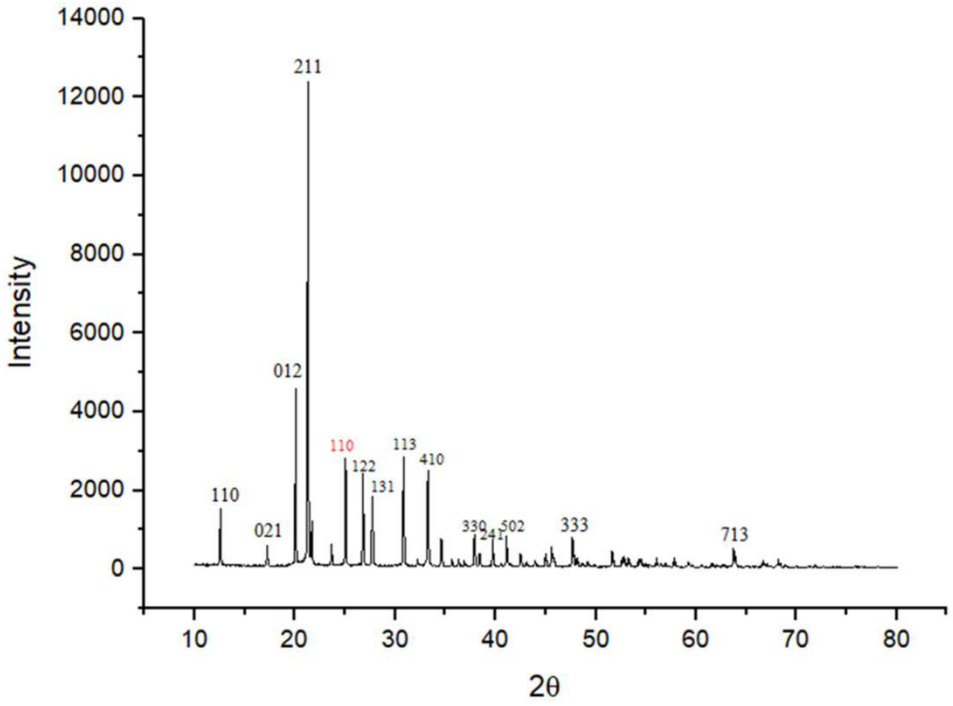

Figure 5.22. XRD of 0.05TiO_2-0.95LMO, where peak indices in red is TiO_2 phase

Figure 5.22 shows XRD trace of 0.05TiO_2-0.95LMO synthesised by cold sintering at 120 ^oC for 20-40 minutes at a pressure of 69 MPa. The trace reveals two distinct phases of TiO_2 and LMO with no reaction. 0.05TiO_2-0.95LMO resonated at microwave frequencies with a ε_r of 5.9 and *Qf* of 31,518 GHz. The relative density of sample is 92%.

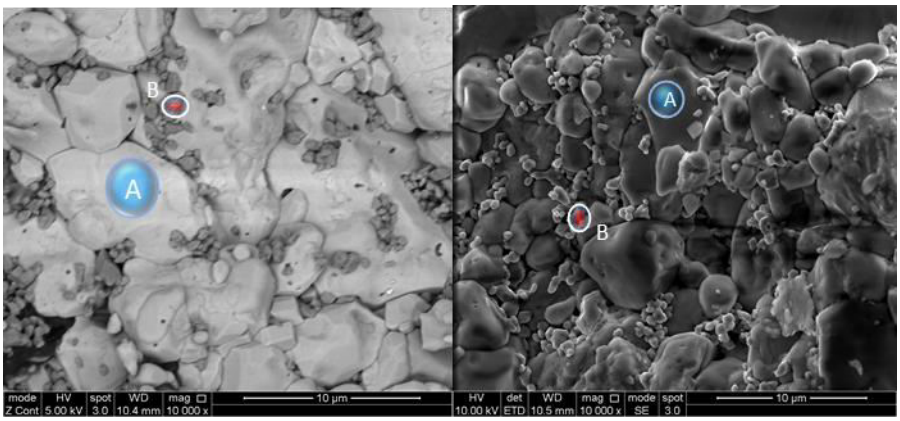

Figure 5.23. SEM of 0.05TiO_2-0.95LMO, where areas marked by A(large grains) and B (small grains) represent LMO and TiO_2 phases respectively

Figure 5.23 shows SEM images with a clear dense composite of TiO_2-LMO, featuring few pores . Consistent with the XRD data, no interaction is apparent between the TiO_2 and LMO.

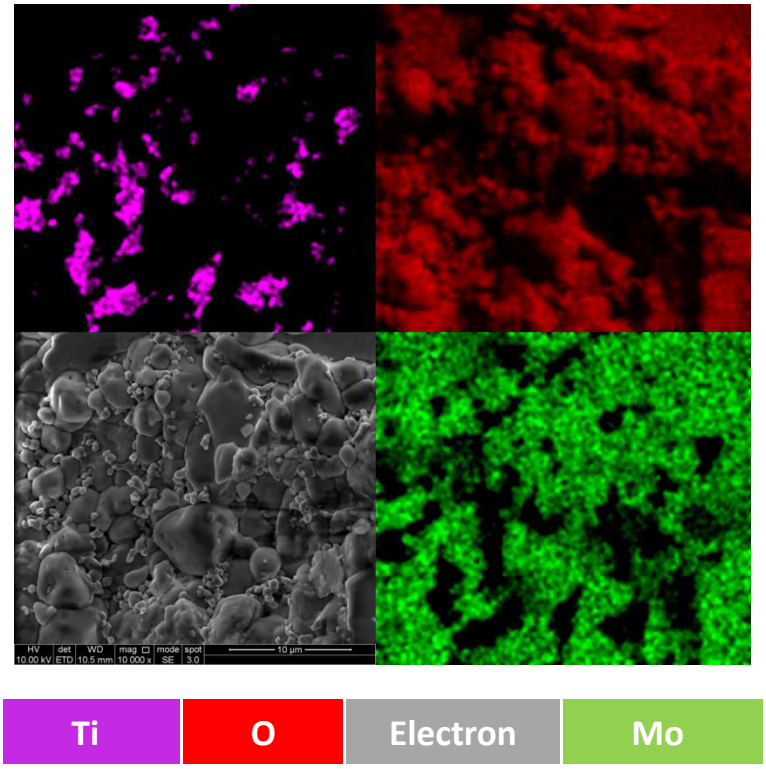

Figure 5.24. Energy dispersive X-ray mapping image of $0.05TiO_2$-0.95LMO, where each element is represented by a color in the key below image

Figure 5.24 shows energy dispersive X-ray mapping image of $0.0.5TiO_2$-0.95LMO where the two phases within composite can be clearly observed, confirming little or no reaction between the two end members.

0.1TiO_2-0.9LMO

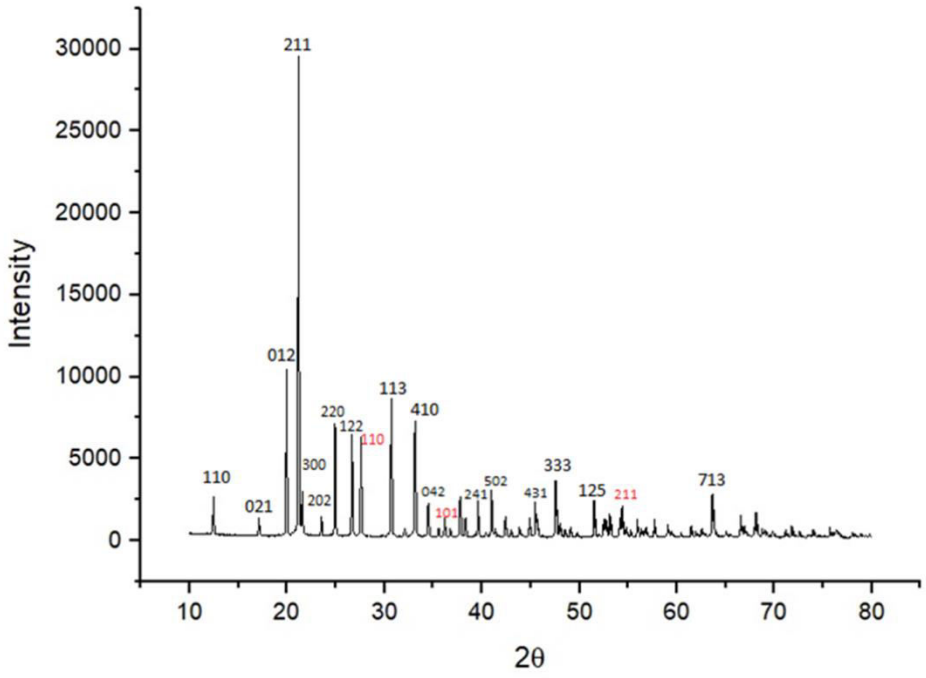

Figure 5.25. XRD of 0.1TiO_2-0.9LMO, where peak indices in red is TiO_2 phase

Figure 5.25 shows XRD trace of 0.1TiO_2-0.9LMO synthesised by cold sintering at 120 ^oC for 20-40 minutes at 69 MPa. The trace reveals two distinct phases of TiO_2 and LMO with no reaction.

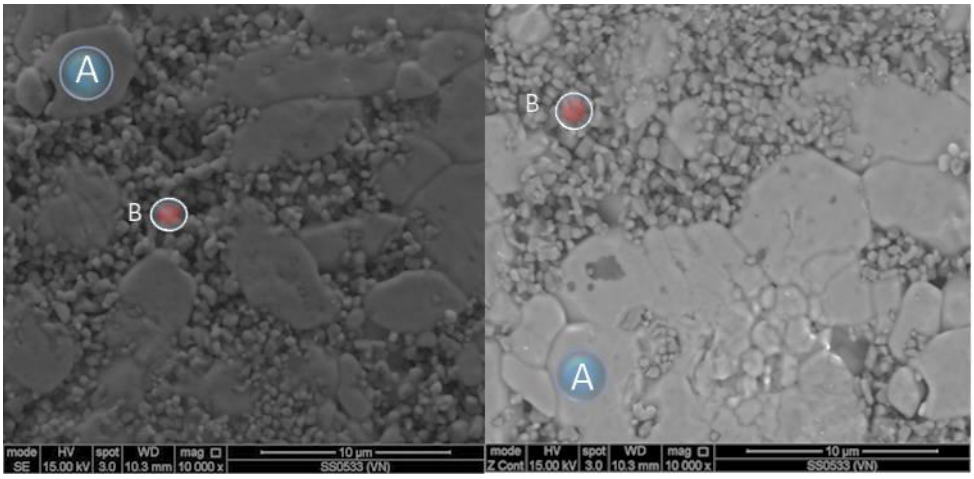

Figure 5.26. SEM of 0.1TiO_2-0.9LMO, where areas marked by A(large grains) and B (small grains) represent LMO and TiO_2 phases respectively

Figure 5.26 shows SEM image with a clear dense composite of TiO_2-LMO, featuring few pores . Consistent with the XRD data, no interaction is apparent between the TiO_2 and LMO.

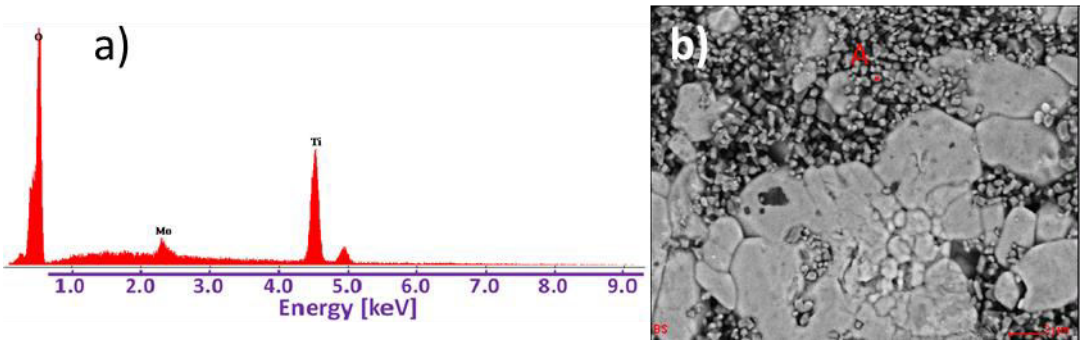

Figure 5.27. Energy dispersive X-ray spectrum of $0.1TiO_2$-0.9LMO a) from the area (A, TiO_2) selected in b).

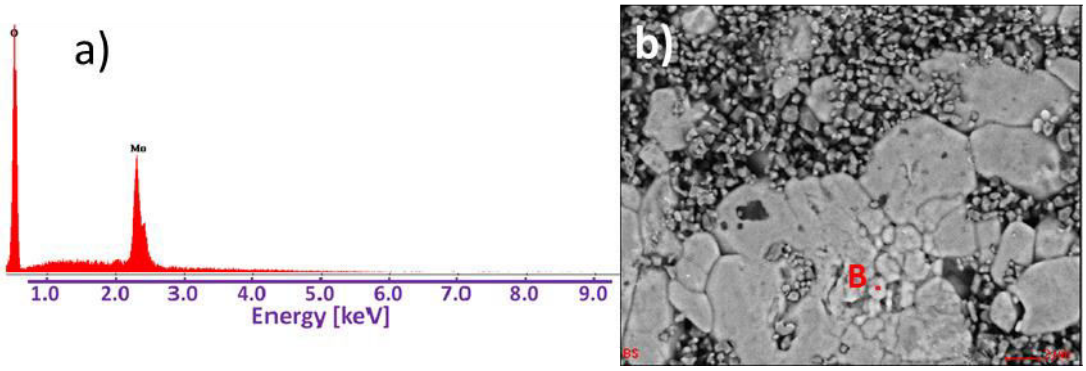

Figure 5.28. Energy dispersive X-ray spectrum of $0.1TiO_2$-0.9LMO a) from the area (B, LMO) selected in b).

Figure 5.27 and Figure 5.28 show energy dispersive x-ray spectroscopy of $0.1TiO_2$-0.9LMO for two different areas. Selected area (A) in Figure 5.27 shows a concentration of TiO_2, whereas selected area (B) in Figure 5.28 shows a high concentration of LMO. The results are consistent with XRD results with no interaction occurring between the end members.

$0.1TiO_2$-0.9LMO resonated at microwave frequencies with a ε_r of 6.9 and *Qf* of 21,324 GHz and TCF = -97 ppm/^oC. The relative density was 94%. It is evident that TCF tuned closer to zero with respect to LMO with little detriment to *Qf* for up to 10% TiO_2. However, attempts to increase the TiO_2 concentration further resulted in poor densification and a composite that was mechanically unstable. Despite initial promising results, these composites were considered unsuitable for further study and exploitation.

5.4 $Y_3Fe_5O_{12}$-LMO

As discussed in the literature survey, $Y_3Fe_5O_{12}$ is a garnet which is known to have a ferrimagnetic response. In the context of the thesis, it is used as a comparison with BF12.

$0.05Y_3Fe_5O_{12}$-0.95 LMO

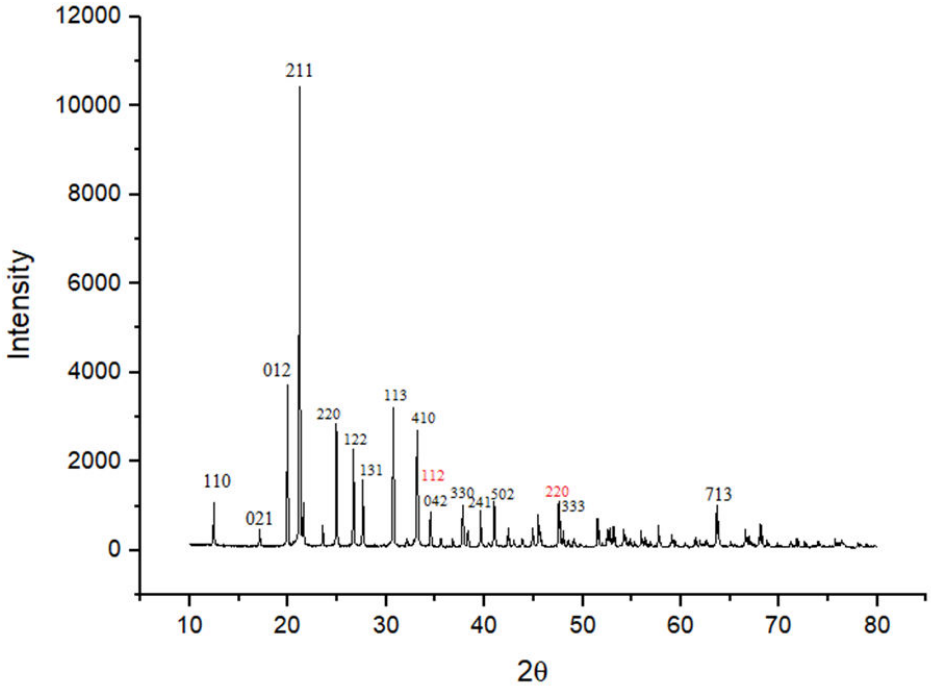

Figure 5.29. XRD of $0.05Y_3Fe_5O_{12}$-0.95LMO, where peak indices in red is $Y_3Fe_5O_{12}$ phase

Figure 5.29 shows XRD trace of 0.05 $Y_3Fe_5O_{12}$-0.95LMO synthesised by cold sintering at 120 ^oC for 40 minutes at 69 MPa. The trace reveals two distinct phases of $Y_3Fe_5O_{12}$ and LMO with no impurities. The relative density of sample is 96%.

Figure 5.30 shows a spectroscopic plot of the relationship between the imaginary component of the electric modulus (M'') and frequency of cold sintered $0.05Y_3Fe_5O_{12}$-0.95LMO measured at 43 ^oC where extracted bulk resistance (R)= 1.5 $*10^5$ **Ω**cm , and bulk extracted bulk capacitance= 2.15 $*10^{-12}$ F/cm.

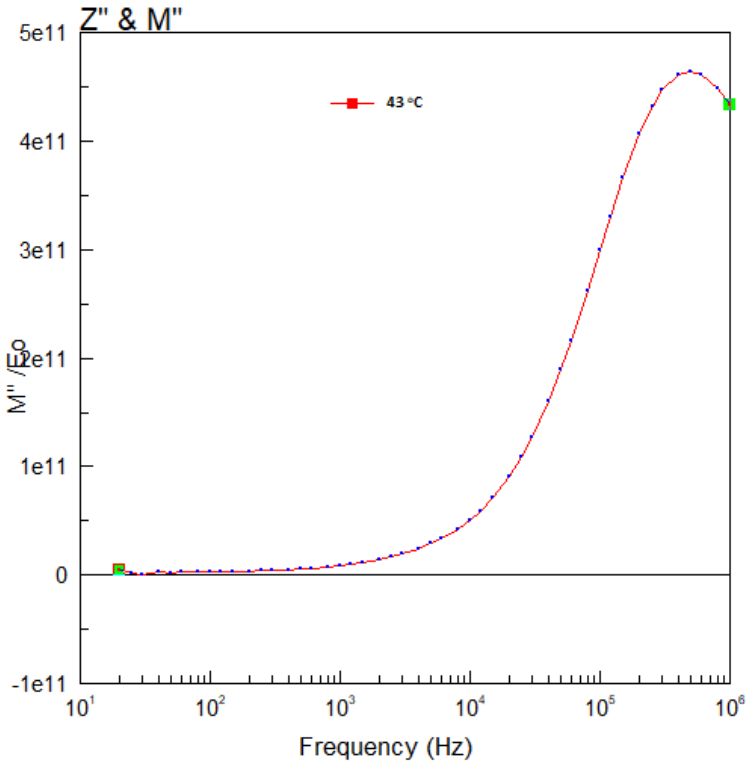

Figure 5.30. Spectroscopic plot of the relationship between the imaginary component of the electric modulus (M'') and frequency of cold sintered $0.05Y_3Fe_5O_{12}$-0.95LMO measured at 43 °C

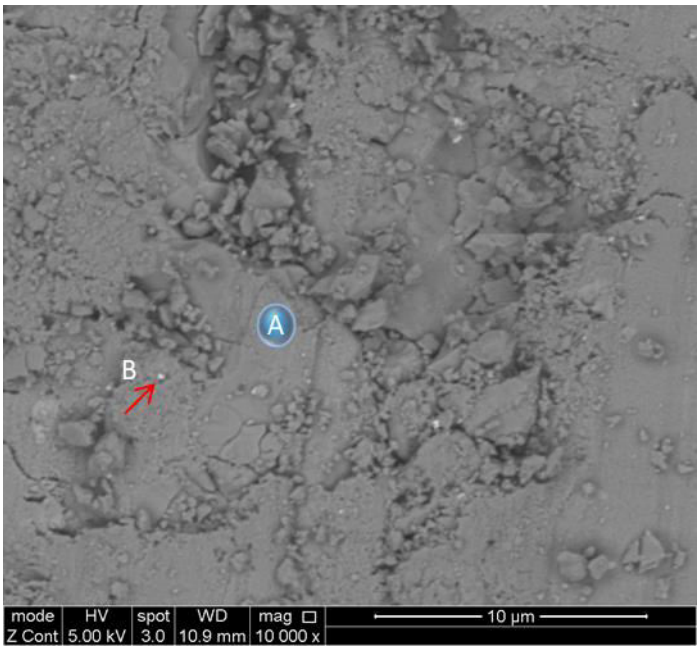

Figure 5.31. SEM of $0.05Y_3Fe_5O_{12}$-0.95LMO, where areas marked by A(large grains) and B (small grains) represent LMO and $Y_3Fe_5O_{12}$ phases respectively

Figure 5.31 shows SEM image with a dense composite of $Y_3Fe_5O_{12}$-LMO. Consistent with the XRD data, no interaction is apparent between the $Y_3Fe_5O_{12}$ and LMO.

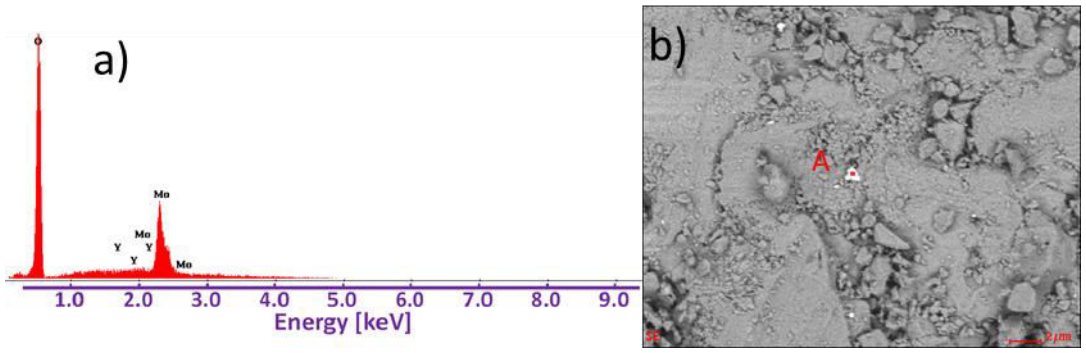

Figure 5.32. Energy dispersive X-ray spectrum of 0.05 $Y_3Fe_5O_{12}$- 0.95LMO a) from the area (A, $Y_3Fe_5O_{12}$) selected in b).

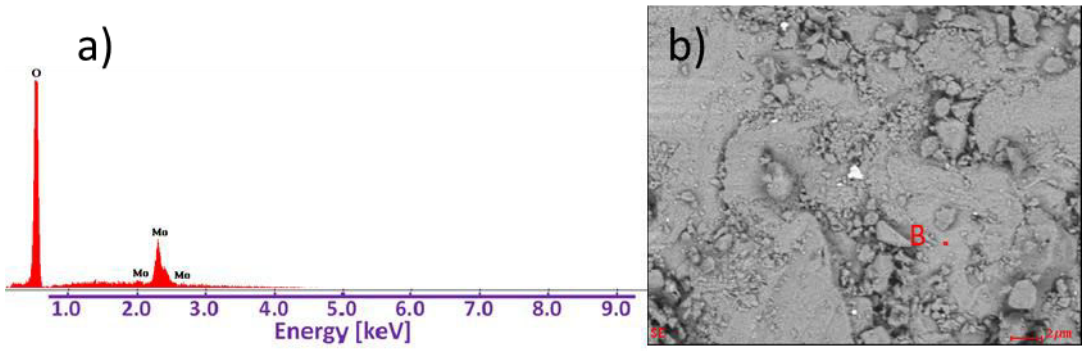

Figure 5.33. Energy dispersive X-ray spectrum of 0.05 $Y_3Fe_5O_{12}$-0.95LMO a) from the area (B, LMO) selected in b).

Figure 5.32 and Figure 5.33 show energy dispersive x-ray spectroscopy of $0.05Y_3Fe_5O_{12}$-0.95LMO for two different areas. Selected area (A) in Figure 5.32 shows $Y_3Fe_5O_{12}$ phase, whereas selected area (B) in Figure 5.33 is from LMO. No apparent interaction between the end members has occurred.

0.1$Y_3Fe_5O_{12}$-0.9 LMO

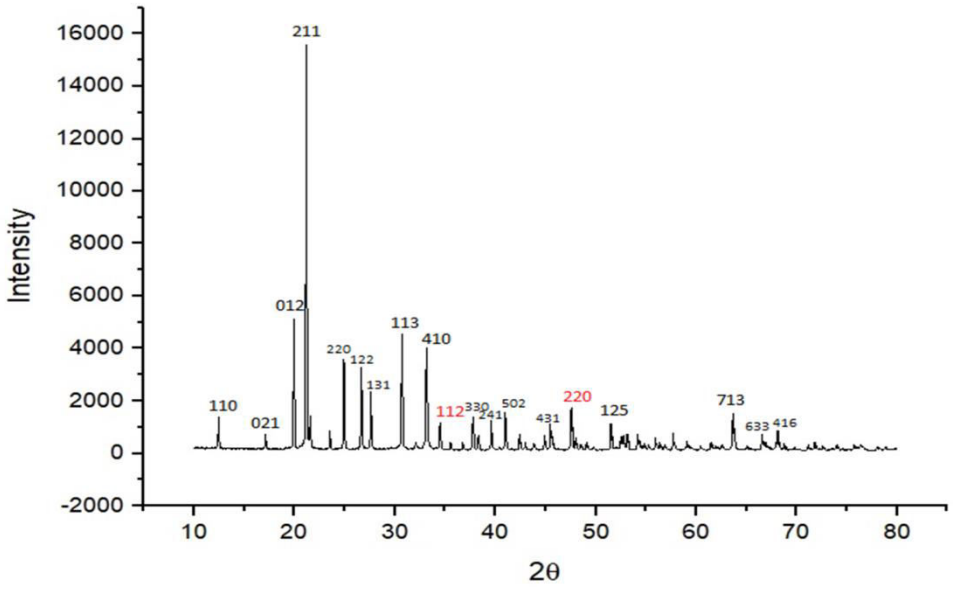

Figure 5.34. XRD of 0.1$Y_3Fe_5O_{12}$-0.9LMO, where peak indices in red is $Y_3Fe_5O_{12}$ phase

Figure 5.34 shows XRD trace of 0.1 $Y_3Fe_5O_{12}$-0.9LMO synthesised by cold sintering at 120 ^oC for 40 minutes at 69 MPa. The trace reveals two phases of $Y_3Fe_5O_{12}$ and LMO with no reaction.

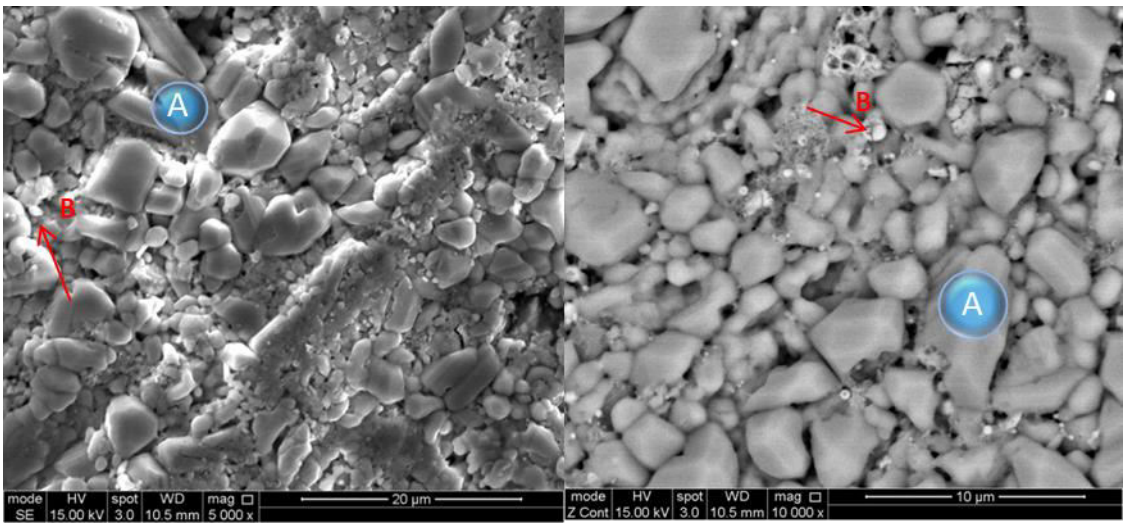

Figure 5.35. SEM of 0.1$Y_3Fe_5O_{12}$-0.9LMO, where areas marked by A (large grains) and B (small grains) represent LMO and $Y_3Fe_5O_{12}$ phases respectively

Figure 5.35 shows SEM image with a dense composite of $Y_3Fe_5O_{12}$-LMO. Consistent with the XRD data, no interaction is apparent between the $Y_3Fe_5O_{12}$ and LMO.

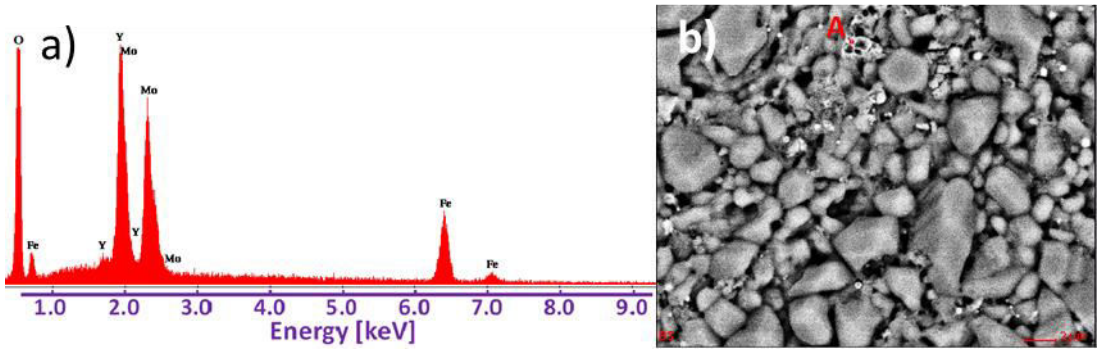

Figure 5.36 Energy dispersive X-ray spectrum of $0.1Y_3Fe_5O_{12}$-0.9LMO a) from the area (A, $Y_3Fe_5O_{12}$) selected in b).

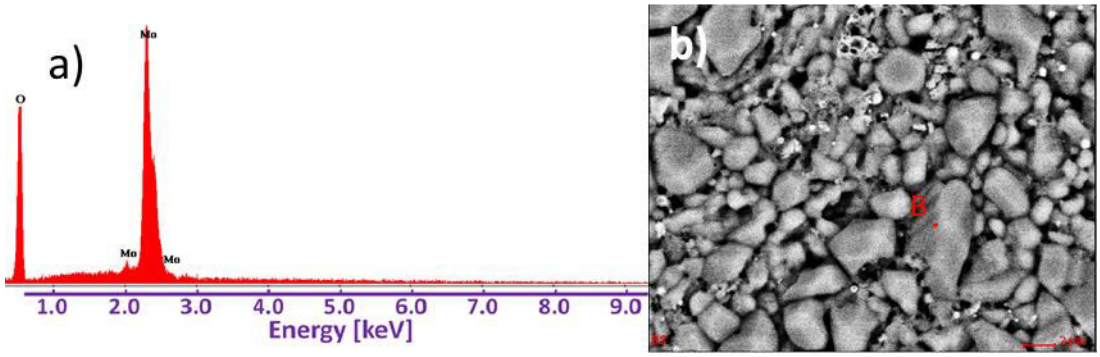

Figure 5.37. Energy dispersive X-ray spectrum of $0.1Y_3Fe_5O_{12}$-0.9LMO a) from the area (B, LMO) selected in b).

Figure 5.36 and Figure 5.37 show energy dispersive X-ray spectroscopy of $0.1Y_3Fe_5O_{12}$-0.9LMO for two different areas. Selected area (A) in Figure 5.36 shows $Y_3Fe_5O_{12}$ phase, however, Mo appears in the spectrum most likely because of the high 15KV used in SEM which penetrated below the sample's surface. In the selected area (B) in Figure 5.37 only Mo peaks appear consistent LMO. The SEM data emphasizes the XRD results that there are two distinct phase with no interaction.

$0.1Y_3Fe_5O_{12}$-0.9LMO resonated at microwave frequencies with ε_r of 8 but with a low Qf = 1416 GHz. In principle there should be little difference in the properties between the 0.1BF12-0.9LMO and $0.1Y_3Fe_5O_{12}$-0.9LMO. Each contains 10 wt% of a magnetic component with the dominant dielectric response airing from the LMO. Nonetheless, the 0.1BF12-0.9LMO has a markedly higher Qf. The dielectric properties of the BF12-LMO system are

thus considered significantly more promising with potential applications as magnetodielectric RF substrates.

$0.15Y_3Fe_5O_{12}$-0.85 LMO

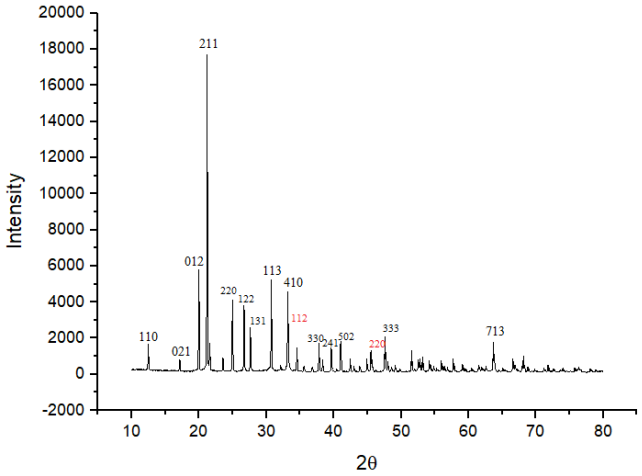

Figure 5.38. XRD of $0.15Y_3Fe5O_{12}$-0.85LMO, where peak indices in red is $Y_3Fe_5O_{12}$ phase

Figure 5.38 shows XRD trace of $0.15Y_3Fe_5O_{12}$-0.85LMO synthesised by cold sintering at 120 ^oC for 40 minutes at 69 MPa. The trace reveals two phases, $Y_3Fe_5O_{12}$ and LMO with no evidence of reaction.

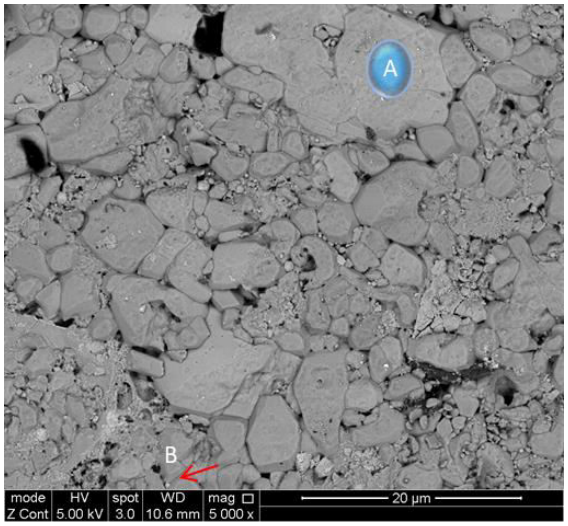

Figure 5.39. SEM of $0.15Y_3Fe_5O_{12}$-0.85LMO, where areas marked by A(large grains) and B (small grains) represent LMO and $Y_3Fe_5O_{12}$ phases respectively

Figure 5.39 shows SEM image with a dense composite of $Y_3Fe_5O_{12}$-LMO. Consistent with the XRD data, no interaction is apparent between the $Y_3Fe_5O_{12}$ and LMO.

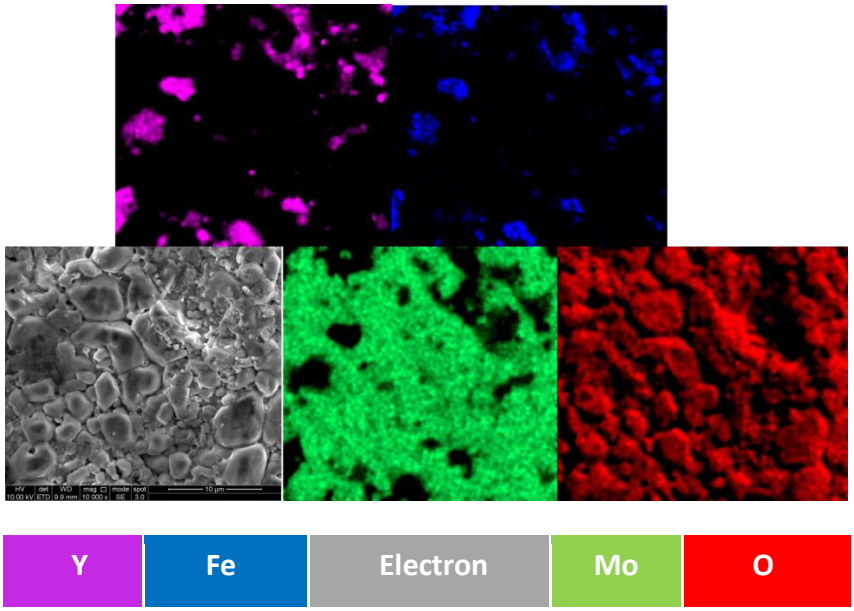

Figure 5.40. Energy dispersive X-ray mapping image of $0.15Y_3Fe_5O_{12}$-0.85LMO, where each element is represented by a color in the key below image

Figure 5.40 shows an energy dispersive X-ray mapping image of $0.15Y_3Fe_5O_{12}$-0.85LMO in which the two end member phases are clearly indicated. The relative density of sample is 93%. This sample did not resonate at MW frequencies.

5.5 BF12-Na_2MoO_4

The success in fabricating BF12-LMO composites suggested that further studies should be carried out to ascertain whether TCF could be further tuned to zero by starting with Na_2MoO_4 (- 70 MK^{-1}) instead of LMO as an end member (-160 MK^{-1}) [6]. The higher ε_r of Na_2MoO_4 (13) could also potentially lead to a high ε_r composite.

0.1BF12-0.9Na_2MoO_4

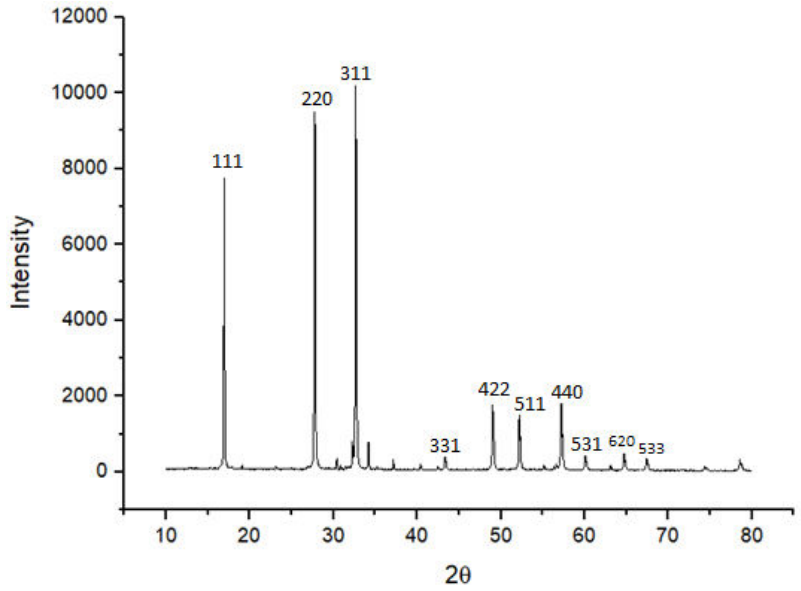

Figure 5.41. XRD of 0.1BF12-0.9Na_2MoO_4, where BF12 phase couldn't be detected

Despite promising end member properties, Na_2MoO_4 - BF12 composites were brittle and exhibited crazing throughout their microstructure. Figure 5.41 shows XRD of a crushed pellet of the composite. BF12 could not be detected in the diffraction data nor was it visible in SEM images (Figure 5.42). Dielectric properties at MW frequencies could not be measured, presumably due to the many internal cracks. Further studies were thus abandoned but, in hindsight, these issues might be solved through superior control of the cold sintering process and this composite may well show promise in the future.

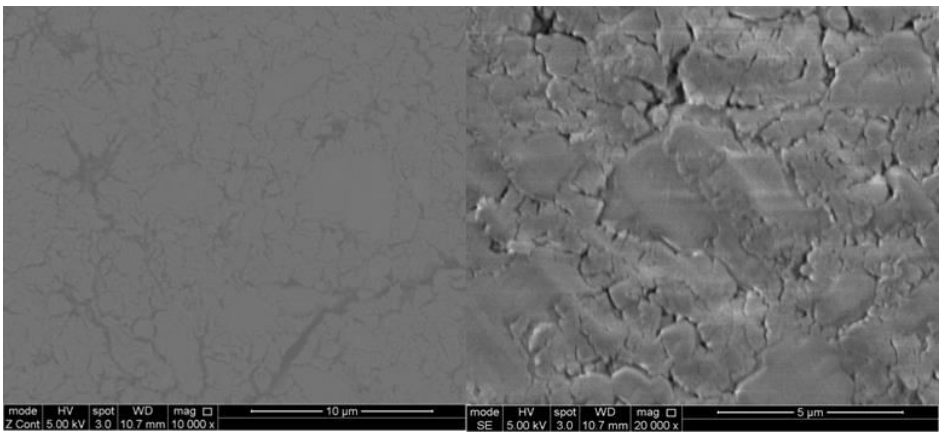

Figure 5.42. SEM of 0.1BF12-0.9Na_2MoO_4

5.6 BF12-K_2MoO_4

K_2MoO_4 was also explored as a possible alternative end member to LMO to form K_2MoO_4-BF12 composites. While –at the best of my knowledge- no previous work has been carried out of cold sintered K_2MoO_4 , however, Guo et al. [2] have reported that $K_2Mo_2O_7$ cold sinters at 120 ^oC with ε_r =9.8 and *Qf* =16,000 GHz.

K_2MoO_4

Figure 5.43 shows an XRD trace of K_2MoO_4 synthesised by cold sintering at 120 ^oC for 40 minutes at 69 MPa. SEM images (Figure 5.44) of undoped cold sintered K_2MoO_4 exhibit a dense microstructure, free from porosity although some microcracking is observed.

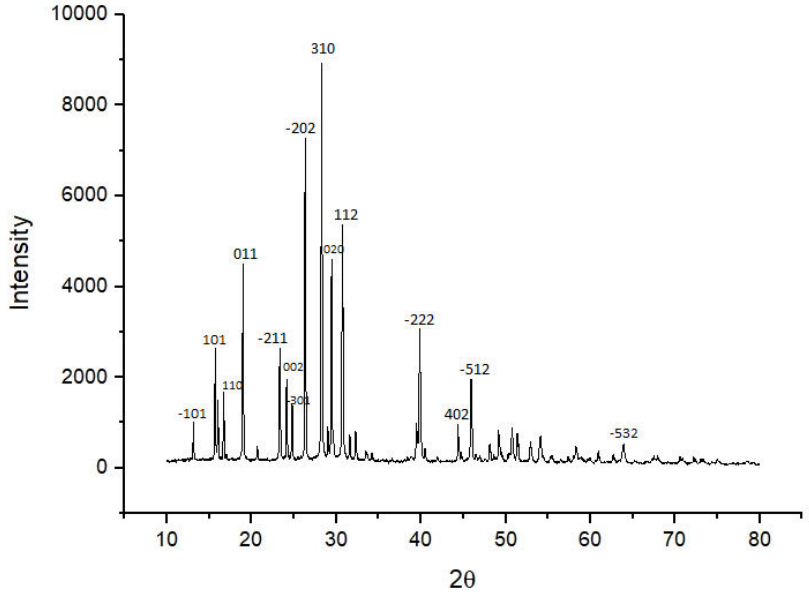

Figure 5.43. XRD of cold sintered K_2MoO_4

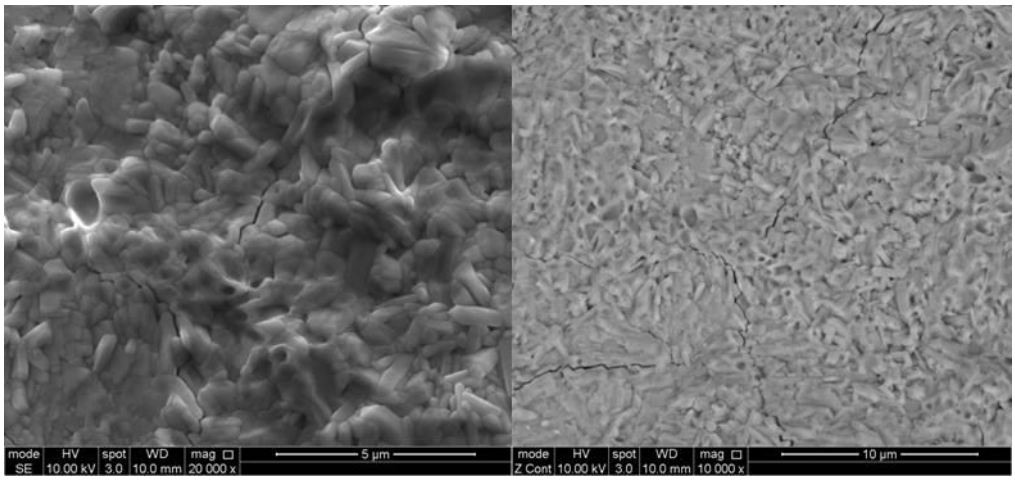

Figure 5.44. SEM of cold sintered K_2MoO_4 at 120 ^oC

K_2MoO_4 resonated at 7.5 GHz with ε_r of 6.5, Qf of 5907 GHz and TCF of -45 ppm/^oC. The relative density of sample was however only 80% which was inconsistent with the SEM images shown in Figure 5.44. This low density presumably derives from internal pores within the bulk of the ceramic, whilst the surface remains dense.

0.05BF12-0.95K_2MoO_4

Figure 5.45 shows XRD trace of 0.05BF12-0.95K_2MoO_4 synthesised by cold sintering at 120 ^oC for 40 minutes at 69 MPa. Peaks of BF12 and K_2MoO_4 can be identified with no reaction phase observed.

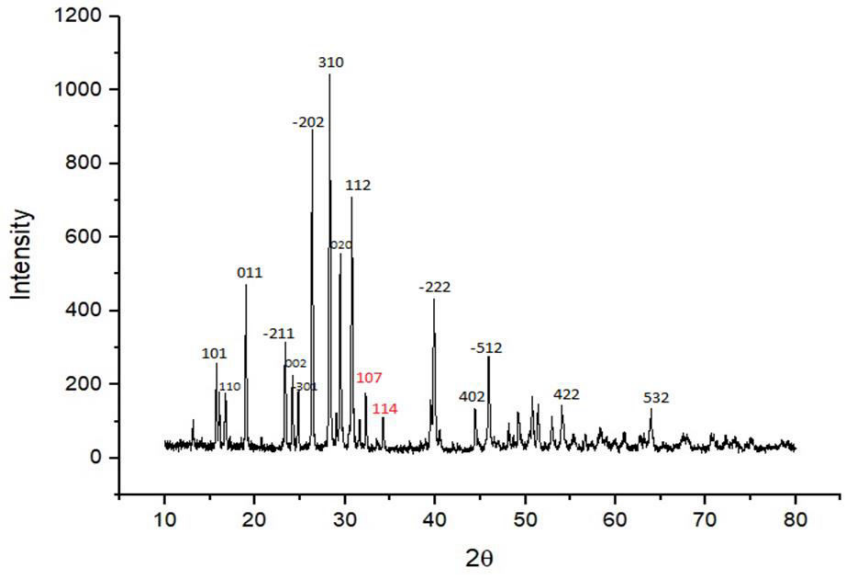

Figure 5.45. XRD of 0.05BF12-0.95K_2MoO_4, where peak indices in red is BF12 phase

Figure 5.46 shows SEM image with a clear dense composite of 0.05BF12-0.95K_2MoO_4, which also exhibits low surface porosity . Consistent with XRD trace, no interaction occurred between the two phases.

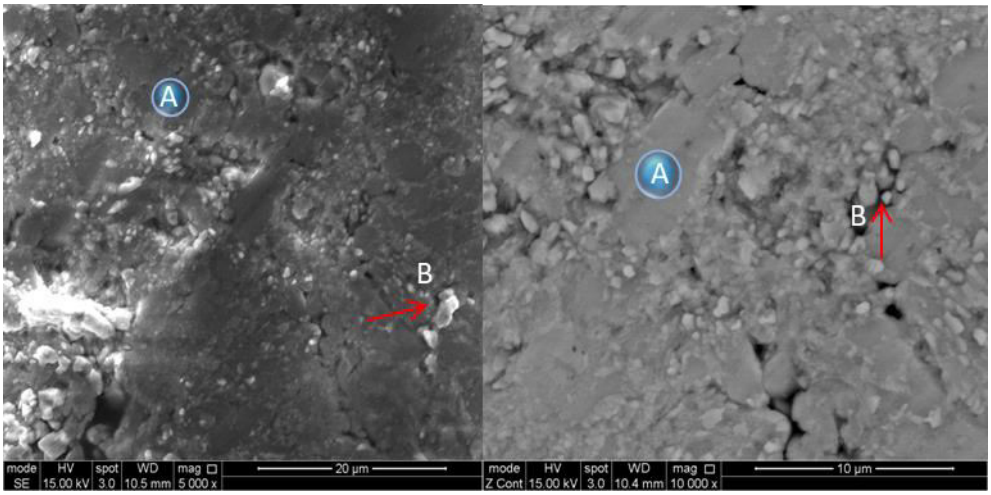

Figure 5.46. SEM of 0.05BF12-0.95K_2MoO_4 , where areas marked by A(large grains) and B (small grains) represent K_2MoO_4 and BF12 phases respectively

0.05BF12-0.95K_2MoO_4 resonated at microwave frequencies with ε_r of 6.3, Qf ~ 14,544 GHz and TCF of -66 ppm/°C. The relative density of sample is 96%.

0.1BF12-0.9K_2MoO_4

Figure 5.47 shows XRD trace of 0.1BF12-0.9K_2MoO_4 synthesised by cold sintering at 120 ^oC for 40 minutes at a pressure of 69 MPa. The trace reveals two phases of BF12 and K_2MoO_4 with no reaction.

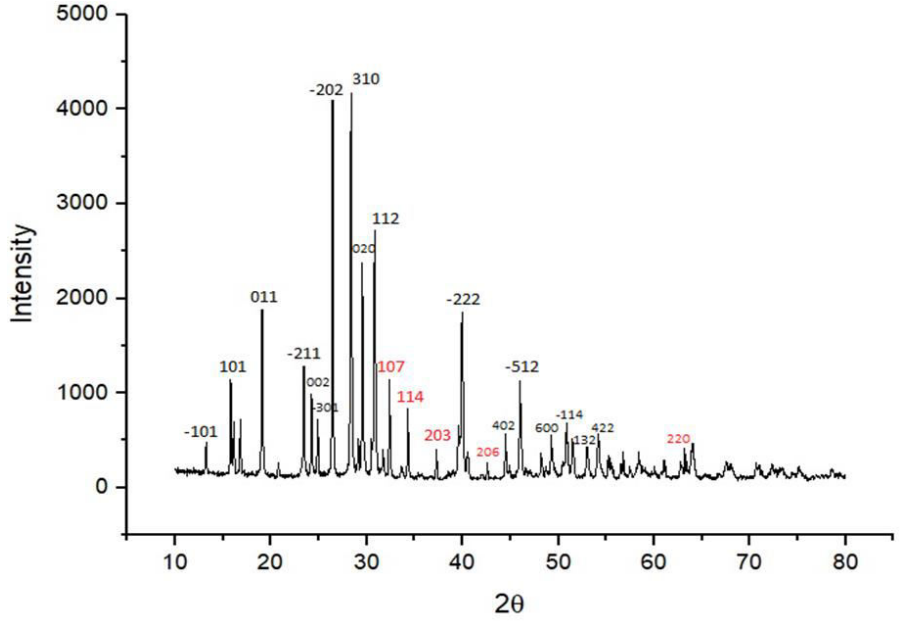

Figure 5.47. XRD of 0.1BF12-0.9K_2MoO_4, where peak indices in red is BF12 phase

Figure 5.48 shows SEM image with a clear dense composite of 0.05BF12-0.95K_2MoO_4 with little visible porosity . Consistent with XRD trace, no interaction occurred between the two phases.

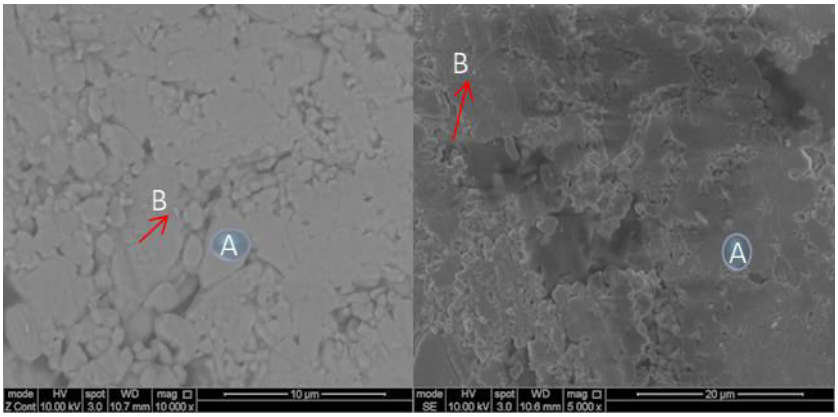

Figure 5.48. SEM of 0.1BF12-0.9K_2MoO_4, where areas marked by A(large grains) and B (small grains) represent K_2MoO_4 and BF12 phases respectively

Figure 5.49 shows an energy dispersive x-ray spectrum of 0.1BF12-0.9K_2MoO_4 alongside the associated region from the sample. Figure 5.50 shows the EDS layered image of the selected area of 0.1BF12-K_2MoO_4 composite, revealing two distinct phase consistent with BF12 and K_2MoO_4.

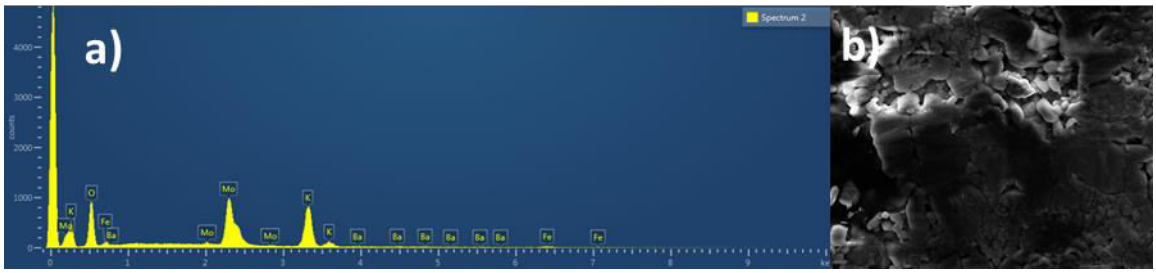

Figure 5.49 Energy dispersive X-ray spectrum of 0.1BF12-0.9K_2MoO_4 a) is taken from the whole area of b)

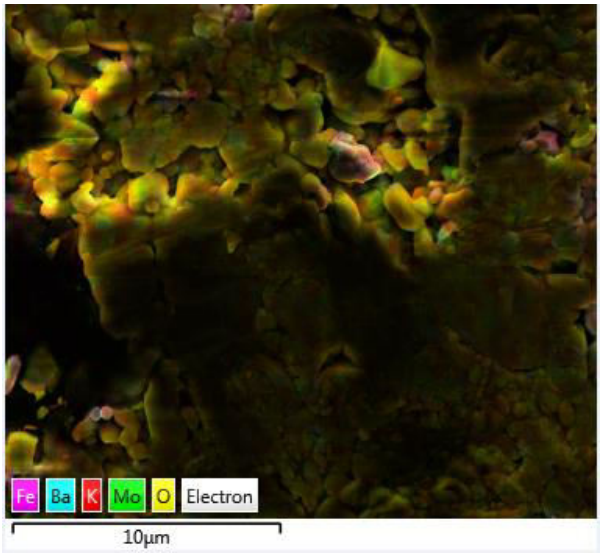

Figure 5.50. Energy dispersive X-ray mapping image of 0.1BF12-0.9K_2MoO_4, where each element is represented by the color code inset in the image

Table 5.3 shows the weight percentage of elements in 0.1BF12-0.9K_2MoO_4 which are in approximate agreement with the batched composition.

Element	Wt%	Wt% error (+,-)
O	24.9	0.69
K	28.64	0.62
Fe	5.01	0.98
Mo	40.21	0.86
Ba	1.24	0.78

Table 5.3. Weight percentage of elements of 0.1BF12-0.9K_2MoO_4

0.1BF12-0.9K_2MoO_4 showed promising properties and resonated at microwave frequencies to give ε_r = 6.9, *Qf* =18,979 GHz and TCF of -54 ppm/^oC. The relative density of sample is 98%.

0.15BF12-0.85K_2MoO_4

Figure 5.51 shows XRD trace of 0.15BF12-0.85K_2MoO_4 synthesised by cold sintering at 120 ^oC for 40 minutes at 69 MPa. The trace reveals only peaks from the end member compounds.

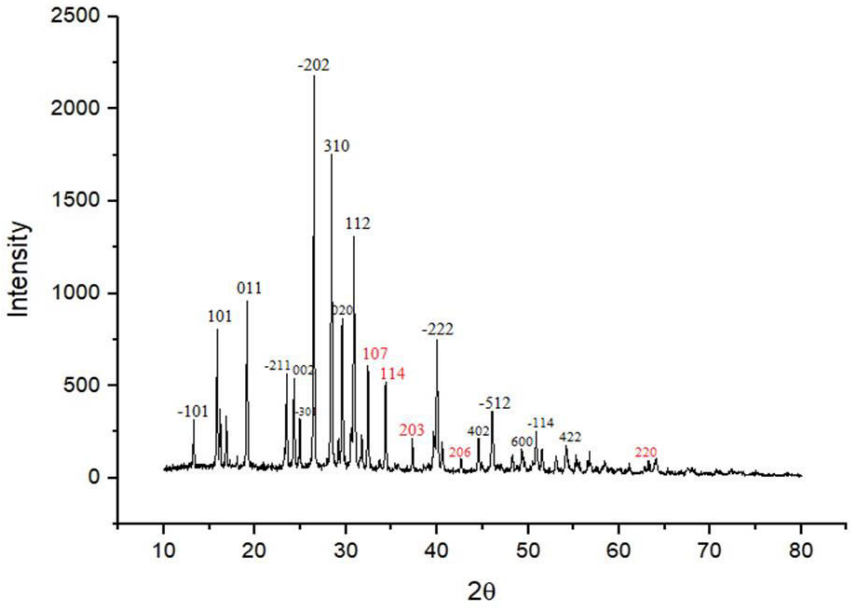

Figure 5.51. XRD of 0.15BF12-0.85K_2MoO_4, where peak indices in red is BF12 phase

SEM images (Figure 5.52) reveal a dense composite of 0.15BF12-0.95K_2MoO_4, with little porosity. Consistent with the XRD trace, no interaction was apparent between the two phases.

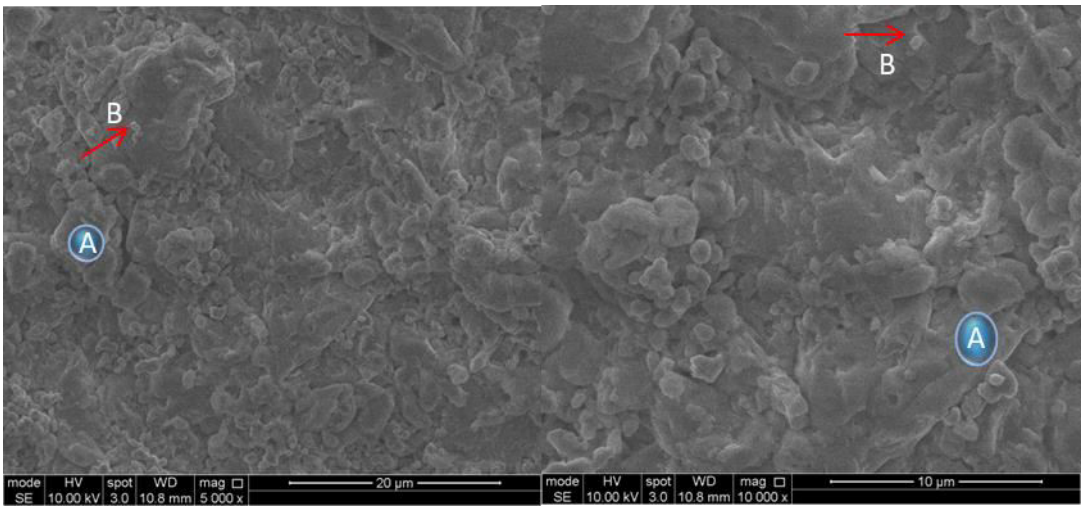

Figure 5.52. SEM of 0.15BF12-0.85K_2MoO_4, where areas marked by A(large grains) and B (small grains) represent K_2MoO_4 and BF12 phases respectively

0.15BF12-0.85K_2MoO_4 had relative density of 93% and resonated at microwave frequencies with ε_r = 7.2, *Qf* = 11,104 GHz and TCF = -39 ppm/°C. ε_r and *TCF* increase with increasing of *x* for *x*BF12-(1-*x*)K_2MoO_4 but *Qf* reaches a maximum at *x*=0.1.

5.7 $BaTiO_3$-LMO (nano $BaTiO_3$)

$BaTiO_3$ is a high ε_r compound which could potentially modify the composite properties. Nano powders were initially chosen for this study as it was anticipated that they could be better incorporated into the composite. There was no anticipation that $BaTiO_3$ would cold sinter at 120 °C, since Guo et al have reported that additions of TiO_2 nano-powder and $Ba(OH)_2$ must be used before densification occurs [3], [7].

0.1$BaTiO_3$-0.9LMO

Figure 5.53 shows XRD trace of 0.1$BaTiO_3$-0.9LMO synthesised by cold sintering at 120 °C for 40 minutes at 69 MPa. $BaTiO_3$ powder in these composites is >50 nm diameter in order to optimise packing and surface reactions. The trace reveals only peaks associated with $BaTiO_3$ and LMO.

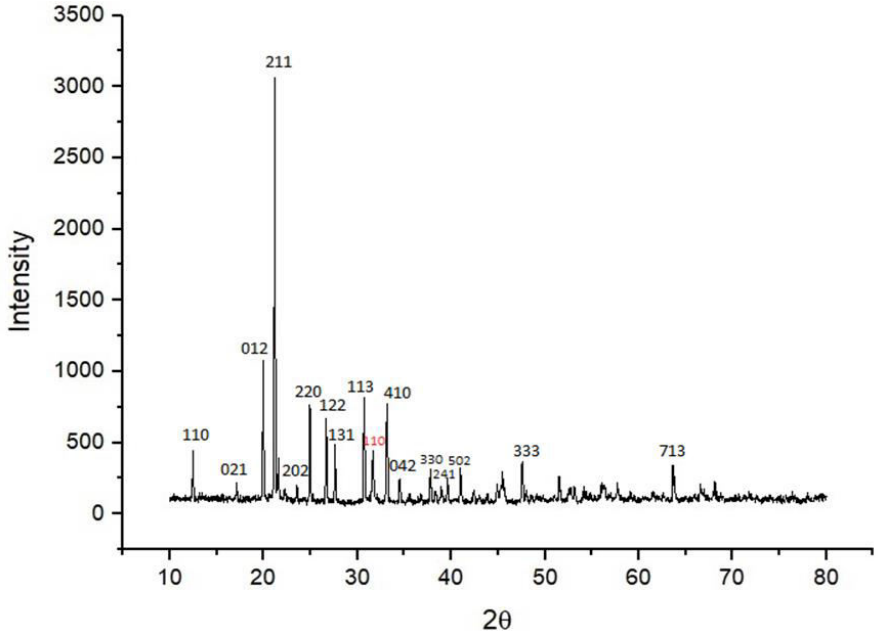

Figure 5.53. XRD of 0.1$BaTiO_3$-0.9LMO , where peak indices in red is $BaTiO_3$ phase

SEM images however, reveal a poor distribution of nano particles of $BaTiO_3$ in the matrix of LMO with evidence of porosity (Figure 5.54). No interaction occurred between $BaTiO_3$ and LMO but there has been an agglomeration of the BT nano-particles during mixing/pressing.

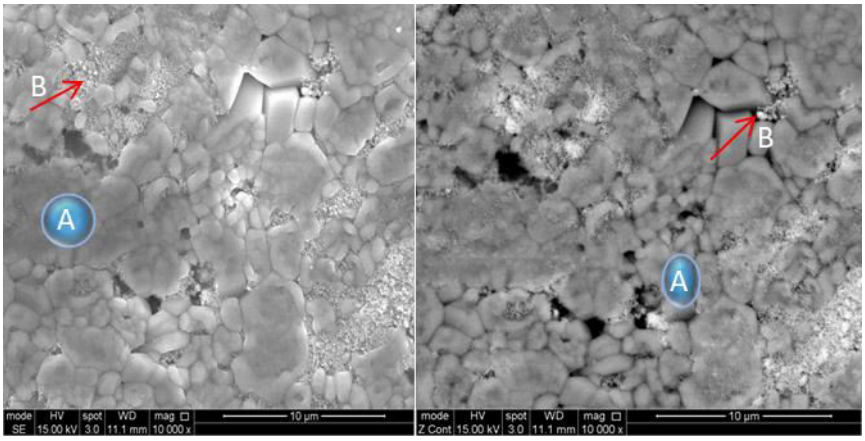

Figure 5.54. SEM of 0.1$BaTiO_3$-0.9LMO . A = large grains and B = small grains of LMO and $BaTiO_3$ phases respectively

Microwave dielectric properties could not be obtained from these samples, presumably as a result of the agglommeration of nano-particles creating low-density ferroelectric regions in the sample. Consequently, further work was undertaken to fabricate $BaTiO_3$ – LMO composites using micron sized particles of $BaTiO_3$.

5.8 $BaTiO_3$-LMO (micro $BaTiO_3$)

0.05$BaTiO_3$-0.95LMO

Figure 5.55 shows the XRD trace of 0.05$BaTiO_3$-0.95Li_2MoO_4 synthesised by cold sintering at 120 ^oC for 40 minutes at 69 MPa. The trace reveals only peaks from $BaTiO_3$ and LMO.

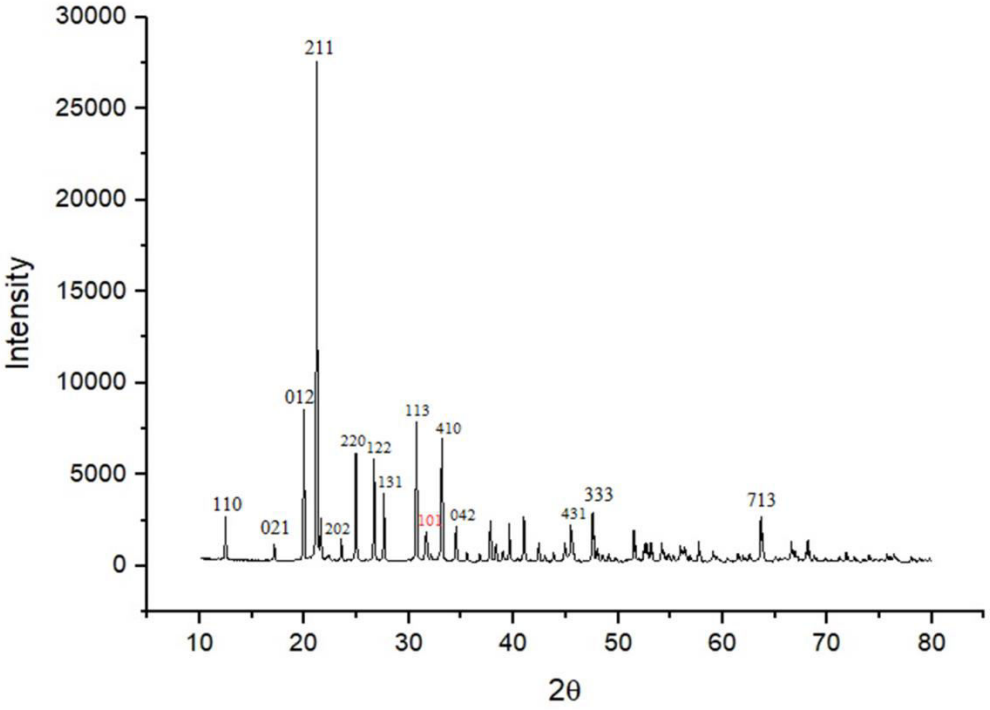

Figure 5.55. XRD trace of $0.05BaTiO_3$-0.95LMO, where peak indices in red is $BaTiO_3$ phase

In contrast to the LMO with $BaTiO_3$ nano-particles, $0.05BaTiO_3$-0.95LMO resonated at microwave frequencies with ε_r of 6.2 but with Qf = 1726 GHz and TCF of -161 ppm/°C. The relative density of sample was 96%.

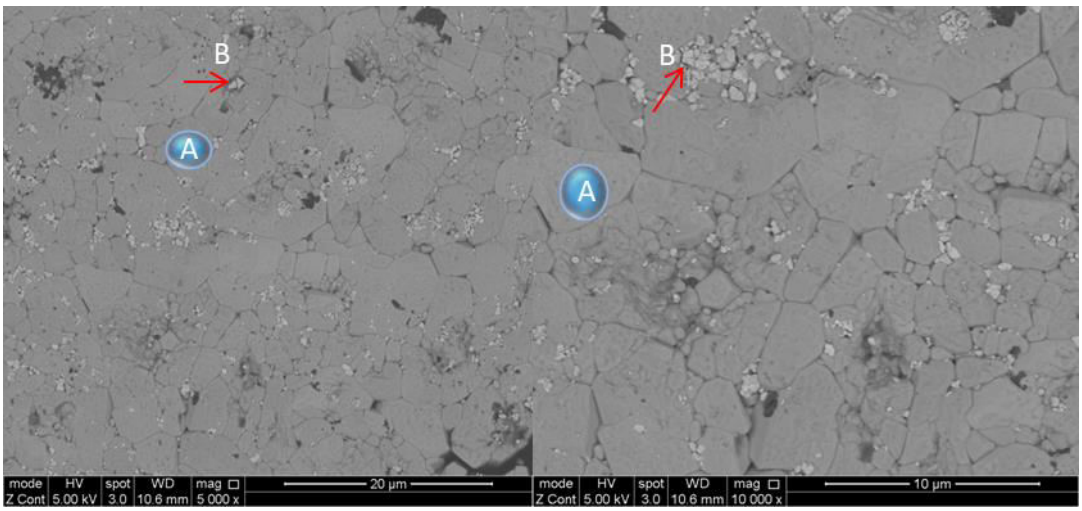

Figure 5.56. SEM of $0.05BaTiO_3$-0.95LMO , where areas marked by A(large grains) and B (small grains) represent LMO and $BaTiO_3$ phases respectively

Figure 5.56 shows the SEM image with a $0.05BaTiO_3$-0.95LMO composites pores apparent no evidence of an intermediate phase. Although there is some agglomeration of

micron sized $BaTiO_3$, the distribution (Figure 5.56) is better than the nano scale $BaTiO_3$ composites (Figure 5.54) which resulted in more dense samples with measurable microwave properties. Figure 5.57 and Figure 5.58 show energy dispersive x-ray spectra from 0.05 $BaTiO_3$-0.95LMO for two different areas. Selected area (A) in Figure 5.57 is the LMO phase and (B) from Figure 5.58 is from a regions of the $BaTiO_3$ phase. However, the signal remains dominated by Mo due to beam spreading in the interior of the sample and the large spot size required to obtain reasonable counts for the spectra.

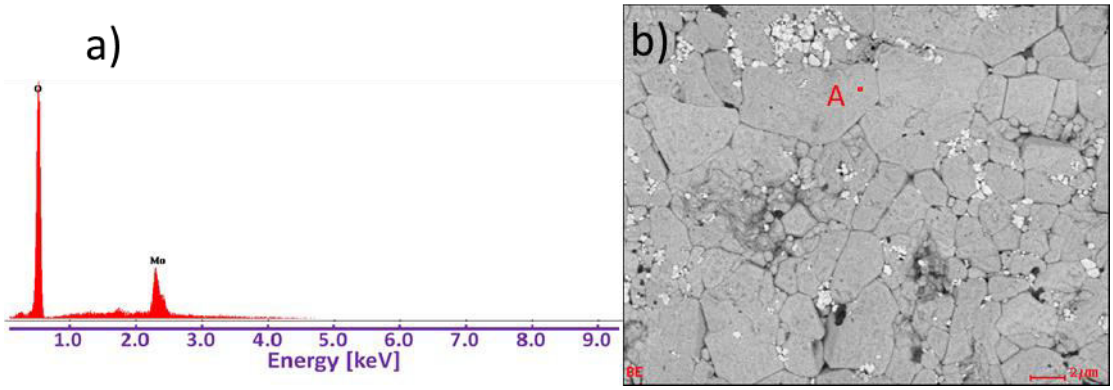

Figure 5.57. Energy dispersive X-ray spectrum of 0.05$BaTiO_3$-0.95LMO a) from the area (A, LMO) selected in b).

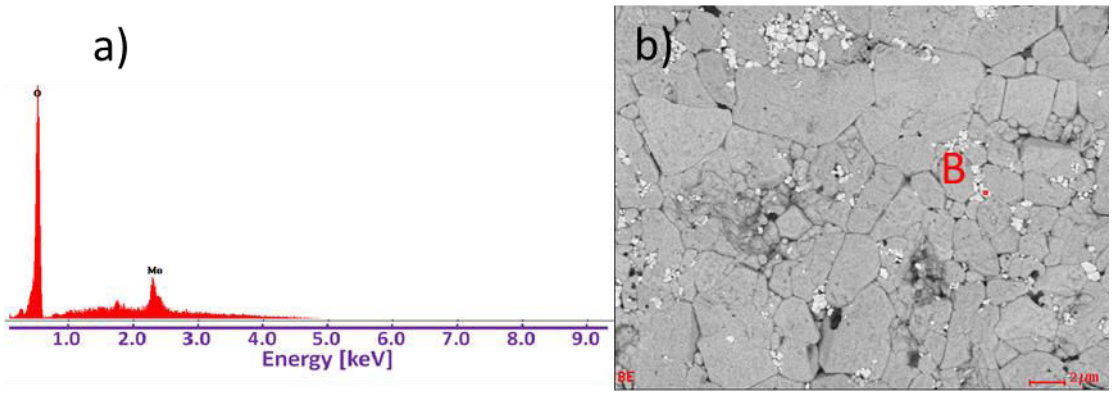

Figure 5.58. Energy dispersive X-ray spectrum of 0.05$BaTiO_3$-0.95LMO a) from the area (B, $BaTiO_3$) selected in b).

Figure 5.59 shows Arrhenius plots of bulk σ data obtained from spectroscopic plots of the imaginary component of the electric modulus (M'') which shows 0.05$BaTiO_3$-0.95LMO. The σ of composite increases with temperature ascending as expected with as the resistance of the sample decreases. The values of activation energy associated with the bulk

response extracted from the data reveal that the cold sintered composite 0.05$BaTiO_3$-LMO has an activation energy of 0.12 eV compared to 0.25 eV of 0.1BF12-0.9LMO. Such a low value (0.12 eV) suggests that there is the possiblility of proton conduction in these materials based on retained OH groups from the cold sintering process. However, significant more work is required to establish unambiguously if this is the case.

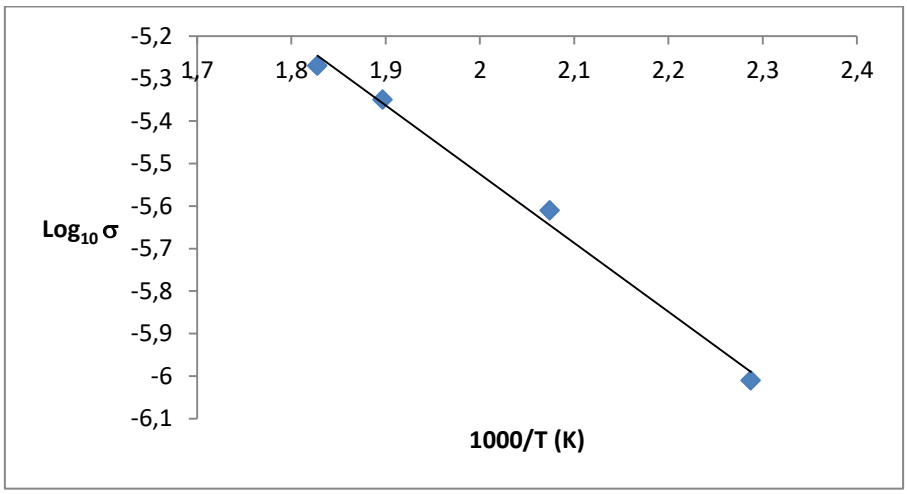

Figure 5.59. σ Vs. temperature dependance of cold sintered 0.05$BaTiO_3$-0.95LMO

0.1$BaTiO_3$-0.9LMO

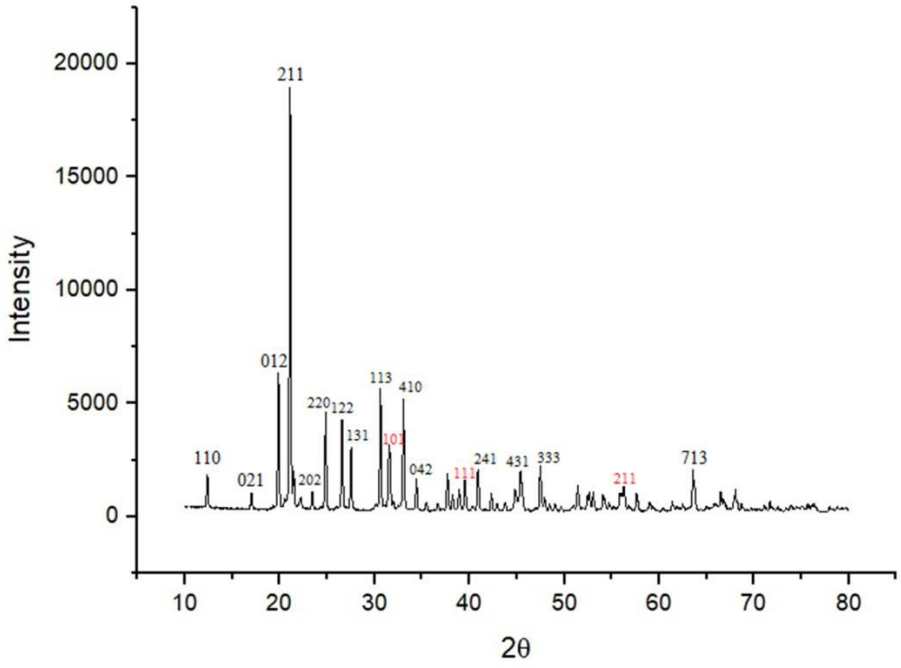

Figure 5.60. XRD of 0.1$BaTiO_3$-0.9LMO, where peak indices in red is $BaTiO_3$ phase

Figure 5.60 shows XRD trace of $0.1BaTiO_3$-0.9LMO synthesised by cold sintering at 120 ^oC for 40 minutes at 69 MPa. The trace reveals peaks from LMO and $BaTiO_3$.

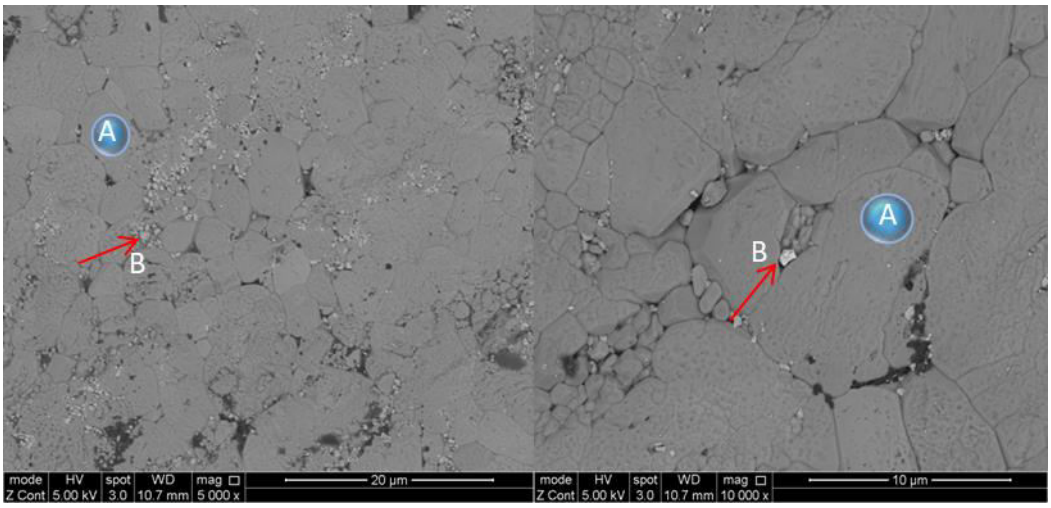

Figure 5.61. SEM of $0.1BaTiO_3$-0.9LMO, where areas marked by A(large grains) and B (small grains) represent LMO and $BaTiO_3$ phases respectively

SEM images (Figure 5.61) show a dense composite with low porosity and no intermediate phases. The distribution of micro scale $BaTiO_3$ in composite (Figure 5.61) looks better than nano scale $BaTiO_3$ (Figure 5.54) which resulted in more dense samples, however, with non measurable microwave properties probably because of a low quality factor.

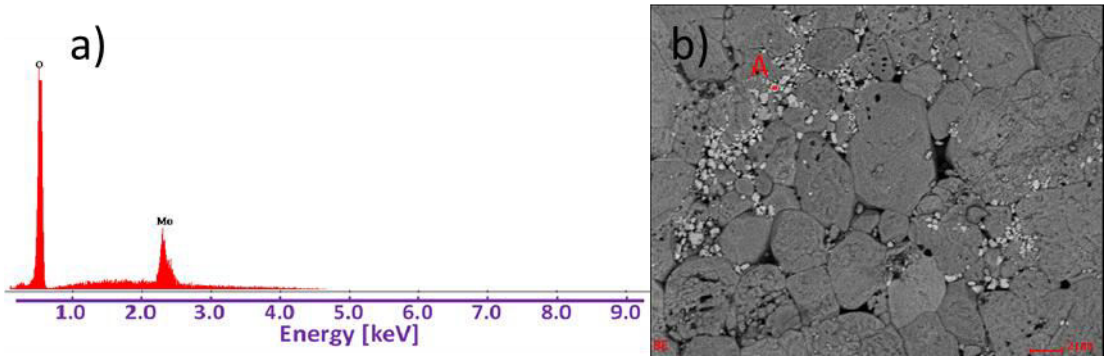

Figure 5.62. Energy dispersive X-ray spectrum of $0.1BaTiO_3$-0.9LMO a) from region A ($BaTiO_3$) selected in b).

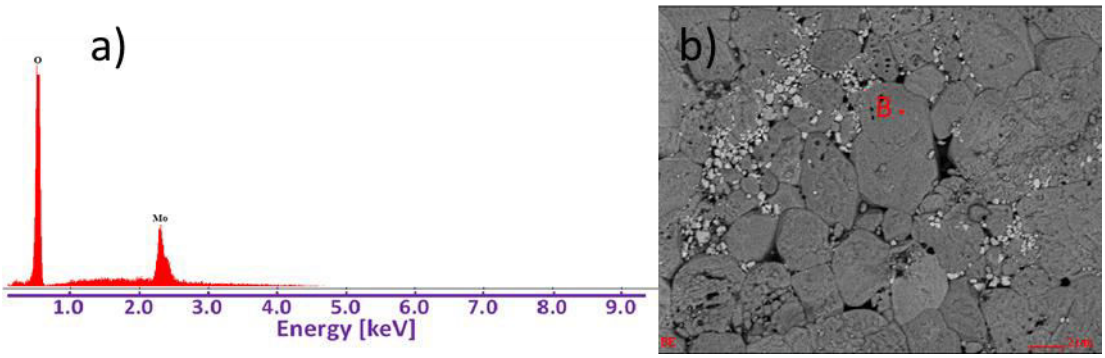

Figure 5.63. Energy dispersive X-ray spectrum of 0.1$BaTiO_3$-0.9LMO a) from the area (B, LMO) selected in b).

Figure 5.62 and Figure 5.63 show energy dispersive X-ray spectra of 0.1 $BaTiO_3$-0.9LMO for two different areas. Selected area (A) in Figure 5.62 is from grains consistent in contrast with $BaTiO_3$ but the spread of the beam and the small size of the particles has meant that the $BaTiO_3$ and Ti are too weak to be detected. However, area (B) in Figure 5.63 shows clearly LMO phase.

Microwave properties of 0.1$BaTiO_3$-0.9LMO couldn't be measured probably because of the low *Qf* of the composite as the $BaTiO_3$ concentration increased. The relative density of sample is 96%.

0.15$BaTiO_3$-0.85LMO

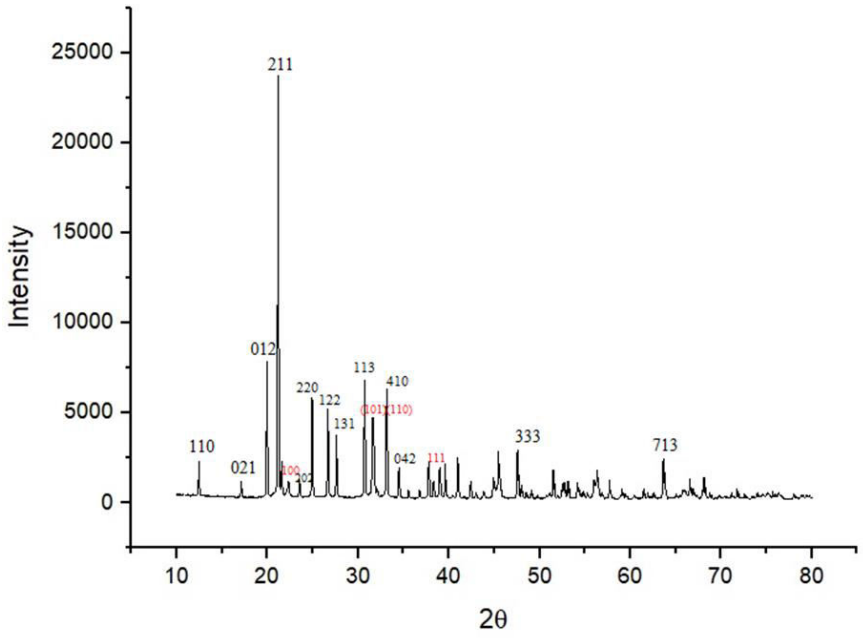

Figure 5.64. XRD of 0.15$BaTiO_3$-0.85LMO, where peak indices in red is $BaTiO_3$ phase

Figure 5.64 shows XRD trace of $0.15BaTiO_3$-0.85LMO synthesised by cold sintering at 120 ^{o}C for 40 minutes at a pressure of 69 MPa. The trace reveals only $BaTiO_3$ and LMO.

Microwave properties of $0.15BaTiO_3$-0.85LMO could not be obtained, most likley due to the low *Qf* of these composites which manifest as broad unstable peaks on the VNA oscilloscope.The relative density was 97%.

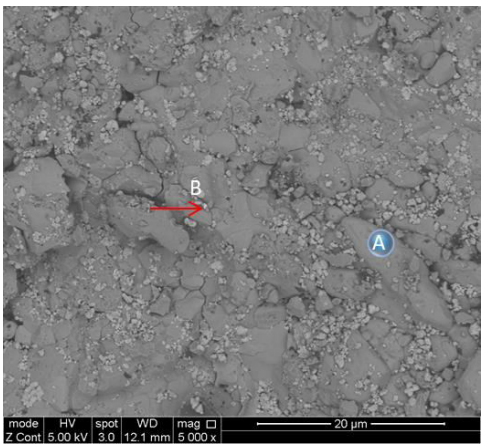

Figure 5.65. SEM of $0.15BaTiO_3$-0.85LMO. A are large grains and B are small grains of LMO and $BaTiO_3$, respectively

Figure 5.65 shows SEM image of a dense composite of $0.15BaTiO_3$-0.85LMO. Two distinct phases are oserved.

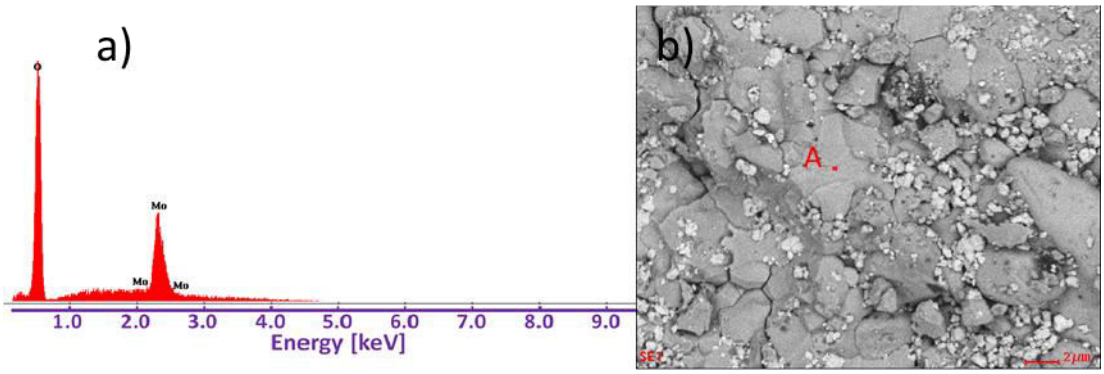

Figure 5.66. Energy dispersive X-ray spectrum of $0.15BaTiO_3$-0.85LMO a) from the area (A, LMO) selected in b)

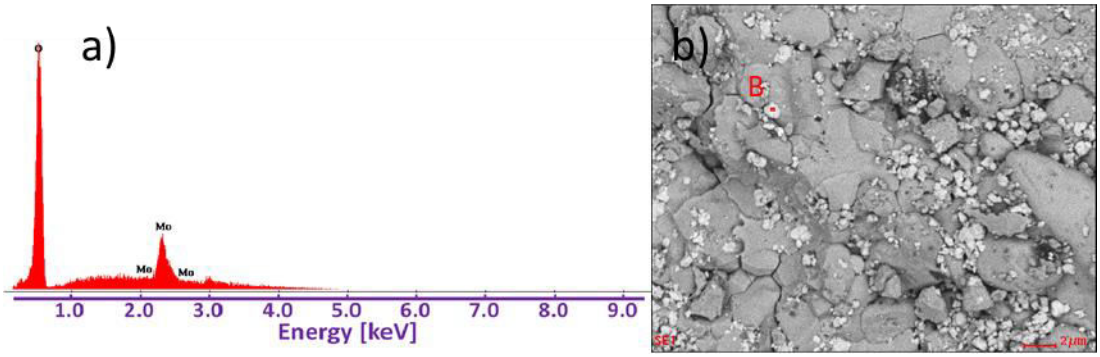

Figure 5.67. Energy dispersive X-ray spectrum of 0.15$BaTiO_3$-0.85LMO a) from the area B ($BaTiO_3$) selected in b)

Figure 5.66 and Figure 5.67 show energy dispersive X-ray spectra of 0.15 $BaTiO_3$-0.85LMO. Area (A) in Figure 5.66 is from the LMO phase whereas (B) in Figure 5.67 is from the $BaTiO_3$ phase. The small size of the $BaTiO_3$ and penetration of the electron beam into the depth of the sample have resulted in only a weak signal from $BaTiO_3$.

Figure 5.68 shows Arrhenius plots of bulk σ data obtained from spectroscopic plots of the imaginary component of the electric modulus (M'') which shows 0.15$BaTiO_3$-0.85LMO. The σ of composite increases with temperature ascending as expected with resistence reduction through the specimen. The values of activation energy associated with the bulk response extracted from the data reveal that the cold sintered composite $BaTiO_3$-LMO has an activation energy of 0.16 eV.

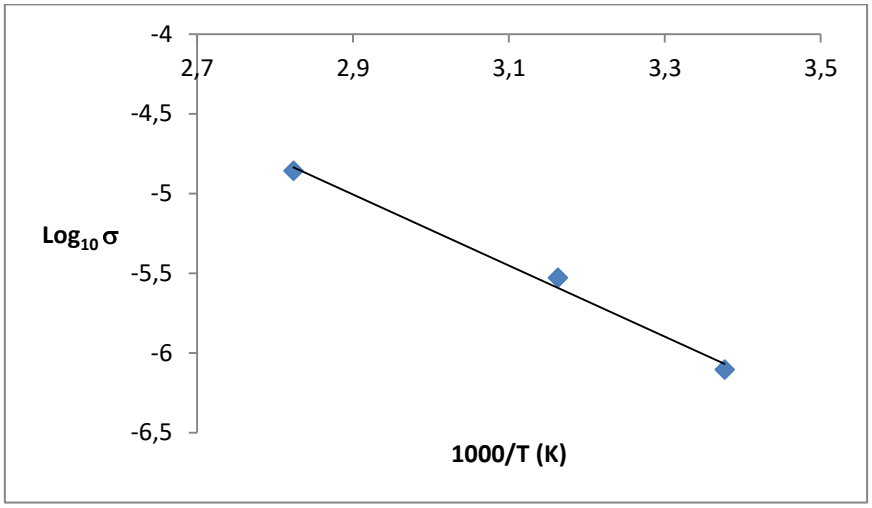

Figure 5.68. σ Vs. temperature dependance of cold sintered 0.15$BaTiO_3$-0.85LMO

The relative density increases with increasing *x* for *x*$BaTiO_3$-(1-*x*)LMO composites but in addition, σ extracted from the imaginary components of the electric modulus (M'') also increases with *x.* Impedance measurements couldn't be taken at *x*=0.1 because of noise

forming at electric modulus peak (M''). The increase in conductivity directly relates to the volume fraction and connectivity at LMO grain boundaries of the $BaTiO_3$ phase. To fully understand the conductivity and the role of percolation in $BaTiO_3$-LMO composites, further finite element modelling is required. Given the poor performance of $BaTiO_3$-LMO as a MW material, extensive studies to model this behaviour are unwarranted unlike for BF12-LMO for which the dielectric behavior is exceptional. Nonetheless, given the similarity in particle size between BF12 and $BaTiO_3$ compared with LMO, similar behaviour is anticipated as discussed in section 5.2.

5.9 $Li_{1.5}Al_{0.5}Ge_{1.5}P_3O_{12}$ –LMO (LAGP-LMO)

To further expand the knowledge base of LMO cold sintered composites, LAGP-LMO pellets were prepared. LAGP is unlikley seen as an additive to result in materials with a high *Qf*, since it is known to have a high Li ion mobility. However, Li^+ and PO_4^{3-} are likley to dissolve partially in water in a similar manner to the constituent ions of LMO. Hence, this composite has very different characteristics to many of the ones attempted throughout this study since all others are composed of a cold sintering with a non-cold sintering end-member. Consequently, the values of x at which high densities/mechanical integrity can be achieved should exceed 0.15. A nanopowder source of LAGP was chosen with a particle size of 50 nm. The high surface area of the nano LAGP is anticipated to make this phase readily soluble in water. Moreover, the mixture of MoO_4^{2-} and PO_4^{3-} ions may influence the crystallisation of amorphous phase.

0.05 LAGP-0.95LMO

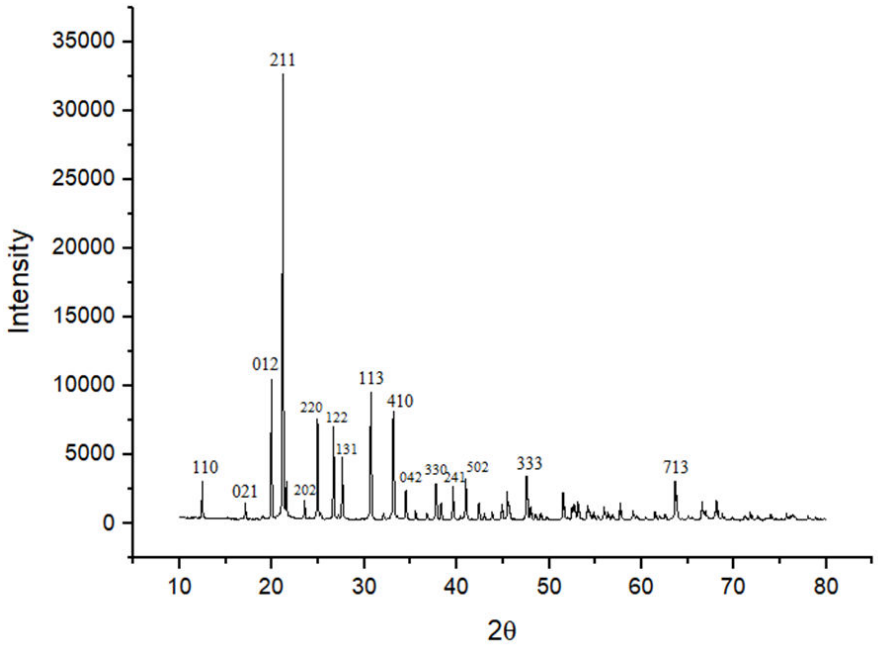

Figure 5.69. XRD of 0.05LAGP-0.95LMO. LAGP could not be detected.

Figure 5.69 shows XRD trace of 0.05LAGP-0.95LMO synthesised by cold sintering at 120 ^{o}C for 40 minutes at 69 MPa. The trace exhibits LMO phase but no LAGP is detected.

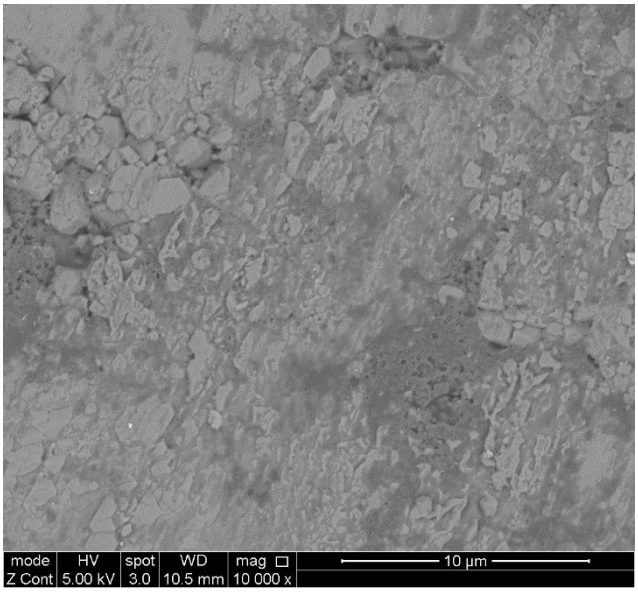

Figure 5.70. SEM of 0.05LAGP-0.95LMO. LAGP particles could not be observed

Figure 5.70 shows SEM image of dense composite of 0.05LAGP-0.95LMO with low porosity having a relative density of 93%. The contrast is inconclusive whether a single or two phase mix is present. Figure 5.71 and Figure 5.72 show energy dispersive X-ray spectra of 0.05LAGP-0.95LMO for two different areas. No clear evidence of an LAGP phase could be detected. 0.05LAGP-0.95LMO resonated at microwave frequencies with ε_r = 5.2 but a low *Qf* = 1959 GHz and TCF of -170 ppm/°C.

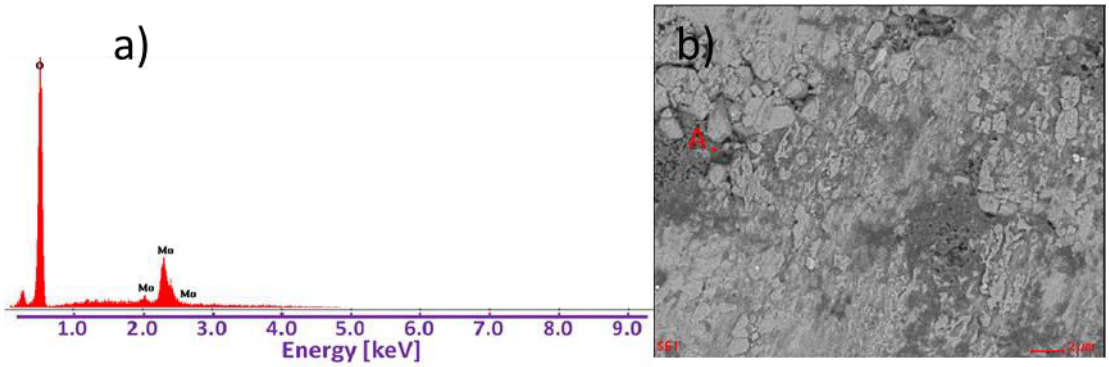

Figure 5.71. Energy dispersive X-ray spectrum of 0.05LAGP-0.95LMO a) from the area (A) selected in b)

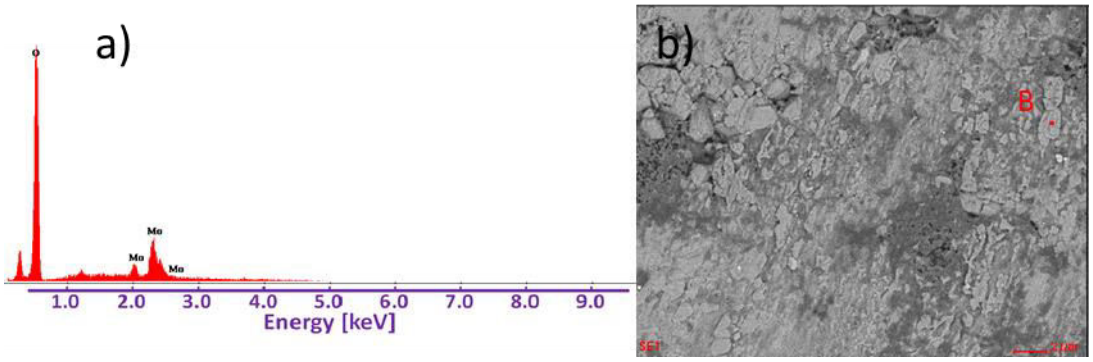

Figure 5.72. Energy dispersive X-ray spectrum of 0.05LAGP-0.95LMO a) from the area (B) selected in b)

Figure 5.73 shows spectroscopic plot of the relationship between the imaginary component of the electric modulus (M'') and frequency of cold sintered 0.05LAGP-0.95LMO measured at 43 ^{o}C where extracted R=7.4*10^{5}**Ω**cm, and C=1.71*10^{-12} F/cm.

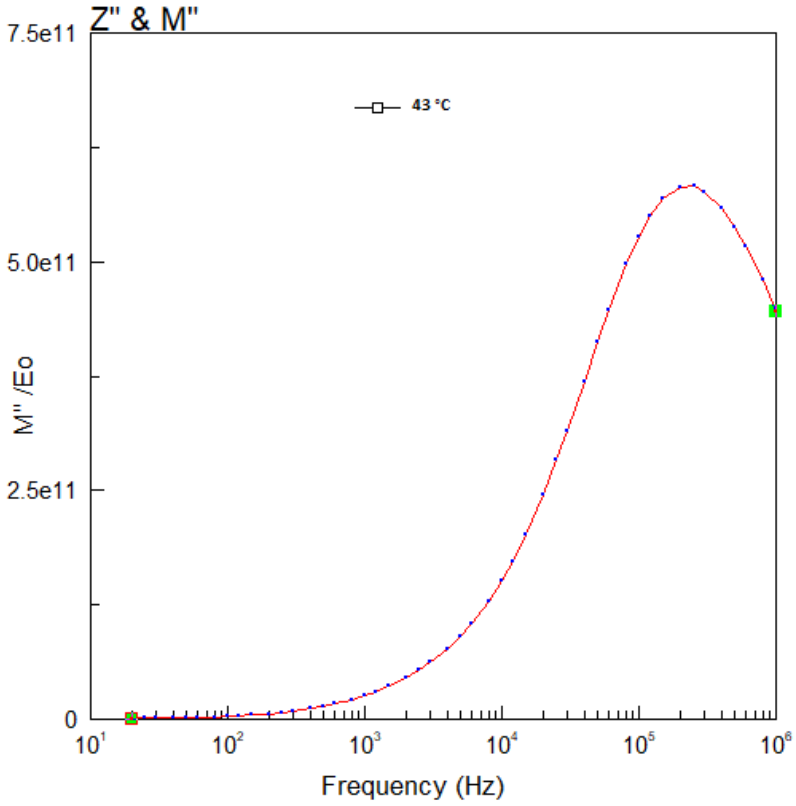

Figure 5.73. Spectroscopic plot of the relationship between imaginary component of the electric modulus (M'') and frequency of cold sintered 0.05LAGP-0.95LMO measured at 43 °C

0.1 LAGP-0.9LMO

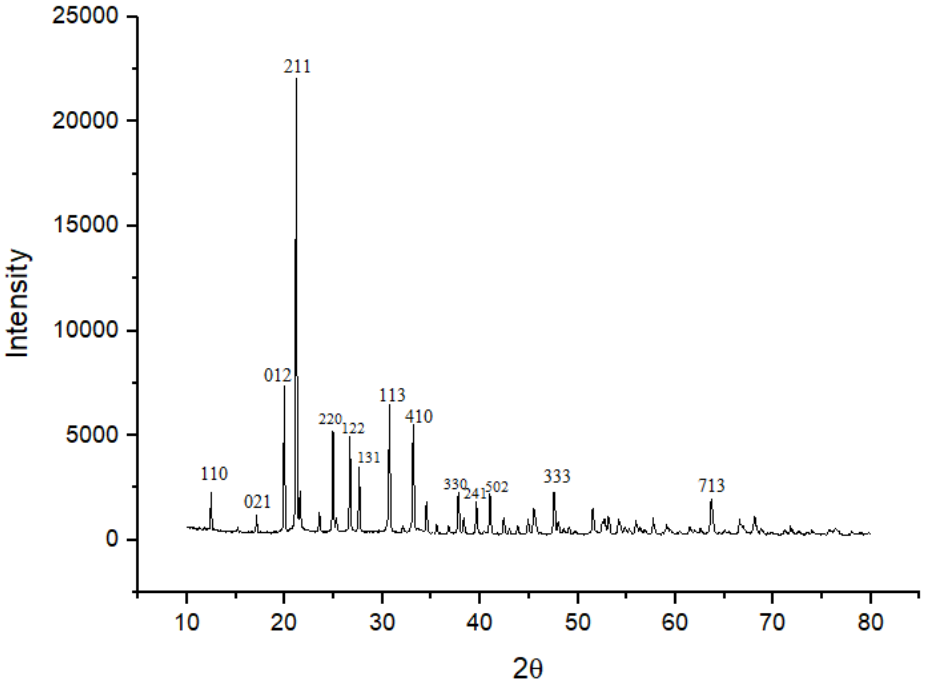

Figure 5.74. XRD of 0.1LAGP-0.9LMO, where LAGP phase couldn't be detected

Figure 5.74 shows an XRD trace of 0.1LAGP-0.9LMO synthesised by cold sintering at 120 ^{o}C for 40 minutes at 69 MPa. Peaks from LMO are present but the LAGP phase could not be detected. Figure 5.75 shows an SEM image of a dense (95%), 0.1LAGP-0.9LMO composite featuring very low porosity. Only one phase was evident from the contrast in the image and from energy dispersive X-ray spectroscopy, Figure 5.76 and Figure 5.77. 0.1LAGP-0.9LMO resonated at microwave frequencies with ε_r = 6, Qf = 1200 GHz and TCF = -83 ppm/°C.

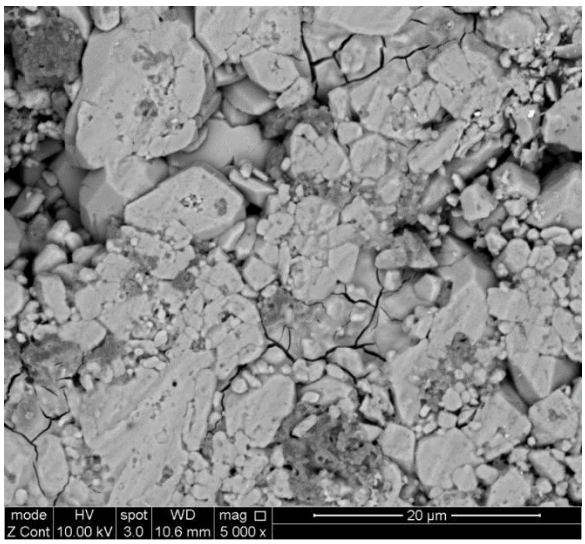

Figure 5.75. SEM of 0.1LAGP-0.9LMO. LAGP could not be detected.

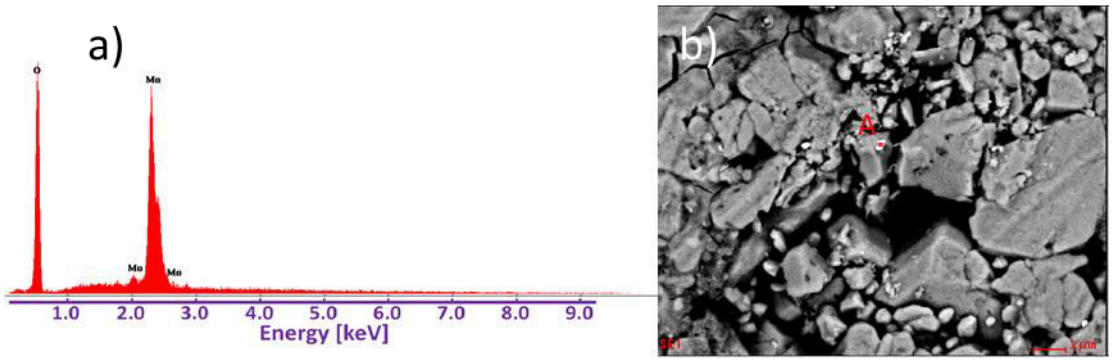

Figure 5.76. Energy dispersive X-ray spectrum of 0.1LAGP-0.9LMO a) from the area (A) selected in b)

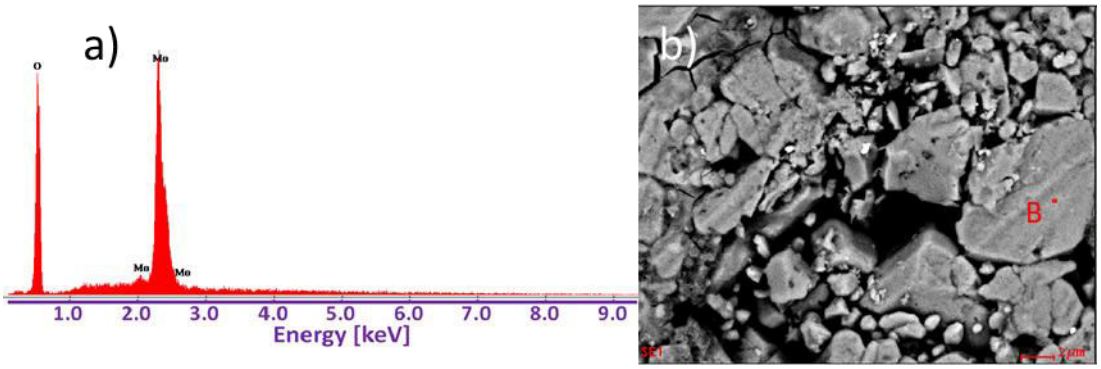

Figure 5.77. Energy dispersive X-ray spectrum of 0.1LAGP-0.9LMO a) from the area (B) selected in b)

Figure 5.78 shows spectroscopic plot of the relationship between the imaginary component of the electric modulus (M'') and frequency of cold sintered 0.1LAGP-0.9LMO measured at 45 ^{o}C where extracted R=2.5 *10^{5} **Ω**cm, and C= 2.48 *10^{-12} F/cm.

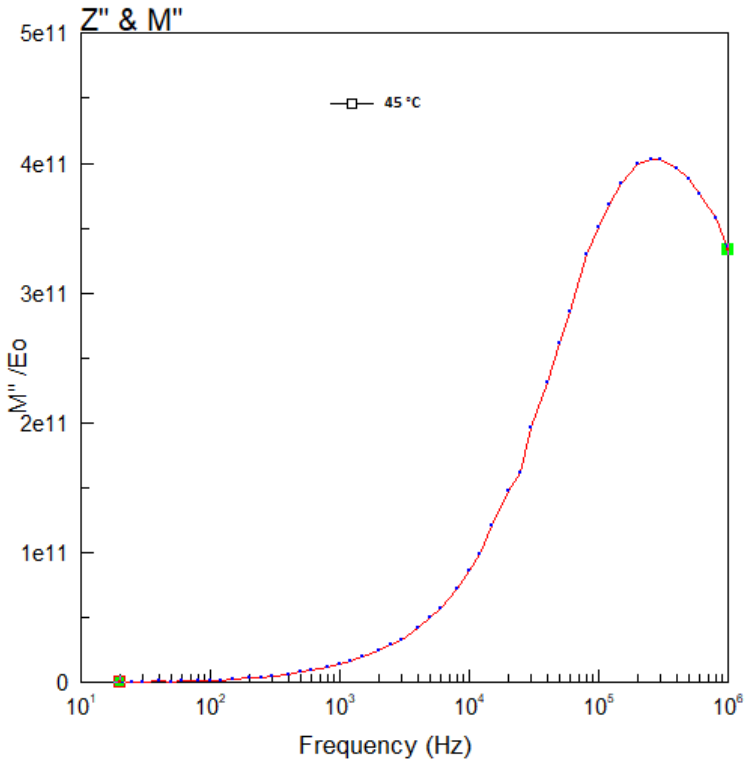

Figure 5.78. Spectroscopic plot of the relationship between the imaginary component of the electric modulus (M'') and frequency of cold sintered 0.1LAGP-0.9LMO measured at 45 °C

0.15 LAGP-0.85LMO

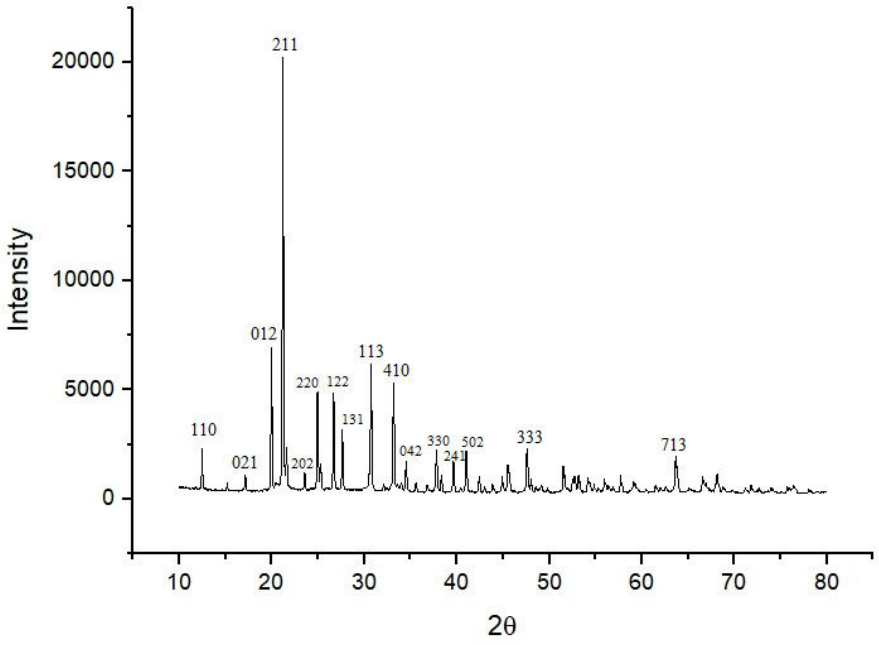

Figure 5.79. XRD of 0.15LAGP-0.85LMO. No LAGP was detected.

Figure 5.79 shows the XRD trace of 0.15LAGP-0.85LMO synthesised by cold sintering at 120 ^{o}C for 40 minutes at 69 MPa. The trace reveals only LMO.

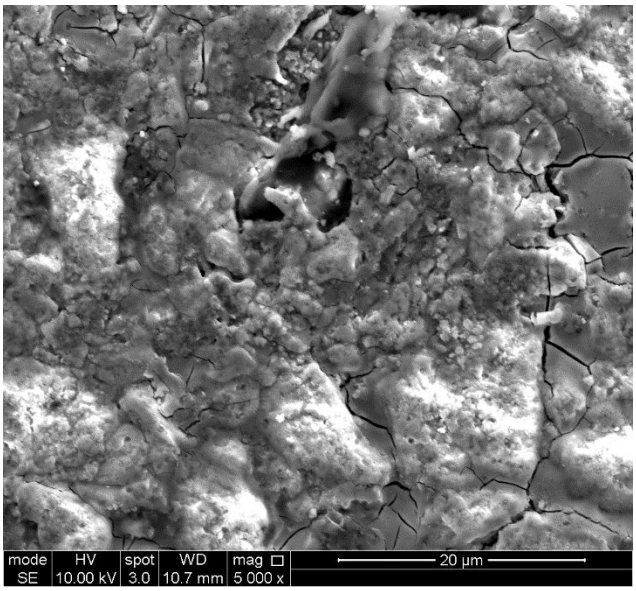

Figure 5.80. SEM of 0.15LAGP-0.85LMO, where phase of LAGP couldn't be detected in this measurement

Figure 5.80 shows an SEM image a composite of 0.15LAGP-0.85LMO with relative density, 94%. Only one contrast was apparent with Mo dominant in energy dispersive X-ray spectra, Figure 5.81 and Figure 5.82.

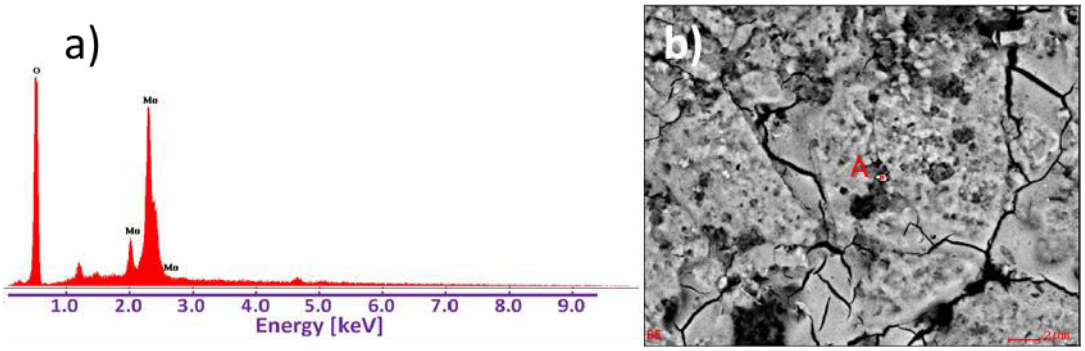

Figure 5.81. Energy dispersive X-ray spectrum of 0.15LAGP-0.85LMO a) from the area (A) selected in b)

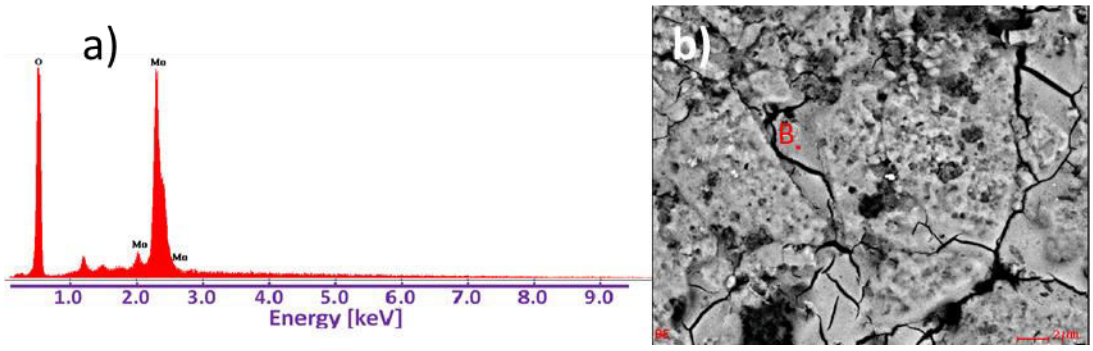

Figure 5.82. Energy dispersive X-ray spectrum of 0.15LAGP-0.85LMO a) from the area (B) selected in b)

0.15LAGP-0.85LMO resonated at microwave frequencies with ε_r = 6.3, *Qf* = 812 GHz and TCF = -43 ppm/°C. Figure 5.83 shows a spectroscopic plot of the relationship between the imaginary component of the electric modulus (M'') and frequency of cold sintered 0.15LAGP-0.85LMO measured at 42 °C where extracted R= 1.6 *10^5 **Ω**cm, and C=2.48*10^{-12} F/cm.

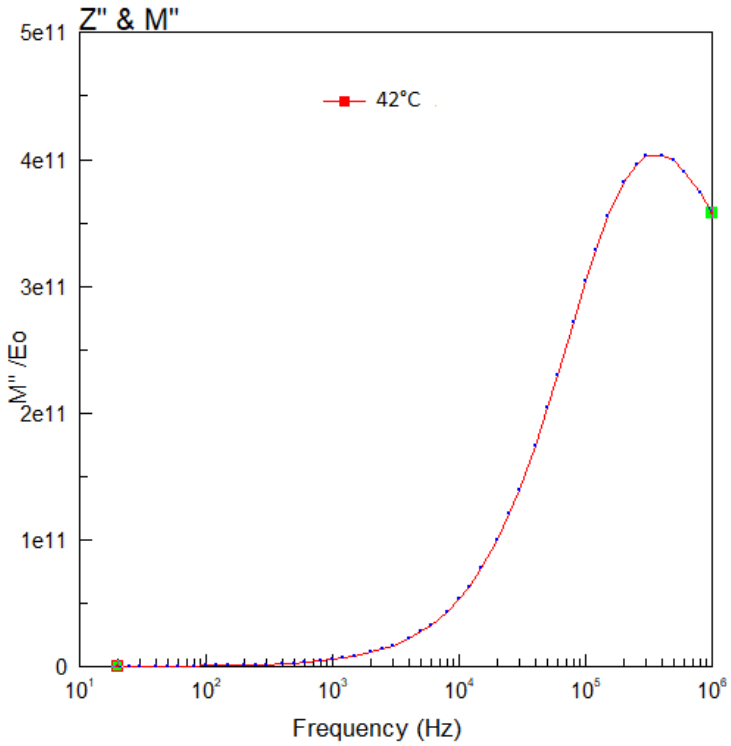

Figure 5.83. Spectroscopic plot of the relationship between the imaginary component of the electric modulus (M'') and frequency of cold sintered 0.15LAGP-0.85LMO measured at 42 °C

0.3LAGP-0.7LMO

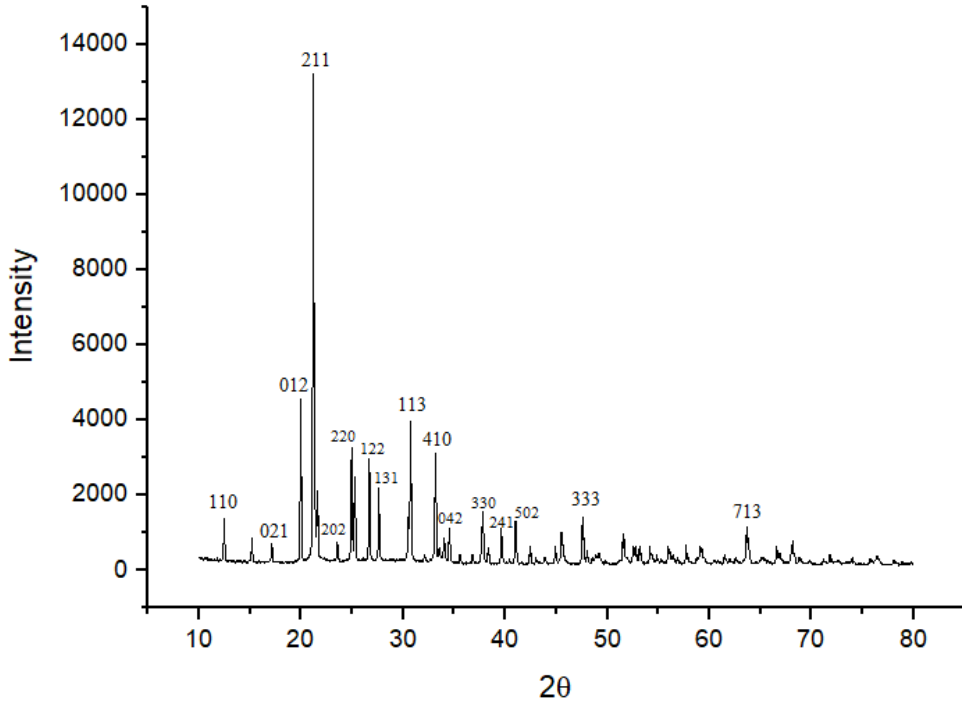

Figure 5.84. XRD of 0.3LAGP-0.7LMO. LAGP phase could not be detected.

Figure 5.84 shows an XRD trace of 0.3LAGP-0.7LMO synthesised by cold sintering at 120 ^{o}C for 40 minutes at 69 MPa. The trace reveals only LMO with no peaks identified for LAGP. The relative density of 0.3LAGP-0.7 LMO is 95% .

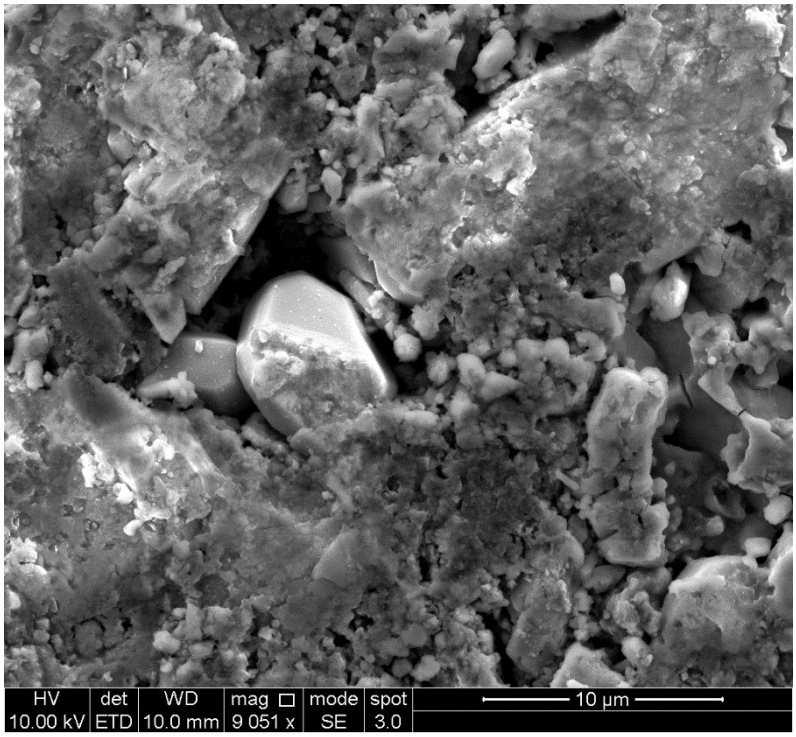

Figure 5.85. SEM of 0.3LAGP-0.7LMO, where dual phase could be detected clearer in Figure 5.86.

Figure 5.85 shows an SEM image with of composite of 0.3LAGP-0.7LMO. It was difficult to identify the different phases by SEM but EDS mapping, Figure 5.86 revealed for the first time regions of different composition, thereby confirming that at least two phases were present in the microstructure.

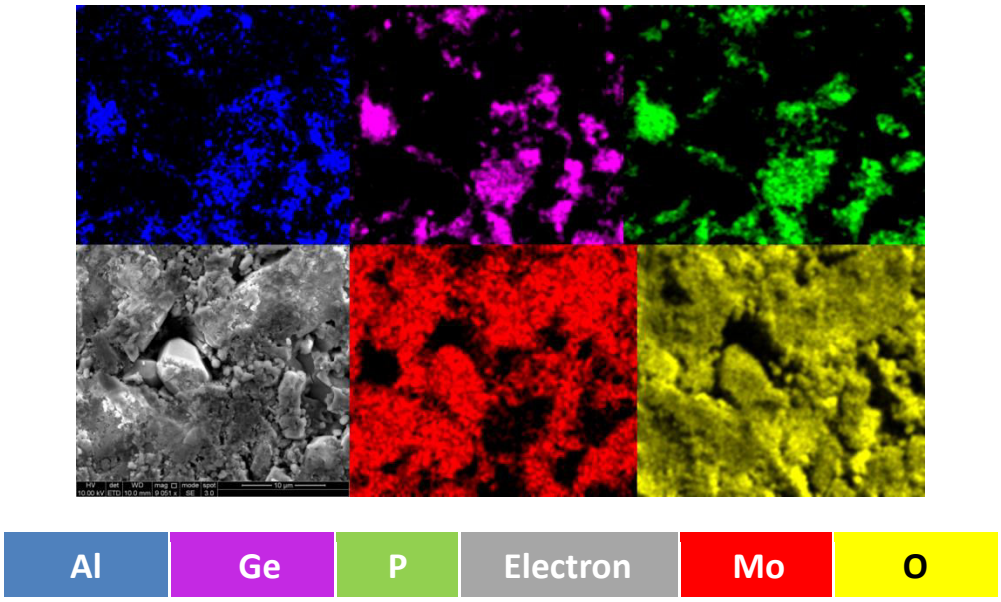

Figure 5.86. Energy dispersive X-ray mapping image of 0.3LAGP-0.7LMO, where each element is represented by a color in the key below image

In general, the absence of peaks of LAGP in the XRD traces of LAGP-LMO composites suggests that the LAGP almost fully dissolves during the cold sintering process and solidifies from solution into an amorphous phase. The absence of classic two phases contrast in SEM images again suggests that the LAGP has amorphised and formed a glassy phase through the microstucture. The low Z contrast of LAGP should make any phase appear darker in SEM images, the absence of clear regions of dark contrast may indicate that Li^+, PO_4^{3-} and MoO_4^{2-} ions all contribute to the composition of a glassy phase during precipitation in the cold sintering process. However, furtherwork is required to support this premise using TEM.

5.10 Conclusion

*x*BF12-(1-*x*)LMO composites were cold sintered at 120 ^{o}C and their microwave properties measured. All ceramics showed a good densification with low porosity and high quality factor. TEM showed no evidence of interaction of BF12 with LMO. ε_r increased to 5.8 for compositions with x = 0.15 with *Qf* = 17,000GHz while μ showed a systematic increase as a function of *x*. The impedance analysis accompanied by FEM suggest that for > 10 vol.% BF12 a percolation pathway exists in the composite with the current choosing the path of least resistance via the higher conducting BF12 phase. The combination of novel properties and easy integration into PCBs make cold sintered composites of this type attractive for future RF applications. Another seven composites were cold sintered at 120 ^{o}C as well and

had their properties measured. Composites based on K_2MoO_4 also showed promise and are worthy of further investigation from the perspective of MW properties. LAGP-LMO composites resonated poorly but achieved high densities and should be investigated further in terms of their ionic and electronic conductivities.

In general, unless the second end member also cold sinters (i.e. LAGP), the practical limit of composition was x = 0.15. Above this value, ceramics became brittle and lost mechanical integrity. Nonetheless as discussed above BF12-LMO composites show great promise as magnetodielectric substrates for RF applications.

5.12 References

[1] H. Kähäri, M. Teirikangas, J. Juuti and H. Jantunen, "Dielectric Properties of Lithium Molybdate Ceramic Fabricated at Room Temperature," *J. Am. Ceram. Soc.,* vol. 97, p. 3378–3379, 2014.

[2] D. J. Guo, D. H. Guo, A. L. Baker, P. M. T. Lanagan, D. E. R. Kupp, P. G. L. Messing and P. C. A. Randall., "Cold Sintering: A Paradigm Shift for Processing and Integration of Ceramics," *Angew. Chem. Int. Ed.,* vol. 55, p. 11457–11461, 2016.

[3] H. Guo, A. Baker, J. Guo and C. A. Randall, " Cold Sintering Process: A Novel Technique for Low-Temperature Ceramic Processing of Ferroelectrics," *J. Am. Ceram. Soc.,* vol. 99, p. 3489-3507, 2016.

[4] J. Guo, X. Zhao, T. H. D. Beauvoir, J. Seo, S. S. Berbano, A. L. Baker, C. Azina and C. A. Randall, "Recent Progress in Applications of the Cold Sintering Process for Ceramic–Polymer Composites," *Adv. Funct. Mater. ,* vol. 28, At. 1801724, 2018.

[5] F. Grant, "Properties of Rutile (Titanium Dioxide)," Rev. Mod. Phys, vol. 31, p. 646-674, 1959.

[6] G. Zhang, H. Wang, J. Guo, L. He, D. Wei and Q. Yuan, "Ultra-low Sintering Temperature Microwave Dielectric Ceramics Based on Na_2O-MoO_3 Binary System," J. Am. Ceram. Soc., vol. 98, p. 528-533, 2015.

[7] H. Guo, J. Guo, A. Baker and C. A. Randall, "Hydrothermal-Assisted Cold Sintering Process: A New Guidance for Low-Temperature Ceramic Sintering," ACS Appl. Mater. Interfaces., vol. 8, p. 20909−20915, 2016.

[8] J. Fisher, H. Sun, Y. Kook, J. Kim and P. Le, "Growth of single crystals of $BaFe_{12}O_{19}$ by solid state crystal growth," *J. Magn. Magn. Mater. ,* vol. 416, p. 384-390, 2016.

[9] A. Bahadoor, Y. Wang and M. Afsar, "Complex permittivity and permeability of barium and strontium ferrite powders in X, KU, and K-band frequency ranges," *J. Appl. Phys.,* vol. 97, At. 1853633, 2005.

[10] J.S. Dean, J.H. Harding and D.C. Sinclair, “Simulation of Impedance Spectra for a Full Three-Dimensional Ceramic Microstructure Using a Finite Element Model,” *J. Am. Ceram. Soc.,* vol. 97, p. 885-891, 2014.

[11] C. Rycroft, “VORO plus plus : A three-dimensional Voronoi cell library in C plus plus,,” *Chaos,* vol. 19, At. 3215722, 2009.

[12] J.P. Heath, J.S. Dean, J.H. Harding and D.C. Sinclair, “Simulation of impedance spectra for core-shell grain structures using finite element modeling,” *J. Am. Ceram. Soc.,* vol. 98, p. 1925-1931, 2015.

Chapter 6: General Discussion

The advantages of synthesising BF12-LMO composites by cold rather than using conventional solid state sintering are centred around fabricating dense ceramics consuming less energy throughout the process. Previous studies and research have proved the advantage of low temperature hydrothermal synthesis for sintering performance and minimizing the demand for Gibbs free energy changes [1]. The conventional sintering method demands high temperatures to make mass transport of molecules/ions easier, while CSP is considered more efficient since the aqueous solution acts as a mediator. LMO has been fabricated both traditionally and by CSP. The cold sintered LMO showed an ε_r of (5.3) and relative density (97%), but slightly lower *Qf* (24,320GHz), while the conventionally sintered LMO has been measured with the values of 5.4, 96% and 42,000 GHz for ε_r, relative density and *Qf*, respectively. Further studies are required to understand the slight difference in *Qf* between cold and conventionally sintered ceramics which should include manipulation of sintering conditions such as temperature, pressure and holding time as well as extensive microstructural characterisation.

The impedance analysis of cold sintered composite BF-LMO showed a conductivity lying between end members. The extracted activation energy from Arrhenius plot for the cold sintered BF-LMO composite is 0.25 eV. Those results suggest a percolation pathway favoring the higher conducting and least resistive path of BF12 in the composite. Transmission electron microscopy (TEM) images of BF-LMO composites showed two phases only with no interaction. The densification occurs by dissolution of LMO that surrounds BF grains in water, which themselves do not dissolve. The pressure and temperature in the die result in particle rearrangement and then crystallisation/deposition of a nano-crystalline/amorphous LMO phase around the BF12, as confirmed by HRTEM images.

The reduction in energy associated with cold in comparison to conventional sintering has been the main driving force for the research. However, the lateral dimensions in cold sintering are precisely confined to the width of the die and could reduce the need for extensive post sinter machining of parts to tune their dielectric properties. This latter advantage is important for the fabrication of low-cost RF substrates and devices and could, coupled with the low densification temperature, revolutionize the use of ceramics in RF devices. In addition, it facilitates the ready fabrication of multilayers and graded structures, since in plane shrinkage is absent in cold sintering.

Overall, very good microwave properties have been measured of cold sintered BF12-LMO composites with $17{,}000<Qf<22{,}000$ GHz and $5.6<\varepsilon_r<5.8$ and high relative density (94-97%). Comparison with commercially available dielectric resonators such as $SrTiO_3$- $LaAlO_3$,

Qf = 70,000 GHz, ε_r = 39 are unfavourable but the low sintering temperature and ease of processing classes them equally alongside polymeric materials and thus they have a far greater potential for direct integration into PCBs. In this latter context, the MW properties of BF12-LMO composites are exceptional with twice the ε_r and 2 orders of magnitude lower dielectric loss than achieved by typical polymeric RF substrates. In assessing therefore, the potential usefulness of cold sintered ceramics, it is best to take a pragmatic approach and consider what materials they might replace. 5G systems will operate at much higher frequencies (30 GHz) rather than 4G (1-2 GHz). As frequency increases so does dielectric loss and polymeric substrates may prove too lossy in some 5G applications. Cold sintered ceramic substrates may thus prove useful where loss is critical, though MoO_3 may prove to be a rather expensive raw material for mass production.

Measuring magnetic permeability μ at frequencies around 1-2 GHz turned out to be hard and challenging in this work. BF12-LMO composites were measured at X-band frequency (~8 GHz) in a waveguide using algorithms based on Nicolson-Ross-Weir method. The measured value was ~1 although a systematic increase in μ was observed as the concentration of BF12 increased. At first glance, this seems incongruous and disappointing but Bahadoor et al. [3] show μ = 1 for pure BF12 at frequencies from 8-26.5 GHz, since the mechanisms that give rise to high μ in oxides clamp out by these frequencies. Pellets for the waveguide method were 22.86 x 10.16mm with a thickness of about 2 mm and were cut by hand from 30x30mm sintered pellets. Inaccuracies in polishing to fit the waveguide structure may have affected the measurments. Direct fabrication to dimension where μ could be directly measured (11 mm x 16 mm x 4mm) resulted in ceramics without resonance within the desired frequency range. Attempts to measure μ at MHz frequencies using a wound coil and a network analyser also proved fruitless.

After searching the literature, it became apparent that many research groups had encountered such difficulties with very few examples of μ reported even for conventional ceramics. Not being able to measure μ meant that one initial objective of developing a composite with ε_r/μ = 1 could not be met. Nonetheless, 17,000<*Qf*<22,000 GHz was obtained for cold sintered composites of BF12-LMO far higher than any known convenetional magnetodielectric, suggesting that these substrates have the potential for applications in RF technology. BF12-K_2MoO_4 (BF12-KMO) with 14,000<*Qf*<18,000 GHz also showed promise but $Y_3Fe_5O_{12}$-Li_2MoO_4 (YIG-LMO) composites unexpectedly performed poorly, despite YIGs reputation as a high μ low loss material.

Most of the composites gave a high relative density (>93%) but *x*$BaTiO_3$-(1-*x*)LMO, and *x*BF12-(1-*x*)KMO composites show a consistent increase in relative density with increase of *x*. The solubility of the BF12 and $BaTiO_3$ are not high at 120 ^oC so this cannot account for the increase in density. Rather, it is more likely that the combination of these componenets have an ideal particle size distribution to enhance packing during the initial stages of cold sintering. Some composites like BF12-Na_2MoO_4 produced brittle samples containing

microcracks. Anticipated reasons for this cracking could be related to solubility level of compounds in addition to obtaining the right mechanical conditions of hot pressing such as amount of applied pressure, heating rate, sintering temperature and holding time that may lead to different packing conditions. It is worth noting that the manipulation of these conditions to optimise densification varies with the material. Since the cold sintering process is a dynamic process, there is still much to learn about how different composites perform during cold sintering.

To study what happens in cold sintering when each end member has partial solubility, $Li_{1+x}Al_xGe_{2-x}(PO_4)_3$- Li_2MoO_4 (LAGP-LMO) composites were fabricated. LAGP is best known as a potential solid state electrolyte in Li ion batteries[4] and generally as a conductive material, as Arrhenius plot shows in work of Cui et al. [4]. Consequently it was not anticipated that good MW properties would be produced. LAGP was hard to observe in the composites and it is speculated that the dissolution and preciptation has resulted in an amorphous phase containing phosphate and molybdate ions. LAGP-LMO densified readily however, with a high conductivity as measured by impedance spectroscopy.

Guo et Al [5] demonstrated that by adding a low volume fraction of polymer to ceramics through a cold sintering process better conductivity could be achieved. Guo et al [5] added LAGP with a low volume fraction of polymer (PVDF-HFP) to distribute between grain boundaries and enhance conductivity. In this thesis, LAGP has been mixed with LMO. Conductivity is promising at low temperatures for high LAGP concentration (see chapter 5) while the microwave properties indicated a poor *Qf*. Given the topical nature of LAGP and its potential for solid state batteries, it is recommended that these composites be the subject of future investigation as a matter of urgency.

6.1 References

[1] H. Guo, A. Baker, J. Guo and C. A. Randall, " Cold Sintering Process: A Novel Technique for Low-Temperature Ceramic Processing of Ferroelectrics," *J. Am. Ceram. Soc.,* vol. 99, p. 3489-3507, 2016.

[2] J. Guo, A. L.Baker, H. Guo, M. Lanagan and C. A. Randall, "Cold sintering process: A new era for ceramic packaging and microwave device development," *J. Am. Ceram. Soc.,* vol. 100, p. 669–677, 2017.

[3] A. Bahadoor, Y. Wang and M. Afsar, "Complex permittivity and permeability of barium and strontium ferrite powders in X, KU, and K-band frequency ranges," *J. Appl. Phys.,* vol. 97, At. 1853633, 2005.

[4] Y. Cui, M. Rohde, T. Reichmann, M. Mahmoud, C. Ziebert and H. J. Seifert, "Ionic Conductivity and Stability of the Lithium Aluminum Germanium Phosphate," *ECS Trans.,* vol. 72, p. 139-146, 2016.

[5] J. Guo, X. Zhao, T. H. D. Beauvoir, J. Seo, S. S. Berbano, A. L. Baker, C. Azina and C. A. Randall,

"Recent Progress in Applications of the Cold Sintering Process for Ceramic–Polymer Composites," *Adv. Funct. Mater. ,* vol. 28, At. 1801724, 2018.

Chapter 7: Conclusion

This study has resulted in the fabrication of a composite of BF12-LMO via cold sintering with high *Qf* (≃ 22,000 GHz) and $\varepsilon_r \simeq 5.6$. This novel sintering technique produced samples with high density and low porosity between grains which is impossible to achieve in conventional sintering technique due to unwanted parasitic phases. The combination of novel properties and easy integration into PCBs make cold sintered composites of this type attractive for future RF applications. Many other composites have been fabricated throughout this study using cold sintering process (CSP). Some of them worked well with high *Qf* such as K_2MoO_4-$BaFe_{12}O_{19}$ and some of them were brittle with low *Qf*.

7.1 $BaTi_4O_9$_$BaFe_{12}O_{19}$ composites (conventional sintering)

Conventional sintering of $BaFe_{12}O_{19}$-$BaTi_4O_9$ produced brittle and porous samples with strong interdiffusion and unwanted phases such as $BaFe_4Ti_2O_{11}$, $Ba_6Fe_{45}Ti_{17}O_{106}$. No MW resonance was observed for composites despite end member resonating well.

7.2 $BaFe_{12}O_{19}$-Li_2MoO_4 composites (cold sintering)

BF12-LMO composites were cold sintered at 120 ^oC and their microwave properties measured. All ceramics showed a good densification with low porosity and high quality factor. TEM showed no evidence of interaction of BF12 with LMO. ε_r increased to 5.8 for compositions with x = 0.15 with *Qf* = 17,000GHz while μ showed a systematic increase as a function of *x*. The impedance analysis data suggest that a percolation pathway exists in the composite with the current choosing the path of least resistance via the higher conducting BF12 phase. Moreover, finite element modelling highlights an interesting percolation threshold at 10% BF12 volume fraction of composite. The combination of novel properties and easy integration into PCBs make cold sintered composites of this type attractive for future RF applications.

7.3 K_2MoO_4-$BaFe_{12}O_{19}$ composites (cold sintering)

KMO-BF12 composite was cold sintered and produced dense samples with few pores. $x BaFe_{12}O_{19}$-$(1-x)K_2MoO_4$ resonated at microwave frequencies with a $6.4<\varepsilon_r<7.2$, TCF from -66 to -39 ppm/°C for $0.05<x<0.15$ and a *Qf* ≃14,000 GHz. The relative density of samples was ≃95%. No interaction was noted between the two end members according to XRD and EDS.

7.4 TiO_2-Li_2MoO_4 composite (cold sintering)

TiO_2-LMO composite has been cold sintered and produced dense samples with very few pores. $x TiO_2$-$(1-x)Li_2MoO_4$ resonated at microwave frequencies with a $5.95<\varepsilon_r<6.93$,

and 31,517<*Qf*<21,324 GHz for 0.05<x<0.1, and TCF = -97 ppm/°C for *x*=0.1. The relative density of samples was ≃93%. No interaction was noted between the two end members.

7.5 $Y_3Fe_5O_{12}$- Li_2MoO_4 composite (cold sintering)

YIG-LMO composite was cold sintered and produced dense samples with few pores. YIG-LMO resonated at microwave frequencies with a permittivity ε = 8.1 but a poor *Qf* (1416 GHz) for *x*=0.1. The relative density of samples was ≃94% with no interaction noted between the two end members.

7.6 $BaFe_{12}O_{19}$-Na_2MoO_4 composite (cold sintering)

Composites of Na_2MoO_4 and $BaFe_{12}O_{19}$ were brittle and contained microcracks with no MW resonance.

7.7 $BaTiO_3$-Li_2MoO_4 composite (nano $BaTiO_3$, cold sintering)

The mix of nano-sized BT3 with LMO resulted in brittle and microcracked samples, possibly because of the large difference in grain size between two end members and agglomeration of the nano BT3. However, no interaction was noted.

7.8 $BaTiO_3$-Li_2MoO_4 composite (micro $BaTiO_3$, cold sintering)

Micron-sized BT3 mixed with LMO avoided problems observed with nano powders (section 7.7). This was attributed to a better distribution of micron sized BT3 particles along LMO grain boundaries. The relative density increased with increase of *x* achieving ~98% for x = 0.15. Increasing *x* also resulted in increasing σ extracted from imaginary components of the electric modulus (M''). Microwave measurements however, revealed a poor *Qf* ≈1700 GHz.

7.9 The $Li_{1.5}Al_{0.5}Ge_{1.5}P_3O_{12}$ -Li_2MoO_4 composite (cold sintering)

LAGP-LMO composite was cold sintered and produced dense samples with few pores. *LAGP-LMO* resonated at microwave frequencies with 5.2<ε<6.3, -169 <TCF<-43 ppm/°C, and 812<*Qf* <1958 GHz for 0.05<*x* <0.15. The relative density of samples was ≃94%. LAGP was difficult to observe and was considered potentially amorphous after the cold sintering process.

Chapter 8: Future Work

This study has developed a composite of BF12-LMO via a cold sintering fulfilling a high *Qf* (22,000 GHz) and $\varepsilon_r \simeq 5.6$. Initially, it was intended to construct an MPA out of the best materials in the project but due to time constraints, this objective was not met. It is important therefore that the potential of these composites is realised within a prototype RF component in the near future.

A further objective of the research was to develop a matched ε_r/μ ceramic. Problems in measuring μ prevented this from being achieved despite several internal attempts and interactions with other groups. The measurements obtained are at the X band and therefore not representative of the low frequency μ which is anticipated to be higher. It is important therefore that this is rectified in the future with the fabrication of matched ε_r/μ still a realistic possibility for these materials.

Initial studies on LAGP – LMO composites looked promising for further study. Both end members cold sintered with a likely mixed molybdate/phosphate amorphous phase decorating the grain boundaries of the LMO, as the nano LAGP dissolved. LAGP is a known material with a high Li ion conductivity and this small study at the end of the PhD should be expanded to encompass a wider range of compositions and even the incorporation of other Li ion conducting systems such as Li-La garnets into the cold sintered composite.

High quality factor cold sintered Li_2MoO_4-$BaFe_{12}O_{19}$ composites for microwave applications

Sinan S. Faouri[1*], Ali Mostaed[1], Julian S. Dean[1], Dawei Wang[1], Derek C. Sinclair[1], Shiyu Zhang[2], William G. Whittow[2], Yiannis Vardaxoglou[2] and Ian M. Reaney[1*].

[1]Department of Engineering Materials, University of Sheffield, Sheffield, S1 3JD, UK.
[2]School of Electronic, Electrical and Systems Engineering, Loughborough University, Loughborough, UK.

Abstract

Ceramics-ceramic composites in the series $(1\text{-}x)Li_2MoO_4\text{-}xBaFe_{12}O_{19}$ (LMO-BF12, $0.00 \leq x \leq 0.15$) have been cold sintered at 120°C and their structure and properties characterized. X-ray diffraction, scanning electron microscopy (SEM) and transmission electron microscopy (TEM) confirmed that compositions were dual phase and had a dense microstructure. Composites in the xBF12-(1-x)LMO ($0.0 \leq x \leq 0.15$) series resonated at MW frequencies (~6GHz) with $5.6 \leq \varepsilon_r \leq 5.8$ and Qf =16,000-22,000 GHz, despite the black colour of compositions with $x > 0$. The permeability of the composites was measured in the X band (~8 GHz) and showed an increase from 0.94 (x=0.05) to 1.02 (x=0.15). Finite element modelling revealed that the volume fraction of BF12 dictates the conductivity of the material, with a percolation threshold at 10 vol.% BF12 but changes in ε_r as a function of x were readily explained using a series mixing model. In summary, these composites are considered suitable for the fabrication of dual mode or enhanced bandwidth microstrip patch antennas.

Keywords: *Cold sintering process, Ceramic material, Composite, Dielectric, Finite element modeling (FEM).*

* Corresponding Authors. Department of Materials Science and Engineering, University of Sheffield, Sheffield S1 3JD, UK.
E-mail addresses:
sinan_faouri@yahoo.com (S.S. Faouri)
i.m.reaney@sheffield.ac.uk (I.M. Reaney).

1. Introduction

Microwave (MW) dielectric ceramics have gained considerable attention because of their suitability for the fabrication of substrates, resonators and filters in wireless and satellite communication technology. Microstrip patch antennas (MPAs) have gained significant usage due to their light weight, ease of fabrication and low cost [1]. The main disadvantage of MPAs is their narrow bandwidth (BW) [2] since high permittivity (ε_r) substrates are used to shrink their dimensions to give ultra-small, high bandwidth antennas, the goal of any MW engineer. This classic paradox of increasing ε_r at the expense of BW and quality factor (*Qf*) stimulates designers to derive different methods to enhance bandwidth, such as the use of thicker substrates or parasitic patches [2]. However, thick substrates cause problems in impedance matching, while parasitic patches linearly increase the size of the antenna and complicate its design [2]. The 'holy grail' therefore is to design advanced materials [3] [4-6], composites or metamaterials [7-9] to act as dielectric substrates for MPAs which intrinsically result in larger bandwidths.

4G systems operate in the frequency range (2-8) GHz, while 5G systems will ultimately operate at up to 30 GHz. For low cost antennas that are used in 4G systems, substrates are often polymeric but their dielectric losses may prove too high for 5G applications. Thus, new low cost, low loss substrates may be required. Al_2O_3 has very low dielectric loss/high quality factor (*Qf* > 100,000) and suitable ε_r (10) but it is expensive to produce with a high sintering temperature (>1500 ^{o}C) and is difficult to directly integrate [10]. Al_2O_3 antenna chips are fabricated separately and mechanically attached as a standalone component. Ideally, low loss/high *Qf* ceramics are required which can be directly integrated into existing polymeric circuit boards, creating bespoke higher ε_r, high *Qf* patches for MW antennas and filters. This

would require that a MW ceramic has similar densification temperatures to that of the supporting polymer circuit board.

Ceramics such as Li_2MoO_4 (LMO) have recently been shown by Kahari et al. [11] to densify at 120-150 ^{o}C and thus may prove useful as replacements for polymers where loss is critical. LMO has suitable MW properties for MPAs with ε_r of ~ (5), and high *Qf* (30,000 GHz) [12]. Guo et al. [13] and Wang et al. [14] have demonstrated that cold sintering not only facilitates low temperature densification but also permits the fabrication of composites, hitherto impossible by conventional sintering due to the formation of unwanted parasitic phases at high temperature deleterious to properties [15-17]. Therefore, potential new substrate design space is available through cold sintering by the formation of composites with enhanced properties; the most attractive of which from an antenna perspective would be the inclusion of a magnetic phase to increase permeability, μ.

Ba hexaferrite, $BaFe_{12}O_{19}$ (BF12) is the most widely used material as a permanent magnet in the electroceramic industry, especially in magnetic storage systems, microwave devices and electromagnetic shielding due to its high Curie temperature and low cost [18, 19]. As with all magnetic materials, the permeability of BF12 is frequency dependent from MHz to 10GHz [20] but it is known to resonate with ε_r ~ 25 at MW frequencies albeit with a low *Qf* (2000 GHz, as measured in our study) [20-22]. It is therefore, an ideal end member in a composite ceramic to enhance the MW response of potential antenna substrates. In this contribution therefore, we demonstrate the ability to form dense *x*BF12-(1-*x*) LMO composites. We address the mechanism of densification via cold sintering and illustrate how both ε_r and μ are modified as a function of *x*. The increase in ε_r and conductivity as a

function of *x* is further highlighted through application of finite element analysis to the composite microstructure.

2. Experimental

2.1 Synthesis

Different proportions of BF12 (average grain size of ~2 μm) and LMO (average grain size of ~10 μm) were weighed and mixed for 24 hours using a variable speed ball mill. The resulting powders were sieved and mixed again using a pestle and mortar with 10-20 wt.% water. The wet powder was placed in either a 30×30 mm rectangular or 20 mm diameter cylindrical die applying 55-70 MPa pressure at 120 ^{o}C for 10–40 mins to achieve densification. The pellets were left in a dry furnace at 120 ^{o}C for 24 hours. The density of synthesised pellets calculated based on the geometry of the pellets and compared to theoretical values are listed in Table 1.

Table 1. Density (g/cm^3) of the cold sintered *x*BF12-(1-*x*)LMO samples.

x	Experimental (EX)	Theoretical (TH)	EX/TH (%)
0.05	2.91 ± 0.02	3.08	94 ± 2
0.10	3.08 ± 0.02	3.13	97 ± 2
0.15	3.02 ± 0.02	3.19	95 ± 2

2.2 Structural and Microstructural Characterisation

Crushed pellets of *x*BF12-(1-*x*)-LMO composites were analysed using a Bruker D2 Phaser X-ray diffractometer in the range, 10-80° 2θ at a scanning interval of 0.02^{o}. Scanning

electron microscopy (SEM) and energy dispersive X-ray spectroscopy (EDS) was carried out using a Japan Electron Optics Ltd (JEOL) Inspect F operating at 15kV equipped with an energy dispersive X-ray detector. Conventional transmission electron microscopy (TEM) was performed on an EM420 operating at 120 kV while high resolution transmission electron microscopy (HRTEM) was performed on JEOLR005 operating at 300 kV. TEM specimens were pre-thinned to a thickness of 20 - 50 μm by mechanical grinding in acetone and then ion milled to electron transparency using a GATAN precision ion polishing system (PIPS II).

2.3 Electrical Characterisation

Microwave dielectric properties of *x*BF12-(1-*x*)LMO sintered pellets were measured using a vector network analyser in a 20 mm diameter cavity with a current spacer of 4.87 mm. ε_r was calculated based on the dimensions and resonant frequency (f_o) and the quality factor (*Qf*) was determined from the width of resonant peak 3dB below its maximum height. *x*BF12-(1-*x*) LMO samples were also polished to match dimensions of a waveguide (22.86mm × 10.16mm with a thickness <2mm) and measured in the X band. Permeability (μ) was extracted using the Nicolson-Ross-Weir technique. Impedance spectroscopy (IS) was carried out on silver coated samples in a furnace connected to E4980A Precision LCR Meter, (20 Hz to 2 MHz) at 0.1V and from room temperature to 400°C.

3. Results

3.1 Structure and Microstructure

Figure 1 shows exemplar optical images of cold sintered *x*BF12-(1-*x*)LMO composites in which the black colour arises due to the presence of the ferrimagnetic BF12 phase. XRD

traces of cold sintered *x*BF12-(1-*x*)LMO are shown in Figure 2. Each trace depicts two structures, BF12 and LMO, with no evidence of parasitic phases arising from interfacial reactions. The relative intensities of the BF12 peaks increase with *x*. SEM images of *x*BF12-(1-*x*)LMO composites as a function of *x* are shown in Figure 3. The microstructure exhibits a two phase mix (as confirmed by EDX spectra, Figure 4) with smaller BF12 surrounding larger LMO grains and little porosity. Consistent with the XRD results, no secondary phases were observed in the SEM images.

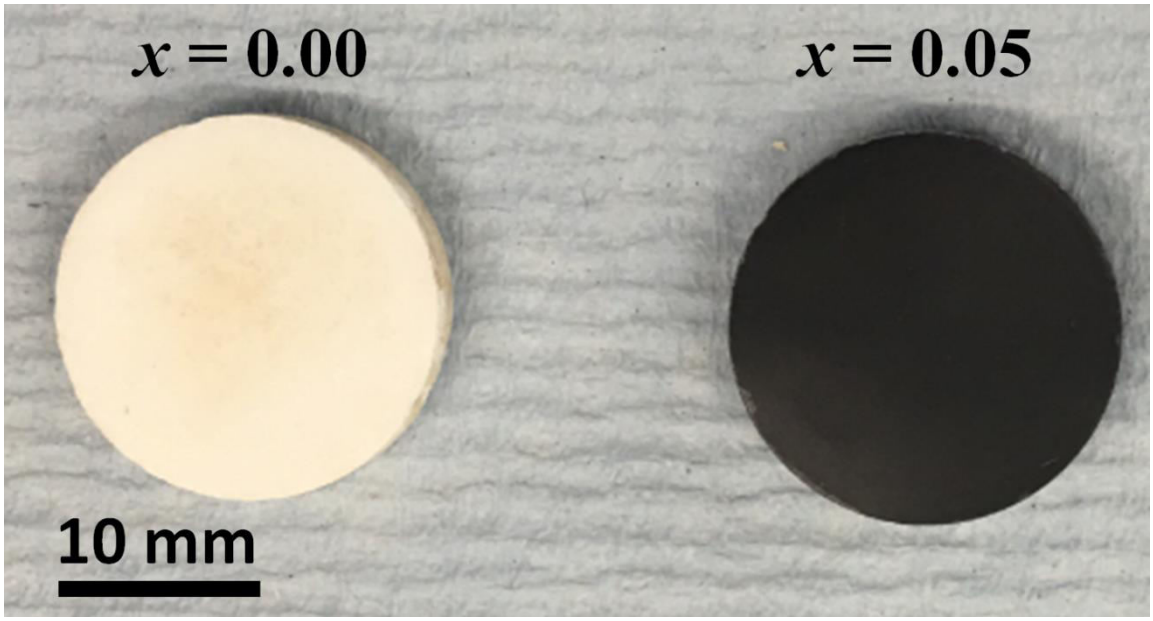

Fig. 1. Exemplar optical images of cold sintered *x*BF12-(1-*x*)LMO samples.

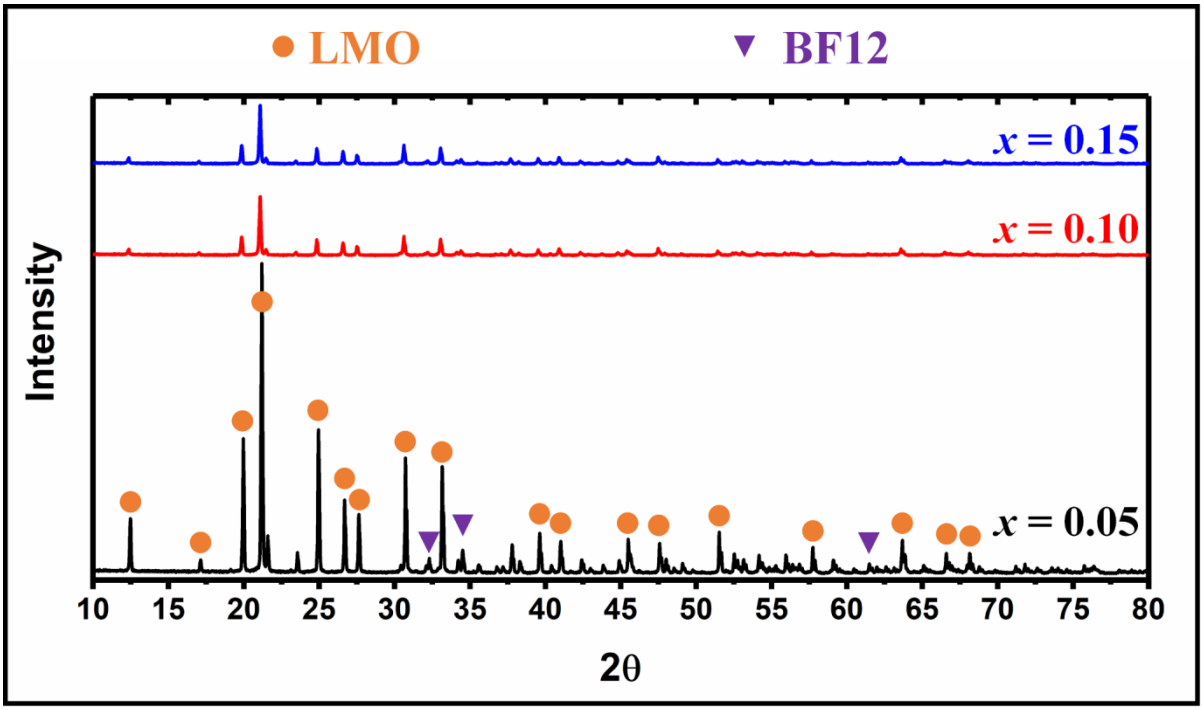

Fig. 2. XRD of cold sintered *x*BF12-(1-*x*)LMO samples.

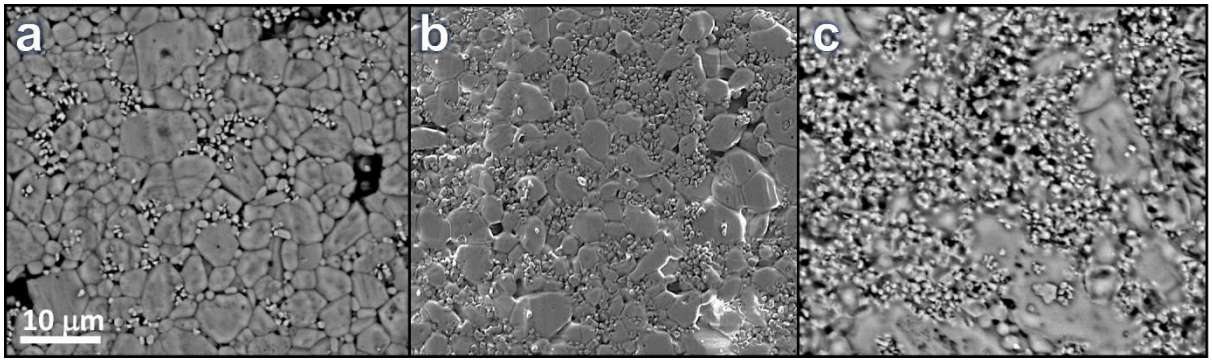

Fig. 3. SEM images obtained from cold sintered (a) 0.05BF12-0.95LMO, (b) 0.1BF12-0.9LMO and (c) 0.15BF12-0.85LMO samples.

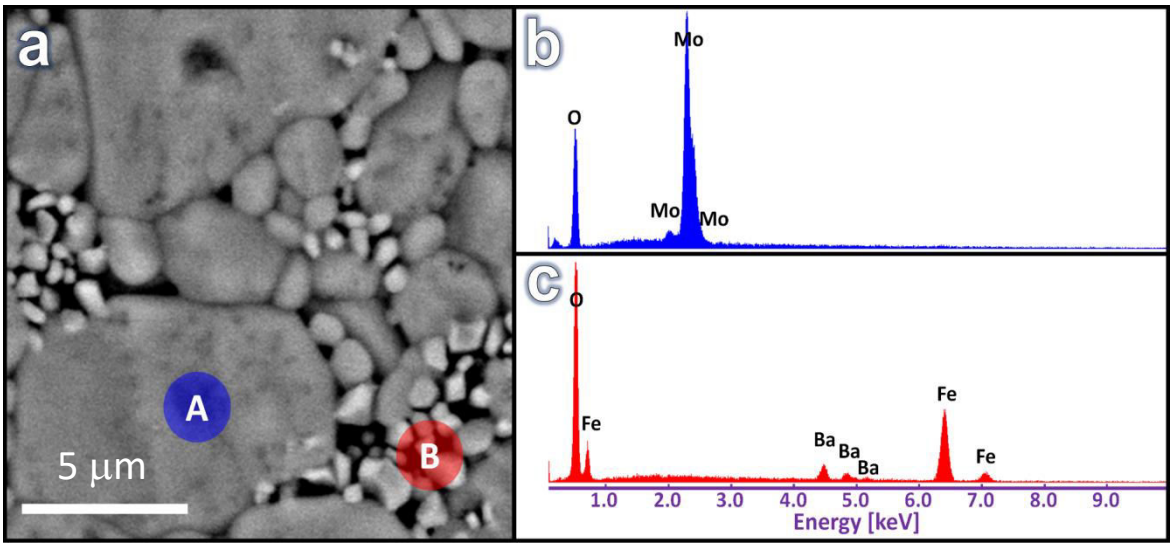

Fig. 4. (a) SEM image of obtained from the adjacent two phases in cold sintered 0.05BF12-0.95LMO sample (scale bar is 5 µm). (b) and (c) show representative energy dispersive X-ray spectra acquired from the large grains (area marked by "A" in (a)) and the small grains (area marked by "B" in (a)), respectively.

Figures 5 (a) and (b) are TEM images of grains of LMO and BF12 in cold sintered 0.15BF12-0.85LMO, respectively. Inset in Figures 5 (a) and (b) are [010] and [100] zone axis diffraction patterns from LMO and BF12, respectively which conclusivley identify each phase. The TEM images confirm the two phase mix identified by XRD and SEM. In addition, HRTEM images from the surface of BF12 particles (e.g. Figures 5(c-e)) reveal that LMO surrounds each grain of BF12. The mechanism of densification therefore, relies on the dissolution of LMO grains into the added water which under a combination of pressure and capillary action surrounds BF12 grains. The BF12 grains themselves do not undergo significant dissolution. Simultaneously, particle rearrangement and enhanced packing occur under pressure in the die. As water evaporates, Li^{+} and $(MoO_4)^{-2}$ ions crystallise on the

surface of the LMO and BF12 grains, thus densifying not only clusters of LMO particles but also regions of BF12. The net result is a dense composite with limited interaction between the end member phases. A schematic of this mechanism is shown in Figure 6.

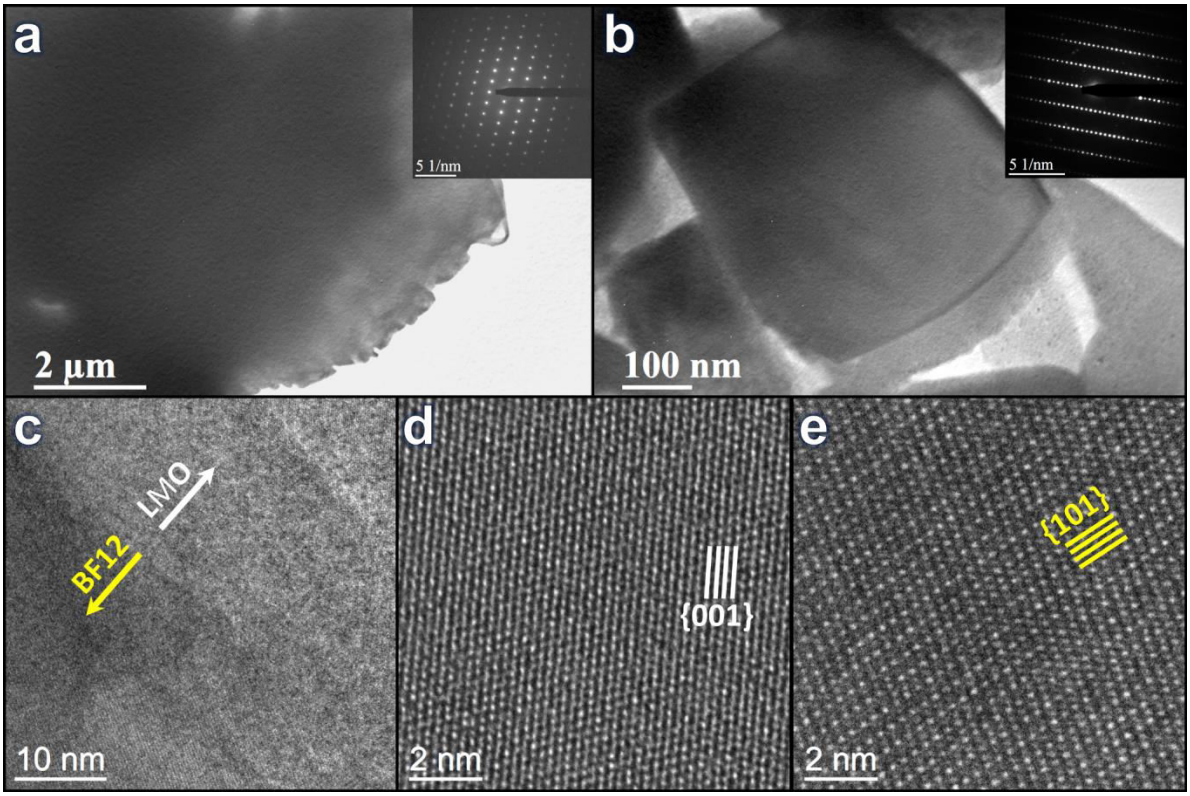

Fig.5 TEM image from cold sintered 0.15BF12-0.85LMO showing (a) a LMO grain; inset is the 010 zone axis diffraction pattern of the LMO grain. (b) a BF12 grain; inset is the 100 zone axis diffraction pattern of the BF12 grain. (c) An HRTEM image obtained from the interface of a BF12 and LMO grains. (d) and (e) show HRTEM images at a higher magnification from the LMO and BF12 sides of the interface shown in (c), respectively. Note that LMO surrounds the BF12 grains.

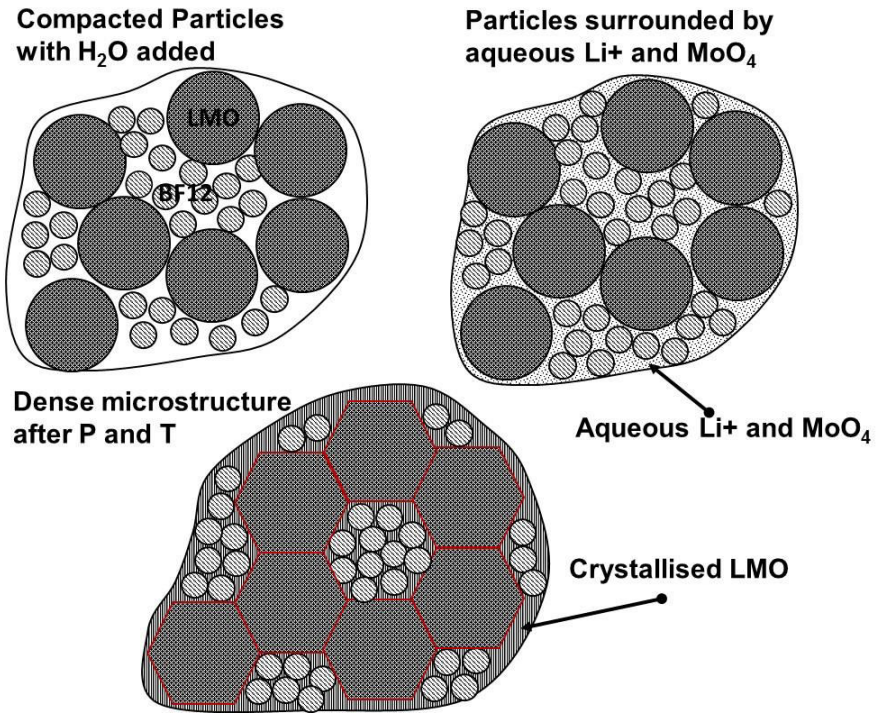

Fig. 6. Schematic representation of the densification of LMO-BF12 composites at 120 ^{o}C.

3.2 Electrical Properties

Figure 7(a) shows ε_r (black line) and *Qf* (blue line) as a function of *x*. ε_r increased with inceasing BF12 concentration but *Qf* decreased from around 24,000 GHz to 17,000 GHz. These results are consistent with BF12 having a higher ε_r (25) and lower *Qf* (<2000GHz) than LMO. However, the values of *Qf* are remarkably high for a composite material and show great promise for MW applications, provided there is also an enhancement in μ from the addition of the BF12 end member.

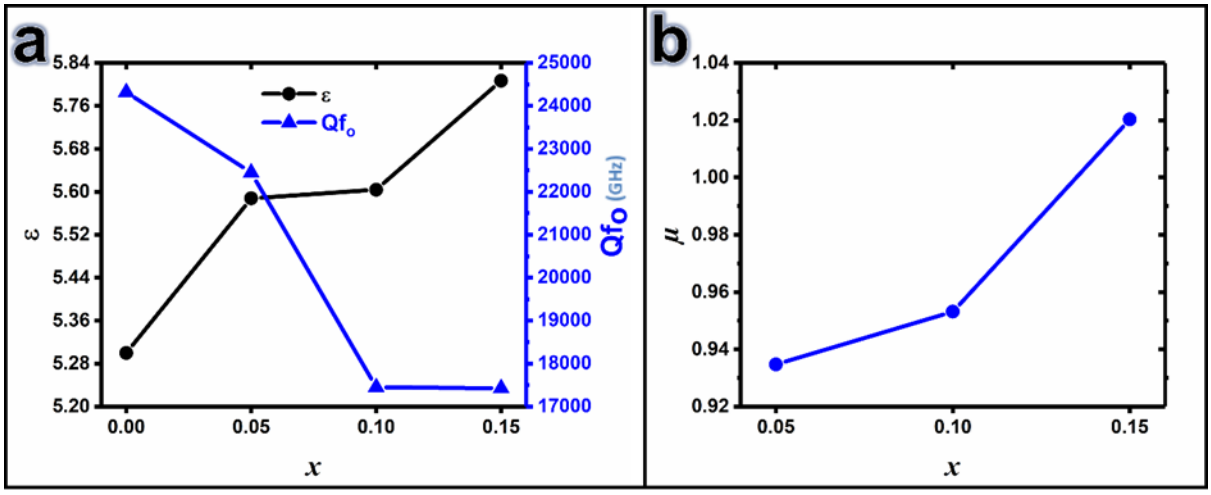

Fig. 7 (a) (ε, *Qf*) and (b) μ at X band frequencies *x*BF12-(1-*x*)LMO composites

Figure 7(b) shows μ measured in the X-band (~8 GHz) for *x*BF12-(1-*x*)LMO composites. μ increases with the volume fraction of BF12 from ~0.93 at x = 0.05 to 1.02 at x = 0.15, consistent with the measured values in the previous research works; e.g. Bahadoor et al. [20] showed μ = 1 for BF12 at frequencies from 8-26.5 GHz. Although these are comparatively low values, μ increases as frequency decreases in BF12, doped BF12 and their composites [23-27]. The increment in μ would therefore be substantial when frequency decreases to 0.5-3 GHz [23-27] and would contribute significantly to the EM response. Nonetheless, the values of μ attained in the X band suggest a systematic increase as a function of x coupled with a high *Qf*.

Figure 8 shows Arrhenius plots of bulk conductivity data obtained from spectroscopic plots of the imaginary components of the electric modulus (M'') which compare cold sintered 0.1BF12-0.9LMO composites with, conventionally sintered BF12 and conventionally sintered LMO. As expected, the BF12 ceramic has much higher bulk conductivity compared to LMO. The conductivity of the composite ceramics is intermediate in magnitude compared to the end members. The values of activation energy associated with the bulk response

extracted from the data reveal that cold sintered 0.1BF12-0.9LMO has an activation energy of 0.25 eV which is comparable to 0.29 eV of the more conductive end member (BF12) and is much lower than 1.28 eV associated with conventionally sintered LMO. These data suggest that a percolation pathway exists in the composite with the current choosing the path of least resistance via the higher conducting BF12 phase.

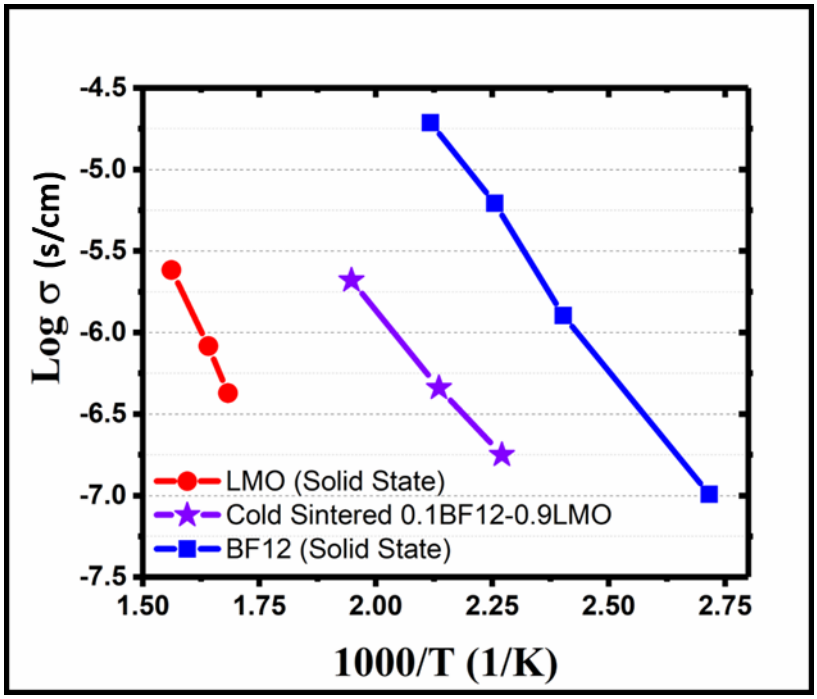

Fig. 8. Arrhenius plot of bulk conductivity of conventionally sintered ceramics of the end members with a cold sintered 0.1BF12-0.9LMO. NB: details for the fabrication of conevntionally sintered BF12 and LMO can be found in [28, 29], respectively.

3.3. Finite Element Modelling of the composite microstructure

Finite element modelling was used to study the *x*BF12-(1-*x*)LMO composite properties for various volume fractions. One challenge in replicating the composite is the simulation of a microstructure that consists of two distinct grain sizes. Adopting a Voronoi tessellation [30] is insufficient to replicate this microstructure, as the algorithm divides up the space

between the initial seed points. The small grains thus grow as they near the larger grains, generating a normal distribution. Here, we use a feature in Voro++ [31] known as radical Voronoi tessellation. Each discretized seed point is weighted with lower and higher values to give smaller and larger BF12 and LMO grains, respectively. A binomial grain size of polydisperse particles is generated which is matched to the experimental distribution. Each of the two materials is assigned experimental values from which we extract the room temperature σ (Figure 8) and ε_r. The values extracted for LMO gave $\sigma = 2.26\times10^{-15}$ Scm^{-1} and $\varepsilon_r = 5.33$, compared to $\sigma = 4.07\text{x}10^{-8}$ Scm^{-1} and $\varepsilon_r = 25$ for BF12. Various volume fractions of LMO were then simulated, generating approximately 2000 small grains for a pure BF12 model, and over 500 large grains for LMO (Figure 9a). The structures were then meshed with between 1-2 million tetrahedral elements and run using the *in-house* finite element package ElCer [30] to simulate the effective ε_r and σ [30, 32].

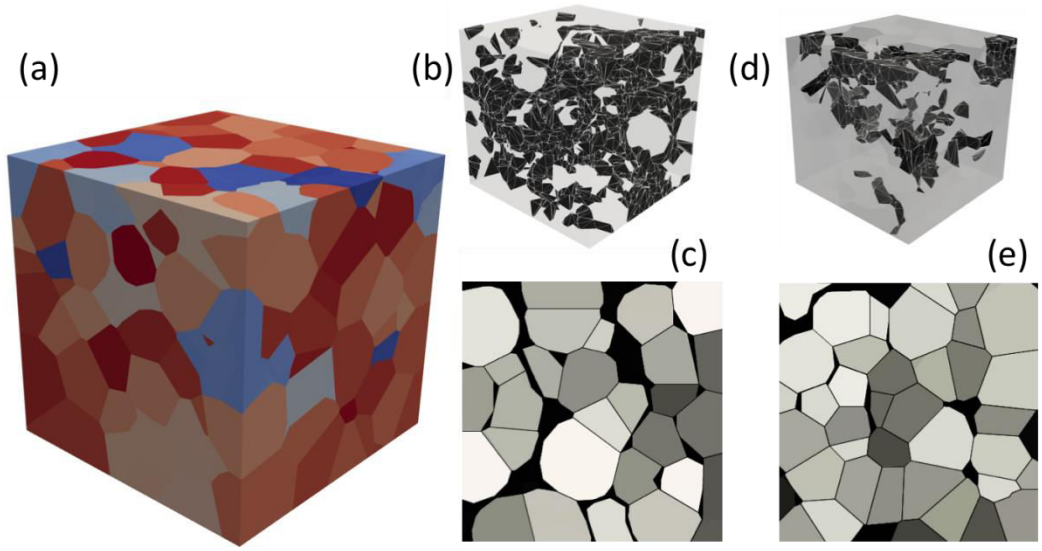

Fig. 9. (a) an example of the full 3D finite element microstructure containing between 500 - 1500 individual grains of an a LMO microstructure. (b) and (d) show the microstructure, by displaying the smaller more conducting BF12 grains in black. (c) and (e) are slice plots of the

models where for simplicity, the black regions are designated as collections of small BF12 grains. For a volume fraction with 20%BF12 (b and c), a continuous network of BF12 grains describes a conductive path from the top to the bottom but which is absent for 5 vol% BF12 (d and e).

In generating these microstructures, the volume fraction of the smaller BF12 is crucial since they surround the larger LMO grains and relatively few are needed to create a conductive network. The BF12 grains effectively by-pass the resistive LMO grains, as shown in Figures 9(b) and 9(c) for 20 vol.% BF12. At lower values of *x*, these paths become discontinuous with gaps forming, Figures 9(d) and 9(e) for 5 vol.%. This percolation threshold is observed directly in the measured σ. Figure 10 highlights the extracted σ and ε_r arising from the FEM simulations. For 5 vol.% BF12, σ rises but at 10 vol.% there is a discontinuous change, attributed to the formation and conducting pathways. For > 10 vol.% BF12, there is gradual convergence towards σ of the BF12 end member. However, for ε_r no percolation effect is observed and the value tends towards LMO, consistent with a parallel summation, predicted by series mixing rules:

$$\frac{1}{\varepsilon} = \frac{V_{BF}}{\varepsilon_{BF}} + \frac{V_{LMO}}{\varepsilon_{LMO}} \quad (1)$$

where V_{BF}, V_{LMO}, ε_{BF} , ε_{LMO} are the volume fractions and ε_r of the BF and LMO phases, respectively.

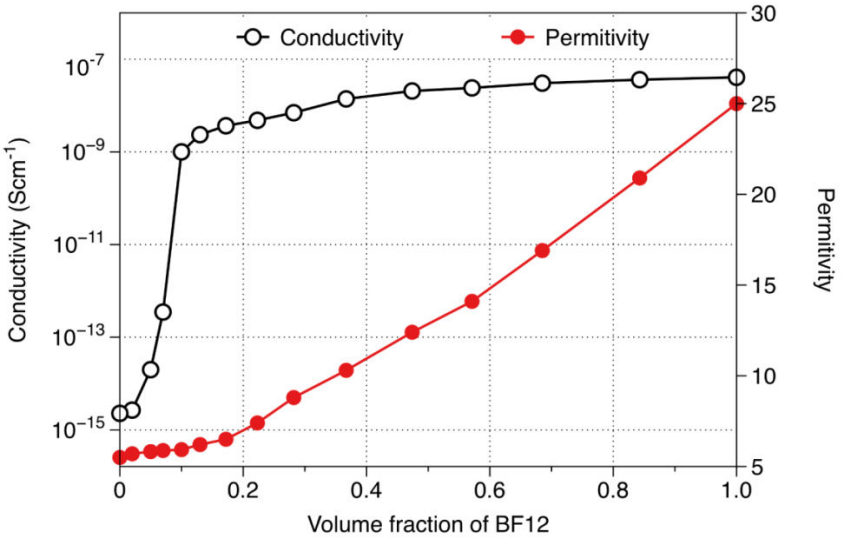

Fig. 10. The extracted conductivity (σ) and permittivity (ε_r) from the finite element simulations highlighting a percolation threshold for conductivity below for $x < 0.1$ volume fraction.

4. Discussion

Cold sintered composites of *x*BF12-(1-*x*)LMO offer several advantages over there conventionally sintered counterparts. Cold sintering is a more efficient processing route for the fabrication of composites, reducing the energy consumed by approximately 50% with a commensurate reduction in CO_2 emissions. In addition, densification is achieved comparatively easily which is not the case for conventionally sintered composites. Most crucially, the negligible interaction between the end members results in only a limited decrease in *Qf* despite the addition of 15 wt% BF12, unlike during conventional sintering where interaction causes a catastrophic deterioration in properties [33, 34]. Guo et al. [13] compared cold with conventionally sintered LMO. They reported that cold sintered LMO showed superior ε_r (5.6 against 5.5) but lower *Qf* (30,500 against 45,000GHz) than conventionally sintered ceramics [13]. One further advantage often overlooked, is that the lateral dimensions in cold sintering are precisely confined to the width of the die, i.e there is

zero lateral shrinkage. This reduces the need for extensive post-sinter machining of parts to tune their dielectric properties. This latter advantage is important for the fabrication of low cost RF substrates and devices and could, coupled with the low densification temperature, revolutionize the manufacturing of ceramics in RF devices.

As discussed by Randall and co-workers [13], cold sintered (120 ^{o}C) ceramics may be integrated with polymers and offer the potential through screen printing of the fabrication of layers of ceramic directly onto circuit boards, thereby enhancing ε_r, μ and *Qf* of the MW substrate. Recently, Wang et al. [14] reported temperature stable cold sintered composite with *Qf* ~ 7000 and ε_r ~17. The direct integration of *x*BF12-(1-*x*)LMO and related cold sintered materials onto PCBs may offer technological solutions in devices where the dielectric loss of the substrate is paramount or potentially when a dual mode RF response is required based on μ and ε_r.

Mechanical property measurements were not performed on these ceramics but they could be handled readily to perform all measurements. Moreover, the intended application would be as substrates integrated into PCBs in which the mechanical properties of the ceramic are less relevant than that of the module as a whole.

5. Conclusions

*x*BF12-(1-*x*)LMO composites were cold sintered at 120 ^{o}C and their microwave properties measured. All ceramics showed a good densification with low porosity and high quality factor. TEM showed no evidence of interaction of BF12 with LMO. ε_r increased to 5.8 for compositions with x = 0.15 with *Qf* = 17,000GHz while μ showed a systematic increase as a function of *x*. The impedance analysis accompanied by FEM suggest that for > 10 vol.% BF12

a percolation pathway exists in the composite with the current choosing the path of least resistance via the higher conducting BF12 phase. The combination of novel properties and easy integration into PCBs make cold sintered composites of this type attractive for future RF applications.

Acknowledgments

Ian M. Reaney and Julian S. Dean would like to acknowledge the Engineering and Physical Sciences Council (EPSRC) grants, EP/L017563/1 and EP/N010493/1.

References

[1] I. Singh, V.S. Tripathi, Micro strip patch antenna and its applications: a Survey, Int. j. comput. technol. appl. 2 (2011) 1595-1599
[2] C.L. Mak, K.M. Luk, K.E. Lee, Y.L. Chow, Experimental study of a microstrip patch antenna with an L-shaped probe, IEEE Trans. Antennas Propag. 48 (2000) 777-783
[3] A.A. Hanzaz, Development of microstrip patch antenna with change in materials and dimensions using MCM technology, 2016 5th International Conference on Electronic Devices, Systems and Applications (ICEDSA) (2016) 1-4
[4] M. Dashti, J.D. Carey, Graphene Microstrip Patch Ultrawide Band Antennas for THz Communications, Adv. Funct. Mater.28 (2018) At. 1705925
[5] G. Kaur, E.S. Goyal, To study the effect of substrate material for microstrip patch antenna, IJETT, 36 (2016) 490-493
[6] M. Islam, R. Rashidul Hasan, M. Rahman, K. Islam, S.M. Al-Amin, Design & Analysis of Microstrip Patch Antenna Using Different Dielectric Materials for WiMAX Communication System, iJES. 4 (2016) At. 5569
[7] C.V. Mahamuni, Performance enhancement of microstrip patch antenna using metamaterial cover, 2016 International Conference on Global Trends in Signal Processing, Information Computing and Communication (ICGTSPICC). (2016) 382-388.
[8] M. Mehrparvar, F. Hodjat Kashani, Microstrip antenna miniaturization using metamaterial structures, 20th Iranian Conference on Electrical Engineering (ICEE2012) (2012) 1243-1246
[9] N. Kulkarni, G.B. Lohiya, A Compact Microstrip Patch Antenna using Metamaterial, IJETT. 42 (2016) 365-369
[10] H.P. Wang, S.Q. Feng, W.Y. Yang, H.P. Ma, G.H. Jia, S.Q. Xu, Sintering behavior and dielectric properties of Al_2O_3 ceramics with $CaMgSi_2O_6$ addition, J. Ceram. Soc. Jpn. 120 (2012) 268-271
[11] H. Kahari, M. Teirikangas, J. Juuti, H. Jantunen, Improvements and Modifications to Room-Temperature Fabrication Method for Dielectric Li_2MoO_4 Ceramics, J. Am. Ceram. Soc. 98 (2015) 687-689
[12] H. Kahari, P. Ramachandran, J. Juuti, H. Jantunen, Room-temperature-densified Li_2MoO_4 ceramic patch antenna and the effect of humidity, Int J Appl Ceram Technol. 14 (2017) 50-55
[13] J. Guo, A.L. Baker, H.Z. Guo, M. Lanagan, C.A. Randall, Cold sintering process: A new era for ceramic packaging and microwave device development, J. Am. Ceram. Soc. 100 (2017) 669-677
[14] D.W. Wang, D. Zhou, S.Y. Zhang, Y. Vardaxoglou, W.G. Whittow, D. Cadman, I.M. Reaney, Cold-Sintered Temperature Stable $Na_{0.5}Bi_{0.5}MoO_4$-Li_2MoO_4 Microwave Composite Ceramics, ACS Sustainable Chemistry & Engineering, 6 (2018) 2438-2444.

[15] F. Zuo, A. Badev, S. Saunier, D. Goeuriot, R. Heuguet, S. Marinel, Microwave versus conventional sintering: Estimate of the apparent activation energy for densification of α-alumina and zinc oxide, J. Eur. Ceram. Soc. 34 (2014) 3103-3110
[16] R. Wroe, A.T. Rowley, Evidence for a non-thermal microwave effect in the sintering of partially stabilized zirconia, J. Mater. Sci. 31 (1996) 2019-2026.
[17] J. Wang, J. Binner, B. Vaidhyanathan, N. Joomun, J. Kilner, G. Dimitrakis, T.E. Cross, Evidence for the microwave effect during hybrid sintering, J. Am. Ceram. Soc. 89 (2006) 1977-1984
[18] D.A. Vinnik, A.Y. Tarasova, D.A. Zherebtsov, S.A. Gudkova, D.M. Galimov, V.E. Zhivulin, E.A. Trofimov, S. Nemrava, N.S. Perov, L.I. Isaenko, R. Niewa, Magnetic and Structural Properties of Barium Hexaferrite $BaFe_{12}O_{19}$ from Various Growth Techniques, Materials. 10 (2017) At. 10060578
[19] R. Nowosielski, R. Babilas, J. Wrona, Microstructure and magnetic properties of commercial barium ferrite powders, JAMME. 20 (2007) 307-310
[20] A. Bahadoor, Y. Wang, M.N. Afsar, Complex permittivity and permeability of barium and strontium ferrite powders in X, KU, and K-band frequency ranges, J. Appl. Phys. 97 (2005) At. 1853633
[21] K.K. Mallick, P. Shepherd, R.J. Green, Dielectric properties of M-type barium hexaferrite prepared by co-precipitation, J. Eur. Ceram. Soc. 27 (2007) 2045-2052
[22] S.V. Trukhanov, A.V. Trukhanov, V.G. Kostishyn, L.V. Panina, A.V. Trukhanov, V.A. Turchenko, D.I. Tishkevich, E.L. Trukhanova, O.S. Yakovenko, L.Y. Matzui, Investigation into the structural features and microwave absorption of doped barium hexaferrites, Dalton Trans. 46 (2017) 9010-9021
[23] X.G. Huang, J.A. Chen, L.X. Wang, Q.T. Zhang, Electromagnetic and microwave absorbing properties of W-type barium ferrite doped with Gd^{3+}, Rare Met. 30 (2011) 44-48.
[24] W. Jing, Z. Hong, S.X. Bai, C. Ke, C.R. Zhang, Microwave absorbing properties of rare-earth elements substituted W-type barium ferrite, J. Magn. Magn. Mater. 312 (2007) 310-313.
[25] Y.P. Wu, C.K. Ong, Z.W. Li, L. Chen, G.Q. Lin, S.J. Wang, Microstructural and high-frequency magnetic characteristics of W-type barium ferrites doped with V_2O_5, J. Appl. Phys. 97 (2005) At.1861514
[26] W. Yuping, Development of Barium Hexaferrite composite materials for microwave absorption, Department of Physics, National University of Singapore, Singapore (2006)
[27] Z. Su, Development of low loss Hexaferrite materials for microwave applications, Department of Electrical and Computer Engineering, Northeastern University, Massachusetts, USA (2016)
[28] J.G. Fisher, H.Y. Sun, Y.G. Kook, J.S. Kim, P.G. Le, Growth of single crystals of $BaFe_{12}O_{19}$ by solid state crystal growth, J. Magn. Magn. Mater. 416 (2016) 384-390
[29] H. Kahari, M. Teirikangas, J. Juuti, H. Jantunen, Dielectric Properties of Lithium Molybdate Ceramic Fabricated at Room Temperature, J. Am. Ceram. Soc. 97 (2014) 3378-3379
[30] J.S. Dean, J.H. Harding, D.C. Sinclair, Simulation of Impedance Spectra for a Full Three- Dimensional Ceramic Microstructure Using a Finite Element Model, J. Am. Ceram. Soc. 97 (2014) 885-891
[31] C.H. Rycroft, VORO plus plus : A three-dimensional Voronoi cell library in C plus plus, Chaos. 19 (2009) At. 3215722
[32] J.P. Heath, J. Dean, J. Harding, D. Sinclair, Simulation of impedance spectra for core-shell grain structures using finite element modeling, J. Am. Ceram. Soc. 98 (2015) 1925-1931
[33] M.M. Rahman, M.S. Sheak, S. Pervin, N. Uddin, F. Ahmed, M.A. Hossain, M. Rahaman, M.S. Bashar, T. Hossain, S. Akhter, Composition, Temperature and Frequency Dependent Magnetic, Dielectric and Electrical Properties of Magnesium-Zinc Ferrites, JBAS. 36 (2012) 199-212
[34] K. Singh, S.A. Band, W.K. Kinge, Effect of Sintering Temperature on Dielectric Properties of $Pb(Fe_{1/2}Nb_{1/2})O_3$ Perovskite Material, Ferroelectrics, 306 (2004) 179-185